TLJM

28

Maschinenbau
Lehrstuhl für
Umformtechnik
und Gießereiwesen

Christoph Hartmann

Spatio-Temporal Optical Flow Methods for Process Analysis

Robust Strain, Strain Rate, and Crack
Propagation Measurement in Shear Cutting

Schriftenreihe Umformtechnik und Gießereiwesen

Spatio-Temporal Optical Flow Methods for Process Analysis

Robust Strain, Strain Rate, and Crack Propagation Measurement in Shear Cutting

Christoph Hartmann

Imprint

dedicated to my family and above all to my wife Anna

Preface

This thesis was written during my work as a research associate at the Chair of Metal Forming and Casting at the Technical University of Munich. I would like to thank all colleagues, employees, and office mates for the great collaboration. Special thanks goes to my PhD supervisor, Prof. Dr.-Ing. Wolfram Volk, for his trust and support, both professionally and personally. At the same time I would like to thank Dr.-Ing. Roland Golle and Prof. Dr.-Ing. Hartmut Hoffmann for the joint technical and non-technical discussions. I would also like to thank Prof. Dr. Ir. Ton van den Boogaard (University of Twente, Vice Dean Research of the Faculty of Engineering Technology and Professor of Nonlinear Solid Mechanics), for his interest in my work, the technical debate on different topics, and for accepting the co-review. I am also grateful to Prof. Dr.-Ing. Wolfgang A. Wall (Technical University of Munich, Institute for Computational Mechanics) for taking over the chair of the examination.

I owe a great debt of gratitude to my whole family. I would like to thank my parents, Sandra and Bernd, for always having been and still being role models for me. All the time, I found myself in an environment that encouraged curiosity, creativity, and ambition. In this context, I would also like to thank my sisters Saskia, Alessa, Tamara, and Nadja for arguing different but meaningful perspectives on our world. They all deserve my utmost respect.

My deepest thanks, respect, and trust goes to my wife Anna, my greatest mentor. Together with our wonderful daughter, Mathilda, you were my support, inspiration, and companion. I am very proud to know you by my side.

The credo 'There is no failure except in no longer trying' (Elbert Hubbard) has accompanied me through this work. I am very glad, happy, and grateful that I had the chance to pursue this as a researcher and engineer. I would like to remain with this thesis, as Persian carpet weavers do with their artwork, and therefore stay with 'The maxim *Nothing avails but perfection* may be spelt *paralysis*' (Winston Churchill).

Christoph Hartmann
Munich, December 2020

Abstract

Shear cutting is an important, economic, and sustainable manufacturing process for the separation of sheet materials. The formation of the cut surface and, increasingly, the properties of the shear affected zone define the quality of the process. Many previous studies have dealt with the influence of process parameters, such as the cutting edge geometry, the cutting speed, and the cutting clearance, on the formation of the cut surface. However, the development of the shear affected zone has hardly been researched so far, especially when it comes to in situ experimental considerations.

With this thesis, I present an overall concept that allows to observe and to quantify the dynamic material behaviour in the shear affected zone from the beginning until complete separation of the sheet material. For this, two essential building blocks are required. On the one hand, I present a tool and sensor concept that allows high-resolution images of the shear cutting process. This is done under boundary conditions corresponding to those of the real process. The developed shear cutting tool meets the requirements of industrial precision stamping tools. On the other hand, I developed a spatio-temporal evaluation routine, which combine different enhanced methods of motion analysis. The motion and deformation fields are calculated using an adapted digital image correlation algorithm. I use variational approaches from computer vision, namely optical flow methods, for the robust calculation of dynamic field quantities and crack evolution. A hybrid framework controls and links all motion estimation algorithms. The algorithm framework further contains a dimensionality reduction routine to cope with the large experimental data from high-speed measurements.

I conducted experiments for closed cutting lines and open cutting lines. Cutting clearance, cutting edge geometry, and cutting velocity are varied for a steel and an aluminum sheet metal. The experimental results of each process configuration allow statements and yield trends about the development of the shear affected zone. I analyzed the material flow, strain localization, strain rate development, and the crack propagation for each of the conducted shear cutting experiments. Finally, I show how inverse analyses can be carried out with the experimental database, and how purely data-based process models may be created using the developed framework. I also show the potentials of the developed evaluation routine both for process analysis as well as for the entire field of experimental mechanics. The spatio-temporal optical flow methods enable the robust calculation of higher-order derivatives directly from the measurement data.

Contents

Nomenclature

Representation of Different Quantities

x, X, ξ, Ξ	scalar
$\mathbf{x}, \boldsymbol{\xi}$	vector
$\mathbf{X}, \boldsymbol{\Xi}$	higher-order tensor
$\boldsymbol{\mathfrak{x}}, \boldsymbol{\mathfrak{X}}$	functional, function, mapping, transformation
$\mathcal{X}, \mathbb{X}$	set, body, element, space

Operators

$(\cdot)^{\mathrm{T}}$	transpose
$(\cdot)^{-1}$	inverse
$(\cdot)^{-\mathrm{T}}$	transpose of the inverse
$\dot{(\cdot)}$	material time derivative
$\lVert \cdot \rVert_2$	$\mathcal{L}_2$-norm, $\mathcal{L}_2$ equivalent Frobenius norm
$\lVert \cdot \rVert_1$	$\mathcal{L}_1$-norm, $\mathcal{L}_1$ equivalent Frobenius norm
$\lVert \cdot \rVert_m$	$\mathcal{L}_m$-norm, $\mathcal{L}_m$ equivalent Frobenius norm
$\nabla(\cdot)$	material gradient operator
$\nabla \cdot (\cdot)$	material divergence operator
$\mathrm{argmax}(\cdot)$	arguments of the maximum
$\mathrm{argmin}(\cdot)$	arguments of the minimum
$\det(\cdot)$	determinant
$\inf(\cdot)$	infimum
$\ln(\cdot)$	natural logarithm
$\max(\cdot)$	maximum
$\min(\cdot)$	minimum
$\sup(\cdot)$	supremum
$\mathrm{tr}(\cdot)$	trace operator
$\times$	cross product
$\cdot$	dot product
$:$	double dot product

Superscripts and Subscripts

$(\cdot)_0$	reference configuration quantity
$(\cdot)_c$	cutting, clean shear
$(\cdot)_{co}$	coarsening
$(\cdot)_b$	burr
$(\cdot)_d$	edge draw-in
$(\cdot)_{eq}$	equivalent
$(\cdot)_f$	fracture
$(\cdot)_{mq}$	modified equivalent
$(\cdot)_{re}$	refinement

Selected Variables and Symbols

$\mathbf{0}$	zero tensor
α	angle
$\boldsymbol{\gamma}$	shear cutting process parameters
δ	step size, grid step
ϵ	threshold
ε	penalty parameter
λ	scaling factor, weighting factor
$\boldsymbol{\varphi}$	model parameters, cut surface model parameters
σ	noise
Γ	shear cutting process influencing parameters
Φ	shear affected zone model parameters
$\mathfrak{D}$	data term
$\mathfrak{R}$	regularization term
$\mathfrak{W}$	warping function
c	normalized motion curl
d	normalized density, Hausdorff distance
h	height
r	radius
s	sheet metal thickness
t	time
$\mathbf{u}$	displacement
w	width

$\mathbf{x}$	position
w	punch travel
E	strain measure
$\mathbf{E}$	strain tensor
$\dot{\mathbf{E}}$	strain rate tensor
F	cutting force
$\mathbf{F}$	deformation gradient
$\dot{\mathbf{F}}$	rate of the deformation gradient
I	image, image intensity
$\mathbf{I}$	identity tensor
W	cutting work

Abbreviations

Acronym	Meaning
aBIC	adjusted Bayesian information criterion
AIC	Akaike information criterion
BIC	Bayesian information criterion
bit	binary digit
CANDECOMP	canonical decomposition
DIC	digital image correlation
DIN	Deutsches Institut für Normung e.V.
DMD	dynamic mode decomposition
FFT	fast Fourier transformation
GIC	generalized information criterion
GT	ground truth
fwd	forward
LASSO	least absolute shrinkage and selection operator
MSSD	mean sum of squared differences
PARAFAC	parallel factor analysis
PC	principle component
PCA	principle component analysis
RAM	random access memory
ROI	region of interest
SOR	successive over relaxation algorithm
SVD	singular value decomposition
VDI	Verein Deutscher Ingenieure e.V.
ZSSD	zero-normalized sum of squared differences

1 Introduction

Data is currently revolutionizing how we do science. Gray, 2007 denoted this the fourth paradigm of science, namely, data-intensive scientific discovery (Hey, 2009, p. 5–11). Three paradigms led science so far: empiricism, theory, and computation. Each paradigm represents a fundamental approach to scientific knowledge. Empiricism draws conclusions from observations and experiments, such as the use of stars constellations for navigation. Theoretical science is based on axioms, strict mathematics, and analytical derivations. Einstein's theory of relativity is a prominent representative. Where analytical models became too expensive or impossible to solve, computational science provided and still provides new insights and approximated solutions for complex systems. Even mathematical proofs could be deduced using computers, such as the four color theorem by Appel et al., 1977 as well as Appel and Haken, 1977. The fourth paradigm is driven by the increasing amount of data available. Large data sets must necessarily be processed using software to extract information (Bell et al., 2009), to do measurements (Stephanopoulos et al., 2004), and to create models (Kaheman et al., 2019; Koch et al., 2020).

In my opinion, computational science and data science may be seen as the natural extensions of theory and empiricism with respect to high performance sensors, growing data storage capabilities, and increasing computational power that still obeys the law of G. Moore, 1965. Numerical analysis and simulations expand the possibilities to analyze and solve theoretical models, whereas data science enables to handle enormous amounts of empirical data and to separate signal from noise. Both schools do not exist separately but interact with each other. Induction and deduction, the two competing but often accompanying fundamental principles of obtaining scientific knowledge, connect empiricism and data science with theory and computational science. Hence, I argue that science is being revolutionized, but that we are experiencing a renaissance of observation-driven science and induction. Currently, modern data-based algorithms shift research and application in the direction of empiricism. How we understand, predict, and manipulate complex systems is based on data.

1.1 Data, Models, and Measurements

Engineers, such as I, are pragmatists. We have always tried to use appropriate combinations of theoretical and empirical tools to solve our problems. Dynamic problems deal with the changes

of states $\mathbf{z}(t) \in \mathbb{R}^n$ of a system evolving in time t. The evolution of the successive states $\mathbf{z}(t)$ may be called a process. Stability and continuity of the process deduce from the characteristics of the state changes. Phenomena such as deformation localization (Hadamard, 1903, p. 241–262; Asaro and Rice, 1977) or crack evolution (Barenblatt, 1962; Ramulu and Kobayashi, 1985) represent dynamic process effects in the field of solid mechanics. In a dynamic system[1]

$$\frac{\mathrm{d}}{\mathrm{d}t}\mathbf{z}(t) = \mathfrak{Z}(\mathbf{z}(t), t; \boldsymbol{\varphi}) \, , \tag{1.1}$$

the vector field $\mathfrak{Z}(\mathbf{z}(t), t; \boldsymbol{\varphi})$ models the process, where $\boldsymbol{\varphi}$ is the set of model parameters. Theory-driven analysis starts from the right hand side of equation (1.1), with the model $\mathfrak{Z}$. Solutions or approximated solutions, the left hand side of equation (1.1), come from analytical derivations or simulations. Observations and experiments are used to validate, verify, and assess the calculated results. Classical solid mechanics investigations follow this methodology and employ the right hand side of equation (1.1) to explore dynamic phenomena, as for example Arriaga and Waisman, 2017 in terms of deformation localization or Crump et al., 2017 regarding crack propagation.

In contrast, data-driven approaches start from the left hand side of equation (1.1) observing the evolution of the system over time. Either real or virtual experiments provide sensor signals $\mathbf{s}(t_i)$ that are snapshots of the system state $\mathbf{z}(t_i)$ at different points in time $t_i = t_0, t_1, t_2, \ldots, t_m$. This often non-structured information must be processed, whereby two variants basically exist. The first option is to calibrate model parameters $\boldsymbol{\varphi}$ from the data, which leads to ordinary regression problems. Here, data-driven and theory-driven approaches fuse under the term inverse analysis. The second option is to set up or identify a mapping $\mathfrak{Z}$ that describes the system for the task at hand and where the number of model parameters is variable. The number of parameters represents a measure of model complexity (Spiegelhalter et al., 2002). A meaningful model has to balance accuracy and precision with model complexity, which is strongly connected to the over- and underfitting problem.

Irrespective of their origin, models divide into white box, gray box, and black box models based on their physical interpretation. Theory-driven models fall into the range of white and gray models (Volk et al., 2019). On the contrary, data-driven models are no longer in the realm of gray and black models but also touch the white area, as Mazzocchi, 2015 and Silva et al., 2019 showed. Finally both, theory-driven and data-driven models depend on measurements, either for validation and verification purposes or for building a knowledge base to learn from.

Modeling and measuring blur in the context of data-driven analysis within their shared descriptive

---

[1]A nonlinear ordinary differential equation system serves as an illustrative example.

framework. Equation (1.1) is embedded in the descriptive framework that defines the system state, and to which models are oriented. Chronological sequences of measurements reflect the system dynamics, the left hand side of equation (1.1). Since the system state to be measured underlies the descriptive framework, the measurement itself does. In order to measure state quantities $\mathbf{z}_i$ at time $t_i = t_0, t_1, t_2, \ldots, t_m$, sensor signals $\mathbf{s}_i$ must be processed, which may be formalized using the forward operator $\mathfrak{M}$ with a parameter set $\boldsymbol{\varphi}$.

$$\mathbf{z}(t_i) = \mathfrak{M}\left(\mathbf{s}\left(t_i\right), t_i; \boldsymbol{\varphi}\right) \tag{1.2}$$

Equation (1.2) shows on the left hand side the system state analogue to equation (1.1), here discrete in time. Also, the right hand side of equation (1.2) presents almost identical in a way that the variables, $\mathbf{z}$ in equation (1.1) and $\mathbf{s}$ in equation (1.2) are processed by parameterized mappings, $\mathfrak{Z}$ and $\mathfrak{M}$. When the map $\mathfrak{M}$ is the identity, the sensor signal directly displays the systems state, such as with a ruler or protractor. The coastline paradox, the seemingly simple problem of determining the length of a coastline, shows that due to the descriptive framework dependency measuring is not an easy task, even for direct measurement (Mandelbrot, 1967). For indirect measurement the determination of $\mathfrak{M}$ becomes an act of modeling, still governed by the underlying descriptive framework. The most prominent among these models are characteristic curves. But those mappings $\mathfrak{M}$ grow increasingly complex, for example, to empower cars with spacial vision (Fernandez, 2018) or to reconstruct three-dimensional objects from computer tomography images (Bai et al., 2017). Data science both challenge and promote measurement technology. Engineers may expand their toolbox to tackle the left hand side of equation (1.1) utilizing such approaches to build interpretable models, to make meaningful measurements, and to solve complex problems.

1.2 Research of Manufacturing Processes

Industry 4.0 is the keyword under which data science enters production engineering (Bauer et al., 2018). To capture data, manufacturing processes must be equipped with sensors and measurement devices that feed intelligent algorithms. The acquired signals must somehow carry all relevant information[2] or at least allow to reconstruct it. The experimental research of manufacturing processes is basically confronted with the same engineering problems[3], which

---

[2]Already Helmholtz, 1887 stated this formally.
[3]Here, I focus on the engineering side and move computational challenges of Industry 4.0, such as real-time capability, into the background.

is to integrate sensors in test benches to observe certain process phenomena. Although scientists from other fields have been successfully using data-driven methods for decades (Langley and Zytkow, 1989), they have only been applied to a lesser extent for manufacturing process analysis.[4]

The separation of data capturing, curation, and analysis characterizes the fourth paradigm and even enables further progress (Szalay and Gray, 2006). In production engineering, however, data capturing, curation and analysis are difficult to divide compared to other fields for their strong interaction. This may be one reason, why practitioners and researchers often stay in their comfort zone working with established techniques, which cuts off almost completely potentials from the branch of data science (Montáns et al., 2019). Data-driven approaches show their capabilities especially in the analysis of complex processes. In modern production, almost every process becomes complex, since minimal downtime, enormous output, and highest accuracy and precision are expected. Among the prime examples is sheet metal processing. Along almost every process chain in sheet metal processing, from micrometer-thick foils to millimeter-thick planks, shear cutting is used to separate the material (Volk and Stahl, 2014).

At first glance, the shear cutting process may seem simple, like cutting paper using a pair of scissors. Given that each cut significantly affects further processing and the properties of the finished component, it is worth taking a closer look. Many works have been devoted to shear cutting, theoretical works, such as those of Bach, 1924 and Jimma, 1963, numerical works, such as those of Popat et al., 1989 and Taupin et al., 1996, and experimental works, such as those of Timmerbeil, 1957a and O. Kienzle and W. Kienzle, 1958. Current research approaches agree that simply looking at the resulting cutting-surface is no longer sufficient to assess and predict component quality (Hamada et al., 2018; Weiss et al., 2019). The so called shear affected zone, the volume of the sheet material that suffers or even benefits from shear cutting, is moving into the focus of research and already of industry, driven by key technologies of the future, such as e-mobility, digitization, and miniaturization. The functional surface of shear cutting becomes a functional volume, where each cut affects the volume's physical properties.

With this thesis, I try to add two things to the scientific discussion on the dynamics of shear cutting as a whole and especially with regard to the development of the shear affected zone: high-resolution insights through unique spatio-temporal full-field observation data, and tools from data science to process and evaluate my experimental work on shear cutting processes as a novel basis for validation, modeling, and design.

---

[4]Please note that at this point I distinguish between data-based and experience-based methods. Experience-based methods (empiricism) has a long tradition in engineering as a whole and also in production and industry.

2 Fundamentals and Framework

A physical theory needs three things: a language, a logic and semantics (Truesdell et al., 1967, p. 9). This statement has a striking analogy to the course of the data. Data creation, which is to express information in a certain language, data preparation, which is to arrange information in a logic, and data evaluation, which is to give information semantics. The classical modeling of physical phenomena uses differential calculus as universal language and logic for descriptions (Hamel, 1908). Semantics result from experience and abstraction, which are expressed with respect to the considered language and logic. Phenomenology is a prime example (Truesdell, 1952). This implies certain principles for the observation and analysis of processes, which also includes measurement techniques or numerical algorithms for their predictive solution.

In this chapter, I aim at presenting the language (consistent nomenclature), logic, and semantics utilized throughout this thesis. Continuum mechanics (section 2.1) serves as a basic skeleton for any formalization, the descriptive framework. Principles of data-driven analysis are covered in section 2.2. In section 2.3, I transfer the terminologies and principles of continuum mechanics and data science to motion estimation. Against this background, the shear cutting process is introduced in section 2.4, with a focus on in situ experimental observations.

2.1 Continuum Mechanics

Continuum mechanics provides a phenomenological theory framework for the description of objects under certain stimuli. In reality, these objects consist of matter. The discrete structure of matter is considered homogenized in space and if necessary in time. Each infinitesimal particle of the homogenized material can be equipped with certain properties. The general tensor calculus adds to mechanics mathematical language and logic. The continuous mathematical modeling of objects and stimuli lead to field quantities. Partial differential equations govern the fields, which yield spatio-temporal initial boundary value problems.

2.1.1 Kinematics

Kinematics describes the geometry of the motion of bodies without considering any stimuli as their cause. A body $\mathcal{B}$ consists of a coherent and compact set of material particles $\mathcal{P}$ with the
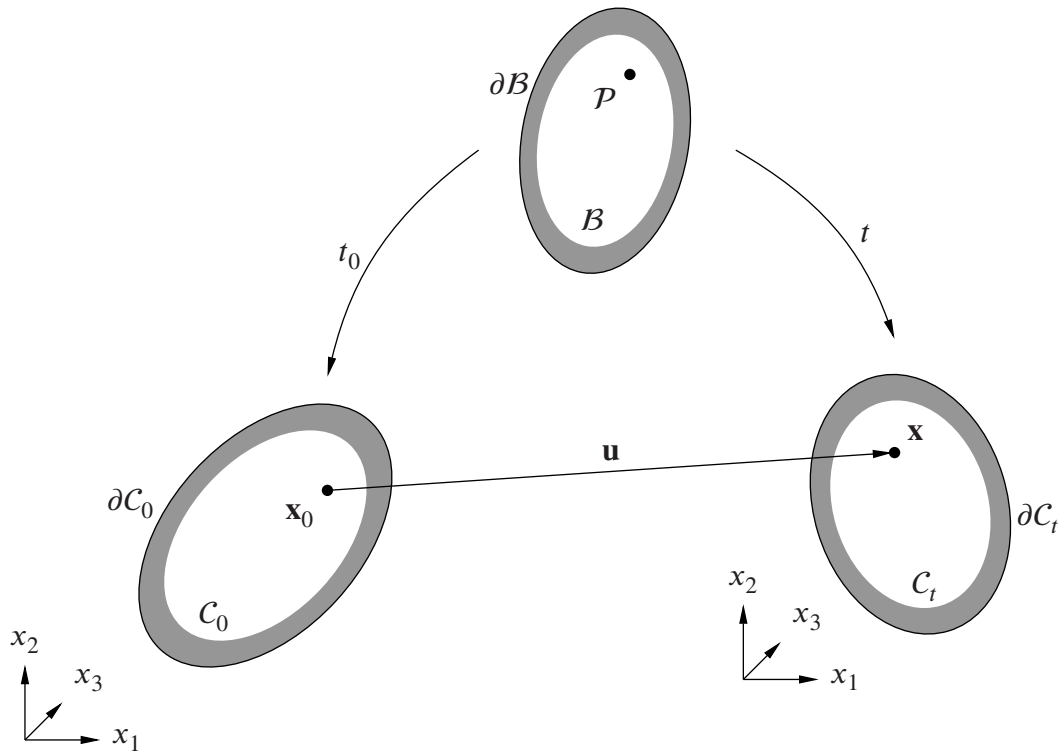
Figure 2.1: The reference configuration C_0 at time t_0 and the current configuration C_t at time t assigns the body B to the physical space $\mathbb{R}^3$. The same applies for the respective boundaries ∂C_0 and ∂C_t for ∂B. The displacement vector $\mathbf{u}$ runs between the reference coordinates $\mathbf{x}_0$ and the current coordinates $\mathbf{x}$ of the material particle P.

regular boundary ∂B. A configuration C with the boundary ∂C assigns uniquely the material particles P of a body B to coordinates $\mathbf{p}$ of a physical space, for example a region in the Euclidean space $\mathbb{R}^3$, see figure 2.1 (Flügge et al., 1965, p. 37).

$$\mathbf{p} : B \to C \subseteq \mathbb{R}^3, \quad P \mapsto \mathbf{p} = \mathbf{p}(P) \tag{2.1}$$

A smooth sequence of configurations C_i reflects the motion of a body in space over time, which gives the motion relation, given in equation (2.2). The motion relation is a bijective non-linear map between a reference configuration[1] C_0 and the current configuration C_t parameterized in time t (Flügge et al., 1965, p. 38). Reference (or material) points $\mathbf{x}_0$ are mapped to current coordinates $\mathbf{x}$ in space[2] at time t, as shown in figure 2.1.

The motion relation, see equation (2.2), may be also expressed with respect to the displacement

---

[1]The reference configuration C_0 commonly represents an initial undeformed state of the body at time $t = 0$.

[2]Here, I limit the description to the Euclidean space $\mathbb{R}^3$. A single ordinary Cartesian coordinate system is considered for all configurations C_i.

u of a material point.

$$\mathbf{x} : \mathcal{C}_0 \times \mathbb{R}^{>0} \to \mathcal{C}_t, \quad (\mathbf{x}_0, t) \mapsto \mathbf{x} = \mathbf{x}(\mathbf{x}_0, t) = \mathbf{x}_0 + \mathbf{u}(\mathbf{x}_0, t) \tag{2.2}$$

To evaluate the change in shape of a body, rigid body motions and deformation must be separated. The material gradient ∇ of the motion relation (2.2) gives the deformation gradient **F**.

$$\mathbf{F} : \mathcal{C}_0 \times \mathbb{R}^{>0} \to \mathrm{GL}^{>0}\left(\mathbb{R}^3\right), \quad (\mathbf{x}_0, t) \mapsto \mathbf{F} = \nabla\mathbf{x}(\mathbf{x}_0, t) = \nabla\mathbf{u}(\mathbf{x}_0, t) + \mathbf{I} \tag{2.3}$$

$\mathrm{GL}^{>0}\left(\mathbb{R}^3\right)$ denotes the space of second-order tensors on $\mathbb{R}^3$ with positive determinant, and **I** represents the identity tensor. Bijectivity and smoothness of the motion relation (2.2) guarantee admissible physical states of deformation, which is equivalent to $\det(\mathbf{F}) > 0$ (Hill, 1979). The two-point tensor[3] **F** describes the local behavior of deformation and allows for transformations between the reference configuration $\mathcal{C}_0$ and the current configuration $\mathcal{C}_t$. For example, $d\mathbf{x} = \mathbf{F}d\mathbf{x}_0$ describes the transport of a line element from the reference configuration $\mathcal{C}_0$ to the current configuration $\mathcal{C}_t$, and $d\mathbf{x}_0 = \mathbf{F}^{-1}d\mathbf{x}$ vice versa. Abraham and Marsden, 2008, p. 58, 108 denote the respective operations as push forward and pull back. Although the deformation gradient **F** does not include rigid body translations, it is not free of rigid body motion, since rigid body rotation remains unaffected of the material gradient ∇.

The polar decomposition in equation (2.4) uniquely divides the deformation gradient **F** into the orthogonal rotation tensor $\mathbf{R} \in \mathrm{SO}\left(\mathbb{R}^3\right)$ and the positive definite and symmetric right stretch tensor $\mathbf{U} \in \mathrm{SYM}\left(\mathbb{R}^3\right)$ (Flügge, 1960, p. 840–843).

$$\mathbf{F} = \mathbf{R}\mathbf{U} \tag{2.4}$$

Here, $\det(\mathbf{R}) = 1$, $\mathbf{R}^{\mathrm{T}} = \mathbf{R}^{-1}$, and $\mathbf{U} = \mathbf{U}^{\mathrm{T}}$. The right Cauchy-Green deformation tensors **C** derive from both the polar decomposition in equation (2.4) and the deformation gradient, see equation (2.3). The right stretch tensor **U** and the right Cauchy-Green deformation tensor **C** do not contain any rigid body motion.

$$\mathbf{C} = \mathbf{U}^2 = \mathbf{F}^{\mathrm{T}}\mathbf{F} \tag{2.5}$$

Due to the separation of rigid body rotation from deformation, the polar decomposition of the deformation gradient **F** in equation (2.4) represents the basis for (finite) deformation analysis and is the origin of various strain tensors (Curnier and Rakotomanana, 1991). As a synthesis of the many definitions for strain tensors, Neff et al., 2016 regard them as injective isotropic tensor

---

[3]The first basis vector is defined in the current configuration $\mathcal{C}_t$ and the second basis vector is defined in the reference configuration $\mathcal{C}_0$.

functions $\mathbf{E}$ of the right stretch tensor $\mathbf{U}$

$$\mathbf{E} : \mathrm{SYM}\left(\mathbb{R}^3\right) \to \mathrm{SYM}\left(\mathbb{R}^3\right) , \quad \mathbf{U} \mapsto \mathbf{E}\left(\mathbf{U}\right) , \tag{2.6}$$

where $\mathrm{SYM}\left(\mathbb{R}^3\right)$ is the space of symmetric tensors on $\mathbb{R}^3$ and further $\mathbf{E}\left(\mathbf{I}\right) = 0$, which is the case for pure rotation, where $\mathbf{F} \in \mathrm{SO}\left(\mathbb{R}^3\right)$. Among the most prominent material strain tensors is the Green strain tensor $\mathbf{E}$.

$$\mathbf{E} = \frac{1}{2}\left(\mathbf{U}^2 - \mathbf{I}\right) = \frac{1}{2}\left(\mathbf{C} - \mathbf{I}\right) = \frac{1}{2}\left(\mathbf{F}^{\mathrm{T}}\mathbf{F} - \mathbf{I}\right) \tag{2.7}$$

Doyle and Ericksen, 1956 parameterized a general class of material strain tensors. Seth, 1961, Hill, 1968a, and Hill, 1968b manifested and expanded this generalized strain tensors, which are called Seth-Hill family. $\mathbf{E}_n$ denotes the material strain tensors.

$$\mathbf{E}_n(\mathbf{U}) = \begin{cases} \frac{1}{2n}\left(\mathbf{U}^{2n} - \mathbf{I}\right) = \frac{1}{2n}\left(\mathbf{C}^n - \mathbf{I}\right) & : n \in \mathbb{R} \setminus 0 \\ \ln\left(\mathbf{U}\right) = \frac{1}{2}\ln\left(\mathbf{C}\right) & : n = 0 \end{cases} \tag{2.8}$$

The tensor $\mathbf{E}_1 = \mathbf{E}$ recovers the Green strain tensor. Curnier and Zysset, 2006 set up a consistent second-order approximation of the tensors $\mathbf{E}_n$ with special regard to computational simplicity incorporating the estimate of Bazant, 1998 for the Hencky strain tensor $\mathbf{E}_0$. For example Böck and Holzapfel, 2004 and Latorre and Montáns, 2016 propose further generalized strain tensors addressing different objectives. Böck and Holzapfel, 2004 aim for straightforward two-point formulations. Latorre and Montáns, 2016 deduce a mapping tensor to transform between arbitrary strain tensors.

In contrast to strain tensors $\mathbf{E}$, strain measures E map the right stretch tensor $\mathbf{U}$ to a scalar non-negative value (Neff et al., 2016).

$$E : \mathrm{GL}^{>0}\left(\mathbb{R}^3\right) \to \mathbb{R}^{>0} , \quad \mathbf{U} \mapsto E\left(\mathbf{U}\right) \tag{2.9}$$

Here, pure rotations, $\mathbf{U} = \mathbf{I}$, lead to $E = 0$. Strain measures may be based, for example, on orthogonal invariant Frobenius norms of strain tensors

$$E_m\left(\mathbf{U}\right) = \alpha||\mathbf{E}\left(\mathbf{U}\right)||_m , \tag{2.10}$$

where α is a scalar factor and m indicates which norm is concerned.

When it comes to dynamic considerations, time derivatives of the respective quantities appear.

The velocity $\mathbf{v}$ of a material point results from the material time derivative of its motion (Flügge, 1960, p. 328).

$$\mathbf{v} : C_0 \times \mathbb{R}^{>0} \to \mathbb{R}^3 , \quad \left(\mathbf{x}_0, t\right) \mapsto \mathbf{v} = \frac{\mathrm{d}}{\mathrm{d}t}\mathbf{x}\left(\mathbf{x}_0, t\right) = \dot{\mathbf{x}}\left(\mathbf{x}_0, t\right) = \dot{\mathbf{u}}\left(\mathbf{x}_0, t\right) \tag{2.11}$$

The material gradient ∇ of the velocity $\mathbf{v}$ yields

$$\mathbf{L} = \nabla\mathbf{v} = \dot{\mathbf{F}} , \tag{2.12}$$

and the strain rate tensor $\dot{\mathbf{E}}$ for the Green strain tensor derives as

$$\dot{\mathbf{E}} = \frac{1}{2}\left(\dot{\mathbf{F}}^{\mathrm{T}}\mathbf{F} + \mathbf{F}^{\mathrm{T}}\dot{\mathbf{F}}\right) . \tag{2.13}$$

Curnier and Zysset, 2006 provide a straightforward calculation of strain rate tensors for the second-order approximation of the Seth-Hill strain tensor family. In contrast, a direct derivation of the strain rate tensors from equation (2.8) remains cumbersome despite various attempts to simplify them, such as by Hill, 1979 or Rosati, 1999.

Strain measures may also be calculated based on their time increments, in order to account for path dependencies.

$$E\left(\mathbf{U}\right) = \int_0^t \dot{E}\left(\mathbf{U}\right) \mathrm{d}t \tag{2.14}$$

2.1.2 Balance Equations

The deformation of a body is caused by certain stimuli. Deformation and stimuli together affect the state and behavior of a body, which are characterized by a certain number of scalar, vector-valued, or tensor-valued physical quantities (Hutter, 1993, p. 27–32). I follow up on the idea of a master balance for the physical quantities, which is an elegant way to describe the spatio-temporal behavior of the physical quantity. The basic principle of this modeling approach dates back to Liouville, 1838 and Gibbs, 1884. The general volume balance for the physical quantity describes its change over time in an arbitrary material volume V (Greve, 2003, p. 57–60). May $\mathbf{q}$ denote the scalar or vector-valued density of the physical quantity, then the general volume balance in material form reads

$$\frac{\mathrm{d}}{\mathrm{d}t} \int_{V_0} \mathbf{q} \, \mathrm{d}V_0 = \int_{V_0} \mathbf{p} \, \mathrm{d}V_0 + \int_{V_0} \mathbf{s} \, \mathrm{d}V_0 + \int_{\partial V_0} \mathbf{f} \cdot \mathbf{n} \, \mathrm{d}A_0 , \tag{2.15}$$

with $\mathrm{d}\mathbf{A}_0 = \mathbf{n} \cdot \mathrm{d}A_0$ and $\mathbf{n}$ the outward surface normal vector. $\mathbf{p}$ denotes the production density, $\mathbf{s}$ the supply density and $\mathbf{f}$ the flux density. The associated local formulation reads

$$\dot{\mathbf{q}} = \mathbf{p} + \mathbf{s} + \nabla \cdot \mathbf{f} \,, \tag{2.16}$$

where in addition C^1-continuity of all fields is assumed (Hutter, 1993, p. 35–36). Combining the general volume balance equations (2.15) and (2.16) with the principles of mechanics (Newton's laws of motion) and thermodynamics, the fundamental laws of continuum mechanics result.

Conservation of Mass

In continuum mechanics, mass represents a conservation quantity, described by its density ρ. No production, supply, or flux occurs. The conservation of mass reads

$$\dot{\rho}_0 = 0 \Leftrightarrow \rho_0 = \rho \, \mathrm{det}\mathbf{F} \,. \tag{2.17}$$

Mass conservation is sometimes disregarded for modeling or computational reasons, such as in the isoparametric Galerkin formulations that Joshi et al., 2000 point out.

Conservation of Linear Momentum and Angular Momentum

Newton's second law of motion conserves linear momentum, hence the production term vanishes. Volume body forces $\mathbf{b}_0$ act as the supply term and surface tractions as the flux quantities. Cauchy postulates that surface tractions can be equivalently described by a second-order tensor, which is called Cauchy stress tensor $\boldsymbol{\sigma}$. The Cauchy stress tensor acts on the current configuration C_t. The Cauchy stress tensor may be transformed into the first Piola-Kirchhoff stress tensor $^\mathrm{I}\mathbf{P}$, which is a two-point tensor[4].

$$^\mathrm{I}\mathbf{P} = \mathrm{det}\,(\mathbf{F})\,\boldsymbol{\sigma}\mathbf{F}^{-\mathrm{T}} \tag{2.18}$$

The second Piola-Kirchhoff stress tensor $^\mathrm{II}\mathbf{P}$ has its basis defined in the reference configuration C_0.

$$^\mathrm{II}\mathbf{P} = \mathrm{det}\,(\mathbf{F})\,\mathbf{F}^{-1}\boldsymbol{\sigma}\mathbf{F}^{-\mathrm{T}} \tag{2.19}$$

---

[4]Analogue to the deformation gradient $\mathbf{F}$, the first basis vector is defined in the current configuration C_t and the second basis vector is defined in the reference configuration C_0.

The conservation of linear momentum reads

$$\rho_0 \dot{\mathbf{v}} = \mathbf{b}_0 + \nabla \cdot {}^{\mathrm{I}}\mathbf{P}^{\mathrm{T}} . \tag{2.20}$$

The angular momentum conservation yields the symmetry of the Cauchy stress tensor $\boldsymbol{\sigma}$, and hence of the second Piola-Kirchhoff stress tensor ${}^{\mathrm{II}}\mathbf{P}$.

$$\boldsymbol{\sigma} = \boldsymbol{\sigma}^{\mathrm{T}} \Leftrightarrow {}^{\mathrm{II}}\mathbf{P} = {}^{\mathrm{II}}\mathbf{P}^{\mathrm{T}} . \tag{2.21}$$

First Law of Thermodynamics

The balance of internal energy is known as the first law of thermodynamics. The scalar quantity μ denotes the internal energy per unit mass. The internal energy is no conservation quantity owing to the production density term ${}^{\mathrm{I}}\mathbf{P} : \dot{\mathbf{F}}$ (Macvean, 1968).[5] The supply density is the heat supply per unit mass ϱ. The outward energy heat flow vector $\mathbf{H}$ represent the flux density.

$$\rho_0 \dot{\mu} = {}^{\mathrm{I}}\mathbf{P} : \dot{\mathbf{F}} + \rho_0 \varrho - \nabla \cdot \mathbf{H} \tag{2.22}$$

Equation (2.22) may also be derived from the conservation of energy using the conservation of linear momentum, see equation (2.20) (Greve, 2003, p. 80–84).

Second Law of Thermodynamics

The second law of thermodynamics makes claims about the direction of physical processes, although it is not a unique statement following defined principles (Clausius, 1865). The entropy per unit mass η and absolute temperature T are introduced for its formulation. The absolute temperature T of a material point is defined as

$$T : C_0 \times \mathbb{R}^{>0} \to \mathbb{R}^{>0} , \quad (\mathbf{x}_0, t) \mapsto T = T(\mathbf{x}_0, t) > 0 \tag{2.23}$$

In continuum mechanics, the heat flux and the heat supply terms in the first law of thermodynamics, see equation (2.22), are assumed to govern the entropy flux and entropy supply[6] through

---

[5]The production density may be substituted by any power-conjugate pair, such as ${}^{\mathrm{II}}\mathbf{P} : \dot{\mathbf{E}}$ or $\boldsymbol{\sigma} : \mathbf{l}$, where $\mathbf{l} = \dot{\mathbf{F}}\mathbf{F}^{-1}$.
[6]Müller, 1971 derived a more general concept for the second law of thermodynamics, but in continuum mechanics the presented approach proved reasonable.

the proportionality factor $\frac{1}{T}$ (Gurtin and Williams, 1966). For any admissible thermodynamic process, the entropy production is non-negative, which leads to the inequality

$$\rho_0 \dot{\eta} \geq \frac{\rho_0 \varrho}{T} - \frac{\nabla \cdot \mathbf{H}}{T} + \mathbf{H} \cdot \frac{\nabla T}{T^2} \ . \tag{2.24}$$

The Clausius-Duhem inequality follows from inequality (2.24) by applying equation (2.22) and substituting the internal energy per unit mass μ by means of the Helmholtz free energy per unit mass $\psi = \mu - \eta T$.

$$- \rho_0 \eta \dot{T} - \rho_0 \dot{\psi} + {}^{\mathrm{I}}\mathbf{P} : \dot{\mathbf{F}} - \mathbf{H} \cdot \nabla T \geq 0 \tag{2.25}$$

Each solution for the system of field equations (2.17) to (2.22) is a thermodynamic process (Hutter, 1993, p. 60). The second law of thermodynamics, see inequality (2.24), acts as a restrictive condition and does not contribute directly to the solution. To solve the equation system additional relations are needed, which specify material behavior. These relations are called constitutive relations.

2.1.3 Constitutive Relations

Materials respond in different ways to certain stimuli. No general theoretical concept justifies a universal material description. But three general principles apply: material frame-indifference[7], determinism, and local action[8] (Flügge et al., 1965, p. 36). Constitutive relations characterize the specific material response behavior in accordance with the considered descriptive framework. Material modeling may be split into inductive (mainly data-driven) and deductive (mainly theory-driven) approaches. But in the end, the determination of the material properties remains an experimental task (Flügge et al., 1965, p. 4; Altenbach, 2015, p. 209).

A fundamental hypothesis is that a set of independent state variables $\mathcal{Z}$ entirely defines the material properties over the duration of a thermodynamic process. These state variables may be scalars, vectors, or even rank tensors (Rice, 1971). The state variables allow to determine the dependent variables. Although the separation between state variables and dependent variables is not unique, in continuum mechanics, certain kinematic quantities and the temperature usually build the state space and the stress, free energy, heat flux, and entropy the dependent variable space. The deformation gradient $\mathbf{F}$ and the absolute temperature T together form an independent basis of the observable state space $\mathcal{Z}_{\mathrm{ob}} = \{\mathbf{F}, T\}$ (Germain et al., 1983). To ensure material

---

[7]Material behavior is independent of the observers perspective.
[8]Only the history of an arbitrary small neighborhood influences the material particles state.

frame-indifference, the deformation gradient $\mathbf{F}$, which contains rigid body rotations, may be substituted by the Green strain tensor $\mathbf{E}$, for example.

A thermodynamic process is either reversible[9], such as ideal elastic deformation, or irreversible[10], such as plastic deformation (G. Taylor, 1931), viscose flow (J. Moore and J. Moore, 1983), and damage (Kachanov, 1958). For reversible processes the observable state space suffice for unique description. In contrast, for irreversible processes, a set of i internal state variables $\mathcal{Z}_{\text{in}} = \{\mathbf{z}_i\}$ expand the state space regarding dissipative phenomena. The constitutive behavior of irreversible processes is governed by two potentials, a state potential and a dissipation pseudo-potential (Halphen and Q. Nguyen, 1975).

The Helmholtz free energy density $\rho_0 \psi \left(\mathbf{F}, T, \mathbf{z}_i; \boldsymbol{\varphi}_{re} \right) = \Psi$ serves as a state potential dependent on the set of state variables $\mathcal{Z} = \mathcal{Z}_{\text{ob}} \cup \mathcal{Z}_{\text{in}}$. The vector $\boldsymbol{\varphi}_{re}$ contains the constitutive parameters of the state potential. The dissipation pseudo-potential is $\rho_0 d \left(\dot{\mathbf{F}}, \dot{\mathbf{z}}_i; \mathbf{F}, T, \mathbf{z}_i; \boldsymbol{\varphi}_{ir} \right) = D$, where the three state variables after the semicolon indicate the relation to the current state of the material point and the vector $\boldsymbol{\varphi}_{ir}$ include the constitutive parameters. The model parameters $\boldsymbol{\varphi}_{re}$ and $\boldsymbol{\varphi}_{ir}$, also called material parameters or constitutive parameters, calibrate each model to the material at hand, which is commonly done using experiments.

Every state variable is driven by its conjugate thermodynamic force, summarized in the set $\mathcal{T} = \mathcal{T}_{\text{ob}} \cup \mathcal{T}_{\text{in}} = \{{}^{\text{I}}\mathbf{P}, \rho_0 \eta, \mathbf{t}_i\}$. Ziegler, 1958 and Ziegler, 1974 deduced an additive decomposition of the thermodynamic forces in a quasi-conservative part that derives from the state potential and a dissipative part based the dissipation pseudo-potential. For the first Piola-Kirchhoff stress tensor ${}^{\text{I}}\mathbf{P}$, this yields

$$ {}^{\text{I}}\mathbf{P} = {}^{\text{cI}}\mathbf{P} + {}^{\text{dI}}\mathbf{P} = \frac{\partial \Psi}{\partial \mathbf{F}} + \frac{\partial D}{\partial \dot{\mathbf{F}}} \ , \tag{2.26} $$

and for the thermodynamic forces conjugate to the internal variables

$$ \mathbf{t}_i = {}^{\text{c}}\mathbf{t}_i + {}^{\text{d}}\mathbf{t}_i = \frac{\partial \Psi}{\partial \mathbf{z}_i} + \frac{\partial D}{\partial \dot{\mathbf{z}}_i} \ . \tag{2.27} $$

In contrast to observable state variables, internal variables do not produce net work. Hence, the quasi-conservative part and the dissipation part of their thermodynamic forces sum up to zero.

$$ \frac{\partial \Psi}{\partial \mathbf{z}_i} + \frac{\partial D}{\partial \dot{\mathbf{z}}_i} = 0 \tag{2.28} $$

Equation (2.28) provides kinetic relations for the internal variable (Stainier, 2013, p. 75). In

---

[9]Entropy production vanishes.

[10]Entropy production occurs during the process.

analogy to Ziegler, 1977, local thermal equilibrium is assumed and the entropy results in

$$\rho_0 \eta = -\frac{\partial \Psi}{\partial T} \ .$$ (2.29)

Following Biot, 1958, the heat flux is governed by a conduction potential $C\left(\frac{\nabla T}{T}; \mathbf{F}, T, \mathbf{z}_i\right)$ that ensures compliance with the second law of thermodynamics, see inequality (2.24).

$$\mathbf{H} = \frac{\partial C}{\partial T}$$ (2.30)

The conduction potential is often seen as a part of the pseudo-dissipation potential, which contains both internal and conductive dissipation (Lemaitre et al., 1998, p.61–65).

As materials behave extremely diverse, countless models for the thermodynamic potentials exist that account constitutive phenomena such as elasticity, plasticity, damage, and their couplings (Egner, 2012). Also, pure inductive, empirical constitutive laws based on rheological considerations may be merged with the consistent framework, although they initially sacrificed compatibility with thermodynamics. S. Su, 2012 and Ranc and Chrysochoos, 2013 showed this for the model of G. Johnson and Cook, 1983 as well as G. Johnson and Cook, 1985. However, embedding inductive models is not unique, as the variants of S. Su, 2012 and Ranc and Chrysochoos, 2013 use quite different choices for the internal variables and potentials.

2.1.4 Initial Boundary Value Problem

The initial boundary value problem of thermodynamics brings together kinematics, balance equations, and constitutive laws, in order to determine how motion and temperature of the body $\mathcal{B}$ evolve in space over time (Seitz et al., 2018). The constitutive laws complete the system of field equations with additional relations between the state variables and dependent variables. The conservation of mass, see equation (2.17), and angular momentum, see equation (2.21), are met without being explicitly stated. The linear momentum in equation (2.20) and the first law of thermodynamics in equation (2.22) represent the problem equations. The evolution of the internal variables $\mathbf{z}_i$ results from equation (2.28) (Stainier, 2013, p. 75). The initial conditions set the reference values in the body $\mathcal{B}$ for the state variables $\mathcal{Z}$ at time $t = 0$.

$$\mathbf{F} = \mathbf{F}_0 \ , \quad \dot{\mathbf{F}} = \dot{\mathbf{F}}_0 \ , \quad T = T_0 \ , \quad \mathbf{z}_i = \mathbf{z}_{i0} \quad \text{in } C_0 \times 0$$ (2.31)

Boundary conditions may be set both for observable state variables $\mathcal{Z}_{\mathrm{ob}}$ (Dirichlet boundary conditions) and their thermodynamic forces $\mathcal{T}_{\mathrm{ob}}$ (Neumann boundary conditions). Dirichlet

boundary conditions on $\partial_\mathbf{u} C_0$ and Neumann boundary conditions on $\partial_\mathbf{P} C_0$ represent disjoint sets.

$$\mathbf{F} = \widehat{\mathbf{F}}, \quad T = \widehat{T} \quad \text{on } \partial_\mathbf{u} C_0 \times t, \quad {}^1\mathbf{Pn} = \widehat{\mathbf{r}}, \quad -\mathbf{H} \cdot \mathbf{n} = \widehat{\mathbf{H}} \quad \text{on } \partial_\mathbf{P} C_0 \times t, \qquad (2.32)$$

where $\partial_\mathbf{u} C_0 \cap \partial_\mathbf{P} C_0 = \emptyset$. The initial boundary value problem represents the strong form, since for each individual material particle $\mathcal{P}$ of the body $\mathcal{B}$ the system of equations is enforced. The strong form can only be solved analytically in special cases on rudimentary geometries. The weak formulation restates the initial boundary value problem with reduced regularity requirements, on which numerical methods, such as the finite element method, are based.

2.2 Principles of Data Science

In general, data science deals with the extraction of knowledge from data (Tukey, 1962). Only modern perspectives specialize the topic towards specific disciplines and large data sets (Cleveland, 2001), which may have led to a certain alienation.

In continuum mechanics, data science methods are applied naturally in constitutive modeling. Phenomenological models, such as the cubic spline model for hyper-elasticity by Sussman and Bathe, 2009 or the generalized forming limit concept to cope with non-proportional loading in sheet metal forming by Volk and Suh, 2014, paved the way towards a purely data-driven material response. Hybrid models attempt to correct existing models based on data sets, as Ibáñez et al., 2019 show for plastic deformation. Kirchdoerfer and Ortiz, 2016 and Kirchdoerfer and Ortiz, 2017 bypass the empirical material model and calculate the stress-strain relations directly from either deterministic or noisy data, which consists of deformation patterns of structures. Leygue et al., 2017 and L. Nguyen and Keip, 2018 extend this approach for different material classes, where the backbone remains a distance minimization between the system state and the training data. Constitutive manifolds can completely replace material models and at the same time preserve the conservation laws (González et al., 2019; Ibañez et al., 2018). Constitutive manifolds rely on manifold learning, which is a method to exploit the geometry of the data (Lopez et al., 2018; Zimmer et al., 2015). The constitutive manifold allows calculating directly tangent moduli for numerical analysis. González et al., 2019 propose a thermodynamically consistent formulation for constitutive manifolds, which copes with Hamiltonian[11] and dissipative phenomena.

---

[11]conservative

Four basic elements lie behind nearly all of these data-driven approaches: dimensionality reduction, which is strongly connected to transformations, regression, which finally revolves around optimization, computation of derivatives, which reveals the character of real discrete data, and validation to avoid over- and underfitting.

2.2.1 Dimensionality Reduction

Natural data, such as image series, audio signals, or any other experimental data, have the remarkable property of being of low rank[12], which even stays true for increasing resolutions of measurement devices and computations. This characteristic is also referred to as sparsity. When sparse data is transformed in a well-chosen basis, only a small number of modes suffice to characterize the underling system (Guckenheimer and Holmes, 1983, p. 411–420). I recognize this concept also in manufacturing technology, such as meta-modeling a gas metal arc welding process by Auerbach et al., 2011 or using control point-based descriptions for geometry and measurement data of my co-workers and me (Hartmann, Eder, Opritescu, Maier, et al., 2018; Hartmann et al., 2017). Dimensionality reduction looks for the descriptive modes in the data.

The singular value decomposition (SVD) is the foundation for many data-driven methods, such as the principal component analysis (PCA) (Jolliffe, 2002, p. 44–46). It allows a stable matrix decomposition that always exists[13]. Brunton and Kutz, 2019, p. 3–4 see the SVD as a generalization of the fast Fourier transformation (FFT), where the FFT provides a generic basis and the SVD a tailored basis for the underlying data. The decomposition of a data matrix $\mathbf{X} \in \mathbb{R}^{n \times m}$ reads

$$\mathbf{X} = \mathbf{U} \mathbf{S} \mathbf{V}^{\mathrm{T}} . \tag{2.33}$$

The unitary matrices $\mathbf{U} \in \mathbb{R}^{n \times n}$ and $\mathbf{V} \in \mathbb{R}^{m \times m}$ have orthonormal columns. The diagonal matrix $\mathbf{S} \in \mathbb{R}^{n \times m}$ contains the ordered singular values.

The SVD enables a hierarchy of $\mathcal{L}_2$-optimal low-rank approximations of the matrix $\mathbf{X}$ (Eckart and G. Young, 1936; Schmidt, 1907), which is also called truncation. The truncation rank r controls of the size of the resulting basis and enables a reduction to a tractable number of dimensions. The truncated SVD reads

$$\mathbf{X} \approx \widetilde{\mathbf{X}} = \widetilde{\mathbf{U}} \widetilde{\mathbf{S}} \widetilde{\mathbf{V}}^{\mathrm{T}} . \tag{2.34}$$

---

[12]Almost all natural data can be meaningfully mapped into tensors.
[13]The SVD is also defined for complex-valued matrices. Here, the descriptions are limited to real values.

The matrices $\widetilde{\mathbf{X}}$, $\widetilde{\mathbf{U}}$, $\widetilde{\mathbf{V}}^{\mathrm{T}}$ and $\widetilde{\mathbf{S}}$ for given r are calculated according to

$$\underset{\widetilde{\mathbf{X}},\ \text{s.t.}\ \mathrm{rank}(\widetilde{\mathbf{X}})=r}{\mathrm{argmin}}\quad ||\mathbf{X} - \widetilde{\mathbf{X}}||_2 = \widetilde{\mathbf{U}}\widetilde{\mathbf{S}}\widetilde{\mathbf{V}}^{\mathrm{T}}\ . \tag{2.35}$$

If r equals the rank of $\mathbf{X}$, the solution is exact, i.e. $\mathbf{X} = \widetilde{\mathbf{X}}$, which preserves all non-singular values. The choice of the truncation rank r depends on many factors, such as noise, singular value distribution, or the rank structure of the data matrix. Gavish and Donoho, 2014 propose an approach to find an optimal hard value for r to truncate the data. The PCA prepares the data before calculating the SVD. The row-wise mean is subtracted from the data and the variance is set to unity, which ensures orthogonal singular values, which are the PCs (Pearson, 1901).

The concept of SVD and PCA can be transferred to tensors, using methods such as parallel factors analysis PARAFAC (Harshman, 1970) or canonical decomposition CANDECOMP (Hitchcock, 1927). This becomes relevant for data structures with different types of information arranged in higher-dimensional arrays, which for example include measurements of displacements, temperatures, and forces. Tensor decomposition maintains the structure in the independent array dimensions (Brunton and Kutz, 2019, p. 41).

2.2.2 Regression

The most basic form of regression is curve fitting, such as in the eponymous publication by Galton, 1886, but data science expands the concept to provide parsimonious, comprehensible, and interpretable models (R. Johnson and Wichern, 2007, p. 360, R. Johnson and Wichern, 2014). Model selection turns the problem into an ill-posed, either over- or underdetermined problem (Brunton and Kutz, 2019, p. 117). Regularization provides tools to influence the model building process beyond pure mapping of the database with respect to certain distance measure. I understand regularization as a possibility to add prior knowledge[14] to the problem in order to identify stable, interpretable, and generalizable solutions.

Overdetermined problems have no exact solution, since more equations than unknowns govern the system. This calls for an optimization, which minimizes a certain error. The mathematical framework for overdetermined linear and nonlinear systems read

$$\underset{\boldsymbol{\varphi}}{\mathrm{argmin}}\left(||\mathbf{A}\boldsymbol{\varphi} - \mathbf{x}||_2 + \lambda\mathfrak{R}\left(\boldsymbol{\varphi}\right)\right)\ , \tag{2.36}$$

---

[14]In my opinion, this property makes it especially suitable for engineers.

$$\underset{\boldsymbol{\varphi}}{\mathrm{argmin}}\left(\mathfrak{D}\left(\mathbf{A}, \boldsymbol{\varphi}, \mathbf{X}\right) + \lambda \mathfrak{R}\left(\boldsymbol{\varphi}\right)\right) . \tag{2.37}$$

In both expressions, the first term represents the actual objective, also referred to as data term, which tries to minimize the difference in an $\mathcal{L}_2$-norm sense[15] between the model, $\mathbf{A}\boldsymbol{\varphi}$ in the linear case, and the data, vector $\mathbf{x}$ in the linear case. The second term is a regularization term with the scaling factor λ and the regularizer $\mathfrak{R}$ that contains the model parameters $\boldsymbol{\varphi}$.

In contrast, underdetermined problems have infinite number of solutions. To select the desired solution, additional constraints have to be made in the optimization. For underdetermined linear and nonlinear systems, the mathematical framework turns into

$$\underset{\boldsymbol{\varphi}}{\mathrm{argmin}}\,\mathfrak{R}(\boldsymbol{\varphi}) \text{ subject to } ||\mathbf{A}\boldsymbol{\varphi} - \mathbf{x}||_2 \leq \epsilon , \tag{2.38}$$

$$\underset{\boldsymbol{\varphi}}{\mathrm{argmin}}\,\mathfrak{R}(\boldsymbol{\varphi}) \text{ subject to } \mathfrak{D}(\mathbf{A}, \boldsymbol{\varphi}, \mathbf{X}) \leq \epsilon . \tag{2.39}$$

The threshold ϵ indicates, which error between model and data is tolerated.

For both, over- and underdetermined problems, the choice of the regularizer $\mathfrak{R}$ controls and designs the calculated solutions. Various formulations of regularization terms exist (Z. Chen and Haykin, 2002; Girosi et al., 1995). A classical formulation for regularizers combines the $\mathcal{L}_1$-norm and the $\mathcal{L}_2$-norm that reads

$$\mathfrak{R}(\boldsymbol{\varphi}) = \lambda_1 ||\boldsymbol{\varphi}||_1 + \lambda_2 ||\boldsymbol{\varphi}||_2 . \tag{2.40}$$

The factors λ_1 and λ_2 weight the different proportions of $\mathcal{L}_1$-norm and $\mathcal{L}_2$-norm. Setting $\lambda_1 = \lambda_2 = 0$ leads to the Moore-Penrose pseudo-inverse for the solution of expression (2.36) (E. Moore, 1920; Penrose, 1955). Other methods without regularization use re-weighted least squares (Holland and Welsch, 1977) or QR-decomposition based schemes (Trefethen and Bau, 1997, p. 56–62). The least absolute shrinkage and selection operator (LASSO) entirely relies on the $\mathcal{L}_1$-norm, hence $\lambda_1 > 0$ and $\lambda_2 = 0$ (Santosa and Symes, 1986; Tibshirani, 1996). Whittaker, 1922 and Tikhonov, 1963 utilizes exclusively the $\mathcal{L}_2$-norm for regression, hence $\lambda_1 = 0$ and $\lambda_2 > 0$. A mixture of $\mathcal{L}_1$-norm and $\mathcal{L}_2$-norm is realized in the elastic net algorithm, where $\lambda_1 > 0$ and $\lambda_2 > 0$ (Zou and Hastie, 2005). In general, the $\mathcal{L}_1$-norm promotes sparse solutions, where the $\mathcal{L}_2$ norm strives for minimum approximation error, which is clear, since the measure for error is usually the $\mathcal{L}_2$-norm. Phillips, 1962 gives an alternative formulation of the regularizer defined by equation (2.40) in matrix notation.

---

[15]The $\mathcal{L}_2$-norm is the classical error measure and hence used here, but also other measures may be employed.

Gradient descent algorithms are the workhorse for solving the minimization problems. The general task is to identify the global minimum of a multi-dimensional function, accordingly the gradient must vanish [16]. As the multi-dimensional surface becomes more complex more advanced gradient descent algorithms are used to identify search direction and step size. But the basic principle holds as well for enhanced gradient descent algorithms, such as conjugate and bi-conjugate gradient descent (Fletcher, 1976) or stochastic gradient descent methods (Sra et al., 2012, pp. 351–368, Taddy, 2019, p. 303–307).

2.2.3 Computation of Derivatives

To calculate derivatives of discrete data is an essential task in numerics. For a set of noisy data points $\widetilde{y}_i = y(x_i) + \sigma(x_i)$, where the recursive rule $x_{i+1} = x_i + \delta$ gives the underlying grid, the basic problem is to find a piecewise smooth function $\frac{d}{dx} f$ that best possible approximates $\frac{d}{dx} y$. Hanke and Scherzer, 2001 see the numerical differentiation as the inverse problem of numerical integration, which illustrates that numerical differentiation is an ill-posed problem due to the discontinuous dependence between the data $\widetilde{y}_i$ and the derivative $\frac{d}{dx} f$. Further the problem is ill-conditioned, since arbitrarily small changes in the data $\widetilde{y}_i$ may lead to arbitrarily large changes in the derivative $\frac{d}{dx} f$.

Classical differences methods, such as finite differences, have the tacit assumption that the underlying data is exact, which means $\sigma = 0$ (Anderssen and Bloomfield, 1974). The forward finite differences for $\sigma = 0$ reads

$$\frac{d}{dx} y \approx \frac{d}{dx} f = \frac{y_{i+1} - y_i}{\delta} \ , \tag{2.41}$$

which gives an approximation error $\mathcal{O}(\delta)$ linear in the grid step δ. In contrast, the forward finite differences for $\sigma \neq 0$ reads

$$\frac{d}{dx} y \approx \frac{d}{dx} f = \frac{\widetilde{y}_{i+1} - \widetilde{y}_i}{\delta} \tag{2.42}$$

and the approximation error $\mathcal{O}\left(\delta + \frac{\sigma}{\delta}\right)$ becomes also dependent on the noise σ. For certain constellations of grid step δ and noise σ, especially for small grid steps δ, the approximation error deteriorates. For growing grid steps the approximation errors of the exact forward finite differences, see equation (2.41), and the noisy forward finite differences, see equation (2.42), converge. A common way to enforce the exactness of the data values is to choose large

---

[16]Additional test may be necessary, since saddles also lead to vanishing gradients

grid steps $\left(\delta \approx \sqrt{\sigma}\right)$ compared to the noise, what accompanies the loss of information[17]. Another shortcoming of finite differences schemes is that the solution $\frac{\mathrm{d}}{\mathrm{d}x}f$ is not smooth but partially constant on the grid. Enhancements of the classical finite differences methods may be summarized under the term local methods. One basic principle is to enlarge the neighborhood, or window, around the evaluation point x_i and use the $k_1 + k_2 + 1$ grid points $x_{i-k_1}, \dots, x_i, \dots, x_{i+k_1}$ and the associated data points $\widetilde{y}_{i-k_1}, \dots, \widetilde{y}_i, \dots, \widetilde{y}_{i+k_2}$ for computation. Savitzky-Golay filtering fits polynomial functions of order $h < k_1 + k_2$ on the data in the considered neighborhood using least-squares regression without regularization (Cleveland, 1979; Watson, 1964). Hence, Savitzky and Golay, 1964 extended the method of the moving average to conserve higher statistical moments. I want to point out that their basic idea is again to make the data to be differentiated exact by using an intelligent prefiltering to achieve y from $\widetilde{y}$ and subsequently compute the derivative from an almost exact y. Hence, the enhanced local methods try to decouple step size δ from noise level σ, however, the solution $\frac{\mathrm{d}}{\mathrm{d}x}f$ still remains non-smooth.

Global methods approximate $\frac{\mathrm{d}}{\mathrm{d}x}f$ based on the whole set of $k + 1$ grid points $x_0, x_1, \dots, x_k$ and associated data points $y_0, y_1, \dots, y_k$. A successful global approach is to understand differentiation as the solution to a minimization problem. The ill-posed problem is reformulated in the form of an overdetermined regularization, see equation (2.37), which yields

$$\operatorname*{argmin}_{u} \left(\mathfrak{D}\left(Au, \widetilde{y}\right) + \lambda \mathfrak{R}\left(u\right) \right) , \tag{2.43}$$

where $u = \frac{\mathrm{d}}{\mathrm{d}x}f$ represents the derivative, and $Au = \int_{x_0}^{x_k} u \, \mathrm{d}x$ is an integration. As proposed in section 2.2.2, different choices for the data term $\mathfrak{D}$ and the regularizer $\mathfrak{R}$ are possible. For unknown noise, the $\mathcal{L}_2$-norm is commonly chosen, since it is appropriate to cope with Gaussian noise (Green, 2002). Chartrand and Staneva, 2008 propose to adjust the data term only, if the noise distribution in the data is known. Response surface models, such as presented by Volk et al., 2011 for hydraulic bulge test evaluation, work without regularization and hence set $\lambda = 0$ in expression (2.43). Hence, I interpret the parameterized response surface model as a predefined filter above the entire domain, where the selected neighborhood of points $k_1 + k_2$ is equal to the total number of points $k + 1$. As pointed out in section 2.2.2, the regularization term $\mathfrak{R}\left(u\right)$ give additional possibilities to control the minimization and hence to design the results. Cullum, 1971 suggested the regression framework by Tikhonov, 1963 for numerical differentiation, where the regularizer becomes $\mathfrak{R}\left(u\right) = \int_{x_0}^{x_k} ||\nabla u||_{\mathcal{L}_1}^2 \, \mathrm{d}x$ using the $\mathcal{L}_1$-norm. This regularizer forces the function u and thus the solution $\frac{\mathrm{d}}{\mathrm{d}x}f$ to be smooth in contrast to local methods. Knowles and Wallace, 1995 depart from the regression framework by Tikhonov, 1963 and propose a different

---

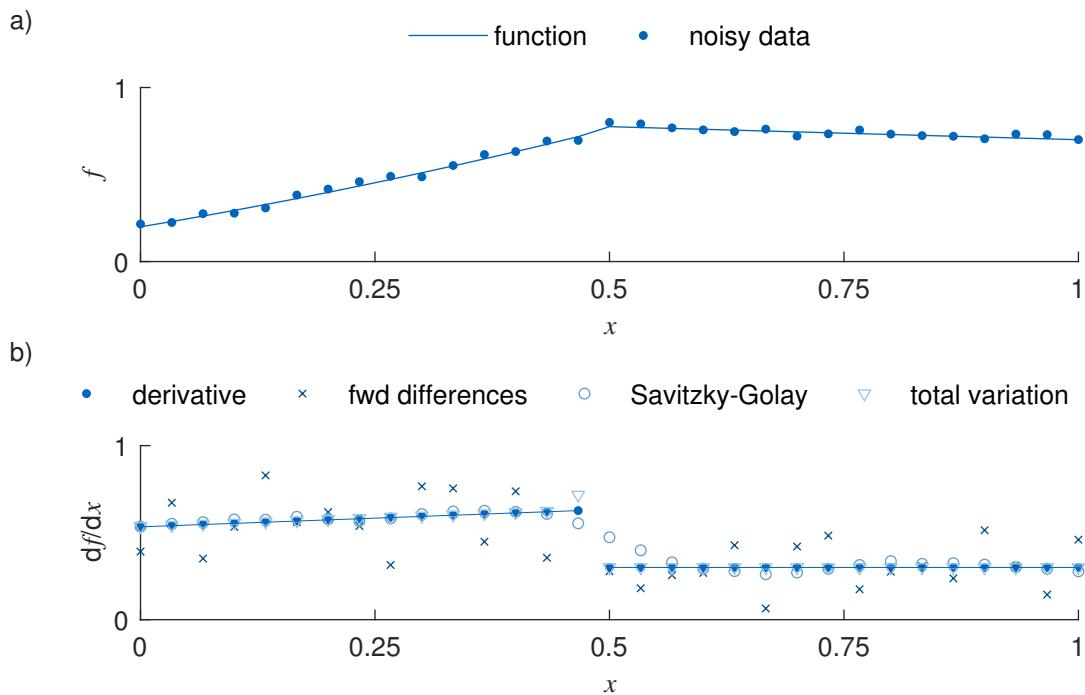[17]This procedure is referred to as regularization by coarse discretization (Natterer, 1983)

Figure 2.2: Comparison of different methods to compute a derivative from noisy data. a)
shows the underlying function and derived data subject to Gaussian noise. In
b), the analytical derivative is compared to results from forward finite differences,
Savitzky-Golay filtering, and total variation.

global variational method that also meets smooth results for $\frac{d}{dx} f$. Chartrand, 2011 showed that partly smooth derivatives can be achieved even if the data contains discontinuities using a total variation regularization term $\Re(u) = \int_{x_0}^{x_k} ||\nabla u||_1 \, dx$.

Figure 2.2 illustrates results for noisy data differentiation. The results are computed using different schemes for numerical differentiation, forward finite differences, local moving Savitzky-Golay filtering, and the global total variation approach of Chartrand, 2011. Figure 2.2 a) shows the exact function f as well as a modified variant that is subject to Gaussian noise and gives the noisy data. As an additional difficulty, the ground truth data has a discontinuous slope at $x = 0.5$. Forward finite differences show massive noise amplification, see figure 2.2 b). Savitzky-Golay filtering yields robust results, but overrides the discontinuity. Total variation is robust and even resolves the discontinuity in the computed derivative.

In general, the estimated derivative depends highly on the window size, filter order, and filter function in case of local methods and on the regularization terms respective parameters for the global methods. Gu and Wahba, 1991 and Krishnan and Seelamantula, 2013 emphasize that the choice of these settings is non-trivial and careful validation of the results should be done.

2.2.4 Validation

A good model balances complexity and error, as the early ideas of Occam[18] and Pareto[19] already suggests. Data-driven models often suffer from overfitting, which means that the model renders the data almost perfectly, but can not generalize or extrapolate (Larson, 1931). Two concepts to counteract overfitting are (cross-)validation and information criteria (Brunton and Kutz, 2019, p. 144).

(Cross-)validation splits the data into a training set 80-90% and a test set 10-20% (Arlot and Celisse, 2010). For k-fold cross-validation, sets of model parameters are calculated using k random portions 70-80% of the training set. The averaged set of model parameters defines the cross-validated model. The withheld test data is used to finally evaluate the model, which is particularly interesting in regions of extrapolation. The leave p-out cross validation removes p samples from the training data that are repealed for validation. Model parameters are determined with the remaining data and validated against the p samples. This is repeated for all permutations of training data and validation data. Analogously to cross-validation, the accuracy of the averaged model can be assessed using the test data.

The foundation of different information criteria is the Kullback-Leibler divergence D (Kullback and Leibler, 1951), which measures the distance between two models $\mathfrak{K}_1\left(\mathbf{X}, \boldsymbol{\varphi}_1\right)$ and $\mathfrak{K}_2\left(\mathbf{X}, \boldsymbol{\varphi}_2\right)$ that are parameterized by the sets $\boldsymbol{\varphi}_1$ and $\boldsymbol{\varphi}_2$. The criterion originates from statistics to characterize entropy and information theory by Shannon, 1948.

$$D\left(\mathfrak{K}_1, \mathfrak{K}_2\right) = \int \mathfrak{K}_1\left(\mathbf{X}, \boldsymbol{\varphi}_1\right) \ln\left(\frac{\mathfrak{K}_1\left(\mathbf{X}, \boldsymbol{\varphi}_1\right)}{\mathfrak{K}_2\left(\mathbf{X}, \boldsymbol{\varphi}_2\right)}\right) d\mathbf{X} \tag{2.44}$$

The Kullback-Leibler divergence D may be also interpreted as the information loss when $\mathfrak{K}_1$ is represented through $\mathfrak{K}_2$. Hence $\mathfrak{K}_1 = \mathfrak{K}_2$ yields $D = 0$ and no information gets lost. For a number of proposed models, the one with the lowest Kullback-Leibler divergence is regarded as the best model. The fundamental difference between information criteria based on equation (2.44) and assessments using classical error measures lies in the consideration of the model parameters and thus the explicit penalty of overfitting. Akaike, 1974 proposed a practical implementation of equation (2.44) based on the maximum likelihood estimation by Fisher, 1922. This criterion is called Akaike information criterion (AIC). The AIC score D_{AIC} is calculated by

$$D_{\mathrm{AIC}} = 2h - 2\ln\left(L\left(\hat{\boldsymbol{\varphi}}|\mathbf{x}\right)\right), \tag{2.45}$$

---

[18]law of parsimony: Occam's razor
[19]80/20 rule

where h is the number of model parameters and L the maximum likelihood estimate using the parameters $\hat{\boldsymbol{\varphi}}$ to fit the samples $\mathbf{x}$. The term $2h$ penalizes high numbers of model parameters. The AIC score is a relative criterion to select a model from a given set of models, however, it has no meaning for the absolute performance of the model (Burnham and Anderson, 2010, p. 62). Schwarz, 1978 changed the term, which penalizes the number of model parameters in a way that the correct model is guaranteed to be found in the proposed set of models if it is included. This criterion is called the Bayesian information criterion (BIC) with the score D_{BIC}

$$D_{\mathrm{BIC}} = \ln{(n)}\, h - 2 \ln{(L\,(\hat{\boldsymbol{\varphi}}|\mathbf{x}))} \;, \tag{2.46}$$

where n, the number of data points in $\mathbf{x}$, enters the first term. Other specific information criteria originate from AIC and BIC, such as the generalized information criterion (GIC) or the adjusted Bayesian information criterion (aBIC) (Dziak et al., 2020; Stoica and Selen, 2004)

2.3 Motion Estimation

Motion estimation methods extract kinematics from image sequences. In my opinion, two main currents exist that deal with the topic in different ways, although they pursue the same objective. On the one hand, computer vision represents a separate, interdisciplinary field of research in mathematics, computer science, and data science, which deals exclusively with image processing. In the language of computer vision, free motion is optical flow and motion estimation one of the royal disciplines (Gibson, 1950, p.117–144; Horn and Schunck, 1981). On the other hand, practitioners and engineers pragmatically search for suitable solutions to observe and evaluate their experiments. Digital image correlation (DIC) has proven suitable in many use-cases (B. Pan, 2018) – probably the reason why solid mechanics almost exclusively rely on digital image correlation. Different wording of these currents in itself illustrates their separation. If I search for the terms 'digital image correlation' or 'DIC' in the reference book of Szeliski, 2011 on applications of computer vision, I will not get a single hit, but 75 hits for the term 'optical flow'. Vice versa, the handbook by Sharpe, 2008 on experimental solid mechanics has no single hits for the term 'optical flow', but 205 hits for the terms 'digital image correlation' and 'DIC'. In this work, I try to merge both currents. Therefore, I introduce a consistent description of the two-dimensional motion estimation problem based on the continuum mechanics framework (section 2.1) and the principles of data science (section 2.2). The subsequent presentation of two fundamental approaches in motion estimation refers back to this description.
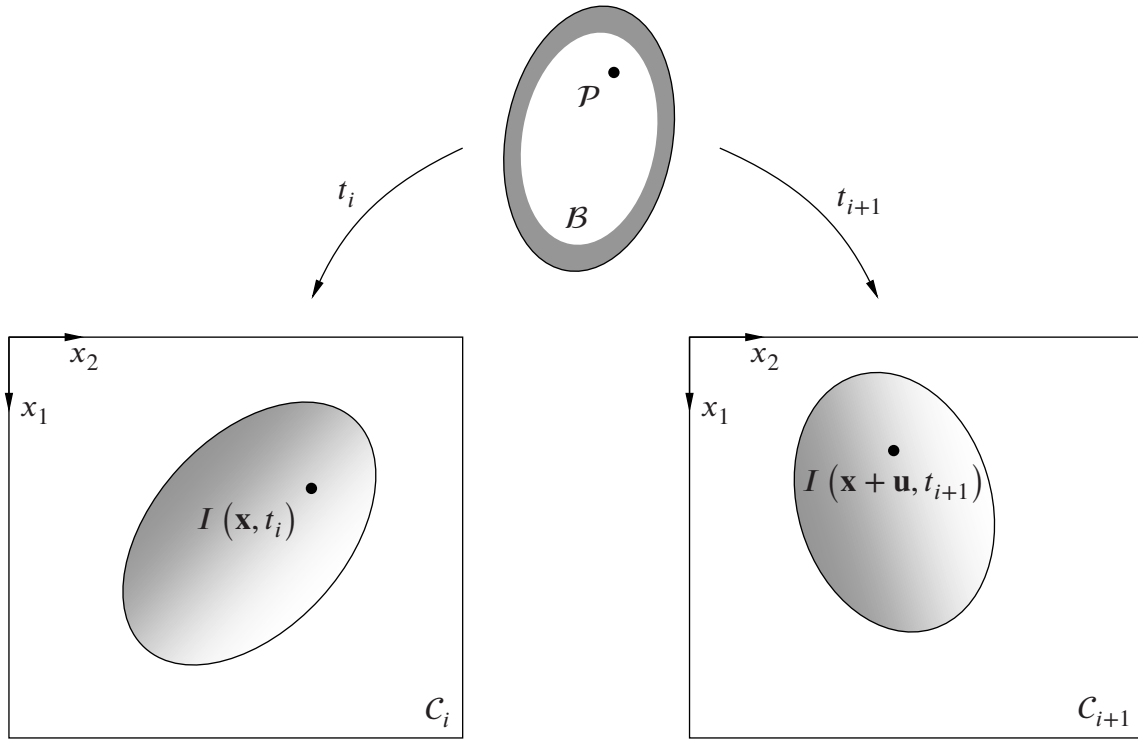
Figure 2.3: Capturing images is analog to the assignment of configuration C_i at time t_i and configuration C_{i+1} at time t_{i+1} for the body B in continuum mechanics. In addition, each material particle P is attributed with an intensity I.

2.3.1 Problem Formulation

In analogy to continuum mechanics, I understand capturing an image as creating a configuration $C \subseteq \mathbb{R}^2$, see equation (2.1). Material particles P of a body B are assigned to a two-dimensional coordinate system, as shown in figure 2.3. Further, each material particle is attributed with an intensity $I \in \mathcal{I} \subseteq \mathbb{R}$.

$$I : C \to \mathcal{I}, \quad P \mapsto I = I(P) \tag{2.47}$$

A smooth sequence of configurations C_i, capturing multiple images or a video, contains the motion of a body in space over time. The objective of motion estimation is to identify the motion relation (2.2), i.e. the displacement field $\mathbf{u}$, underlying the image sequence. The predetermined region of interest (ROI) defines the boundaries of the evaluation.

To track material particles, they must carry certain information (Clocksin et al., 2002). In case of images, a material particle owns a certain intensity I to track.[20] Motion estimation turns into the problem of finding the displacement field[21] $\mathbf{u}$ that transforms image $I_i = I(\mathbf{x}, t_i)$ into

---

[20]For the sake of simplicity, I use the terms image and image intensity as synonyms in the following.

[21]The terms "flow" and "flow field" are frequently used in the discussion of computer vision.

image $I_{i+1} = I\left(\mathbf{x} + \mathbf{u}, t_{i+1}\right)$. To solve for $\mathbf{u}$, I interpret I as the density of a continuous physical quantity and set up its local balance equation, following the principle of a master balance presented in section 2.1.2,

$$\frac{\mathrm{d}}{\mathrm{d}t} I = p_I + s_I + f_I \,, \tag{2.48}$$

where the three terms on the right side represent the intensity production p_I, intensity supply s_I, and intensity flux f_I. Interestingly, this continuum mechanics perspective is similar to both, the generic projected-motion equation of Liu and Shen, 2008 and the generalized brightness change constraint equation of Haussecker and Fleet, 2001 that are based entirely on geometrical considerations.

The most common assumption on the behavior of the intensity I is the brightness constancy. Applied to equation (2.48), it proposes that I has neither divergence nor production, supply, and flux. Thus, intensity behaves like the mass, see equation (2.17). Taking two images into account tacitly implies assumptions on derivatives and permits to rewrite the brightness constancy.

$$\frac{\mathrm{d}}{\mathrm{d}t} I = 0 \Leftrightarrow I\left(\mathbf{x} + \mathbf{u}, t_{i+1}\right) - I\left(\mathbf{x}, t_i\right) = 0 \,. \tag{2.49}$$

Other assumptions on the behavior of the intensity are also conceivable, but rarely used, such as the spatial intensity gradient constancy

$$\nabla I\left(\mathbf{x} + \mathbf{u}, t_{i+1}\right) - \nabla I\left(\mathbf{x}, t_i\right) = 0 \,. \tag{2.50}$$

This fundamental framework of motion estimation leads to an ill-posed problem. Each material point has a scalar intensity value, but for two-dimensional motion its displacement vector contains two unknown components u_1 and u_2. Using the formulation for underdetermined problems (2.39), the estimated displacement $\mathbf{u}$ solves

$$\underset{\mathbf{u}}{\mathrm{argmin}}\, \mathfrak{R}\left(\mathbf{u}\right) \text{ subject to } ||I\left(\mathbf{x} + \mathbf{u}, t_{i+1}\right) - I\left(\mathbf{x}, t_i\right)||_2 \leq \epsilon \,. \tag{2.51}$$

With regard to regression, see section 2.2.2, $I\left(\mathbf{x}, t_i\right)$ may be regarded as the data and $I\left(\mathbf{x} + \mathbf{u}, t_{i+1}\right)$ as the model parameterized by $\mathbf{u}$.

Two approaches are pursued to solve the ill-posed problem of motion estimation. Block-matching methods work using local constraints and include methods such as DIC, the default in experimental solid mechanics. Variational methods act globally and contain the optical flow estimation known from computer vision.
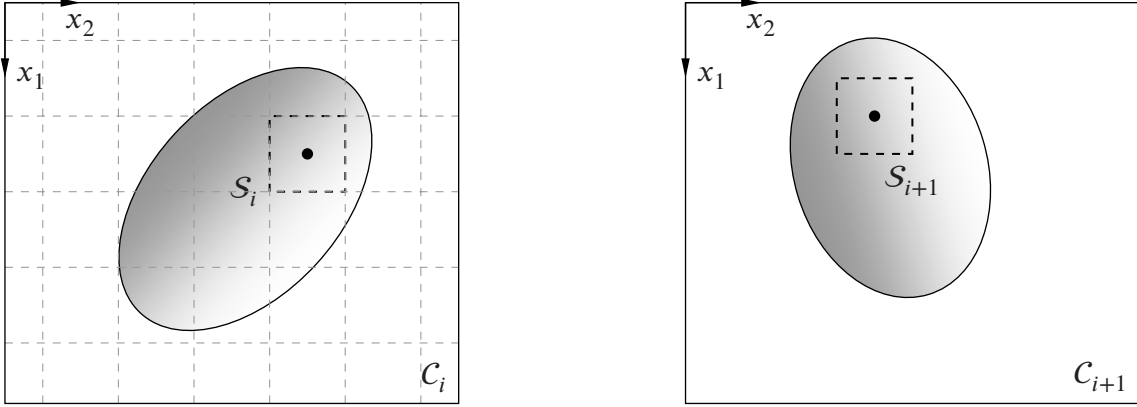
Figure 2.4: Block-matching methods divide the configuration C_i into blocks, such as S_i. The aim is to search for a corresponding block S_{i+1} in configuration C_{i+1} at time t_{i+1} that matches S_i in terms of certain criteria.

2.3.2 Block Matching Methods

Block-matching methods stem from image registration, where a single displacement vector is sought, which brings two images in the best possible agreement. Instead of using the whole image, Peters and Ranson, 1982 split it into blocks to calculate multiple displacement vectors, as shown in figure 2.4. Block-matching methods prescribe local constraints for these image blocks. Each block represents a neighborhood of material particles $S = \{P_1, P_2, \dots, P_{N^2}\} \subseteq C_t$. The additional constraints enable to solve expression (2.51) locally between S_i and S_{i+1}. Block-matching estimates, how the center of the neighborhood moves between image $I(\mathbf{x}, t_i)$ and image $I(\mathbf{x} + \mathbf{u}, t_{i+1})$ solving the overdetermined problem that using expression (2.37) in general may be written

$$\underset{\mathbf{u}}{\mathrm{argmin}} \left(||I\left(\mathbf{x} + \mathbf{u}, t_{i+1}\right) - I\left(\mathbf{x}, t_i\right)||_2 + \lambda \mathfrak{R}\left(\mathbf{u}\right) \right) \forall \mathbf{x} \in S_i \,, \tag{2.52}$$

where S occupies all $\mathbf{x}$ in the neighborhood. All frequently discussed and applied block-matching approaches, see for example the reviews by B. Pan et al., 2009 and Kamble et al., 2016, ignore the regularizer $\mathfrak{R}$, and hence, tacitly set $\lambda = 0$. As a consequence, the solution of expression (2.52) relies entirely on the data term. Black and Anandan, 1996 call this the single motion assumption – one block, one displacement vector. Without regularization, the calculation of the displacement $\mathbf{u}$ becomes a distance minimization, where the calculation of the square root is usually omitted.

$$\underset{\mathbf{u}}{\mathrm{argmin}} \left(I^2\left(\mathbf{x} + \mathbf{u}, t_{i+1}\right) - 2I\left(\mathbf{x} + \mathbf{u}, t_{i+1}\right) I\left(\mathbf{x}, t_i\right) + I^2\left(\mathbf{x}, t_i\right) \right) \forall \mathbf{x} \in S_i \tag{2.53}$$

Two categories of block-matching methods exist: least-squares methods, which directly solve expression (2.53) and cross-correlation methods, which further reduce expression (2.53).

Least-Squares Methods

Least-squares methods directly estimate displacements $\mathbf{u}$ from expression (2.53). The data term yields the similarity measure $C_S = \left(I\left(\mathbf{x} + \mathbf{u}, t_{i+1}\right) - I\left(\mathbf{x}, t_i\right)\right)^2$ to be minimized in the region S_i. An overdetermined system results, since each material particle $\mathcal{P} \in S_i$ must satisfy expression (2.53), which may be solved using different numerical methods (Press, 2007, p. 487–562). Lucas and Kanade, 1981 facilitate the brightness constancy using a first order Taylor approximation to accelerate the least-squares calculations

$$\mathbf{u}\frac{\partial}{\partial \mathbf{x}} I\left(\mathbf{x}, t_i\right) + \Delta t\frac{\partial}{\partial t} I\left(\mathbf{x}, t_i\right) \approx \mathbf{u} \cdot \nabla I + \Delta t\frac{\partial}{\partial t} I \approx 0 , \qquad (2.54)$$

where $\Delta t = t_{i+1} - t_i$. An overdetermined system of approximated brightness constancy equations results for each region S_i. For the solution, Lucas, 1984, p. 21–24 proposes a weighted[22] least-squares with a gradient descent algorithm. The Lucas-Kanade method is also referred to as local optical flow method.

Cross-Correlation Methods

The original cross-correlation method by Peters and Ranson, 1982 omit the quadratic terms in expression (2.53) and deduce a simple similarity measure entirely based on the mixed term $I\left(\mathbf{x} + \mathbf{u}, t_{i+1}\right) I\left(\mathbf{x}, t_i\right)$. The cross-correlation method results in a maximum search problem

$$\underset{\mathbf{u}}{\mathrm{argmax}}\left(I\left(\mathbf{x} + \mathbf{u}, t_{i+1}\right) I\left(\mathbf{x}, t_i\right)\right) \forall \mathbf{x} \in S_i . \qquad (2.55)$$

The mixed term $I\left(\mathbf{x} + \mathbf{u}, t_{i+1}\right) I\left(\mathbf{x}, t_i\right)$ is called cross-correlation criterion C_C, which scores the similarity of two regions with respect to image intensity (T. Chu et al., 1985).

Enhanced Methods

The classical least-squares and cross-correlation both exhibit three major problems: the similarity scores C_S and C_C depend on the size of the block, both measures are insensitive to affine

---

[22]A centered Gauss kernel is used to calculate the weights for each element in the block.

transformation (Clocksin et al., 2002), and the brightness constancy, see equation (2.49), is not invariant to illumination changes across the image sequence.

Different enhanced least-squares criteria and cross-correlation criteria have been proposed to overcome these issues. To counteract the sensitivity to absolute values, intensities may be normalized and centralized in various ways (Giachetti, 2000; Tong, 2005). Suitable warping functions[23] $\mathfrak{W}(\mathbf{x}; \boldsymbol{\varphi})$ parameterizing the displacement $\mathbf{u}$ ameliorate the problem to recognize affine transformations (Lu and Cary, 2000; Schreier and Sutton, 2002). A warping function does nothing more, but to increase the number of model parameters per block from two, u_1 and u_2, to six $\varphi_1, \varphi_2, \ldots, \varphi_6$, which suffice to describe in-plane affine transformation. An improved model expression, $I\left(\mathfrak{W}(\mathbf{x}; \boldsymbol{\varphi}), t_{i+1}\right)$, results and substitutes the original $I\left(\mathbf{x} + \mathbf{u}, t_{i+1}\right)$. The optimization solves for the parameters $\boldsymbol{\varphi}$ that enable affine transformations of the block. Farnebäck, 2003 propose an enhanced model based on polynomial expansion to improve the robustness against noise. The review of Baker and Matthews, 2004 deals with enhanced algorithms and extensions of approximated least-squares methods. Black and Anandan, 1996 soften the single motion assumption, which has positive effect on all major problems.

2.3.3 Variational Methods

Variational methods, or optical flow methods, follow a global approach to solve the motion estimation problem, see expression (2.51), and consider the ROI as a whole. In contrast to block-matching methods, where the data term is focused, for variational methods the choice of regularization $\mathfrak{R}$ dominates the solution of the underdetermined problem (Weickert and Schnörr, 2001). The fundamental variational framework result from an augmentation of expression (2.51) and reads

$$\operatorname*{argmin}_{\mathbf{u}} \left(||I\left(\mathbf{x} + \mathbf{u}, t_{i+1}\right) - I\left(\mathbf{x}, t_i\right)||_2 + \lambda \mathfrak{R}\left(\mathbf{u}\right) \right) . \tag{2.56}$$

Expression 2.56 uses Lagrange multipliers λ (Lagrange, 1797, p. 198), which converts the constrained problem into an unconstrained problem.[24] Lagrange et al., 1811 initially performed static analysis with his method, but later used it also for variational calculus (Fraser, 1992). The term variational methods expresses this origin.

Horn and Schunck, 1981 used the spatial displacement gradients for regularization, a close relative of the deformation gradient, see equation (2.3), and the approximated brightness constancy,

---

[23]Warping functions parameterize deformation in the region $\mathcal{S}$ similar to basis functions in finite elements.

[24]This approach is similar to penalty methods, known for example from contact modeling, in that an additional penalizing term in the objective function eliminates the constraints (Hestenes, 1969).

see equation (2.54), as data term. The proposed model corresponds to the first order regression by Tikhonov, 1963, see section 2.2.2, to solve ill-posed problems, which represents an isotropic penalty. The Horn-Schunck minimization expression reads

$$\underset{\mathbf{u}}{\mathrm{argmin}} \left(\left(\mathbf{u}\frac{\partial}{\partial \mathbf{x}} I\left(\mathbf{x}, t_i\right) + \Delta t\frac{\partial}{\partial t} I\left(\mathbf{x}, t_i\right) \right)^2 + \lambda ||\nabla \mathbf{u}||_2^2 \right) . \tag{2.57}$$

The minimizer (2.57) must satisfy the Euler-Lagrange equation,

$$0 = \left(\mathbf{u} \cdot \nabla I + \Delta t \frac{\partial}{\partial t} I \right) \nabla I - \lambda \Delta \mathbf{u} , \tag{2.58}$$

where $\Delta \mathbf{u} = \mathbf{u}_{i+1} - \mathbf{u}_i$ and which yields a unique solution (Schnörr, 1991). Horn and Schunck, 1981 set up a standard finite difference scheme with homogeneous Neumann boundary conditions $\frac{\partial \mathbf{u}}{\partial \mathbf{n}}$ on the image boundary to approximate the solution for equation (2.58). Mitiche and Mansouri, 2004 proved the convergence of the Horn-Schunck method.

Various adaptions, extensions, and specifications of the baseline Horn-Schunck variational method exist. When using $\mathcal{L}_2$-norm-based approaches motion discontinuities are lost, see section 2.2.3. In contrast, Aubert and Kornprobst, 1999 showed that $\mathcal{L}_1$-norm-based formulations resolve discontinuities in the displacement fields. Brox et al., 2004 introduced a theoretical framework for the use of warping functions in optical flow estimation. When using linearized data terms, such as that in equation (2.54), the models are initially limited to small displacements, which restricts their straightforward application. Papenberg et al., 2006 discuss the use of different non-linearized data terms and justify the use of warping functions mathematically. Multi-scale schemes extend the usability of variational methods to large deformation, as shown in the framework of Anandan, 1989. Barron et al., 1994 and Sun et al., 2010 give an extensive overview on the performance of different variational methods.

2.3.4 Applied Motion Estimation

Commercial tools typically used in experimental solid mechanics are based on block-matching methods, such as the well-known evaluation methods of gom GmbH, Braunschweig, Germany, Dantec Dynamics GmbH, Ulm, Germany, Instron, Darmstadt, Germany, Limess Messtechnik und Software GmbH, Krefeld, Germany, LaVision GmbH, Göttingen, Germany, Photo-Sonics International Ltd. Oxfordshire, UK, correlatedSolutions Inc., Columbia, United States, or MatchID, Gent, Belgium, to name but a few. Classical fields of application of these evaluation routines are motion analysis in multi-body systems or strain analysis in experiments for the

identification of material parameters. In addition to these commercial providers, there are various open source software packages, including competitive programs such as the implementations of Blaber et al., 2015 or J. Yang and Bhattacharya, 2019.

Common to both commercial and open source systems is that they understand spatially and temporally coupled motion phenomena such as instabilities or discontinuities as a postprocessing result of motion analysis but not as a part of the evaluation itself. On the one hand I explain this on the background of simple user handling, universal operability and application-oriented computation times. On the other hand, I currently see hardly any demand for measurement systems that resolve such special phenomena in evaluation. These motion phenomena are still subject to current research both in modeling and in experimental recording facing the same problems as in the motion estimation evaluation. This observation shows a certain self-locking characteristic and may be responsible that the analysis of those motion phenomena is rarely found in practice. Nevertheless, processes exist which are based on such extreme phenomena or even have them as their functional basis. Shear cutting represents one such process.

2.4 Shear Cutting

The German standards DIN8580, 2003 and DIN8588, 2013 assign shear cutting to the main group 'cutting' and its subgroup 'severing'. Shear cutting, also called shearing, denotes a manufacturing process for chipless[25] separation of sheet metals between two blades moving past each other. The German standard DIN9870-2, 1972 distinguishes between closed and open cutting lines. A closed cutting line has a self-contained contour, such as in punching or blanking[26]. An open cutting line begins and ends at the sheet metal boundary, like for trimming or embossing. The doctrine denotes blades for open and closed cutting lines differently (Lange, 1990, p. 148–149; Hoffmann et al., 2012, p. 681). The terms upper and lower blade is used in the context of open cutting lines, punch and die in the context of closed cutting lines. However, to be concise, I often use the terms punch and die for both processes without deficiencies.

2.4.1 Shear Cutting Process Description

Shear cutting tools carry and guide the pair of blades and may also contain other functional components, such as a blank holder (DIN9869-1, 1967; DIN9869-2, 1969). The blank holder

---

[25]Without formation of a shapeless substance.
[26]For translations of technical terms throughout the thesis I refer to the reference book by the CIRP, 2019.

a) closed cutting line

$$F = 0 \quad F > 0 \quad F > 0 \quad F > 0 \quad F \neq 0 \quad F < 0$$
$$\dot{F} = 0 \quad \dot{F} \approx C \quad \dot{F} > 0 \quad \dot{F} < 0 \quad |\dot{F}| \gg 0 \quad \dot{F} > 0$$

punch

blank holder

sheet metal

die

b) open cutting line

$$F = 0 \quad F > 0 \quad F > 0 \quad F > 0 \quad F \neq 0 \quad F < 0$$
$$\dot{F} = 0 \quad \dot{F} \approx C \quad \dot{F} > 0 \quad \dot{F} < 0 \quad |\dot{F}| \gg 0 \quad \dot{F} > 0$$

upper blade

blank holder

sheet metal
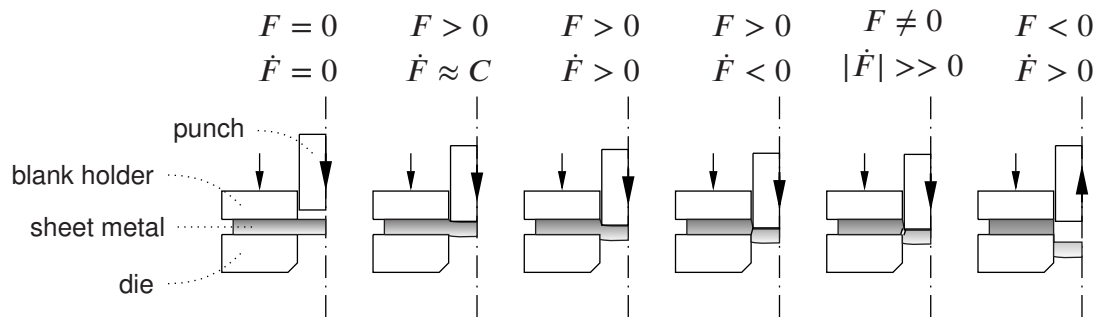
lower blade
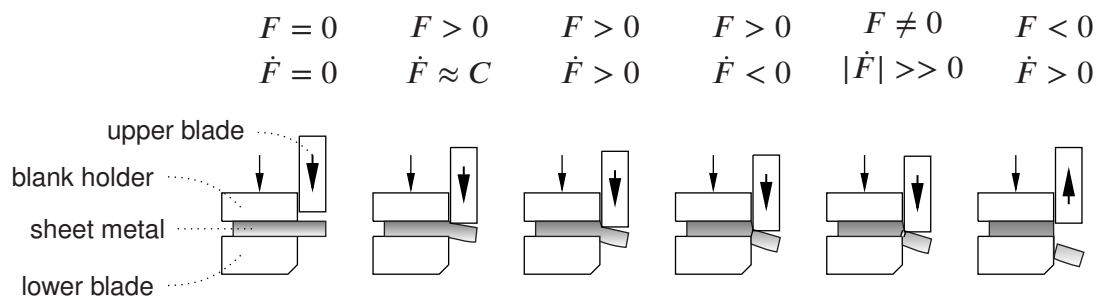
Figure 2.5: Scheme of the shear cutting process. a) shows the basic tool design and the process sequence for a closed cutting line, where the dot-dash line represents a symmetry axis. b) shows the basic tool design and the process sequence for an open cutting line. The small arrow on the blank holder represents the blank holder force, the large arrow the cutting force F acting on the punch and upper blade, respectively.

clamps the sheet metal during the shearing process. It not only prevents unintentional lifting of the sheet metal but may also act as a stripper, serve as a positioning unit, or manipulate the material flow into the cutting clearance (Buchmann, 1963). Figure 2.5 shows the basic shear cutting tool design and process for closed and open cutting lines.

A press provides the process forces, where the cutting force F denotes the force measured at the blades and serves as process descriptive force quantity.[27] First, the blank holder clamps the sheet metal and fixes it in the proper position. The punch still has to travel towards the sheet metal surface and hence no cutting force occurs. When the punch hits the sheet metal surface, all components in the force flow–press and tool components, blades, and sheet metal–experience elastic deformation. The cutting force therefore increases steeply and almost constantly. Together with the cutting force, a bending moment arises due to the cutting clearance, which acts as a lever

---

[27]When measuring process forces, forces at the press, tool, and punch must be differentiated. The press force and the force at the tool contain the blank holder force, whereas the punch force F do not contain it. Friction in the overall system can also influence the forces.

arm (Timmerbeil, 1956; Veenstra and Ramaekers, 1978). The cutting clearance[28] c_c denotes the distance between the blade edges (VDI3368, 1982). The bending moment coexists with the cutting force until complete material separation (Romanowski, 1959, p. 32). It causes an inhomogeneous distribution of stresses along the blade contours, where the highest compressive stresses occur directly at the blade edge roundings[29] (Bach, 1924, p. 30–32; Romanowski, 1979, p. 15). Resulting friction depends on the friction conditions and the normal pressure (Klocke et al., 2001). The blank holder force counteracts the bending moment and prevents a deflection of the sheet metal on its side. On the opposite side, the bending moment is supported for closed cutting lines, but not for open cutting lines and the sheet metal evades the punch motion. When the sheet metal reaches its elastic limit, irreversible deformations enter the shear cutting process. The irreversible deformations concentrate on the shear affected zone, a limited area between and around the blade edges (Hamada et al., 2018; Levy and van Tyne, 2012). The progressive deformation is dominated by hardening effects, like strain hardening and strain rate hardening. But different phenomena oppose the domination of the hardening effects. The kinematics of the process reduce successively the cross section between the blade edges, equivalent to a geometric softening (W. Johnson and Slater, 1967). In the sheet metal, damage and increasing temperatures[30] may lead to softening. The combination of hardening and softening effects results in an increasing but degressive cutting force curve until the maximum cutting force. After the maximum cutting force, softening effects dominate the hardening effects. Cracks initiate and propagate until complete material separation. Typically, two macro cracks, which originate from the blade edges, propagate through the material in shear cutting and, for appropriate process setup, converge. Depending on the process boundary conditions, the crack initiation may start at either blade edge. For closed cutting lines and uniform blade edge rounding, the first crack forms at the die, because the tensile stresses of stretching and bending add up there (Meyer, 1962; Timmerbeil, 1957a). More precisely, the crack initiation occurs at the lower end of the die edge rounding. This also applies to the crack initiation at the punch edge rounding (Bühler and Pollmar, 1971; O. Kienzle and W. Kienzle, 1958). In shear cutting processes with open cutting line and uniform blade edge rounding, the first crack appears at the upper blade, because there tensile stresses from stretching and bending accumulate. The crack propagation through the material represents an additional geometric softening effect, which leads to a steep decrease of the cutting force. When the macro cracks consolidate, and complete material separation takes place. Since all components in the force flow are preloaded elastically, an abrupt relief of the potential energy occurs that leads to oscillations, especially of the punch (Doege et al., 1977;

---

[28]The cutting clearance is usually specified relative to the sheet metal thickness.
[29]The geometry of the blade edges is commonly assumed round, and hence, can be characterized by its radius.
[30]Irreversible plastic work dissipates into heat, see section 2.1.2.

Hirsch et al., 2011). The curve of the cutting force shows the oscillating behavior and its decay. The punch motion turn at the bottom dead center of the press stroke and the sheet metal under the punch is ejected. Still a certain force acts on the punch due to the elastic spring back of the sheet metal, also during back stroke but with different sign. For open cutting lines these forces are smaller as for closed cutting lines, because of lower friction forces from material spring back (Buchmann, 1962, p. 102–114). The two major geometrical design features are the cutting clearance and the blade edge geometry. In general, the two blade edge geometries must not be the same (VDI3368, 1982). The front side of the blades may also be machined. Oblique grounding of the blades leads to a pulling cut with lower process forces but greater immersion depths. Also lateral forces appear and the processed sheet metal can be distort (Krabbe, 1953, p. 38–39; Kopp et al., 2016). The pulling cut can also be induced through the movement of the blades (DIN8588, 2013). I focus on the full-edged shear cutting in this thesis, where the front sides of the blades are flat and their movement is perpendicular to the blade edges.

2.4.2 Cut Part Characteristics

The shear cutting process leaves prestrained and predamaged material in the shear affected zone and generates a characteristic cut surface.[31] Depending on the specific application, the shear affected zone and the cut surface together must fulfill certain requirements: geometric ones at the cut surface and physical ones in the shear affected zone. The guideline VDI2906-2, 1994 suggests to describe the geometry of the cut surface based on the heights h_i and widths w_i of the shear affected zone (subscript 's'), the edge draw-in (subscript 'd'), the clean-shear (subscript 'c'), the fracture (subscript 'f'), and burr ('subscript 'b'), which is shown in figure 2.6 a). In addition, two angles α_i are introduced to clarify the rotations of clean-shear surface and fracture surface against the sheet metal plane. The edge draw-in, the clean-shear and the burr develop during irreversible deformation. The fracture surface is the result of the unifying macro cracks. When the macro cracks do not converge, degenerated cut surfaces with secondary clean-shear emerge (Keller, 1951; Timmerbeil, 1956). In essence, given the sheet metal thickness s, the guideline VDI2906-2, 1994 proposes an eight parameter model to describe the cut surface with the model parameter vector $\boldsymbol{\varphi} = (\varphi_1, \varphi_2, \ldots, \varphi_8)$, as shown in figure 2.6 b).[32]

The description of the physical properties in the shear affected zone is oriented, if at all, towards the application case. No standardized models exist, but for example the investigations of Feistle

---

[31]The dimensional accuracy with respect to the sheet plane may be evaluated according to DIN6930-2, 2011.

[32]The parameter ϕ_1 defines the onset of the edge draw-in, however, edge draw-in converges against the sheet metal surface. An asymptotic function representation instead of a hard threshold value according to the guideline VDI2906-2, 1994 would better describe this characteristic.
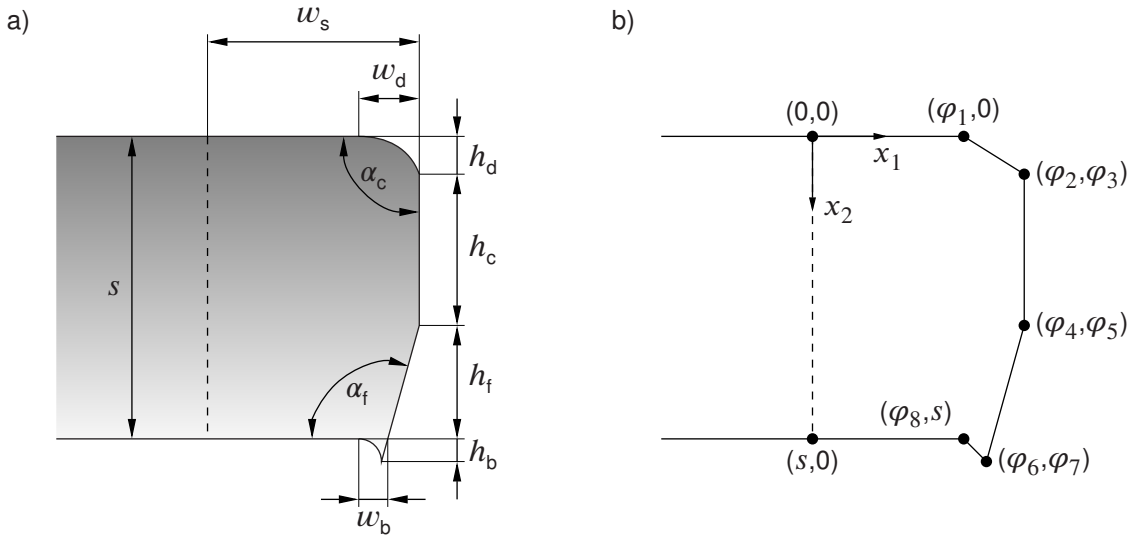
Figure 2.6: a) shows commonly used cut surface parameters as defined by the guideline VDI2906-2, 1994. b) draws the essence of a) in the form of an eight parameter model with the model parameter vector $\boldsymbol{\varphi} = (\varphi_1, \varphi_2, \ldots, \varphi_8)$.

et al., 2015 for edge fracture or Weiss et al., 2017 for loss reduction in electrical sheet metal apply data-based models tailored to a specific problem. I summarize the problem specific, tailored descriptions of the shear affected zone in the set $\boldsymbol{\Phi}$.

The geometric and physical properties of the sheared edge are determined by various influencing factors, such as the sheet metal material, the cutting line, the shear cutting tool, the press, the lubrication, and the part quantity. These things are usually fixed in practice and I summarize them in the set $\boldsymbol{\Gamma}$. To influence the geometric and physical properties of the sheared edge, process parameters may be adjusted. I collect the variable process parameters in set $\boldsymbol{\gamma}$. The central process parameters of shear cutting in the adjustable set $\boldsymbol{\gamma}$ are the cutting clearance, the blade edge rounding, and the punch velocity (Doege and Behrens, 2010, p. 371–373, Hoffmann et al., 2012, p. 83–89,97).

The cutting clearance is one of the most important process parameters for adjusting the desired cut surface quality (Mori et al., 2010). For closed cutting lines, for example Timmerbeil, 1957a, O. Kienzle and Meyer, 1963, p. 72–80, and Hörmann, 2008, p. 84–85 consistently report an increase in clean-shear with smaller cutting clearance due to higher hydrostatic pressure. Hörmann, 2008, p.87–88 observes a reduced edge draw-in and burr height with decreasing cutting clearance, which is supported for example by Schenk et al., 1978 and Wu et al., 2012. When the reduction of cutting clearance reaches a certain limit, the high hydrostatic stress state causes the macro cracks to pass each other, and degenerate cut surfaces with secondary clean-shear appear (Keller, 1951; Timmerbeil, 1956). Nothhaft, 2014 describes varying clean-shear

for different cutting clearances in open shear cutting. For open cutting lines, hydrostatic stress state and tensile stress due to the free bending yield a certain minimum clean-shear. Burr height stays constant before this minimum is reached and increases afterwards, which Hoogen, 1999, p. 144–145 explains on the basis of changed crack trajectories. Edge draw-in behaves similar to closed cutting lines and increases for an increasing cutting clearance (Hoogen, 1999, p. 138–146; Hilditch and Hodgson, 2005). The blade edge geometry also exerts a considerable influence (O. Kienzle and Meyer, 1963, p. 83–84). As edge rounding or wear increases, crack-promoting stress peaks are smoothed, crack initiation is delayed, and clean-shear increases (Hörmann, 2008, p. 95–99; Nothhaft, 2014, p. 85–97). These increasing deformations result in a higher edge draw-in and burr height. Therefore, the blade edge rounding is often specifically adjusted or can also be the result of wear (Timmerbeil, 1957b). Hoffmann et al., 2012, p. 687 states that punch velocity has a marginal influence on the cut surface under 0.5 m/s punch impact velocity, but over 1.5 m/s changes it significantly, which is supported for example by findings of Itoh et al., 1987 and Marouani et al., 2009. Extreme punch velocity promotes early fracture initiation and the cut parts have a large homogeneous fracture surface (Subramonian et al., 2013). The angle of the fracture surface and the edge draw-in depends on the adjusted cutting clearance. However, N. Ong and Chan, 1989 showed that the correct choice of the cutting clearance yields small edge draw-in and orthogonal fracture surface. The occurrence of a smooth cut can be almost completely avoided and burr-free shear cutting is possible, however, for example process loads and wear inhibit wider use (Jana and N. S. Ong, 1989).

2.4.3 Investigation of Shear Cutting

Since the 1920s, a large number of scientists, engineers, and practitioners studied shear cutting processes in numerous setups and with varying process parameters. One main objective drives these investigations, the enhancement of geometric and physical properties of the cut sheet metal part.[33]

The core of each investigation is to obtain a suitable mapping $\mathfrak{S}$ between the c-dimensional input $(\boldsymbol{\gamma}, \boldsymbol{\Gamma})$ and p-dimensional output $(\boldsymbol{\varphi}, \boldsymbol{\Phi})$ of the shear cutting process

$$\mathbb{R}^c \to \mathbb{R}^p , \quad (\boldsymbol{\gamma}, \boldsymbol{\Gamma}) \mapsto (\boldsymbol{\varphi}, \boldsymbol{\Phi}) = \mathfrak{S}(\boldsymbol{\gamma}, \boldsymbol{\Gamma}) . \tag{2.59}$$

---

[33]The reduction of wear, an often discussed objective in shear cutting, finally traces back to the properties of the cut sheet metal component.

The mapping $\mathfrak{S}$ is in general high dimensional and highly nonlinear due to the complex interactions between process conditions, process parameters, and sheet metal behavior. Hence, the vast majority of investigations focus on reduced subspaces.

To formulate the problem consistently, at least one full set of input data $(\boldsymbol{\gamma}, \boldsymbol{\Gamma})$ must be determined to set up the shear cutting process. However, the complexity of the input to evaluate $\mathfrak{S}$ is reduced with the number of process parameters $\boldsymbol{\gamma}$ and conditions $\boldsymbol{\Gamma}$ to be varied. The output domain often consists exclusively of geometric properties of the cut surface $\boldsymbol{\varphi}$, which are straightforward to measure and suffice for quality assessment in many conventional applications.[34] Often even the eight parameter model shown in figure 2.6 is further simplified, for example setting $\varphi_2 = \varphi_4$ and omitting φ_8. In general, the mapping $\mathfrak{S}$ itself can take any form of black, gray or white box model.

In the descriptive framework of continuum mechanics, equation (2.59) presents as initial boundary value problem. Next to integral quantities such as punch travel or cutting force, state variables are utilized to describe and analyze the shear cutting process, to predict cut part properties, and to validate considered assumptions. During shear cutting, the material in the shear affected zone undergoes extreme state changes. The state of each material particle finally falls back solely on its dynamic motion history, since no external heating or other external stimuli intervene in the shear cutting process. Hence, dynamic motion history not only governs the final shape of the cut surface, but also dictates the physical properties of the shear affected zone.[35]

As any heating is caused by the shearing process itself, an indicator of the dynamics is the temperature development. Two causes drive a temperature increase: surface friction between contact surfaces (Uetz and Föhl, 1978) and dissipation of irreversible deformation work in heat (Farren and I. Taylor, 1925). Frictional heat is generated on different scales. Landman et al., 1992 claim that interactions in the top atomic layers of the contact surfaces generate heat. On the other hand, Rigney and Hirth, 1979 argue for larger plastic deformation processes. Kennedy, 1982 showed that at least 95% of dissipation takes place within 5 μm of the contact surface. Irreversible deformation inside the material also leads to dissipation in heat. The proportion of dissipation from deformation work is often formulated as a constitutive law, see for example the works of Zehnder, 1991 and Rosakis et al., 2000, which all goes back to the experimental work of G. Taylor and Quinney, 1934. Stainier and Ortiz, 2010 proposed an alternative method based on variational calculus, where the proportion of dissipation arises directly from the definition

---

[34]The geometric properties may suffice in many cases, because they inherently carry information of the material deformation but in reduced dimension.

[35]Here, I make the reasonable assumption that the chaotic portion of the process to be negligible.

of the state potential and pseudo-dissipation potential, see section 2.1.3. Based on an high-resolution in situ temperature measurement, Demmel et al., 2015 impressively show, how the temperature development at the punch edge traces the dynamics during shear cutting. Both the temperature phenomena caused by friction and the temperature increases caused by deformation could be resolved by measurement (Demmel, 2014, p. 88–100). Abrupt increases in temperature characterize shear cutting shortly before material separation. The only possible explanation for such a phenomenon is extreme localization of deformation prior to fracture (Landau et al., 2016; Roessig and Mason, 1999). As a consequence, material point motion in the shear affected zone is complex in both, time (over the process duration) and location (over the shear affected zone). The initial punch indentation leads to moderate deformations and almost homogeneous rates. In this phase shear cutting presents good-natured. But with the onset of clean-shear formation, the characteristics changes. Deformation begins to localize and concentrates on specific areas. With further penetration of the punch, these effects amplify and accelerate. Hence, the observation scale changes, metaphorically from sheet thickness to blade edge shape and from tenths of a second to hundredths of a second.

Micrographs provide qualitative evidence of severe local deformations and extreme localization at different punch penetration depths (Sonkamble et al., 2019; Zhu et al., 2020). Gotoh and Yamashita, 2001 and Z. Chen et al., 2003 analyzed material microstructure and could clearly prove the presence shear bands during shear cutting. Li, 2000 further demonstrated that shear bands are not straight between the blade edges but appear in various shapes and forms depending on the process setup. This experimental findings point some analogies to the theoretical works on slip lines of Jimma, 1963 and Kasuga et al., 1977. Around the blade edges, a competition takes place between hydrostatic pressure and damage about crack initiation. Crack propagation and final material separation also are subject to the complex interactions during shear cutting (Z. Chen et al., 2003). Qualitative investigations on microstructure are very objective. Grain appearance visualizes the deformation during shear cutting and sets the benchmark for any kind of quantitative in situ analysis. Quantitative in situ analysis aim at not only making the mapping in equation (2.59) transparent and interpretable, but also measurable and comparable with respect to the descriptive framework.

The initial boundary value problem of shear cutting is given by a system of non-linear coupled partial differential equations. To solve for the initial boundary value problem, shear cutting needs to be modeled appropriately, which resembles the aforementioned theory-driven idea of dynamic analysis. Since no generally valid analytical approaches exist to solve this type of coupled partial differential equation problems, possible solutions are approximated numerically. Geometrical issues, such as large deformation or the different scales of blade edge geometry, sheet

metal, and punch travel, place high demands on discretization and numerical solution methods (Brokken et al., 2000, Manopulo, 2011, p. 91–92). Simulation requires appropriate constitutive description of the sheet material that copes with elastic, plastic, and failure phenomena during shear cutting. The classical approach to material modeling of sheet metal is difficult for shear cutting. High hydrostatic pressures, extreme strains, sudden temperature rises, and high strain rates can not be sufficiently emulated using established tests for parameter identification in sheet metal processing. Essentially, the hardening and damage behavior of the material must be described under the realistic boundary conditions. The hardening behavior includes the flow criterion and the flow curve. In sheet metal processing, research and modeling of sheet metal materials takes place mainly against the background of sheet metal forming. Due to the semi-finished product characteristics, material laws are formulated specifically with regard to the sheet plane and experimental test methods are developed for this purpose. Shearing tests also evaluate the material behavior only in the sheet plane (Traphöner et al., 2018; Yin et al., 2014). In contrast, shear cutting operates perpendicular to the sheet metal plane and a direct transfer of the results is therefore difficult (Bolka et al., 2015). To model damage and fracture, a large number of different material failure criteria exist. The simplest type of these criteria are independent of the development of the state variables and their thermodynamic forces. Critical values for equivalent stress or equivalent strain indicate when fracture occurs in the material (Keeler, 1961, p. 23–45, G. Johnson and Cook, 1985; Kuhn et al., 1973). For example, C. Wang et al., 2014 and Bohdal et al., 2014 built their simulation routines around hard strain thresholds to predict failure in shear cutting. Another family of models include the deformation history to predict material failure, either formulated coupled or uncoupled. In uncoupled models, damage does not influence the material behavior in principle. Fracture criteria take the form of an accumulating function with respect to state variables and fracture occurs at a critical limit value (Cockroft and Latham, 1968; Freudenthal, 1950). For instance, Hambli and Potiron, 2000, Hambli and Reszka, 2002 and Lemiale et al., 2009 simulated shear cutting processes using uncoupled fracture criteria. Coupled models include damage to predict material behavior prior to material failure, which may be done using damage variables as proposed by Lemaitre, 1985 or based on micro-mechanical interactions, such as in Gurson-Tvergaard-Needleman models, which was established by Gurson, 1977 and extended by C. Chu and Needleman, 1980, Tvergaard, 1981, Tvergaard, 1982, and Needleman and Tvergaard, 1984. Hambli, 2001 and Wen et al., 2013 propose models that use damage variables in the sense of Lemaitre, 1985. Klingenberg and Singh, 2003, Rachik et al., 2002, and Lemiale et al., 2009 work successfully using Gurson-Tvergaard-Needleman model.

This small potpourri of numerical investigations already indicates, that despite, or perhaps because of the complex characteristics of shear cutting, different failure models can be used

to achieve the desired results. Testing to identify the material-specific failure behavior and the respective model parameters requires elaborate experimental procedures (Wierzbicki et al., 2005). Often tests are combined with inverse analysis, which moves the theory-driven idea of simulation in the direction of data-based modeling. Different methods exist to solve the inverse problems for constitutive parameter identification, as reviewed by Avril et al., 2008. For example Komori, 2013 calibrate material failure parameters for shear cutting simulation through inverse analysis of plane strain test and uniaxial tensile test. However, the characteristics of shear cutting make it almost impossible to characterize the material under conditions comparable to those of the process itself. Material testing under high hydrostatic pressures, at elevated temperatures, and the extreme strains cannot be accurately reproduced in simplified materials testing setups. Hence, material parameter identification methods calibrate models in order to extrapolate in the space of state variables and thermodynamic forces. As described in section 2.2 model extrapolation based on real discrete data may amplify uncertainties and exhibit deficiencies.

Especially for the determination of the crack initiation, it has therefore become established to carry out parameter adjustments in the form of strongly underdetermined inverse analyses based on the cut surface or integral measures, such as cutting force and punch travel (Goijaerts et al., 2000; Hambli and Reszka, 2002; Hatanaka, Yamaguchi, and Takakura, 2003). What is tacitly accepted with this approach is that all other physical model errors and simplifications–tribology is to be emphasized (Kitamura et al., 2016; Moghadam et al., 2020)–and numerical deficiencies are included in the calibration of the material damage behavior. As a result, material damage behavior loses its physical meaning and hence model interpretability suffers. Krinninger et al., 2017 explicitly name the problems of such strongly underdetermined inverse analyses. However, they see also an opportunity to create purely application-oriented simulation models, that initially have no claim to be interpretable. These models allow to explore a limited space of process variations around the data basis used for calibration and are appropriate for designing the cut surface but not properly the shear affected zone. The investigations of K. Wang et al., 2015 confirm that also elaborate material parameter identification can not circumvent the issue. They use the result of shear cutting simulation for predicting edge fracture. Qualitative agreement with the experimental results is achieved, however, only a simplified substitute model is able to reproduce qualitative statements of the experiments.

In general, experimental analysis of shear cutting face the same problem as simulation: large deformation, high dynamics, localization, fracture, and different scales, as for example K. Wang and Wierzbicki, 2015 experienced during their examinations. In addition, shear cutting has properties that make it impossible to look at it without changing the boundary conditions. The shearing takes place under plane strain (Manopulo, 2011, p. 89–90), which I also denote the

natural boundary conditions of the process.[36] Material particles move almost exclusively parallel to the punch travel and perpendicular to the punch contour. This justifies a two-dimensional analysis of the process, which facilitate the solution of the initial boundary value problem, but complicate observation. Plane strain boundary condition is a spatial constraint[37], which contradicts with the constraint free boundaries that commonly prevail in experiments, such as in tensile testing. Due to the different three-dimensional stress states in regions closer to and along the cutting edge, the motion measurements at an open sheet edge does not correspond to motions in regions of the sheet, which are farther away from the edge. Hence, the spatial constraint initially prevents direct observation of the shear cutting process. But despite or perhaps due to the progress of numerical analysis, experimental approaches to determine state variables play an important role for process understanding, simulation validation, and data-based modeling including inverse procedures.

Experimental evaluations categorize into in situ and ex situ analysis. Ex situ quantities are for example micro and nano hardness, constitutive parameters, which may be attributed to Φ, and cut surface characteristics φ. Ben Ismail et al., 2009 and Ghadbeigi et al., 2020 measure nano hardness to determine the size of the shear affected zone and Young's modulus distribution after shear cutting. The measurement of micro hardness is also suitable to study the material in the shear affected zone, as for example Weiss et al., 2017 propose. The cut surface characteristics φ are by far the most commonly used quantities to verify and validate numerical models. However, the eight parameter model from VDI2906-2, 1994 is usually considerably simplified. Many studies give out one single primary goal and therefore often validate their models solely in the respect of this single parameter, as for example Rachik et al., 2002 and Hu et al., 2015 using the burr height. The two parameter approach of Hatanaka, Yamaguchi, Takakura, and Iizuka, 2003 use a combination of edge draw-in height and burr height, that of Bohdal et al., 2014 clean-shear height and fracture height. Marouani et al., 2012 utilized three parameters: edge draw-in height, clean-shear height, and fracture height to validate their predictions. Sontamino and Thipprakmas, 2019 use a four parameter description, which consists of edge draw-in height and width, clean-shear height, and fracture height. Especially from an application-oriented point of view this extreme dimensionality reduction from the full output set (φ, Φ) to a handful of parameters makes sense. However, the reduction comes with specialization and can not confirm the physical interpretability of the whole model, in general.

The in situ analysis include quantities, such as cutting force and punch travel, temperature, and

---

[36]The plane strain boundary condition does not hold anymore for high curvature changes along the cutting line or when material exhibits strong anisotropic behavior. However, the plane strain assumption has established to investigate the shear cutting process and also covers many practical applications.

[37]Dirichlet boundary condition in sense of the initial boundary value problem, see section 2.1.4.

kinematic quantities, which are absorbed over the duration of the process. Rafsanjani et al., 2009 used the maximum punch force values to validate their model. The whole cutting force-punch travel curve represents an integral in situ measure of the shear cutting process. Cutting force and punch force are easy to measure and therefore established to confirm and calibrate numerical results (Lemiale et al., 2009; K. Wang and Wierzbicki, 2015). Also more elaborate force measurement systems exist to split the cutting force into its lateral and vertical components, see for example Gustafsson et al., 2016 and Kopp et al., 2016.

In situ full-field observations based on optical measurements are rare in shear cutting. But full-field analysis yield locally resolved information and hence stronger features for process description, validation, and calibration. The predecessors of the in situ motion analysis are the grid methods. In his investigations, Timmerbeil, 1957b has already shown that strains in the shear zone at the sheet edge can be measured ex situ via grid lines. By using a square-grid Z. Chen et al., 1999, Zheng et al., 2005, and Yu and Zhao, 2012 show strain localization around the blade edges and the existence of shear bands. The evaluation of the square grids is based on the large deformation analysis of Hsu, 1966. Leung et al., 2004a present a square grid-based approach with remeshing to measure severe plastic deformations and apply it to shear cutting. This method has been further extended by Leung et al., 2004b using interrupted experiments and re-etching of the specimen. All grid-based methods have in common that they apply grids before the shearing experiments. In order to keep the grid features intact for the subsequent evaluation, they change the boundary conditions of the process to avoid smearing. Hence, the deformation is analyzed under plane stress but not plane strain conditions. Pathak et al., 2019 take up the idea of grid methods, but use the microstructure as carrier of deformation information. Using micrographs inherently avoids the violation of the process boundary conditions, which Pathak et al., 2019 do not comment on. The microstructure is converted into strain values using a shear test for reference, which was additionally evaluated with DIC. They also found a high sensitivity to gage length evaluating the micrographs. In situ motion analysis greatly extend the grid methods temporal resolution, which results merely pseudo-like from interrupted experiments.

During my survey I identified two families of in situ motion analysis in shear cutting that exist and develop independent from each other. One family goes back on the works of Stegeman et al., 1999 and Goijaerts, 1999, p. 20–22, the other on Takahashi and Aoki, 1996a and Takahashi and Aoki, 1996b. Stegeman et al., 1999 and Goijaerts, 1999, p. 20–22 look at the open side of the sheet metal during shear cutting and deduce displacement and strains based on DIC and specifically prepared specimen. They accept the completely different stress and strain state in the observed area, which seems peculiar because Goijaerts, 1999, p. 22–26 criticize this simplification in the context of failure identification using either planar or axisymmetric

shearing. However, no relationship is established between these two situations. K. Wang and Wierzbicki, 2015 and Ghadbeigi et al., 2020 follow this strongly simplified approach and used commercial DIC software to evaluate the image sequences. They prepare their samples using airbrush paint, which transmits the deformation information of the material. Unfortunately, for very large deformations, the paint is no longer a good transmitter of deformation, because it exhibits different material behavior (Forsström et al., 2020). The in situ analysis family of Takahashi and Aoki, 1996b and Takahashi and Aoki, 1996a tackle the boundary condition problem by utilizing lateral glass stops, which prevent bulging of the sheet metal sample and should maintain a plane strain state across the entire cutting line. However, a detailed analysis, if the boundary condition actually remains constant along the whole cutting line, is missing. Hence, they still rely on the assumption that the strain and stress state are constant. Aoki and Takahashi, 2003 use the same setup and evaluate the motion based on correlations in the frequency domain using Fourier transformation. Sasada and Togashi, 2014 and Sasada and Tamura, 2016 stay in line with Takahashi and Aoki, 1996a but switch to commercial DIC software.

What unites all in situ observations is that they fail at the latest with the onset of fracture and only give reliable results before the onset of clean-shear for different reasons. The used measurement equipment prevents adequate spatial and temporal resolutions to capture high dynamics and localized deformation, although only quasi-static punch velocities are utilized. All studies rely entirely on block-matching methods for motion evaluation. The block size dependence is comparable to the gage length sensitivity Pathak et al., 2019 exposed and cross scale analysis are difficult. Hence, Aoki and Takahashi, 2003 and Ghadbeigi et al., 2020 emphasize more on the qualitative character of their results, although they present quantitative values for displacements and strains. Stegeman et al., 1999 and Goijaerts, 1999, p. 20–22 focus on the analysis of the deformation in a limited area around the punch edge, where they analyzed only the moderate part of the deformation during formation of the edge draw-in. Sasada and Togashi, 2014 and Sasada and Tamura, 2016 also focus on the material motion during edge draw-in for varying cutting clearance. K. Wang and Wierzbicki, 2015 use the full-field deformation data to validate their simulation results in early process stages, but switch back to ex situ methods for fracture evaluation, which reduces the analysis on crack location in contrast to crack evolution.

In general, a fundamental discrepancy between the countless number of numerical analysis and the few in situ experimental studies on shear cutting exist, probably due to the high effort that this experiments entail. But in particular to verify and validate numerical analysis in situ analysis are necessary. On the other hand, high-resolution full field motion data opens opportunities for data-driven approaches in modeling, prediction, and control. In shear cutting, large deformation, high dynamics, localization, and fracture remain the open problems that still have to be solved.

3 Aims and Scope

This chapter sets out the aims and scope of the thesis respecting the introduced descriptive framework and the previous scientific treatments of the shear cutting process. First, I conclude on the current state of knowledge (section 3.1). Starting from previous methods to survey shear cutting, I discuss the gap between computer vision and standard full-field measurement methods in solid experimental mechanics. The discussion culminates in open potentials for experimental process analysis, especially for dynamic and complex processes, such as shear cutting. In section 3.2, I seize on these potentials and formulate the research objective of the thesis. Section 3.3 structures the conducted work and gives the basic structure of the investigations.

3.1 Conclusions on Current Knowledge

Shear cutting combines severe deformations, high dynamics, localization, and fracture. The dimensions in which these phenomena take place are at least one scale below the process environment represented by the sheet metal width and length, active elements dimensions, shear cutting tool, and press. Shear cutting modeling and measuring may be seen as a kind of multi-scale task.

Numerical analyses initially do not require any observation of the shear cutting process, which may be one reason why they enjoy great popularity. The challenges of the shear cutting process also impede in simulation and even extend to material characterization. Current state of the art numerical procedures perform a reduced inverse calibration of their simulation models, for example based solely on the finished cut component. The calibration process smears constitutive behavior, tribology, and numerical settings, which impairs interpretability. These models allow to explore a limited space of process variations appropriate for cut surface prediction, but questionable when it comes to the shear affected zone. As long as only the cut surface is provided, the reduced-inverse calibration is highly underdetermined and ill-posed, not only for each individual parameter but also in their dependencies. A single cut surface geometry may be achieved using various sets of parameters and the result highly depends on the chosen initial values. Time resolved experimental data decouples many of these parameters and massively reduce the solution space. An overall in situ experiment to observe and measure deformation

evolution of the shear affected zone including crack formation would form the basis of enhanced inverse analysis.

Shear cutting experiments are commonly evaluated ex situ. Step-by-step experiments within one stroke try to reproduce the course of the process by stringing together ex situ experiments, but what gets lost entirely are the dynamics of the shear cutting process. Integrated observations either use simplistic, academic setups with improper boundary conditions, such as by K. Wang and Wierzbicki, 2015, or require an elaborate concept to maintain the natural process boundary conditions, such as by Takahashi and Aoki, 1996b. The few in situ studies on deformation in the shear affected zone only consider either closed or open cutting lines. Process dynamics are left out completely and every analysis ends with the onset of clean-shear formation. Up to this point only mild gradients and moderate rates occur in the shear cutting process, comparable with classical quasi-static experiments in solid mechanics, such as tensile testing. The actual separation phase, in which material deformation localizes, cracks form, and fracture propagates, is not considered. Questions on how localization, crack initiation and fracture propagation, develop the characteristics of the shear affected zone remain open. But I argue that this is exactly the starting point to understand the dynamics of the shear cutting process. As the deformation progresses, the localization changes the required observation scale from sheet material thickness to cutting clearance and beyond. The discontinuities, growing gradients, and extreme rates pose challenges for the computation of derivatives, required in the continuum mechanics descriptive framework. The basis to investigate those kind of phenomena is a sufficient resolution in space and time, which places high demands on sensors and hardware used. Highly resolved signals accumulate to large amounts of data that require appropriate dimensionality reduction and handling. The previous in situ investigations provide only incomplete information on the overall dimensionality of their measured data. Data preparation and curation are not addressed, which may be due to the fact that the gathered data sets were small, hence feasible, and that commercial software was utilized for subsequent evaluation. For motion estimation, the previous in situ observations have in common that they rely on DIC, the classical block-matching algorithm using correlation criteria. From an engineer's point of view, DIC is the most obvious technique, as it has proven itself for innumerable tasks in experimental solid mechanics. To enable proper DIC, adequate image resolution and unique material texture is needed, where block size must balance local accuracy with global precision. Hence, block-matching methods suit not well to cross-scale analyses, especially in combination with numerical derivatives, and in particular are not designed to accurately capture discontinuities. Variational methods for motion estimation allow to model the expected solution. On the one hand, these measurement models can satisfy the descriptive framework and on the other hand they can fulfill the measurement task across

different scales. If at all, the spatial and temporal resolution represent a natural observation horizon. In contrast to block-matching methods, the variational models can be trained to handle large gradients, high rates, and discontinuities. In fluid mechanics, variational methods from computer vision are already successfully used to measure complex motion. They complement and extend measurements based on particle image velocimetry, the experimental fluid mechanics pendant to DIC.

The current state of knowledge brings to light a significant need to understand the dynamics of the shear affected zone during shear cutting. Previous work, however, has paid only minor attention to the occurring extreme phenomena, which may be due to the use of classical measurement methods. However, modern sensor technology in combination with tools from the field of data science reveal potentials that can make it possible to measure the complete shear cutting process. My research objective is rooted in these potentials.

3.2 Research Objective

The research objective of this thesis is to observe, quantify, and understand the dynamics of shear cutting–from the beginning until complete material separation. The prototype for the shear cutting test bench should be an industrial precision stamping tool, not its academic simplification. In essence, I will answer the following four questions:

How to design a temporally and spatially resolved observation of the entire shear cutting process, which maintains the natural process conditions?

How to curate and evaluate data to capture the extreme phenomena of shear cutting?

How do modifications in the shear cutting process affect its dynamics and the development of the shear affected zone?

What consequences may be drawn for the modeling, design, and control of shear cutting from its dynamic behavior?

On a meta-level, these questions also answer how classical experimental engineering work can be enriched with methods from data science, in particular computer vision, where spatio-temporal optical flow methods open up multi-scale evaluation of motion instabilities (higher-order derivatives) and discontinuities.

3.3 Structure of the Work

The structure of the work mimics the creation, curation, and evaluation of data. In addition to the actual recording of the raw data, the creation includes the integration in the descriptive framework. Based on the state variables of the modeling context, measurement information can be gathered from the data followed by their analysis and interpretation.

In chapter 2 *Fundamentals and Framework*, I have formulated the descriptive framework, which is rooted in continuum mechanics. The unified framework for continuum mechanics, data-driven approaches, and motion estimation forms the inductive structure of the thesis and spans around its work content, shown in figure 3.1. Therein, the analysis of the dynamics of shear cutting divides into the three main actions as common when data intensive experiments are conducted–to create data, to curate data, and to evaluate data.

In chapter 4 *Approach and Experiments*, I introduce the fundamental idea for realistic data acquisition in shear cutting. The basis of the data collection is a concept to observe the shear cutting process appropriately using a novel shear cutting tool (section 4.1) and specialized experimental setup (section 4.2). I consider experiments for different shear cutting test configurations (section 4.3) that are evaluated holistically (section 4.4). The basis of the investigation are highly resolved spatial and temporal observations of the shear cutting process under its validated, natural boundary conditions. Force, punch travel and high-speed image acquisition are integrated into the shear cutting tool. In contrast to previous work, I based the layout and design of the shear cutting tool on requirements from industrial precision punching tools. The proposed novel method to guide and align all active cutting tool elements prevents academic simplifications. This shear cutting tool strictly maintains constant process conditions under different test configurations and variable process parameters. Process parameters are varied to study their influence on the dynamics of shear cutting and the shear affected zone. Modifications of cutting clearance, punch velocity, and blade edge geometries are conducted. Two different 4 mm sheet materials are cut, S355MC mild steel (material number 1.0976, DIN EN 10149-2, 1995) and aluminum EN AW 5083 (material number 3.3547, DIN EN 485-2, 2016). Besides the analysis of closed cutting lines, I include open cutting lines and two-stage shear cutting test configurations. High-resolution sensor signals from force, punch travel, and high speed acquisition amount to large data sets for each shear cutting experiment that require suitable data curation.

The gathered experimental data can not be handled by conventional tools. I therefore developed methods and hybrid algorithms to curate and evaluate the experimental data, which is presented

in chapter 5 *Methods*. I answer the question of how the experimental raw data can be translated into measurement information combining different data handling and processing techniques in section 5.1, to section 5.4. The developed handling routine synchronizes all sensor signals based on a single time trigger. I prepare the raw sensor signals appropriately based on the process characteristics. Since the actual process characteristics reveal only during evaluation, raw data preparation interacts with data evaluation. Data evaluation splits into formative data evaluation, which contains the computations of measurement data from the prepared raw sensor signals, and summative data evaluation, which reflects the proposed methods, discusses the experimental results, and draws further conclusions. The formative data evaluation is composed of in situ and ex situ analysis.

Ex situ analysis results in the cut surface geometry. To determine the characteristics of each cut surface, I set up a robust, sampling-based evaluation algorithm to overcome user dependence in state-of-the-art manual determination and numerical gradient-based feature detection. The in situ analysis is based on the force, punch travel, and high-speed image data sets. The heart of the work is the in situ deformation analysis, which has four main instances: displacement estimation, strain estimation, strain rate estimation, and fracture evaluation. I tailored each instance towards the dynamic analysis of the shear cutting process.

The results from the formative evaluation culminate in the summative evaluation. Chapter 6 *Results* presents the experimental outcomes. I use a reference experiment to introduce the different results (section 6.1) and structure the investigation according to the different shear cutting test configurations examined (section 6.2 and section 6.3).

The interpretation of the results is subject to chapter 7 *Discussion*. At the beginning, I prove the research approach with the assumptions made (section 7.1) and discuss the accuracy and precision of the experimental results (sections 7.2). The significance of the results is discussed and approved against the background of the concepts and methods developed. I understand this as the formative instance in data evaluation. The summative step discusses the results in front of the state of knowledge with focus on dynamics, localization, and the shear affected zone in section 7.3. The findings allow to comprehend the dynamics of different shear cutting processes and the development of the shear affected zone.

I close the work with chapter 8 *Conclusion*. Starting from the topic of modeling and inverse analysis (section 8.1), I classify the results in an application-oriented way with regard to process design and control (section 8.2). Finally, I present connecting points to material testing, direct measurement of higher-order derivatives, and future research directions concerning manufacturing technologies and experimental mechanics (section 8.4).

descriptive framework
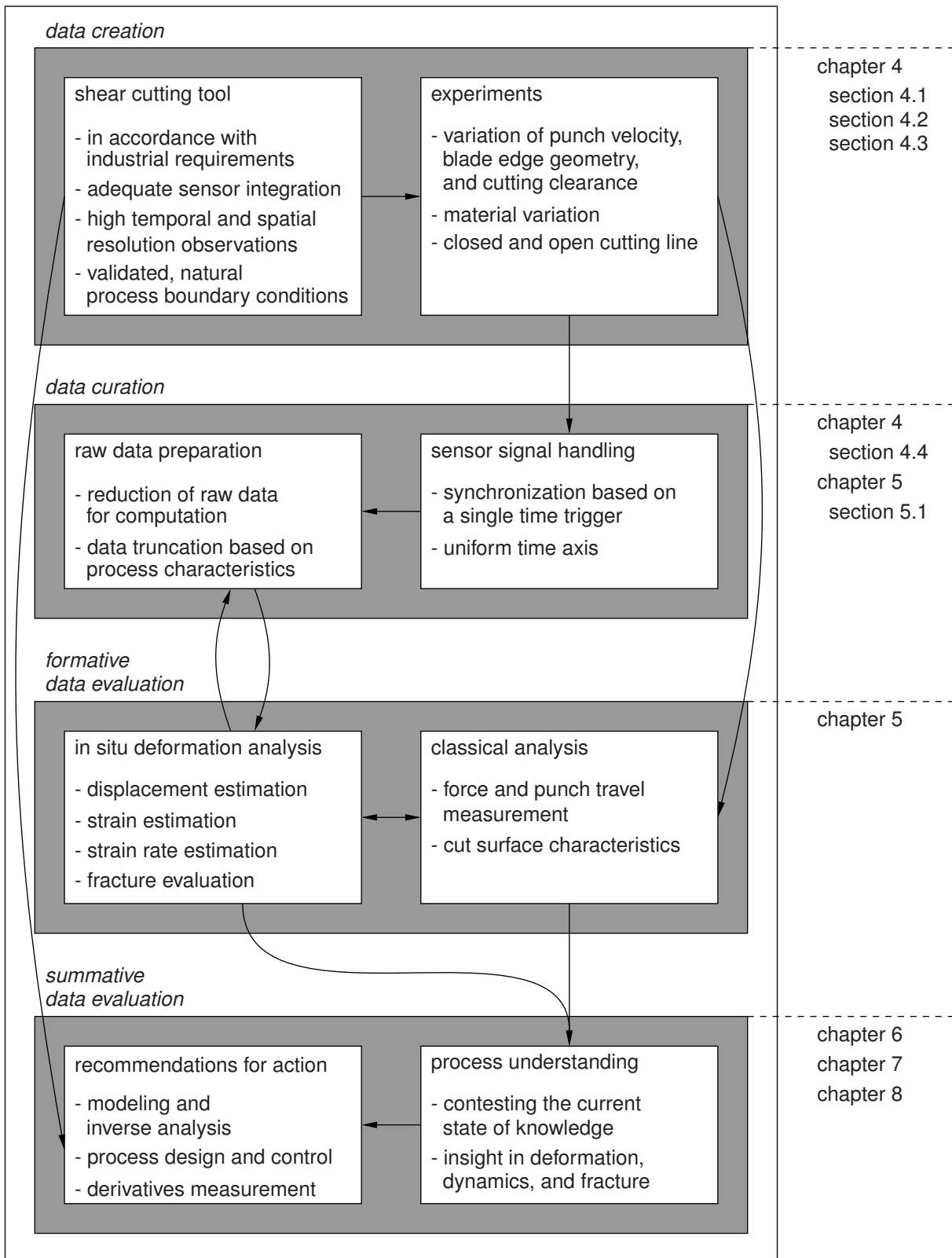
Figure 3.1: Structure of the research work.

4 Approach and Experiments

The research is based on the ability to record full-field motion in situ during shear cutting with high spatial and temporal resolution. Therefore, the basic research approach is reflected in the concept for shear cutting tool (section 4.1). It allows unbiased observation of shearing for almost arbitrary process parameter settings and test configurations (section 4.2 and section 4.3). Data preparation and the formulation of the experimental objectives complete the research approach (section 4.4).

4.1 Shear Cutting Tool

The developed shear cutting tool opens the possibility to investigate the shear cutting process under industrial process conditions. Three scientific objectives mainly drove the design and engineering: extensive process observation, known boundary conditions, isolated variation of process parameters. In contrast to previous approaches, my aim was to build up a shear cutting tool that meets the requirements of industrial practice, despite the diverse scientific objectives. Therefore, I started with a design and engineering for a precision shear cutting tool and tailored the whole setup towards the scientific objectives. This procedure lead to a shear cutting tool that combines high stiffness, accuracy, precision, and elaborate packaging.

The shear cutting tool is designed as a four column guide frame. Guide columns with central collar and backlash-free ball guides position the top tool plate, the blank holder plate and the bottom tool plate against each other, see figure 4.1 a). To ensure high stiffness in the $x_1 x_3$ plane, guide columns have a diameter of 32 mm. The three tool plates with a thickness of 40 mm each were eroded simultaneously in a single setup so that holes and pockets required for positioning align perfectly. They consist of through-hardened tool steel X153CrMoV12 (material number 1.2379, DIN EN ISO 4957, 2018). The square upper supporting plate carries the top tool plate and serves for the fixation at the press ram. The lower supporting plate has the same square geometry and carries the bottom tool plate. Both supporting plates are 40 mm thick and consist of tool steel X153CrMoV12. The thickness of the tooling and supporting plates guarantees high stiffness in x_2 direction. The shear cutting tool is basically symmetrical with respect to the $x_1 x_2$-plane and the $x_2 x_3$-plane. Intentional asymmetries achieve an always identical assembly

a) full assembly

x_3

x_1

x_2

400 mm

340 mm

400 mm

upper supporting plate

top tool plate

blank holder plate

bottom tool plate

lower supporting plate

b) exploded view

x_3

x_1

x_2

guide bushing

force measurement unit

punch

lifting unit

spring set

guide column

blank holder element

sheet metal

metal plate

die module

spring set

guide bushing
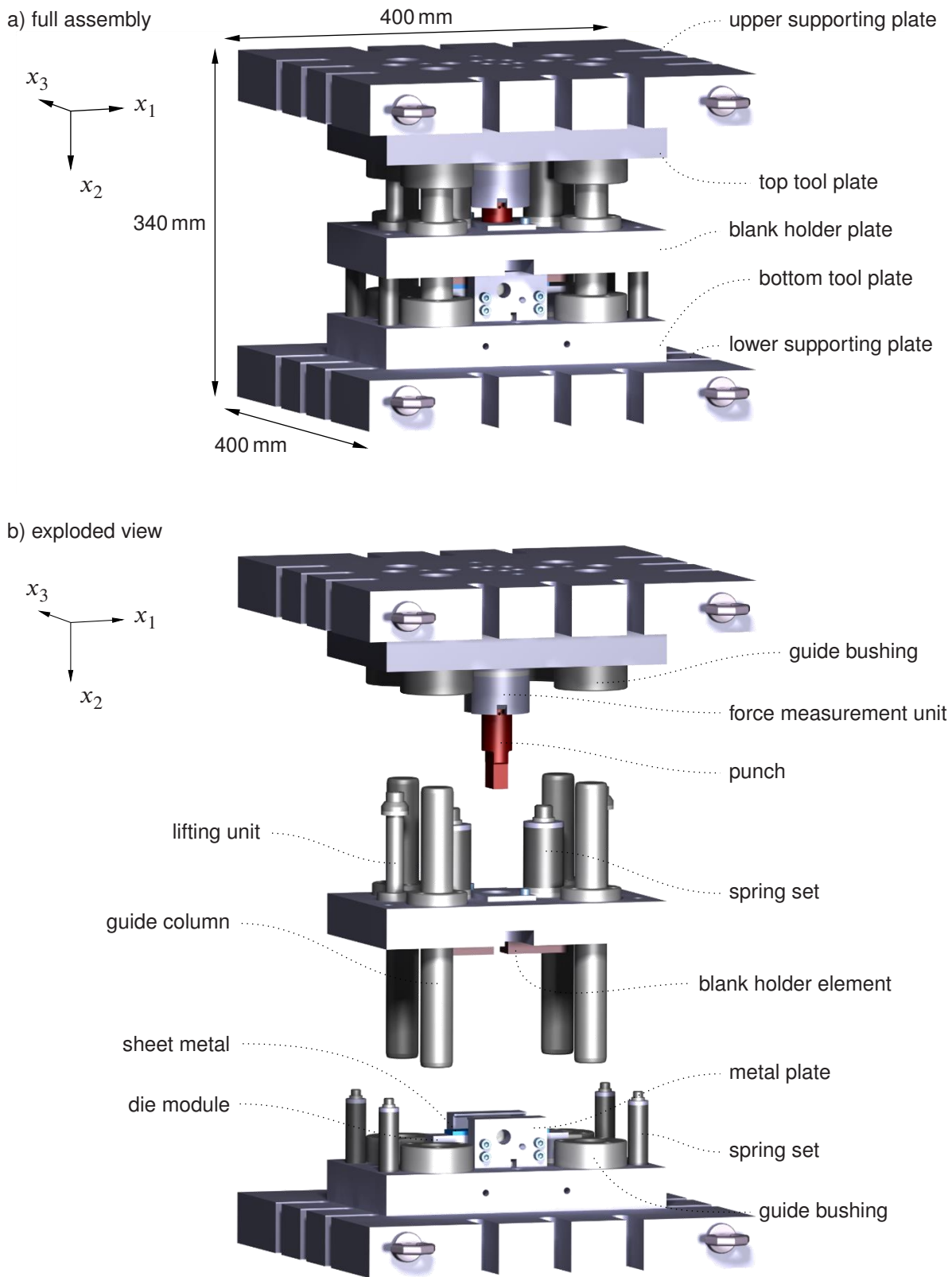
Figure 4.1: Shear cutting tool developed for the in situ motion observations. a) full assembly of the shear cutting tool. b) exploded view of the three main tool parts.

of the individual tool parts. The shear cutting tool has a 400 mm by 400 mm mounting area on the upper and lower supporting plate and a total height of 340 mm in unloaded condition.

The bottom tool plate fixes the die module, which supports the exchangeable die insert, see figure 4.1 b), figure 4.2 a) and detailed in figure 4.4. Die module and die inserts were manufactured from through-hardened tool steel X153CrMoV12. An oxide ceramic intermediate plate of ZrO_2 electrically isolates the die module from the bottom tool plate. Such oxide ceramic isolation elements are integrated throughout the whole shear cutting tool, which prepares it for temperature measurements according to Demmel, 2014 and Demmel et al., 2015. Different die inserts allow for different cutting clearances by variation of the distance between the die edges. The specified manufacturing tolerances allow an exact adjustment of the cutting clearance in the range of $\pm 3\,\mu$m. Four auxiliary springs sit in the corners of the bottom tool plate and hold the blank holder plate in a certain height for easy assembly and loading with sheet metal samples.

The blank holder plate carries two spring sets that generate the blank holder force when the top tool plate travels downwards. The blank holder elements transfer this force to the sheet metal. Two lifting units next to the two springs ensure that the blank holder plate follows the top tool plate during the return stroke. A cylindrical guide bushing in the center of the blank holder plate positions the punch in the x_1x_3-plane and locks rotations around the x_1-axis and x_3-axis. The cylindrical guide bushing has a diameter of 30 mm. The guide bushing consists of oxide ceramic ZrO_2 and electrically isolates the punch from the blank holder plate. Guiding the punch in the blank holder plate reduces the free length of the punch with respect to the process plane, which ensures high process stability. The circumferential tolerance of the punch in the guide bushing is between $2\,\mu$m and $4\,\mu$m.

The punch is made of cemented carbide material CF-H40S+. The punch has a floating bearing in the force measurement unit, which is fixed at the top tool plate. The cutting force measurement is integrated in the upper part of the force measurement unit, where the installed load cell only receives a defined part of the applied force, see figure 4.2. The installed piezoelectric load cell is a single-component quartz crystal load washer of the type 9031A from Kistler Group, Winterthur, Switzerland, with a measuring range of 60 kN. The load washer was preloaded with a force of 9.0 kN, which corresponds to 15% of the maximum test force. In the installed setup, the force measurement unit can measure up to 120 kN maximum cutting force. Further, the force measurement unit contains an oxide ceramic intermediate plate that electrically isolates the punch from the top tool plate. The top tool plate defines the position of the punch along the x_2-axis. I want to emphasis that the rotational degree of freedom around the x_2-axis remained free so far.

a) setup without glass stop   b) setup with glass stop

x_3 x_3
        x_1 x_1

    x_2 x_2

load cell ·········   ········· force measurement unit

                                   ········· ceramic plate

punch ········   ········· punch mount

guide bushing ·········

                                   ········· ceramic plate

                                                                                        188 mm

                                   ········· blank holder element

sheet metal ·········

spacer ·········   ········· ceramic plate   ········· illumination access

        ········· die insert

metal plate ·········   ········· die module   glass stop ········· measuring hole
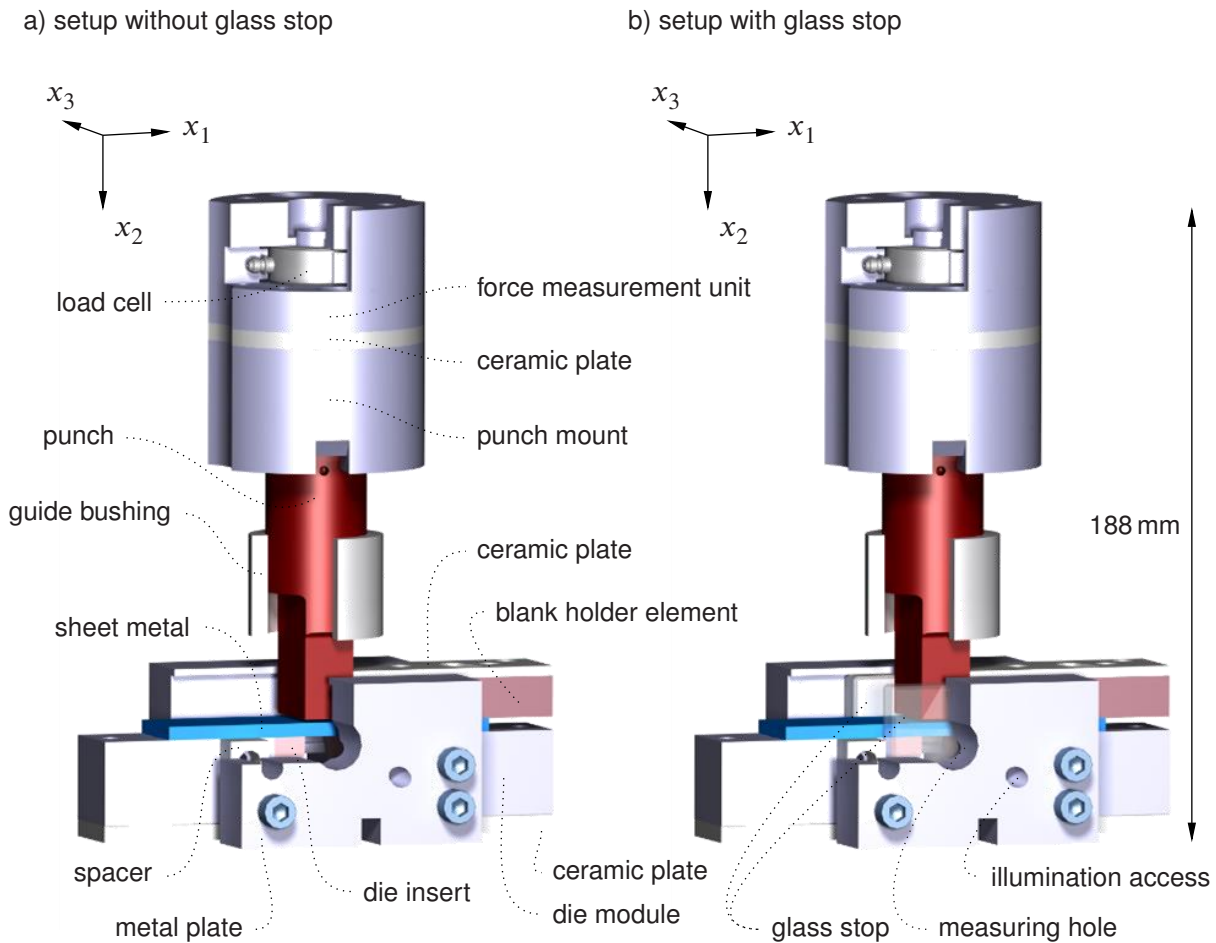
Figure 4.2: Schematic representation of the selected tool parts, active elements and sheet metal sample for shear cutting experiments. Some components are cut for better visibility. Setup a) is without glass stops, which yields a plane stress boundary condition. Setup b) is with glass stops, which yields a plane strain boundary condition.

The core of the shear cutting tool forms two glass stops, which rest on both sides of the active elements in parallel to the x_1x_2-plane, see figure 4.2 b). Each glass plate is 10 mm thick. Two metal plates with a thickness of 20 mm fix the glass stops at the die module using four bolts on each side. The metal plates also press the glass stops onto the blank holder elements, which are ground together with the die module in the assembled state for perfect alignment. I tightened all bolts equally with a torque wrench. The thickness of the metal plates and additional spacers ensures even application of bolt forces to the glass plates, see figure 4.2 b). The fixation does not create an electrically conductive contact between the die module and the bottom tool plate. Between the two glass stops, the punch moves along the x_2-axis and may be observed through the measurement hole in the metal plate. The glass stops not only enable the observation of the punch movement, and hence the shear cutting process, but also act as a plain bearing for the rotational degree of freedom of the punch around the x_2-axis. Consequently, the punch aligns

exactly with the blank holder elements, the die module, and the die insert. The basic prerequisite for this novel guidance concept is the precise manufacture of all components engaged, especially in x_3-direction. Punch, die module, die inserts and blank holder elements are ground in for this purpose within 5μm tolerances with a nominal dimension of 25 mm in x_3-direction. I secured all functionally relevant dimensions in the shearing tool with a coordinate measuring machine of type LH 87 from Wenzel Group GmbH & Co. KG, Wiesthal, Germany (detailed in appendix F.1.3). The inner plane of the glass that is in contact with all active elements is referred to as the observation plane. The observation plane can be viewed from outside through the measuring hole in the metal plate. Next to the measuring hole I have added an access to illuminate the observation plane, as shown in figure 4.2 b). The decisive task of the glass stops is to maintain the plane strain boundary condition of the shear cutting process in the observation plane. The shear cutting tool can reproduce both open and closed cutting lines. The same specimen geometry can be used for any kind of test, which ensures constant conditions and comparability for all experiments. Different sample placement realizes open and closed cutting lines along with the changed boundary condition at the sheet metal. No further modifications of the shear cutting tool are required to change between open and closed cutting lines.

4.1.1 Specimen Geometry

The specimen is a simple sheet metal strip, as shown in figure 4.3. It basically has only one critical dimension, its width in x_3-direction with a nominal dimension of 25 mm. The specimen width must be manufactured to the ground dimension of the die module, die insert, hold-down elements, and punch in the x_3-direction. The tolerance for this ranges from 0 to 5μm, where undersize is not permitted to guarantee contact with the glass stop. A material-dependent critical specimen length in x_1-direction should not be exceeded in order to ensure a clean clamping between the die module, die insert, and blank holder elements. I use a sample length of 100 mm. Using adjusted blank holder elements and punch lengths, specimen of different thickness in x_2-direction can be cut. A thickness of 4 mm is used in the experiments.
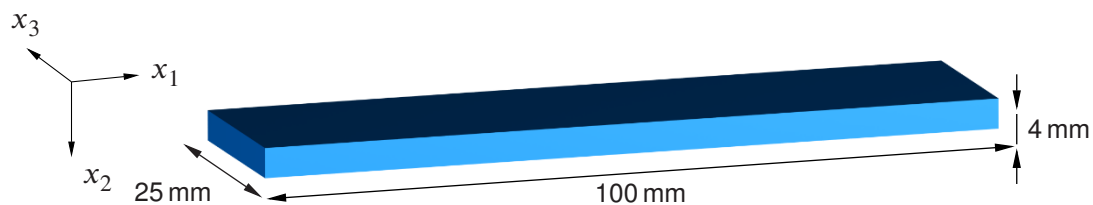
Figure 4.3: Specimen geometry for all experiments.
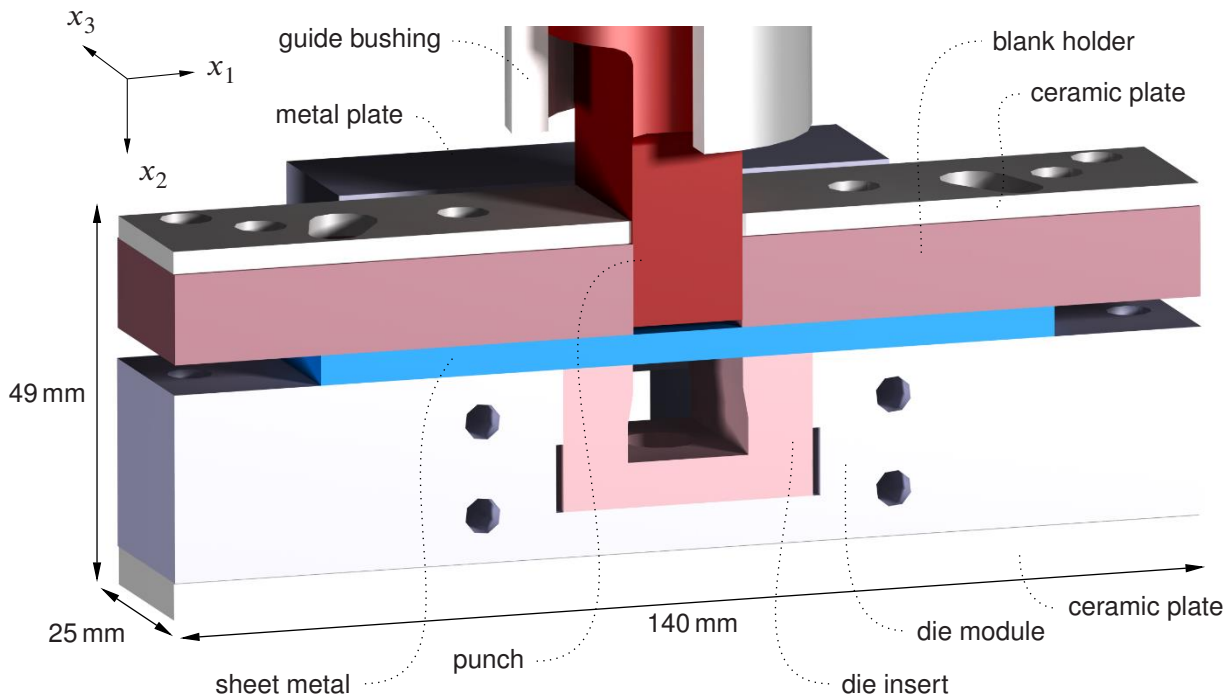
Figure 4.4: Schematic representation of the active elements and sheet metal sample for shear cutting experiments with closed cutting line.

4.1.2 Closed Cutting Line

When the cutting line is closed, the edges of the sheet metal are not separated during shear cutting, as with blanking and piercing. Closed cutting lines are therefore characterized by a symmetry boundary condition in the two-dimensional view. In the developed shear cutting tool this process is reproduced by inserting a single sample in such a way that it is cut twice by the cutting active elements. This is done symmetrically to the x_2x_3-plane, as shown in figure 4.4. The glass stops on both sides of the active elements close the cutting line in the sense of the plane strain boundary condition. The cutting line length amounts to 50 mm. The die-side sheet metal is considered a component, the punch-side sheet metal is considered waste, which corresponds to piercing.

The sheet metal sample is inserted by removing one of the glass stops together with the metal plate from one side of the shear cutting tool to allow access. The camera-side glass stop remains fixed to the shear cutting tool and stops the sheet metal sample along the x_3 axis in the observation plane. Mobile spacers ensure a central, reproducible positioning of the sample symmetric to the x_2x_3-plane. In the positioned state, the glass stop and the metal plate are reattached.

4.1.3 Open Cutting Line

An open cutting line results in the sheet metal evading below the punch, as is the case with trimming, embossing, and cropping. In the developed shear cutting tool, this sample-side boundary condition can be set by inserting two sheet metals symmetrically. In principle, this condition could also be achieved by inserting a single specimen. However, in such a setup the cutting clearance may widen due to occurring lateral forces. The symmetrical arrangement with respect to the $x_2 x_3$-plane avoids a widening of the cutting clearance, as the resulting lateral forces compensate each other. A gap of 2 mm between the inserted specimens ensures free movement of the open sheet ends. The two sheet metal sample are positioned using a spacer, which ensures reproducibility. Each of the two open cuts has a cutting line length of 25 mm. The die-side sheet metal is considered a component, hence the open cutting line tests resemble a trimming operation.

4.2 Experimental Setup

The experimental setup includes the entire infrastructure, which I have developed, validated, and verified to conduct the shear cutting experiments. In addition to the entire experimental arrangement, this also includes the linking of the sensors for data transfer and data recording as well as the calibration of the sensor systems. The in situ experimental setup is tailored to capture the dynamics of different shear cutting processes with high temporal and spatial resolution. I also understood the ex situ acquisition of geometric raw data as a part of the experimental setup. With this perspective, the output of the experimental setup consists of all the raw data collected, which is subsequently employed for further processing and analysis.

4.2.1 Experimental Arrangement

The developed shear cutting tool is the heart of the experimental arrangement. To carry out the experiments it is installed in a testing machine. I used a testing machine of the type 1484/DUPS-M from Zwick Roell GmbH and Co. KG, Ulm, Germany (detailed in appendix F.1.1) with a nominal pressing force of 200 kN and a maximum press ram velocity of 3 mm/s.

In addition to the load cell built into the force flow of the shearing tool, a high speed camera and an optical displacement sensor are mounted externally at the tool, as shown in figure 4.5. For the measurement, the load cell is connected to a charge amplifier of the type 5015A from
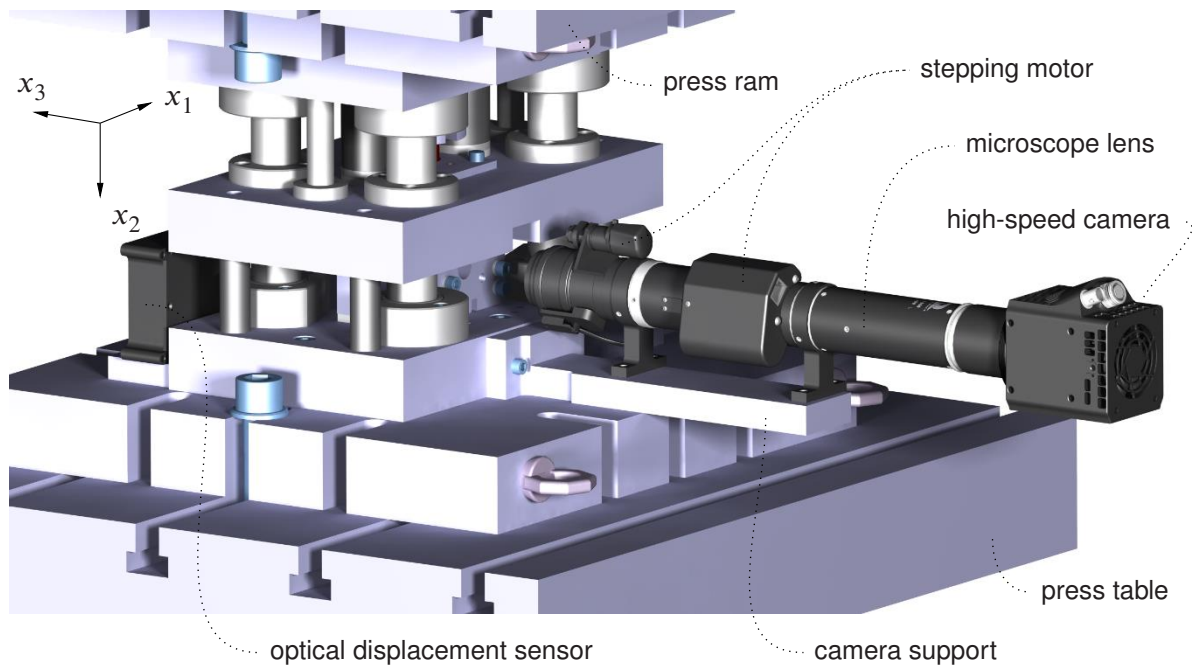
Figure 4.5: Overview of the measurement equipment mounted at the shear cutting tool.

Kistler Group, Winterthur, Switzerland. I implemented an optical displacement sensor of type optoNCDT 2300 from Micro-Epsilon Messtechnik GmbH and Co. KG, Ortenburg, Germany. The optical displacement sensors measures the distance between the top tool plate and the bottom tool plate during the shear cutting process and therefore reproduces the motion of the punch. It operates with a recording frequency of 20 kHz with an spatial accuracy of 0.8 μm. The installed high-speed camera is of the type Os3-S2 from Integrated Design Tools Inc., Pasadena, United States (detailed in appendix F.1.2). The high-speed camera has a maximum resolution of 1024 pixel by 1280 pixel at a frame rate of 5 kHz. Reduced resolution allow to work with even higher frame rates, for example 7 kHz using a resolution of 720 pixel by 1280 pixel with 8-bit color depth. The high speed camera is attached to a microscope lens with a magnification of 12.5 of the type Fusion 125 by Qioptiq GmbH and Co. KG, Göttingen, Germany. Two stepping motors enable a precise and reproducible adjustment of the microscope focus and magnification. The camera support carries the high-speed camera-microscope system and is installed perpendicular to the observation plane at the bottom tool plate, so that shearing can be observed through the measuring hole. The observation plane is illuminated by a macro light source of the type Xenon Nova 300 from Karl Storz SE and Co. KG, Tuttlingen, Germany, with a power of 300 W. The light source transmits the light via an optical guide into the tool through the illumination access. The optical guide ends open in the illumination access to achieve maximum light intensity.

4.2.2 Data Capturing

I divide data capturing into in situ and ex situ data. The ex situ data consists of raw sensor signals from geometry digitization. The in situ data comprises time-resolved raw signals for displacement measurements, force measurements, and image acquisition. For in situ data also the joint recording of sensor signals is important especially with regard to dynamic measurements.

In Situ Data

The in situ data capturing is designed so that all implemented sensors work together and output synchronous signals. The shear cutting tool is equipped with three sensors: a high-speed camera, an optical displacement sensor, and a piezoelectric force measurement. The testing machine may also provide force and displacement information.

As shown in figure 4.6 on the left side, the sensors installed provide signals of different dimensions. The displacement sensors and force measurements are time-resolved scalar quantities, whereas the high-speed camera provides two-dimensional image information. Initially, all sensor signals on the tool side are not synchronized. This means that even if the recording frequencies of the sensors are selected equally, the information output did not occur at exactly the same time. A common clock is therefore necessary to record all signals on one single time axis. This clock is determined by the trigger, which is the center of the in situ data recording, see figure 4.6. Two different trigger modes are available for the experiments. For experiments with the test machine, the displacement signal of the test machine is used as the trigger generator. Within the test machine environment, the force and displacement signals are already synchronous. In order to bring the tool sensors to the time axis of the test machine, the sensor signals are written to ring buffers. The tool displacement sensor and the tool force measurement write to the random-access memory (RAM) of the central measuring computer, which is used as ring buffer 1. As interface for the digitization of the analog sensor data serves a data acquisition unit of type NI PCIe-6351 from National Instruments Corporation, Austin, USA. The central measuring computer's RAM has a size of 32 GB. The high-speed camera has an internal ring buffer, where the data is stored, ring buffer 2. Ring buffer 2 has a size of 16 GB, which is equivalent to 15691 images at maximum resolution of 1024 pixel by 1280 pixel. The first trigger edge activates the writing process on both ring buffer 1 and ring buffer 2. When the trigger edge is released a second time, all sensor signals of the tool are output from the ring buffers at exactly the same time and on point with the time axis of the testing machine. For shear cutting experiments, the
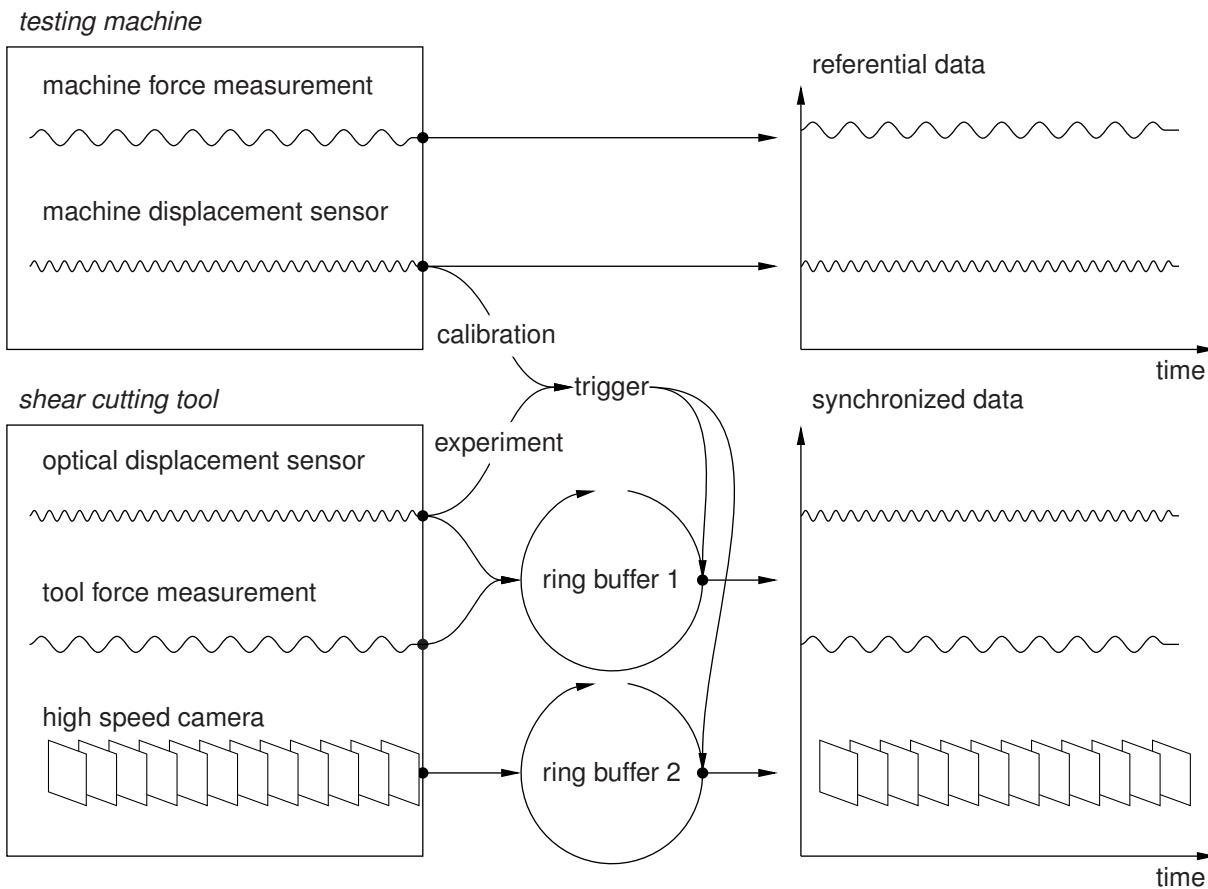
Figure 4.6: Diagram of data transfer and communication between the sensors of the testing machine and the shear cutting tool. Centralization on a single trigger enables synchronous data recording of all sensor signals.

displacement sensor of the cutting tool acts as triggering device. The compilation of all raw sensor signals on a single time axis shows the right side of figure 4.6.

In this setup, the discretization of the common time axis is determined by the sensor with the lowest recording rate, in this case the high-speed camera, which is 5 kHz. For a maximum spatial resolution of 1024 pixel by 1280 pixel, this results in a theoretical maximum temporal resolution of the in situ data acquisition system of 0.2 ms The storage capacity of the camera-internal ring buffer, ring buffer 2, also sets a boundary condition for the configuration. The duration of the relevant process window of the cutting process must be recorded with a storable number of images. Therefore, a compromise between spatial resolution and temporal resolution must be found for each experimental configuration. Since these exact recording settings are individually adapted to each test and can already be understood as part of the results, I present them together with the respective test results.

The testing machine control and testing machine sensor acquisition runs independently of the

tool-side sensors on a secondary measuring computer in the software Test Expert II V3.0 from Zwick Roell GmbH and Co. KG, Ulm, Germany. The central measuring computer solely handles the tool-side sensors. I wrote a measurement program to handle the displacement and force measurement signals, which is implemented in the software NI LabView 2018 SP1 from National Instruments Corporation, Austin, United States. The software IDT Motion Studio 2.15 from Integrated Design Tools Inc., Pasadena, United States, operates the high speed camera.

Ex Situ Data

The geometry of the sheet metal component cut surfaces is determined ex situ. I performed tactile measurements for all shear cut parts using the contour measuring device of the type MarSurf XCR 20 from Mahr GmbH, Goettingen, Germany (detailed in appendix F.1.4) with a resolution of $\sim 0.5 \,\mu$m. The associated MarWin XCR20 control software was used to drive the probe arm. The raw data of the tactile geometry measurement are five two-dimensional contour lines of the cut surface for each component. I distributed the five measurements equally along the cutting line. In addition to the two-dimensional tactile measurements, a three-dimensional digitization of a section of the cut surface was carried out for selected parts using a laser confocal microscope type VK-X150K from Keyence Corporation, Osaka, Japan (detailed in appendix F.1.5). I digitized sections of 1 mm width in x_3-direction over the entire sheet thickness using the associated control software VK-H1XV2D. The measurement results in a raw surface model of the cut surface.

4.2.3 Calibration of Tool Sensors

In addition to the actual data acquisition, the experimental setup also offers the possibility of calibrating the force and displacement sensors installed in the shear cutting tool. No additional calibration system is required. The referential force and displacement signals of the test machine were used as calibration measure. For the calibrations, the springs had been removed from the shear cutting tool. If the test machine acts as a trigger, synchronous characteristic curves can be recorded, which allow simple conversion of the signals on the tool-side into actual force and displacement values. The tests showed that there is no rate dependency of the characteristic curves, so that the recording of characteristic fields is not necessary. An auxiliary punch was moved against a pressure plate to calibrate the complete measuring range of the force measurement. To calibrate the displacement sensor system, the traverse of the test machine was moved to the corresponding end positions.

In addition, the test machine-controlled trigger enables a continuous control of the calibration and verification of the tool-side measurement data during test execution and data evaluation. For this purpose, force curves of idle strokes were recorded on the test machine, during which the punch could move freely and only the installed spring assemblies were engaged. I installed the glass stops in order to take any friction effects into account. Five idle stroke force curves were recorded for statistical averaging. Subtracting the idle stroke force from the force signal at the machine traverse makes it possible to extract the punching force.

4.3 Design of Experiments

The experimental design systematizes the scope of the investigations. To analyze the dynamics of the shearing process, different combinations of material, shearing process and process parameters are tested. I processed the raw data of the employed shear cutting tests according to a predefined workflow. Along the workflow the data is curated and evaluated.

4.3.1 Sheet Metal Samples

Two different materials were investigated, a hot-rolled fine-grained steel S355MC (material number 1.0976, DIN EN 10149-2, 1995, detailed in appendix F.2.1) and an aluminum EN AW 5083 (material number 3.3547, DIN EN 485-2, 2016, detailed in appendix F.2.2) with a sheet metal thickness of 4 mm each. The strip material had a width of 100 mm and a length of 4 m. The width of 100 mm corresponds to the specimen dimension in x_1-direction, the strip thickness anyway to the tested sheet thickness of the specimen in x_2-direction. The production of the specimen consists exclusively in the exact manufacturing of the specimen width in x_3-direction along the cutting line. There, the width of the specimen should be equal to the dimension of the ground in tool active elements. For this purpose, I first roughly preprocessed the strips to an actual dimension of 25.5 mm. In a subsequent grinding process, the samples received their exact final geometry within a tolerance of 0 to 5μm. Grinding is the only step in the preparation of the sheet metal specimen before the shear cutting experiment is carried out. It is worth noting that all observations and evaluations work without any artificial speckle patterns, which are quite common especially in solid mechanics experiments. In my analysis, I use the natural structure of the sheet metal material, which results from the grinding of the samples (Hartmann and Volk, 2019a).
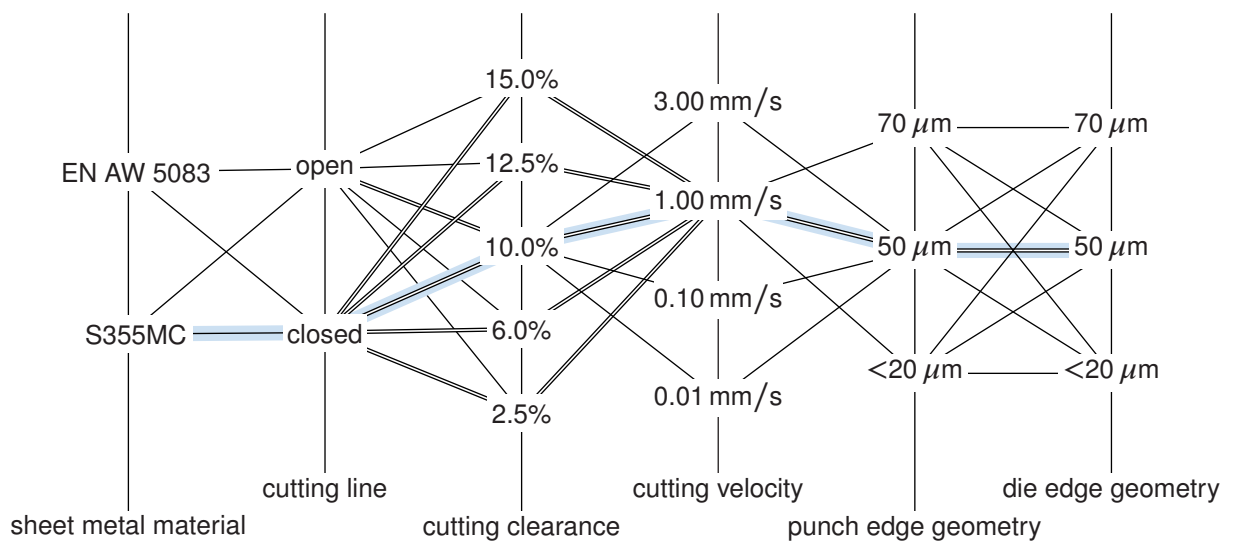
Figure 4.7: Parallel coordinates diagram of the shear cutting experiments. Blue highlights the reference experiment. For the sheet metal material S355MC all test paths are run through. The double line shows the subspace for aluminum EN AW 5083.

4.3.2 Experimental Plan

The experimental plan combines the available degrees of freedom that span the experimental space. The experimental space under investigation has six independent dimensions. In addition to the sheet metal material and the characteristic of the cutting line, the four process parameters, cutting gap, cutting speed, punch edge geometry, and die edge geometry, define these dimensions. The respective dimensions have different resolutions, as shown in figure 4.7. Similarly, the dimensions are permuted at different degrees. Each path in the parallel coordinates diagram represents a shear cutting experiment. I made three trials for each path.

Each dimension in the experimental space has a specific value, which defines the reference experiment. The reference material is the steel S355MC sheet metal. Reference shear cutting experiments have a closed cutting line and use 10% cutting clearance, 1 mm/s cutting velocity, and identical blade edge rounding of 50 μm. Blue highlights the reference experiment path in the parallel coordinates diagram of figure 4.7. For the sheet metal material S355MC all test paths are run through, which are deposited in the parallel coordinates. For aluminum EN AW 5083 a reduced subspace was analyzed, which is illustrated by the double lines. The process parameters cutting clearance, cutting velocity, and blade edge geometry vary individually while keeping the others constant. The cross-shaped arrangement of the connecting lines in figure 4.7 illustrates this. Within the subspace of the blade edge geometries, a full factorial variation takes place, which expresses the laminar arrangement of the connecting lines.

ex situ geometry data   geometry analysis   cut surface characteristics

synchronized in situ data   apply calibration   punch travel curve

apply calibration   cutting force curve

motion estimation   displacement field

strain estimation   deformation gradient

strain rate estimation   rate of deformation gradient

Δt
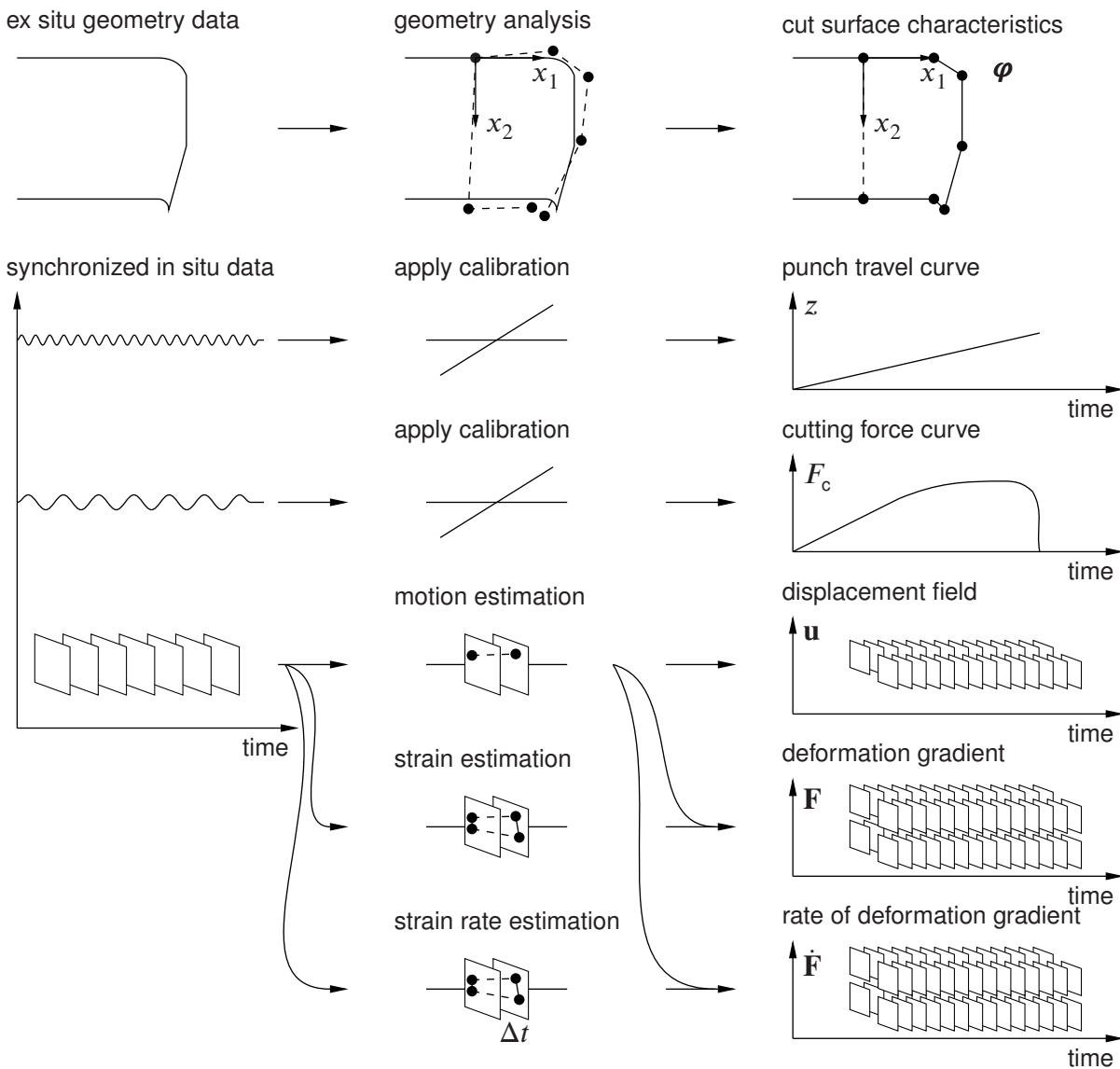
Figure 4.8: Diagram of data transfer and communication between the sensors of the testing machine and the shear cutting tool. Centralization on a single trigger enables synchronous data recording of all sensor signals.

4.4 Workflow of Data Processing

The presentation, significance and interpretability of experimental studies depend not only on the experiments themselves, but also on the processing and evaluation of the collected data. The workflow of data processing is therefore understood as the complementing content of the research approach, in which not only pure data processing but also the target values of the evaluation are defined with regard to the descriptive framework.

When a test of the experimental plan is carried out with the developed shear cutting tool and recorded with the developed measuring concept, a large amount of raw sensor information results as output. This information is divided into ex situ geometry information on the one hand and temporally resolved local and integral in situ sequences on the other. The raw data volume of a single test[1] is ~16 GB, whereby I would like to point out that not arbitrarily high sampling rates are the driver for size of the data set, but the spatial sensor information. This amount of information is generated three times for each shear cutting experiment. Consequently, each single path in the experimental plan has a data volume of ~48 GB from which results must be extracted. In order to make the curation and evaluation of the raw data transparent, I have defined a workflow for raw data processing. The workflow is shown in figure 4.8.

4.4.1 Ex Situ Data

The geometric information is available in the form of multiple two-dimensional data sets. With in total ~15 MB for each cut part, which gives ~45 MB for each experimental path, these records represent only a small fraction of the data volume of an experimental raw record. Therefore, data handling does not require a special focus in the analysis. The guideline by VDI2906-2, 1994 is used to describe the cut surface, which is equivalent to the eight parameter model introduced in section 2.4. The cut surface characteristics of each experiment, as well as each path in figure 4.7, are determined from five curves of three sheet metal samples. The first line in figure 4.8 illustrates the data processing of the cut surfaces. This procedure has proven itself many times over. In contrast to the often manual, user-dependent definition of the cutting area parameters, I have calculated them robustly, transparently, and automatically using sampling methods. The developed evaluation routine for the calculation of the cut surface characteristics is explained in section 5.3. The ex situ geometric digitization data of the cut surfaces uses the same cut surface description. The analysis of the surface model draws individual progressions of each characteristic along the cutting line. These progressions are used to evaluate, validate, and verify the plane strain boundary condition imposed on the sheet metal samples during experiments, which is presented in section 7.1.

4.4.2 In Situ Data

The in situ data make up the majority of the raw data, with only a small part being accounted for by the integral variables punch travel and cutting force, ~4 MB for each cut component and

---

[1]Data from ex situ geometry digitization is excluded, since it is only available for selected tests.

~12 MB for each experimental path. As with the ex situ measurements, no special data handling is required here either. The data processing combines the three tests of each experimental configuration. The result is a representative punch travel curve and a representative cutting force curve in a uniform time axis. With ~48 GB the image data sets of the high speed camera clearly represent the largest part of the data. Effective data handling and dimension reduction must therefore be taken into account in image data processing. However, since the raw image sequences do not directly reflect the continuum mechanics target values, a priori no satisfactory data selection can be made. Contrary to classical approaches to dimension reduction, the developed evaluation algorithms therefore continuously incorporate evaluation results and thus process knowledge about the shear cutting process. Hence, dimensional reduction and data evaluation run in parallel. This data handling routine is explained in detail in section 5.1.

The continuum mechanics target values for the evaluation of the experimental raw data correspond to kinematic observable state variables of material points. The aim is to record the state of motion of each material point of the shear affected zone throughout the entire shear cutting process. The basis for this is the estimation of the temporally resolved displacement field $\mathbf{u}$. All kinematic state variables can be derived from the time-resolved displacement field, such as the deformation gradient $\mathbf{F}$ and the rate of the deformation gradient $\dot{\mathbf{F}}$. In figure 4.6 this visualizes the direct connection from the motion estimation to the deformation gradient $\mathbf{F}$ and the rate of deformation gradient $\dot{\mathbf{F}}$. In total ten different time resolved fields deduce initially from the image sequence, two components of the displacement field and each of four components of the deformation gradient and the rate of the deformation gradient.

To determine the deformation gradient from the displacement, spatial partial derivatives must be calculated. The rate of deformation gradient includes a further numerical derivative in time direction. The calculation of numerical derivatives of real, discrete measurement data, such as the estimated displacement field, involves certain uncertainties. Next to other opportunities, variational motion estimation offers approaches to avoid sequential numerical derivations. Therefore, in this thesis I pursue different approaches to determine the displacement field, but also the deformation gradient and the rate of the deformation gradient. The motion estimation variant is chosen depending on the objective of evaluation, the current process dynamics and the local appearance of the phenomenon to be detected in the shear affected zone. Thus, the previously mentioned engineering and modeling of measurement methods is incorporated into my work within the scope of the test evaluation. The integral measuring variables, punch travel and cutting force serve as time criteria. The developed evaluation methods for the analysis of the dynamics of the shear cutting process form the scientific core of the thesis besides the novel experimental shear cutting tool setup. I present them in detail in the sections 5.1 and 5.2.

5 Methods

The presented research approach includes evaluations which are not possible with standard software and tools. Therefore, I developed an evaluation methodology that is tailored to the analysis of the shear cutting process. The in situ evaluation methodology is basically divided into the analysis of deformation (section 5.1) and the analysis of fracture (section 5.2). The deformation analysis is based on either block-matching or variational motion estimation, which are adapted to handle the large number of images provided from the high-speed imaging. The fracture evaluation uses a variational model. A new method for the robust determination of the cut surface geometry complements the in situ analyses (section 5.3). In addition to the actual evaluation systematic, the selection of the corresponding numerical parameters in the algorithms (section 5.4) plays an important role. For reasons of clarity, I attached the pseudo codes of the developed algorithms as a collection in the appendix F.3. The developed methods allow for the first time to measure the dynamics in the shear affected zone during shear cutting over the entire process–from sheet metal to the cut surface.

5.1 Deformation Analysis

The presentation of the general problem framework in motion analysis in section 2.3 uses a continuous description. However, in practice, the image sequence data is discrete not only in the time dimension. The images $I_i : \mathcal{G} \rightarrow \mathcal{I}$ have finite color depth $\mathcal{I}$ and are defined on a two-dimensional rectangular grid $\mathcal{G} = \{1, 2, 3, \ldots, N_1\} \times \{1, 2, 3, \ldots, N_2\}$. The conducted digital 8-bit gray scale images have a color depth range of 256 values, $\mathcal{I} = \{0, 1, 2, \ldots, 255\}$. A maximum grid size of $N_1 = 1280$ and $N_2 = 1080$ ensues, since the grid nodes represent the pixel centers. Because the discrete notation is often cumbersome, I used a mixed notation for reasons of clarity and convenience, but without loss of validity.

5.1.1 Displacement Estimation

For a large part of the displacement estimation between two images I_0 and I_1, I employ a classical block-matching method, namely DIC. The used blocks, or subsets, are squares with

an edge length l_S and a number of contained pixels $|S|$. I utilize the zero-normalized sum of squared difference (ZSSD) criteria with affine warping of B. Pan et al., 2013 given by

$$C_{\text{ZSSD}}(\mathbf{u}) = \int_S \left(\frac{I_0 - J_0}{L_0} - \frac{I_1(\mathbf{u}) - J_1(\mathbf{u})}{L_1(\mathbf{u})} \right)^2 \mathrm{d}\mathbf{x}_0 , \tag{5.1}$$

where $L_i^2(\mathbf{u}) = \int_S \left(I_i(\mathbf{u}) - J_i(\mathbf{u}) \right)^2 \mathrm{d}\mathbf{x}_0$ and $J_i(\mathbf{u}) = \frac{1}{|S|} \int_S I_i(\mathbf{u}) \, \mathrm{d}\mathbf{x}_0$. Here, $I_1(\mathbf{u})$ describes the deformed image I_1 and since I_0 is not deformed the bracket notation is omitted. The reliability-guided DIC introduced by B. Pan, 2009 and B. Pan et al., 2010 is applied, which was inspired by the reliability guided phase unwarping[1] by X. Su and W. Chen, 2004. The main difference between the reliability-guided and conventional methods lies in the calculation path and initial guess for the sub-pixel calculation regime. Conventional methods work well under the assumption of continuous, homogeneous deformation. Reliability guided routines are more appropriate for heterogeneous deformation analysis. The calculation path is based on a seed point from which subsequent calculations originate and evolve over the image. The four correlation values of the subsets next to the seed point are determined and ordered according to their correlation values. High correlation values are prioritized, since the correlation value may be also seen as a reliability measure. The four neighbors of the subset with the highest correlation value are evaluated next in the reliability guided regime. An intelligent storing and queuing keeps track of the computations made and avoid double calculations until every subset has been conducted. In a second step, I use the inverse compositional Gauss-Newton algorithm by Baker and Matthews, 2001 for sub-pixel calculations, where the displacements $\mathbf{u}$ are recovered from a displacement mapping function $\mathfrak{W}(\boldsymbol{\xi}; \boldsymbol{\varphi})$ with warping parameter vector $\boldsymbol{\varphi}$. The shape functions of the warping are described in the local coordinates $\Delta\boldsymbol{\xi}$ with respect to the center pixel in each subset S_i. The mapping vector $\boldsymbol{\varphi}$ parameterizes this local subset deformation. I applied second-order shape functions, since they balance local model complexity and accuracy. The second-order shape functions $\boldsymbol{\xi} = (\xi_1, \xi_2)$ are formulated as follows

$$\xi_i \left(\Delta\xi_1, \Delta\xi_2 \right) = u_i + \frac{\partial u_i}{\partial x_1} \Delta\xi_1 + \frac{\partial u_i}{\partial x_2} \Delta\xi_2 + \frac{1}{2} \frac{\partial^2 u_i}{\partial x_1^2} \Delta\xi_1^2 + \frac{\partial^2 u_i}{\partial x_1 \partial x_2} \Delta\xi_1 \Delta\xi_2 + \frac{1}{2} \frac{\partial^2 u_i}{\partial x_2^2} \Delta\xi_2^2 , \tag{5.2}$$

where $\boldsymbol{\varphi} = \left(u_1, \frac{\partial u_1}{\partial x_1}, \frac{\partial u_1}{\partial x_2}, \frac{\partial^2 u_1}{\partial x_1^2}, \frac{\partial^2 u_1}{\partial x_1 \partial x_2}, \frac{\partial^2 u_1}{\partial x_1^2}, u_2, \frac{\partial u_2}{\partial x_1}, \frac{\partial u_2}{\partial x_2}, \frac{\partial^2 u_2}{\partial x_1^2}, \frac{\partial^2 u_2}{\partial x_1 \partial x_2}, \frac{\partial^2 u_2}{\partial x_1^2} \right)$ represents the mapping parameter vector and $i \in \{1, 2\}$. The inverse compositional Gauss-Newton algorithm uses an incremental warp $\mathfrak{W}(\boldsymbol{\xi}, \Delta\boldsymbol{\varphi})$. The inverse of the incremental warp $\mathfrak{W}(\boldsymbol{\xi}, \Delta\boldsymbol{\varphi})^{-1}$ is composed

---

[1]Warping may be understood as geometric transformations following certain predefined rules.

with the current estimated warping $\mathfrak{W}(\boldsymbol{\xi}, \boldsymbol{\varphi})$ to get the updated warping

$$\mathfrak{W}^{(i+1)}(\boldsymbol{\xi}, \boldsymbol{\varphi}) = \mathfrak{W}^{(i)}\left(\mathfrak{W}\left(\boldsymbol{\xi}, \Delta\boldsymbol{\varphi}^{(i+1)}\right)^{-1}, \boldsymbol{\varphi}\right) . \tag{5.3}$$

The procedure reflects the inverse compositional part mentioned in the algorithms name. The Gauss-Newton part comes from the current subset update with $\mathfrak{W}(\boldsymbol{\xi}; \Delta\boldsymbol{\varphi})$, which is based on a first-order Taylor expansion

$$I_1^{(i+1)}\left(\mathbf{x}_0 + \mathfrak{W}^{(i+1)}(\boldsymbol{\xi}; \Delta\boldsymbol{\varphi})\right) = I_1^{(i)}\left(\mathbf{x}_0 + \boldsymbol{\xi}\right) + \nabla I_1^{(i)}\frac{\partial \mathfrak{W}}{\partial \boldsymbol{\varphi}}\Delta\boldsymbol{\varphi}^{(i+1)} , \tag{5.4}$$

where ∇I_0 is the spatial intensity gradient of the reference subset and $\frac{\partial \mathfrak{W}}{\partial \boldsymbol{\varphi}}$ is the Jacobian matrix of the warping function $\mathfrak{W}(\boldsymbol{\xi}; \boldsymbol{\varphi})$. I calculated the spatial intensity gradient based on convolution using the weighted finite differences kernel suggested by B. Pan et al., 2013. In the sub-pixel estimation the identification of the actual transition of color depth between pixel centers is focused. Hence, the used weighted finite differences kernel places an emphasis on edge detection, similar to the operator proposed by Sobel and Feldman, 1968. Baker and Matthews, 2004 proved the inverse compositional Gauss-Newton method to be equal to the conventional forward additive Newton-Raphson method in theory, however, they differ greatly in the numerical implementation. Algorithm 1, see appendix F.3.1, shows the pseudo code of the implemented DIC core.[2] The algorithm has three main parameters: a convergence threshold ϵ_c for the sub-pixel calculation, the subset size $|\mathcal{S}|$, and the grid step δ, which defines the distance between the subset centers. The convergence value is set to 10^{-6} pixel for all experiments. I chose the subset size $|\mathcal{S}|$ and grid step δ specifically, based on an accuracy and precision analysis. Second-order polynomial shape functions are used for the sub-pixel calculations. Algorithm 1 needs two images as input, the subsets to be evaluated, and a seed point to start calculations. The output is the two-dimensional displacement field $\mathbf{u}$ in sub-pixel accuracy.

In order to cope with the large amount of data, I implemented an image handling routine for dimensionality reduction built around the DIC core of algorithm 1, see algorithm 2 in appendix F.3.2. The basis of the handling routine is an updated Lagrangian framing, which is common in motion estimation. The main task of the handling routine is to reduce the dimension of the problem in temporal direction, which is essential to make calculations feasible and to avoid error accumulation[3]. The routine extracts certain images from the high volume image stack, recorded during the shear cutting experiments with the high-speed camera, and uses the reduced

---

[2] In the work by Hartmann, Eder, Opritescu, Maier, et al., 2018, my coworkers and I draw a detailed analysis on the implementation, precision, and accuracy of a predecessor of algorithm 1.

[3] Error accumulation originates from deterministic errors in motion estimation algorithms within an updated Lagrangian framework (Hartmann, J. Wang, et al., 2018).

selection for the displacement calculations. The selection of the images is not possible a priori, as the raw image data does not allow direct conclusions about the kinematic evaluation dimensions that appear on different scales. The dimension reduction is therefore carried out in exchange with algorithm 1. I use the run variable v, which describes the image selection interval and specifies the time interval between images that are used for the displacement calculation. v is time normalized by multiplying it by the acquisition rate. Without dimension reduction, a constant v of 1 would result over the entire image sequence. I adapt the image selection interval v between two images based on a displacement threshold $\epsilon_{\mathbf{u}}$ and a displacement gradient threshold $\epsilon_{\nabla \mathbf{u}}$. These thresholds are compared with the maximum values for displacements and displacement gradients resulting from the displacement calculation in algorithm 1. The gradient calculation performs a local bi-cubic spline interpolation of the displacement data, to exclude grid step effects in dimensionality reduction as far as possible. The combination of the two thresholds ensures that time phenomena and motion non-linearity are detected within a predetermined temporal accuracy. Two scaling parameters λ_{co} and λ_{re} control the algorithms reduction characteristics. λ_{co} denotes the coarsening parameter and λ_{re} the refinement parameter. λ_{co} stretches the image interval v in time and is responsible for the dimensionality reduction. λ_{re} is its counterpart that shrinks v in time, if the threshold values are exceeded. To avoid infinite loops λ_{co} and λ_{re} should be selected differently. In total, algorithm 2 has four parameters that control the dimensionality reduction and are set globally for all experiments. I set the displacement threshold value $\epsilon_{\mathbf{u}} = \frac{l_S}{2}$ to avoid motions across the subset boundaries and $\epsilon_{\nabla \mathbf{u}} = 0.1$ to limit subset distortion. Values of $\lambda_{\mathrm{co}} = 2$ for coarsening and $\lambda_{\mathrm{re}} = 1.5$ for refinement proved suitable for the acquired raw data regarding computational costs. Algorithm 1 and algorithm 2 calculate the vertical and horizontal components of the displacement field $\mathbf{u} = (u_1, u_2)$ as three-dimensional arrays, one temporal and two spatial dimensions x_1 and x_2 of the observation plane. Due to the dimensionality reduction, the time axis is not linear, but variable according to the temporal stretching and shrinking. However, the strong threshold values allow interpolation in time to complete the results in a target-oriented way for the evaluation.

5.1.2 Strain Estimation

The aim of the strain calculation is to determine the deformation gradient $\mathbf{F}$, which can be converted into arbitrary strain tensor and strain measure, see equation (2.6) and equation (2.9). The deformation gradient represents the Jacobian of the displacement field, the calculation of which is carried out within the deformation analysis in section 5.1.1. In order to cope with both, discontinuities and noise, I use the numerical differentiation methodology according to

Chartrand, 2017. The regression framework in expression (2.36) forms the basis of this two-dimensional numerical derivation. The total variation used preserves discontinuities in the solution, see section 2.2.3. The provided optimization problem results independently for both components u_1 and u_2 of the displacement field to

$$\underset{\mathbf{F}_i}{\arg\min} \left(\frac{\lambda_1}{2} ||\mathbf{K}\mathbf{F}_i - u_i||_2^2 + ||\mathbf{D}\mathbf{F}_i||_1 \right) , \tag{5.5}$$

where λ_1 is a scaling parameter, $\mathbf{D}$ represents a discrete gradient operator and $\mathbf{K}$ a discrete integration operator, and $\mathbf{F}_i = (\frac{\partial u_i}{\partial x_1}, \frac{\partial u_i}{\partial x_2})$ corresponds to the estimated components of the deformation gradient. The regularization term $\mathfrak{R} = ||\mathbf{D}\mathbf{F}_i||_1$ in expression (5.5) stabilizes the derivative computation. From a physical point of view, total variation regularizes local divergence in an absolute and weak sense. Expression (5.5) penalizes local divergence of the deformation gradient's first-order derivatives caused by measurement noise, whereas it preserves spatially the global features, patterns, and motion discontinuities in the deformation gradient $\mathbf{F}$ field. Following the concept of Gabay and Mercier, 1976, a dual algorithm allows the decoupling of the spatial direction dependent computations by introducing a splitting variable $\mathbf{w}$ and a Lagrange multiplier Λ in the sense of Hestenes, 1969. Thus, equation 5.5 reformulates

$$\underset{\mathbf{F}_i, \mathbf{w}}{\arg\min} \left(\frac{\lambda_1}{2} ||\mathbf{K}\mathbf{F}_i - u_i||_2^2 + \frac{1}{2\lambda_2} ||\mathbf{w} - \mathbf{D}\mathbf{F}_i - \Lambda||_2^2 + ||\mathbf{w}||_1 \right) . \tag{5.6}$$

The splitting description reduces the original problem, see expression (5.5), to the solution of convenient sub-problems. Using a discrete Fourier transform $\mathfrak{F}(\mathbf{q}) = \hat{\mathbf{q}}$, Chartrand, 2017 further reformulates the sub-problems, which are solved alternately, as shown in algorithm 3, see appendix F.3.3. Algorithm 3 has four parameters, the number of iterations n_{it}, the Lagrange multiplier update parameter λ_3 (originating from Λ), the data term weighting λ_1 and the regularization weighting λ_2. I choose the number of iterations to $n_{\text{it}} = 100$ and $\lambda_3 = 1.6$ globally for all experiments as suggested by Chartrand, 2017. The specific identification of the weighting parameters λ_1 and λ_2 is shown in section 5.4.

5.1.3 Strain Rate Estimation

The strain rate calculation uses the fact that entire video sequences of the experiments are available. This differs significantly from the usual procedure, which always bases the motion estimation on two images in the sense of a progressive updated Lagrangian approach. The additional information, which is available in the form of the sequential images of the video
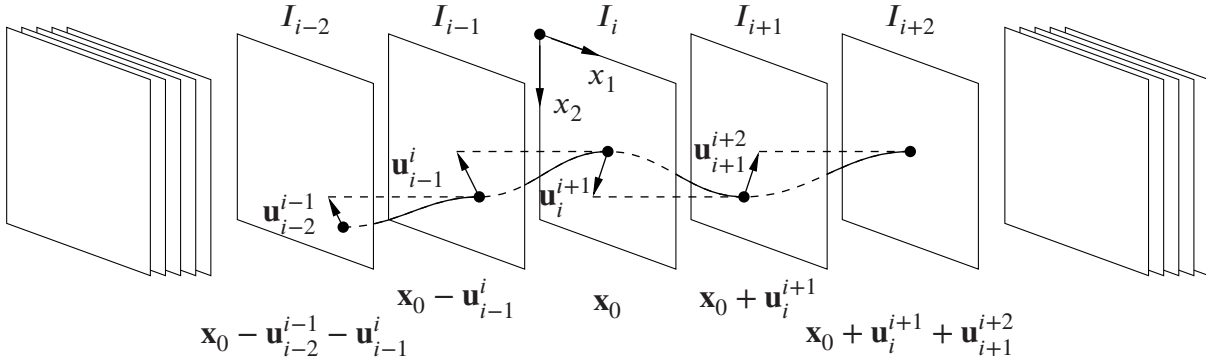
Figure 5.1: Trajectory by displacement increments $\left\{\mathbf{u}_{i-2}^{i-1}, \ldots, \mathbf{u}_{i+1}^{i+2}\right\}$ of a material particle x_0 through five images $\left\{I_{i-2}, \ldots, I_{i+2}\right\}$ with the central image I_i defined as the reference, according to Volz et al., 2011.

sequence, makes the calculation more robust, especially with regard to differential quantities such as strain and in particular strain rate. The proposed method enforces spatio-temporal coherence, which enables a stable estimation of the strain rate.

Existing methods of temporal variation can be divided into temporal regularization (Murray and Buxton, 1987) and trajectorial regularization (Nagel, 1990). While in temporal regularization an assumption is made regarding the displacement gradient, I utilized trajectorial regularization, which stabilizes the spatio-temporal trajectory of a material particle. Instead of a forward-oriented trajectorial stabilization, such as of Black and Anandan, 1991, I follow the regularization concept of Volz et al., 2011 that incorporates both sides of the current time step, see figure 5.1.

Since a first-order trajectorial variation minimizes rate terms, I implemented a second-order variation that only aims to eliminate higher-order rate terms. To realize the second-order variation at least three displacement fields of four consecutive images are required. For reasons of symmetry I use five images, see figure 5.1. The displacement fields $\left\{\mathbf{u}_{i-2}^{i-1}, \ldots, \mathbf{u}_{i+1}^{i+2}\right\}$ between the images $\left\{I_{i-2}, \ldots, I_{i+2}\right\}$ are all calculated with respect to the central reference coordinate system in image I_i. Through this centralized parameterization, $\mathbf{u}_{i+1}^{i+2}$ represents the complement to $\mathbf{u}_i^{i+1}$ to obtain the trajectory from I_i to I_{i+2}. The same applies to $\mathbf{u}_{i-2}^{i-1}$ and $\mathbf{u}_{i-1}^i$. Additional registration steps, as in the procedure of Salgado and Sánchez, 2007, are therefore not necessary. The spatial regularization is based on the generic framework proposed by Hewer et al., 2013.

The variational regularization framework, see section 2.3.3, thus takes the following form

$$\min \underbrace{\left(\mathfrak{D} + \lambda_s \mathfrak{R}_s + \lambda_t \mathfrak{R}_t\right)}_{\mathfrak{E}}, \tag{5.7}$$

where $\mathfrak{D}$ denotes the data term, $\mathfrak{R}_s$ the spatial regularization term with weighting factor λ_s and $\mathfrak{R}_t$ the trajectorial regularization term with weighting factor λ_t in the functional $\mathfrak{E}$.

Data Term $\mathfrak{D}$

The data term contains the brightness constancy, see equation (2.49), and the gradient constancy, see equation (2.50), of two consecutive images. Five images $\{I_{i-2}, \ldots, I_{i+2}\}$ thus lead to four single relations $\mathfrak{D}_{i-2}^{i-1}, \mathfrak{D}_{i-1}^{i}, \mathfrak{D}_{i}^{i+1}$, and $\mathfrak{D}_{i+1}^{i+2}$, which add up to the data term

$$\mathfrak{D} = \mathfrak{D}_{i-2}^{i-1} + \mathfrak{D}_{i-1}^{i} + \mathfrak{D}_{i}^{i+1} + \mathfrak{D}_{i+1}^{i+2} \, . \tag{5.8}$$

The $\mathcal{L}_1$-norm designs each individual term robust, since outliers can occur independently. Volz et al., 2011 proposes to weight the distant terms $\mathfrak{D}_{i-2}^{i-1}$ and $\mathfrak{D}_{i+1}^{i+2}$, which is incorporated using the factor λ_{ti}. The factor λ_{ba} balances between the two constancy assumptions. The components of the data term thus result in

$$\begin{aligned}
\mathfrak{D}_{i-2}^{i-1} = \lambda_{ti} \Big(&||I_{i-1} \left(\mathbf{x}_0 - \mathbf{u}_{i-1}^i\right) - I_{i-2} \left(\mathbf{x}_0 - \mathbf{u}_{i-1}^i - \mathbf{u}_{i-2}^{i-1}\right) ||_1 + \\
&\lambda_{ba} ||\nabla I_{i-1} \left(\mathbf{x}_0 - \mathbf{u}_{i-1}^i\right) - \nabla I_{i-2} \left(\mathbf{x}_0 - \mathbf{u}_{i-1}^i - \mathbf{u}_{i-2}^{i-1}\right) ||_1 \Big) \, ,
\end{aligned} \tag{5.9}$$

$$\mathfrak{D}_{i-1}^{i} = ||I_i \left(\mathbf{x}_0\right) - I_{i-1} \left(\mathbf{x}_0 - \mathbf{u}_{i-1}^i\right) ||_1 + \lambda_{ba} ||\nabla I_i \left(\mathbf{x}_0\right) - \nabla I_{i-1} \left(\mathbf{x}_0 - \mathbf{u}_{i-1}^i\right) ||_1 \, , \tag{5.10}$$

$$\mathfrak{D}_{i}^{i+1} = ||I_{i+1} \left(\mathbf{x}_0 + \mathbf{u}_i^{i+1}\right) - I_i \left(\mathbf{x}_0\right) ||_1 + \lambda_{ba} ||\nabla I_{i+1} \left(\mathbf{x}_0 - \mathbf{u}_i^{i+1}\right) - \nabla I_i \left(\mathbf{x}_0\right) ||_1 \, , \tag{5.11}$$

$$\begin{aligned}
\mathfrak{D}_{i+1}^{i+2} = \lambda_{ti} \Big(&||I_{i+2} \left(\mathbf{x}_0 + \mathbf{u}_i^{i+1} + \mathbf{u}_{i+1}^{i+2}\right) - I_{i+1} \left(\mathbf{x}_0 + \mathbf{u}_i^{i+1}\right) ||_1 + \\
&\lambda_{ba} ||\nabla I_{i+2} \left(\mathbf{x}_0 + \mathbf{u}_i^{i+1} + \mathbf{u}_{i+1}^{i+2}\right) - \nabla I_{i+1} \left(\mathbf{x}_0 + \mathbf{u}_i^{i+1}\right) ||_1 \Big) \, .
\end{aligned} \tag{5.12}$$

To calculate the optimization, I linearized both constancy assumptions in the data term on the basis of a first-order Taylor approximation to achieve a convex formulation, as common in optical flow computation, see Volz et al., 2011, for example.

Spatial Regularization Term $\mathfrak{R}_s$

The data term $\mathfrak{D}$ introduces four displacement fields $\{\mathbf{u}_{i-2}^{i-1}, \ldots, \mathbf{u}_{i+1}^{i+2}\}$ between the images $\{I_{i-2}, \ldots, I_{i+2}\}$. The spatial regularization term $\mathfrak{R}_s$ models the spatial behavior of the displacement fields $\mathbf{u}$ in the variational approach. I use a third-order regularization term for each individual displacement field that derives from the generic framework proposed by Hewer et al.,

2013. The individual regularization terms $\left\{ \mathfrak{R}_{\mathrm{s},i-2}^{i-1}, \ldots, \mathfrak{R}_{\mathrm{s},i+1}^{i+1} \right\}$ accumulate to the total spatial regularization term $\mathfrak{R}_{\mathrm{s}}$, analogous to the data term.

$$\mathfrak{R}_{\mathrm{s}} = \mathfrak{R}_{\mathrm{s},i-2}^{i-1} + \mathfrak{R}_{\mathrm{s},i-1}^{i} + \mathfrak{R}_{\mathrm{s},i}^{i+1} + \mathfrak{R}_{\mathrm{s},i+1}^{i+2} \tag{5.13}$$

The four individual spatial regularization terms read

$$\mathfrak{R}_{\mathrm{s},i-2}^{i-1} = \lambda_{\mathrm{ti}} \left(\lambda_{\mathrm{s1}} \left(||\mathbf{A}_{i-2}^{i-1} - \nabla \mathbf{u}_{i-2}^{i-1}||_2^2 + \lambda_{\mathrm{s2}} \left(||\mathbf{B}_{i-2}^{i-1} - \nabla \mathbf{A}_{i-2}^{i-1}||_2^2 + \lambda_{\mathrm{s3}} \left(||\nabla \mathbf{B}_{i-2}^{i-1}||_2^2 \right) \right) \right) \right) , \tag{5.14}$$

$$\mathfrak{R}_{\mathrm{s},i-1}^{i} = \left(\lambda_{\mathrm{ti}} + 1 \right) \left(\lambda_{\mathrm{s1}} \left(||\mathbf{A}_{i-1}^{i} - \nabla \mathbf{u}_{i-1}^{i}||_2^2 + \lambda_{\mathrm{s2}} \left(||\mathbf{B}_{i-1}^{i} - \nabla \mathbf{A}_{i-1}^{i}||_2^2 + \lambda_{\mathrm{s3}} \left(||\nabla \mathbf{B}_{i-1}^{i}||_2^2 \right) \right) \right) \right) , \tag{5.15}$$

$$\mathfrak{R}_{\mathrm{s},i}^{i+1} = \left(\lambda_{\mathrm{ti}} + 1 \right) \left(\lambda_{\mathrm{s1}} \left(||\mathbf{A}_{i}^{i+1} - \nabla \mathbf{u}_{i}^{i+1}||_2^2 + \lambda_{\mathrm{s2}} \left(||\mathbf{B}_{i}^{i+1} - \nabla \mathbf{A}_{i}^{i+1}||_2^2 + \lambda_{\mathrm{s3}} \left(||\nabla \mathbf{B}_{i}^{i+1}||_2^2 \right) \right) \right) \right) , \tag{5.16}$$

$$\mathfrak{R}_{\mathrm{s},i+1}^{i+2} = \lambda_{\mathrm{ti}} \left(\lambda_{\mathrm{s1}} \left(||\mathbf{A}_{i+1}^{i+2} - \nabla \mathbf{u}_{i+1}^{i+2}||_2^2 + \lambda_{\mathrm{s2}} \left(||\mathbf{B}_{i+1}^{i+2} - \nabla \mathbf{A}_{i+1}^{i+2}||_2^2 + \lambda_{\mathrm{s3}} \left(||\nabla \mathbf{B}_{i+1}^{i+2}||_2^2 \right) \right) \right) \right) , \tag{5.17}$$

where λ_{s1}, λ_{s2}, and λ_{s3} denote factors to weight the different terms. The spatial regularization terms are scaled with λ_{ti} and $\left(\lambda_{\mathrm{ti}} + 1 \right)$, respectively, to balance them with the data terms. $\mathbf{A}$ and $\mathbf{B}$ are tensor-valued auxiliary variables to formulate the so called agreement terms.

$$||\mathbf{A} - \nabla \mathbf{u}||_2^2 = \sum_{i,j=1}^{2} \left(A_{ij} - \frac{\partial u_i}{\partial x_j} \right)^2 \tag{5.18}$$

$$||\mathbf{B} - \nabla \mathbf{A}||_2^2 = \sum_{i,j,k=1}^{2} \left(B_{ijk} - \frac{\partial A_{ij}}{\partial x_k} \right)^2 \tag{5.19}$$

$$||\nabla \mathbf{B}||_2^2 = \sum_{i,j,k=1}^{2} \nabla B_{ijk} \nabla B_{ijk}^{\mathrm{T}} \tag{5.20}$$

The agreement terms model the motion to be analyzed. The variable $\mathbf{A}$, to first appear in the agreement term in equation (5.18), acts as an estimate of the displacement gradient $\nabla \mathbf{u}$, which following equation (2.3) is directly related to the deformation gradient $\mathbf{F}$. By recursion, the agreement terms in equation (5.19) and in equation (5.20) emerge analogously.

Trajectorial Regularization Term $\mathfrak{R}_{\mathrm{t}}$

While the spatial regularization acts individually on the four displacement fields, the trajectorial regularization couples the motions of the material points. The approach used is formulated in

second-order, so that piecewise linear trajectories are created. The trajectorial regularization term $\mathfrak{R}_t$ is the sum of the left and right trajectorial regularization terms

$$\mathfrak{R}_t = \mathfrak{R}_{t,1} + \mathfrak{R}_{t,2} \,, \tag{5.21}$$

where

$$\mathfrak{R}_{t,1} = ||\mathbf{u}_i^{i+1} - 2\mathbf{u}_{i-1}^i + \mathbf{u}_{i-2}^{i-1}||_1 \tag{5.22}$$

and

$$\mathfrak{R}_{t,2} = ||\mathbf{u}_{i-1}^i - 2\mathbf{u}_i^{i+1} + \mathbf{u}_{i+1}^{i+2}||_1 \,. \tag{5.23}$$

The straightforward coupling of the displacement fields without registration between the different time steps is made possible by the uniform observation in a single central reference system.

Physical Consideration

Spatio-temporal regularization enables the integration of physical relationships and assumptions in optical full-field evaluation (Hartmann and Volk, 2019b; Ruhnau et al., 2007; Yao and H. Yang, 2016). Against the background of the descriptive framework, I am able to specify the resulting evaluation variables and their behavior in space and time. Especially with respect to the differential calculus-based continuum mechanics, this modeling of measurement evaluation allow direct and robust determination of state variables, such as the deformation gradient and its rate. I modeled the functional $\mathfrak{E}$, see expression (5.7), in third-order spatial derivatives and second-order rates. In return, the regularized result variables contain robust information of first and second spatial derivatives and the first rate of the full-field motion, and hence, a stable computation of strains and strain rates. I interpret the temporal extension of the weak formulation in the functional $\mathfrak{E}$ in such a way that a temporal uncertainty is added to the spatial uncertainty of a material particle. Classical variational approaches allow for temporal uncertainty only by projection of spatial regularization, see section 5.1.2, or neglect it completely, as in the case of classical block-matching methods[4]. This gives an additional degree of freedom in regularization and takes care of not only spatial but also temporal measurement blur. Using the presented spatio-temporal weak coupling enforces locally the robust computation of the rate of the deformation gradient.[5], which represents direct full-field estimation of a second-order derivative. The extended set of measurement data stabilizes the evaluation process. The

---

[4]Also in block-matching spatio-temporal approaches are used to enhance performance, see for example the DIC acceleration measurement proposed by Le Gourriérec et al., 2020.

[5]Second-order smooth in space and first-order smooth in time.

presented approach can basically be extended to higher-order derivatives by its recursive form both spatially and temporally according to analogous procedures.

Algorithm

The minimization of the functional in expression (5.7) is achieved by calculating the zero values of the Euler-Lagrange equations

$$\frac{\mathrm{d}}{\mathrm{d}t}\frac{\partial \mathfrak{E}}{\partial \dot{\mathbf{u}}} - \frac{\partial \mathfrak{E}}{\partial \mathbf{u}} = 0 \, . \tag{5.24}$$

Considering five successive images, in a third-order spatial, and a second-order trajectorial variation, eight Euler-Lagrange equations for the displacement fields $\mathbf{u}_j^{j+1} = \mathbf{u}^{(j)} = \left(u_1^{(j)}, u_2^{(j)}\right)$ result with $j \in \{i-2, i-1, i, i+1\}$.[6] In Addition, 16 Euler-Lagrange equations for the corresponding displacement gradients $\mathbf{A}_{kl}^{(i)}$, $k, l \in \{1, 2\}$ and 32 Euler-Lagrange equations for the gradients of the displacement gradients $B_{klm}^{(i)}$, $k, l, m \in \{1, 2\}$ emerge, to solve for the auxiliary variables in the spatial regularization term. I want to note, the the index $j \in \{i-2, i-1, i, i+1\}$ refers to the displacement fields $\mathbf{u}^{(i)}$, while the indices $k, l, m \in \{1, 2\}$ in $\mathbf{A}_{kl}$ and $\mathbf{B}_{klm}$ denote the components of the auxiliary variables.

To solve the system of partial differential equations (5.24) a discretization is necessary (Morton and Mayers, 2005, p. 151–156). The discretization is based on the grid $\mathcal{G}$ of the digital images. Using finite differences a coupled discrete nonlinear system of equations is created from the Euler-Lagrange equations. Nonlinearity results from the data term, which is a non-quadratic function of the displacement fields $\mathbf{u}$ due to the $\mathcal{L}_1$-norm. The $\mathcal{L}_1$-norm in the data term is calculated in the algorithm using the robust penalty function $\Psi_{\mathrm{d}}\left(q^2\right) = \left(q^2 + \varepsilon_{\mathrm{d}}^2\right)^{1/2}$ with the derivative $\Psi_{\mathrm{d}}'\left(q^2\right) = \frac{1}{2}\left(q^2 + \varepsilon_{\mathrm{d}}^2\right)^{-1/2}$ to ensure differentiability (Rudin et al., 1992). Furthermore, the trajectorial regularization term imposes nonlinearities, since it is also non-quadratic in the displacements. A Charbonnier et al., 1994 penalty function $\Psi_{\mathrm{t}}\left(q^2\right) = 2\varepsilon_{\mathrm{t}}^2\left(1 + q^2/\varepsilon_{\mathrm{t}}^2\right)^{1/2}$ with the derivative $\Psi_{\mathrm{t}}'\left(q^2\right) = \left(1 + q^2/\varepsilon_{\mathrm{t}}^2\right)^{-1/2}$ substitutes the $\mathcal{L}_1$-norm, as proposed by Volz et al., 2011. To tackle the variational approach, I split the displacements into $\mathbf{u} + \mathrm{d}\mathbf{u}$, where the increment $\mathrm{d}\mathbf{u}$ is to be solved for. I implemented a coarse-to-fine image pyramid hierarchy with n_{lev} levels (Burt and Adelson, 1983) that allows to handle also large deformations despite the made linearizations.[7] Introducing the vector of increments $\mathbf{d} = \left(\mathrm{d}u_1^{(i-2)}, \mathrm{d}u_2^{(i-2)}, \mathrm{d}u_1^{(i-1)}, \mathrm{d}u_2^{(i-1)}, \dots, \mathrm{d}u_1^{(i+1)}, \mathrm{d}u_2^{(i+1)}, 1\right)$ and adopting the motion tensor notation proposed by Knutsson, 1989, Bigun et al., 1991, and

---

[6]I switch the notation from $\mathbf{u}_j^{j+1}$ to $\mathbf{u}^{(j)}$ in order to make the presentation of the algorithm clearer.

[7]Steinbrucker et al., 2009 denote displacements >1 pixel as large.

Farnebäck, 2001, the Euler-Lagrange equation with respect to $\mathrm{d}u_1^{(i-2)}$ finally reads

$$
\begin{aligned}
0 =\ & \lambda_{\mathrm{ti}} \left(\Psi'_{\mathrm{d}} \left(\mathbf{d}^{\mathrm{T}} \mathbf{V}^{(i-2)} \mathbf{d} \right) \mathbf{V}_{11}^{(i-2)} + \lambda_{\mathrm{ba}} \Psi'_{\mathrm{d}} \left(\mathbf{d}^{\mathrm{T}} \mathbf{W}^{(i-2)} \mathbf{d} \right) \mathbf{W}_{11}^{(i-2)} \right) \, \mathrm{d}u_1^{(i-2)} + \\
& \lambda_{\mathrm{ti}} \left(\Psi'_{\mathrm{d}} \left(\mathbf{d}^{\mathrm{T}} \mathbf{V}^{(i-2)} \mathbf{d} \right) \mathbf{V}_{12}^{(i-2)} + \lambda_{\mathrm{ba}} \Psi'_{\mathrm{d}} \left(\mathbf{d}^{\mathrm{T}} \mathbf{W}^{(i-2)} \mathbf{d} \right) \mathbf{W}_{12}^{(i-2)} \right) \, \mathrm{d}u_2^{(i-2)} + \\
& \lambda_{\mathrm{ti}} \left(\Psi'_{\mathrm{d}} \left(\mathbf{d}^{\mathrm{T}} \mathbf{V}^{(i-2)} \mathbf{d} \right) \mathbf{V}_{13}^{(i-2)} + \lambda_{\mathrm{ba}} \Psi'_{\mathrm{d}} \left(\mathbf{d}^{\mathrm{T}} \mathbf{W}^{(i-2)} \mathbf{d} \right) \mathbf{W}_{13}^{(i-2)} \right) \, \mathrm{d}u_1^{(i-1)} + \\
& \lambda_{\mathrm{ti}} \left(\Psi'_{\mathrm{d}} \left(\mathbf{d}^{\mathrm{T}} \mathbf{V}^{(i-2)} \mathbf{d} \right) \mathbf{V}_{14}^{(i-2)} + \lambda_{\mathrm{ba}} \Psi'_{\mathrm{d}} \left(\mathbf{d}^{\mathrm{T}} \mathbf{W}^{(i-2)} \mathbf{d} \right) \mathbf{W}_{14}^{(i-2)} \right) \, \mathrm{d}u_2^{(i-1)} + \\
& \lambda_{\mathrm{ti}} \left(\Psi'_{\mathrm{d}} \left(\mathbf{d}^{\mathrm{T}} \mathbf{V}^{(i-2)} \mathbf{d} \right) \mathbf{V}_{19}^{(i-2)} + \lambda_{\mathrm{ba}} \Psi'_{\mathrm{d}} \left(\mathbf{d}^{\mathrm{T}} \mathbf{W}^{(i-2)} \mathbf{d} \right) \mathbf{W}_{19}^{(i-2)} \right) + \\
& \lambda_{\mathrm{s}} \lambda_{\mathrm{ti}} \lambda_{\mathrm{s1}} \left(\frac{\partial \mathbf{A}_{11}^{i-2}}{\partial x_1} - \frac{\partial^2 (u_1^{i-2} - \mathrm{d}u_1^{i-2})}{\partial x_1^2} + \frac{\partial \mathbf{A}_{12}^{i-2}}{\partial x_2} - \frac{\partial^2 (u_1^{i-2} - \mathrm{d}u_1^{i-2})}{\partial x_2^2} \right) + \\
& \lambda_{\mathrm{t}} \left(\Psi'_{\mathrm{t}} \left(\sum_{k=1}^{2} \left((u_k^{i-2} + \mathrm{d}u_k^{i-2}) - 2(u_k^{i-1} + \mathrm{d}u_k^{i-1}) + (u_k^i + \mathrm{d}u_k^i) \right)^2 \right) \cdot \right. \\
& \left. \left((u_1^{i-2} + \mathrm{d}u_1^{i-2}) - 2(u_1^{i-1} + \mathrm{d}u_1^{i-1}) + (u_1^i + \mathrm{d}u_1^i) \right) \right),
\end{aligned}
\tag{5.25}
$$

where $\mathbf{V}^{(i-2)}$ is the intensity constancy motion tensor, $\mathbf{W}^{(i-2)}$ the intensity gradient constancy motion tensor between image $I^{(i-2)}$ and image $I^{(i-1)}$. The eight Euler-Lagrange equations for the remaining the elements in $\mathbf{d}$ deduce accordingly. The auxiliary variables $\mathbf{A}$ and $\mathbf{B}$ give additional but temporally uncoupled Euler-Lagrange equations. With respect to $\mathbf{A}^{(i-2)}$ the four Euler-Lagrange equations derive using $j, k \in \{1, 2\}$

$$
0 = \mathbf{A}_{jk}^{(i-2)} - \frac{\partial (u_1^{(i-2)} + \mathrm{d}u_1^{(i-2)})}{\partial x_1} + \lambda_{\mathrm{s2}} \left(\frac{\partial^2 \mathbf{A}_{jk}^{(i-2)}}{\partial x_1^2} + \frac{\partial^2 \mathbf{A}_{jk}^{(i-2)}}{\partial x_2^2} + \frac{\partial \mathbf{B}_{jk1}^{(i-2)}}{\partial x_1} + \frac{\partial \mathbf{B}_{jk2}^{(i-2)}}{\partial x_2} \right)
\tag{5.26}
$$

and with respect to $\mathbf{B}^{(i-2)}$ the eight Euler-Lagrange equations derive using $j, k, l \in \{1, 2\}$

$$
0 = \mathbf{B}_{jkl}^{(i-2)} - \frac{\partial \mathbf{A}_{jk}^{(i-2)}}{\partial x_l} - \lambda_{\mathrm{s3}} \left(\nabla \cdot \left(\frac{1}{2} \left(\sum_{a,b,c=1}^{2} \nabla B_{abc}^{(i-2)} \nabla B_{abc}^{\mathrm{T}\,(i-2)} \right) \nabla \mathbf{B}_{jkl}^{(i-2)} \right) \right).
\tag{5.27}
$$

The nonlinear system of Euler-Lagrange equations is solved by sequentially freezing nonlinear coefficients, as proposed for example by Corpetti et al., 2002 and Bruhn and Weickert, 2005. This method finally represents a local linearization of the data term by Frohn-Schauf et al., 2004. An inner fixed-point iteration then solves the remaining coupled linear system of equations of the displacement fields. Using the calculated inner loop, the nonlinearity estimate is adjusted

and the inner fixed point iteration is calculated again. The inner solution of the linear system of equations is approximated using a successive over relaxation algorithm (SOR) with the relaxation parameter r_{SOR} (D. Young, 1950). A convergence criterion $\varepsilon_{\mathbf{d}}$ and the specification of a maximum number of outer iterations n_{out} and inner n_{in} for the two loops control the overall algorithm. The Euler-Lagrange equations of the respective auxiliary variables contain no coupling terms, so that the auxiliary variables $\mathbf{A}$ and $\mathbf{B}$ are solved independently. Due to the non-linearity of in the Euler-Lagrange equations with respect to $\mathbf{B}$, the sequential freezing of non-linear coefficients is also used for this purpose. The entire solution process is done for each pyramid level from coarse to fine, where the previous level results are the initial guess for the finer current level. Algorithm 4, see appendix F.3.4, outlines the developed routine that is controlled by a large set of parameters. I chose and adapted the algorithm specific parameters taking into account the investigations of Bruhn et al., 2006, Volz et al., 2011 and Hewer et al., 2013: penalty parameters $\varepsilon_{d} = 10^{-3}$, $\varepsilon_{t} = 1$, factor $\lambda_{ti} = 0.5$, relaxation parameter $r_{SOR} = 1.97$, number of outer iterations $n_{out} = 10$, number of inner iterations $n_{in} = 1000$, thresholds $\epsilon_{\mathbf{d}} = 10^{-3}$, $\epsilon_{\mathbf{A}} = 10^{-5}$, $\epsilon_{\mathbf{B}} = 10^{-10}$, pyramid levels $n_{lev} = 5$, resize factor $\rho_{re} = 0.85$. The problem specific identification of the weighting factors: λ_{s}, λ_{t}, λ_{ba}, λ_{s1}, λ_{s2}, λ_{s3} is shown in section 5.4.

5.2 Fracture Analysis[8]

Block-matching approaches are well suited for analyzing experiments with moderate local gradients. Unfortunately, such methods are of limited use as soon as cracks evolve, due to the discontinuities in the motion fields. The individual blocks do not allow to resolve local phenomena on single pixel and sub-pixel level properly. Variational motion estimation works without such fixed gage length. In addition, variational approaches permit to model motion discontinuities, as Brox et al., 2004 using a total variation regularization, and local phenomena, as Brox and Malik, 2011, who incorporate descriptor matching to resolve small structures undergoing large motions. Balle et al., 2015 and Balle et al., 2019 detect cracks on the microscopic scale using infimal convolution (Holler and Kunisch, 2014) and total generalized variation (Bredies et al., 2010), respectively. I developed the idea to use such fracture analysis methods as a complement to the spatio-temporal deformation analysis described in section 5.1 and also to embed them into the updated Lagrangian framework. This hybrid allows to resolve crack initiation and propagation even under large non-rigid deformation.

---

[8]The analysis of the material fracture during shear cutting was developed and adopted in cooperation with Sebastian Neumayer, Jan Henrik Fitschen and Gabriele Steidl. The method builds on the deformation analysis in section 5.1. My coworkers and I introduce the method for the acquisition of the material fracture during shear cutting by means of an academic example experiment (Hartmann et al., 2021).

Regularization Model

As usual, the conducted variational model consists of two parts, a data term $\mathfrak{D}$ modeling how well the displacement field $\mathbf{u}$ fits the two input images I_0 and I_1, and a regularization term $\mathfrak{R}$ to model the solution that contains prior knowledge about motion and deformation, see section 5.1.3. The motion fields are computed as the minimizer of the resulting functional $\mathfrak{E}$, as shown in expression (2.56).

$$\mathfrak{E} = \mathfrak{D} + \mathfrak{R} \tag{5.28}$$

The data term $\mathfrak{D}$ contains the linearized brightness-constancy, see equation (2.54), that is penalized with the $\mathcal{L}_1$-norm to stabilize calculations and reduce the influence of outliers.

$$\mathfrak{D} = ||\mathbf{u} \cdot \nabla I_1 + I_1 - I_0||_1 \tag{5.29}$$

For crack analysis, the regularization term choice represents the crucial part that models the motion discontinuities. In the approach, the basic idea is to introduce the displacement gradient $\nabla\mathbf{u}$ in the regularization term and split it into two components $\mathbf{s}$ and $\mathbf{a}$. The first component $\mathbf{s}$ models motion discontinuities, such as cracks, and can rise to large local values, while the second component $\mathbf{a}$ expresses smooth homogeneous deformation patterns. Motion discontinuities occur only sporadically, which is why $\mathbf{s}$ is assumed to be sparse and enters the regularization term via the $\mathcal{L}_2$-norm. Since the part $\mathbf{a}$ of the displacement gradient is assumed smooth, its first derivative is used in the regularizer. Combining both terms leads to the following regularization expression in the reference configuration C_0

$$\begin{aligned}
\mathfrak{R} &= \inf_{\mathbf{a}+\mathbf{s}=\nabla\mathbf{u}} \left\{ \int_{C_0} \lambda_{f1}||\mathbf{s}||_2 + \lambda_{f2}||\nabla\mathbf{a}||_2 \ d\mathbf{x} \right\} \\
&= \inf_{\mathbf{a}} \left\{ \int_{C_0} \lambda_{f1}||\nabla\mathbf{u} - \mathbf{a}||_2 + \lambda_{f2}||\nabla\mathbf{a}||_2 \ d\mathbf{x} \right\},
\end{aligned} \tag{5.30}$$

which is called the total generalized variation introduced by Bredies et al., 2010. The variational model using equation (5.29) and equation (5.30) leads to a convex, but non-smooth expression for which Balle et al., 2019 have shown that a minimizer exists. It is solved using primal-dual algorithms from convex analysis, see algorithm 5 in appendix F.3.5, where every update step has a closed-form solution (Chambolle and Pock, 2011; Pock et al., 2009). Analogously to the strain rate estimation algorithm 4, a coarse-to-fine image pyramid enables large motion analysis. The adopted coarse-to-fine scheme applies a median filter to the image data I_0 and I_1 each step, as sketched in algorithm 5.

Physical Consideration

The regularization is designed to describe the local deformation behavior. If cracks occur in a material, they become visible as jumps in the displacement field. The continuum mechanics definition of strains, see equation (2.6), originating from the deformation gradient $\mathbf{F}$ loses its meaning in the crack, since an emerging surface penetrates the continuous material. The respective spatial gradient in the local deformation analysis diverges directly at the crack (non-classical strains). However, the regularization term, see equation (5.30), uses this property to separate non-classical strains $\mathbf{s}$ from classical strains $\mathbf{a}$ during minimization. The underlying assumption is, that locations showing non-classical strain portions represent cracks.

Algorithm

The data term is rewritten for discretization and reads

$$\mathfrak{D} = ||\frac{\partial I_1(\mathrm{d}\mathbf{u})}{\partial x_1}u_1 + \frac{\partial I_1(\mathrm{d}\mathbf{u})}{\partial x_2}u_2 + I_1(\mathbf{u}) - I_0||_1 \, , \tag{5.31}$$

where the partial derivatives are calculated by forward differences and $I_1(\mathbf{u})$ is evaluated at the grid points based on bi-linear interpolation. To formulate the discretization of the regularization term, the mixed norm

$$||f||_{2,1} = \sum_{j \in \mathcal{G}} ||f(j)||_2 \tag{5.32}$$

is introduced and the total generalized variation regularization term becomes

$$\mathfrak{R} = \min\left\{ \lambda_{\mathrm{f1}}||\nabla\mathbf{u} - \mathbf{a}||_{2,1} + \lambda_{\mathrm{f2}}||\nabla_\varepsilon\mathbf{a}||_{2,1} \right\} \, , \tag{5.33}$$

where the backward differences operator ∇_ε is

$$\nabla_\varepsilon = \left(\frac{\partial}{\partial x_1}, \frac{1}{2}\left(\frac{\partial}{\partial x_1} + \frac{\partial}{\partial x_2} \right), \frac{\partial}{\partial x_2} \right)^{\mathrm{T}} . \tag{5.34}$$

The operator ∇_ε achieves that the components of the Green strain tensor $\mathbf{E}$ are calculated directly within the iteration process. Subsequent derivative computations vanish. The same applies to the local values of the discontinuous part $\mathbf{s}$ of the displacement gradient $\nabla\mathbf{u}$. Algorithm 5 shows the conducted routine, that I further embedded into the updated Lagrangian framework described in section 5.1. For the application in crack analysis, I use $n_{\mathrm{lev}} = 70$ scales, a scaling factor of

$\rho_{re} = 0.97$, and a Gaussian Kernel K_σ standard deviation of $\sigma = 0.3$. $n_{it} = 3000$ iterations are calculated for the primal dual algorithm using the settings $\tau_1 = 0.25$, $\tau_2 = 0.25$, $\theta = 1$.

5.3 Geometry Analysis

The geometry analysis characterizes cut surface according to the guideline VDI2906-2, 1994, see figure 2.6. The raw data is a set of L contour coordinates $\mathbf{x} = (x_1, x_2)_n$, where $n = 1 \dots L$. In order to circumvent user dependence in the evaluation, I automated the procedure.

In contrast to common methods, the developed algorithm is not based on numerical differentiation of the cut surface measurement data but on model parameter sampling. The model parameter vector $\boldsymbol{\varphi}$ describes the cut surface, as presented in section 2.4.1. I interpret the set of model parameters $\boldsymbol{\varphi}$ as the transitions between the five different parts of the cut surface. Hence, the model parameter identification reduces to finding the indices $\iota \in 1 \dots L$ of the ideal transition coordinates from the measured data set. For the sampling procedure, each part is idealized using a polynomial function, where the vector $\mathbf{d}_p$ contains the polynomial order of each contour part. Each tested set of model parameters $\boldsymbol{\varphi}$ yields a residual R to the measured contour data, which is to be minimized. Algorithm 6 calculates the residual between each of the polynomial fits and the cut surface contour. It selects the minimum residual R_m of all admissible model parameter combinations from the raw data set.[9] For the geometry analysis, I utilized fourth-order polynomials for the edge draw-in and first-order polynomials otherwise.

The sampling-based algorithm 6, see appendix F.3.6, is limited by the given model to the description of the cut surfaces in eight parameters. Degenerate cut surfaces could also be tackled with the proposed algorithm by straightforward extension of the cut surface model by corresponding characteristics of degenerate cut surfaces. The description of secondary clean-shear would be possible, for example, by introducing four additional parameters that define the location of two additional points along the cut surface. In this way an additional section along the cut surface to characterize secondary clean shear is available. The eight parameter cut surface model $\boldsymbol{\varphi} = (\varphi_1, \dots, \varphi_8)$ turns into a twelve parameter model $\boldsymbol{\varphi} = (\varphi_1, \dots, \varphi_{12})$.

Adaptive model adjustments along the lines of model creation, see section 2.2.2, can also be implemented with the sampling-based approach. The basic idea is a super-ordinate optimization routine, following the principle of expression 2.37, where algorithm 6 corresponds to the data term $\mathfrak{D}$.

---

[9]The variables l, m, n, and o control the nesting of loops and take care of admissibility with respect to the polynomial regression.

5.4 Algorithm Parameter Selection

The presented motion estimation algorithms contain different evaluation parameters, both the block-matching methods and the variational methods. The quality of motion estimation is commonly assessed by synthetic data image data from known ground truth motion $^{\text{GT}}\mathbf{u}$, such as for example by Barron et al., 1994 and Amiot et al., 2013. As an extension of the work of my coworkers and me in (Hartmann, J. Wang, et al., 2018), I adapt this common methodology for algorithm parameter selection. Since algorithm 1 to algorithm 5 have different numbers and types of algorithm parameters, I employ the D_{BIC} criterion (see section 2.2.4) for assessing the motion estimation quality. Each adjustment of the algorithm parameters lead to different D_{BIC} values. The D_{BIC} value is strongly connected to the mean sum of squared differences D_{MSSD}, since the argument of the logarithm term in the D_{BIC} calculation represents the $D_{\text{MSSD}}(x) = \frac{1}{2N_1N_2}\sum_{l=1}^{N_1}\sum_{k=1}^{N_2}\left(x(k,l) - {}^{\text{GT}}x(k,l)\right)^2$. If all the compared results have the same number of parameters, selecting the model with minimum D_{BIC} value also minimizes the MSSD. The D_{BIC} generalizes the concept of least squares error minimization and also allows to compare models with parameters set to zero. This allows a balanced selection of all algorithm parameters across different methods within one single routine. Algorithm 7, see appendix F.3.7, shows the developed assessment procedure. N synthetic images $\left\{I^{(1)}, \dots, I^{(N)}\right\}$ are created based on ground truth motion data $^{\text{GT}}\mathbf{u}$, motion discontinuities $^{\text{GT}}\mathbf{d}$, and an image template I_0. Using the data variance estimation provided by Garcia, 2010, I estimate the noise σ in the shear cutting experiment from the image sequence $\left\{I_0, \dots, I_{0+n}\right\}$. The estimated noise is applied on the synthetic images by sampling new noise distributions $\sigma^{(j)}$ to mimic real recording conditions throughout the synthetic image sequence.

For the motion estimation algorithm parameter identification I used four different ground truth motions: rigid rotation, tension, shear, and discontinuous rigid translation. I started the algorithm parameter identification based on the values given in the works by Hewer et al., 2013, Volz et al., 2011, Chartrand, 2017, Balle et al., 2019, and my coworkers and me in (Hartmann, J. Wang, et al., 2018), which turned out to require only minor adjustments. Table 5.1 summarizes the finally identified algorithm parameters, which were used for the evaluations of the experimental data. With the identified parameters, all motion estimation algorithms achieved D_{MSSD} values under 1% compared to the ground truth motion data.

Table 5.1: Specific algorithm parameters for motion estimation.

parameter	algorithms 1, 2, and 3				algorithm 4						algorithm 5	
	$\|S\|$	δ	λ_1	λ_2	λ_{s}	λ_{t}	λ_{ba}	λ_{s1}	λ_{s2}	λ_{s3}	λ_{f1}	λ_{f2}
value	16×16	1	1	0.149	1000	10	0.5	2	1	2	0.2	10

6 Results

This chapter contains the results of the experimental program shown in chapter 4 and evaluated with the methods proposed in chapter 5. Besides the classical ex situ geometric cut surface parameters and the integral in situ process parameters, cutting force and punch travel, I show the dynamic, locally resolved behavior of the sheet metal material in the shear affected zone during shear cutting. I explain the chosen representations and illustrations of the experimental results using the reference experiment introduced in section 4.3. The reference experiment serves as an anchor for the comparison of different process parameter configurations. I present the results of the process parameter variation for both materials tested in the three groups of cutting line characterization. Section 4.1.2 focuses on closed cutting lines, where section 4.1.3 examines open cutting lines. I would like to emphasize that this chapter deals with the objective presentation of the experimental program. Additionally, I give a first meaning with regard to the current state of knowledge within the respective sections. Supplemental results are given in appendix F.4. Further discussion, interpretation, and generalization is done in chapter 7 *Discussion*.

6.1 Reference Experiment

The reference experiment was performed using the following configuration: S355MC sheet metal, closed cutting line, cutting clearance 10%, cutting speed 1 mm/s, uniform cutting edge rounding 50 μm. It occupies a central position in the process parameter domain of the conducted experimental space, see figure 4.7. I use the reference experiment first to introduce the appearance of the experimental raw data, second to describe the visualizations of the evaluation results, and third to anchor the conducted parameter studies.

6.1.1 Raw Data

The raw data of the force and displacement measurements as well as the geometry acquisition directly contain the measurement information to be obtained. Signal quality and shape of the expected curves allow operating completely without filter intervention in the case of geometry evaluation. Cut surface characteristics were extracted directly from the raw data, using the sampling method presented in section 5.3. The integral in situ curves for cutting force and punch

travel require only little filter intervention. Due to the expected smooth signal characteristics of the cutting force and punch travel signals, a cubic five-point Savitzky-Golay filter was used.

High-Speed image sequences represent the raw data for the dynamic locally resolved motion analysis. Figure 6.1 a) shows an extract of the raw data for a reference experiment test, which was recorded at 5000 Hz. Since the light is not introduced co-axially due to the space available, but falls obliquely into the observation plane, the inhomogeneous image contrast and gray value spectrum is created. Punch penetration and material deformation continuously change the reflected textures and thus the image structure for evaluation, especially in the shear affected zone. The initially regular surface pattern of the sheet metal caused by the grinding process is increasingly dissolved in the course of the shear cutting process. The ROI defines the relevant section for observation, however, for evaluation the whole image domain is considered. Especially using the proposed variational motion estimation methods, this reduces boundary influences. The ROI covers an area of 4 mm by 4 mm and contains 600 pixel by 600 pixel, which gives a theoretical pixel edge length of ~7 μm. The first images in figure 6.1 a) shows the initial ROI.

In order to disclose the structure of the raw data, I understand the image sequences of the shear cutting process as three-dimensional arrays. The PARAFAC of the three-dimensional array, as explained in section 2.2.1, makes it possible to show the basic information content along the time axis and the two axes of the observation plane x_1 and x_2. I applied the method proposed by Bro, 1997 and Bro and Kiers, 2003 for the PARAFAC analysis of the 8-bit gray scale image sequences. A five-parameter model has been fitted to the data. The normalized results of the image sequence of the reference experiment shows figure 6.1 b). The PARAFAC analysis already reveals the comparably low information content of the shear cutting process in time direction. Along the time axis, the information density, i.e. the temporal change in the three-dimensional raw data array is almost zero based on the assumed model, see last graph in figure 6.1 b). The three-dimensional array data yield no separation across the number of images in the gray scale domain. Since the images are recorded at a constant rate, the image number axis corresponds to the time axis. Hence, the curve reinforces the interacting dimensional reduction in temporal direction, as described in section 5.1.1. The dimensionality reduction aims at a homogenization of the information density along the temporal axis, but in the space of the kinematic output variables. In the observation plane the five-parameter model already gives certain information. In x_1 direction, for example, the punch travel is clearly visible from ~800 pixel. The fixed die emerges in x_2 direction from ~700 pixel on. The algorithms proposed in chapter 5 *Methods* translate the experimental raw data into the language and logic of the descriptive framework.
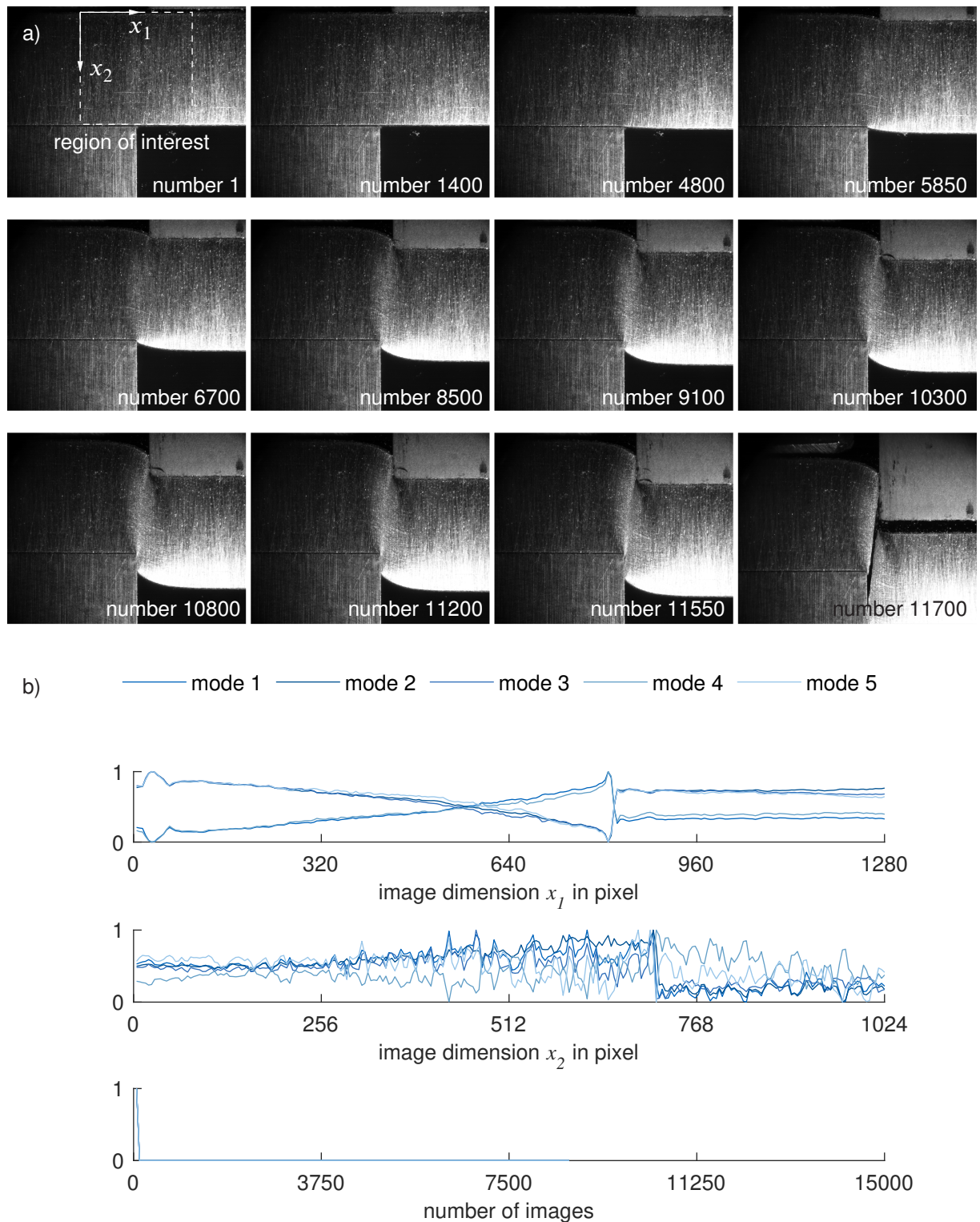
Figure 6.1: 8-bit gray scale image raw data for a test of the reference experiment. a) Selected images of the test sequence. b) PARAFAC analysis of the three-dimensional raw data array for the first five modes along the horizontal image dimension x_1, the vertical image dimension x_2, and the number of images representing the time axis.

6.1.2 Evaluation Results

I based the representative selection of the evaluation results on the integral in situ quantities cutting force and punch travel. Figure 6.2 shows the three cutting force vs. time and punch travel vs. time curves as well as their means for the reference experiment. The cutting force vs. time curve, see figure 6.2 a), takes the typical progression described in section 2.4. After an initial acceleration phase, the punch travel vs. time curve, see figure 6.2 b), shows constant slope, meaning constant cutting velocity. Point A to point D cover the deformation phase. After point D material failure occurs. Point A marks the transition from reversible to irreversible deformation. Point C highlights the maximum cutting force. Atkins, 1980 attributes to the point of maximum cutting force the indication of plastic instability, in analogy to the tensile test. Point B lies in between point A and point C with respect to punch travel. At point B, hardening effects determine the deformation in the shear affected zone leading to the degressive curve shape. Point D shows a state where softening effects dominate after the maximum punch force just before crack initiation. Figure 6.3 gives the cut surface characteristics of the reference experiment using the geometry analysis routine, see section 5.3.
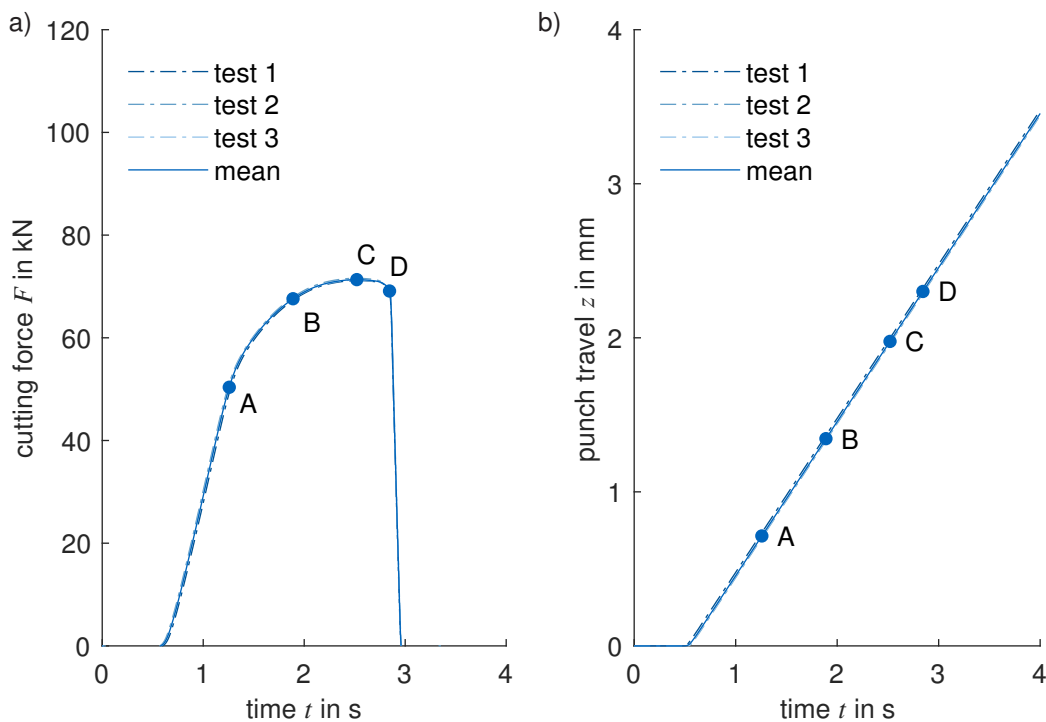
Figure 6.2: Integral in situ data for the reference experiment. a) shows the three cutting force F vs. time t curve and their mean. b) shows the three punch travel z vs. time t curves and their mean. A, B, C, and D indicate the evaluation points for the full-field in situ data analysis.
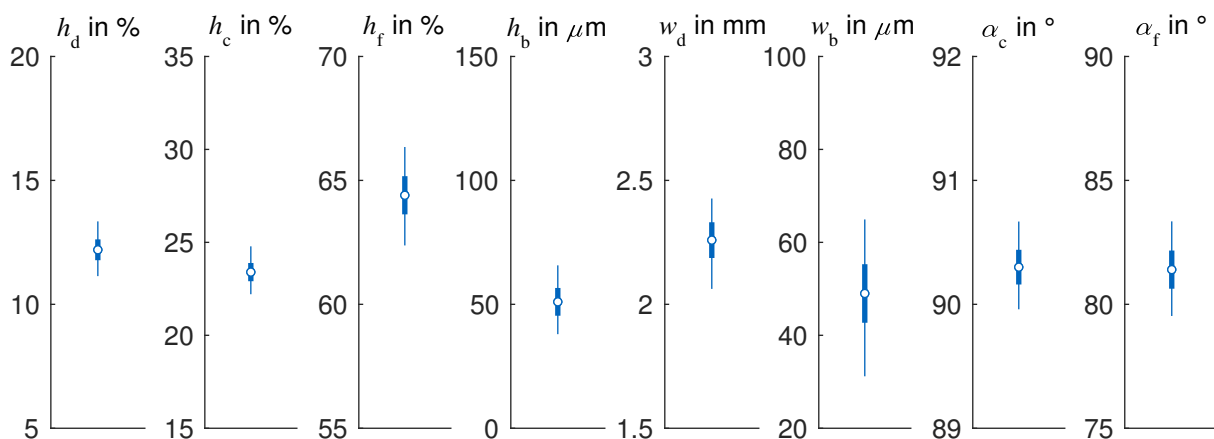
Figure 6.3: Reference experiment cut surface characteristics. (circle: mean, bold line: standard deviation, fine line: minimum and maximum based on 15 measurements)

Displacement

The displacement field **u** represents the raw motion information, as expressed by the motion relation, see equation 2.2. I employ three different fields to examine material particle motion during shear cutting, e.g. material flow, in figure 6.4: the horizontal displacement field u_1 in x_1 direction, see figure 6.4 a), the vertical displacement field u_2 in x_2 direction, see figure 6.4 b), and the field of normalized motion curl c, see figure 6.4 c).[1] The unit for the displacement representation is pixel. I stayed with the original unit that is also used in the algorithms environment. Metric quantities may be calculated straightforward using the pixel edge length of $\sim 7\,\mu$m. The field of normalized motion curl c is computed from the field of motion vector increments $(\mathrm{d}u_1, \mathrm{d}u_2)$ between subsequent images. The black arrows in figure 6.4 c) indicate the field of motion increments. The normalized motion curl c serves as an indicator for local motion complexity, similar to vorticity known from fluid mechanics (Hunt, 1987).

The horizontal displacement field u_1 shows a clear trend in x_2-direction at point A. Until irreversible deformation, the sheet material moves jointly in positive x_1-direction, but more strongly in the upper area, where the blank holder and the punch hit the sheet metal, than at the bottom, where the sheet rests on the fixed die. The jointly executed movement reminds of a rotation, with the middle of the die clearance serving as the center. In point B the horizontal material movement has basically the same pattern of unbroken but open contour lines from the die side to the punch side. The motion retains its rotational characteristic. At the die, material moves horizontally from the punch to the die side, at the punch from the die side to the punch

---

[1]Please note that I set the contour line values to the three intermediate values of the respective color scale. Due to the large differences in values as the shear cutting process progresses, I have introduced separate color scales for points A and B as well as C and D, respectively.

side. At point C a new facet adds to the pattern of horizontal material flow. Above the die edge and below the punch edge, islands of opposing motion are formed in the cutting clearance, as shown by the self-contained contour lines. In these areas, the material flows in reverse direction, i.e. in negative x_1-direction of the die at the punch edge and in positive x_1-direction at the die edge. This movement pattern is maintained until crack initiation in point D and the motion islands are growing. These motion sinks feed burr formations at both blades. A narrow channel of constant horizontal displacement forms in the middle of the cutting clearance between these islands. It has a width of $\sim 130\,\mu$m . Until point A, the sheet metal moves homogeneous in positive x_2-direction, experiencing a fairly uniform reversible compression. With the onset of irreversible deformation, the vertical displacement field u_2 has a consistent and progressive pattern that follows the underlying vertical process kinematics. Starting from point A, the punch induces irreversible deformation. A characteristic vertical deformation pattern emerge, which follows the punch penetration. The fixed die prevents progressive motion of the overlying sheet metal in x_2-direction. The material below the punch face moves further in x_2 direction along with the punch penetration. The cutting clearance acts as a mediator between these two extremes. Within the cutting clearance, the vertical material flow follows a continuous step, e.g. sigmoid shape. The imaginary line of the sigmoid saddle points changes with the punch immersion depth, where its slope coincides with the fracture angle α_f at point D. Furthermore, the u_2 displacement of the sheet metal under the punch contains the vertical portion of reversible motion, the draw-in height h_d, and the clean-shear height h_c. The normalized motion curl c assigns each material particle a scalar number between 0 and 1 representing current motion complexity. No anomalies or regions of particular motion complexity exist in point A. With irreversible deformation entering the shear cutting process, in point B, material behavior becomes inhomogeneous. Material flows more complex in the cutting clearance, mainly around the blade edges. The movement patterns above the die and below the punch are of comparable complexity promoting reflecting the point reflection process characteristics. In point C and again in point D, motion complexity intensifies at the cutting edges compared to the remaining ROI. These areas of the highest motion complexity coincide with the origin of the horizontal deformation islands. Horizontal displacement dictates the distribution of the motion complexity pattern, since the vertical motion pattern stays the same over the process. Vertical displacement influences the orientation of the motion complexity, which agrees with the imaginary line of sigmoid saddle points. The displacement field **u** calculated using algorithm 1 and algorithm 2 behave moderately at first and the complexity varies only mildly across the shear affected zone. At the latest with the onset of motion instability this changes fundamentally. Superimposed motion phenomena and complexity localization characterize the shear cutting process up to crack initiation.
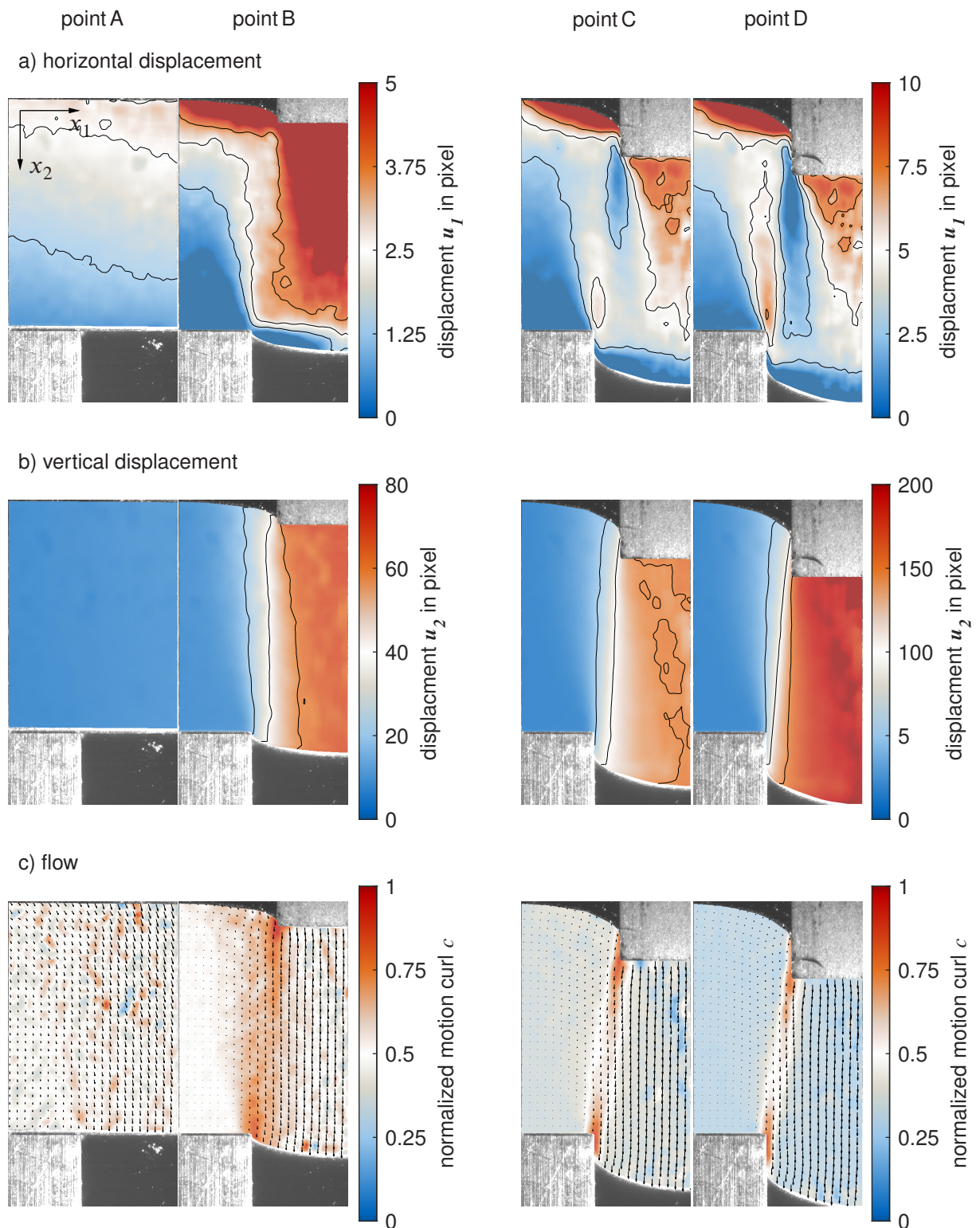
Figure 6.4: Motion fields of the reference experiment at the points A, B, C, and D. a) horizontal displacement u_1 b) vertical displacement u_2 c) normalized motion curl c and flow field indicators.

Strain

To display the local deformation, I use the Green strain tensor **E**, which is calculated from the deformation gradient **F** according to equation 2.7. Figure 6.5 shows the three independent fields of the Green strain tensor components E_{11}, $E_{12} = E_{21}$, and E_{22} for the reference experiment.

The field E_{11} represents the horizontal Green strain tensor component and is shown in figure 6.5 a). The reversible deformations until point A are relatively homogeneous and small. A band with the approximate width of two times the cutting clearance is formed as the irreversible deformation progresses, in point B. The band has tails at the upper and lower end, which extend into the two edge draw-in zones. Horizontal deformation begins to concentrate further at the blade edges, especially when softening effects dominate the shear cutting process after the maximum cutting force. The E_{11} strain localizes increasingly at the blades, which there drive the material apart. The band has an hourglass-shaped strain pattern along the imaginary line that connects the punch edge and the die edge. The horizontal strains reach a maximum value up to 4.76 at the punch edge in point D.

The field of the shear strain, the E_{12} component, develops similar to the horizontal strains, see figure 6.5 b). After point A, the shear deformation concentrates on a band around the cutting clearance. In contrast to the horizontal strain, the shear strain in point B shows approximately constant strain values between the cutting blades within the localization band. Within the shear band, the shear strain localizes and superimposes directly on the cutting edges with incipient deformation instability in point C. This superimposed shear strain localization takes place especially at the outer surfaces of the blades. The maximum value of the Green shear strain component E_{12} is 1.86. The absolute values of the Green shear components are therefore below those of the horizontal strain component. From the sequence point A to point D, the impression gains that the reference shear cutting experiment is dominated by the shear deformation only initially. With the onset of motion instability, the horizontal strain increases disproportionately.

The field of the E_{22} component, see figure 6.5 c), represents the vertical Green strains. The field of the vertical strains shows a considerably more inhomogeneous character than the horizontal strains or the shear strains. In the area between the die and the blank holder, especially at point B, considerably less fluctuation arise than in the moving material under the punch, which is only loaded on one side. Also, at points C and D the absolute values remain in a moderate order of magnitude. The vertical strain pattern homogenizes as the deformation progresses. The band of negative strain values indicates a compressive state, which extends along the lateral surfaces of the blades into the edge draw-in areas.
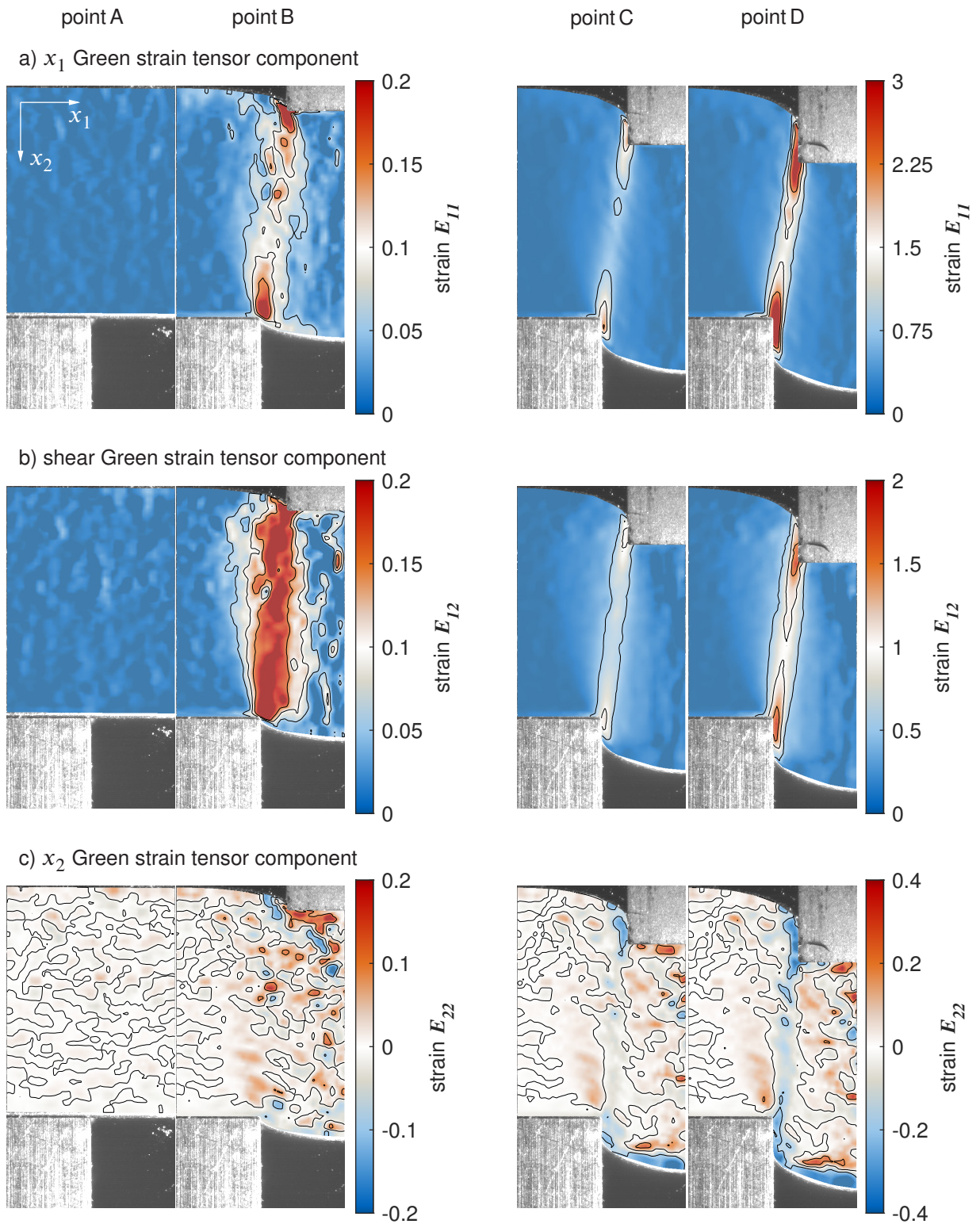
Figure 6.5: *Green strain tensor fields of the reference experiment at the points A, B, C, and D. a)*
x_1 Green strain component E_{11} b) shear Green strain component E_{12} c) x_2 Green
strain component E_{22}.

Strain measures are used as a scalar measure for the deformation, which are calculated on the basis of the tensorial quantities. Figure 6.6 shows the strain distribution of the reference experiment for two different strain measures. Figure 6.6 a) applies the widely used von Mises equivalent strain E_{eq}, which is a variant of equation (2.10), see for example Shrivastava et al., 2012. Figure 6.6 b) uses a strict work conjugate with respect to the von Mises equivalent stress, denoted as modified equivalent strain E_{mq}. Butcher and Abedini, 2017 showed that contrary to E_{eq}, the strain measure E_{mq} holds work conjugation for pure shear regarding the von Mises equivalent stress. I evaluated both strain measures incrementally, in the sense of equation 2.14. The incremental evaluation takes care of non-proportional loading along each material particle's strain path. Figure 6.6 c) shows the distribution of the two principal strains E_1 and E_2 of the Green strain tensor.[2] For each point drawn, this representation is equivalent to Mohr's strain circle for plane strain states. The points are colored according to their normalized density distribution, which I calculated using the kernel density estimation according to Botev et al., 2010.

The von Mises equivalent strain in figure 6.6 a) draws the zone of influence of the shear cutting process, which grows from the outside to the inside of the cutting clearance. With increasing localization and movement instability, the total deformation in points C and point D is limited to the cutting clearance area. In the presented experiment, the affected zone extends further to the punch side, which is mainly caused by the vertical strains E_{22}. The maximum equivalent strain value is 8.61 located at the punch edge for point D.

The modified equivalent strain is exclusively oriented to the dominant deformation mode, which leads to an increased separation between localization and surrounding structure, see figure 6.6 b). Equivalent strain values of up to 5.81 exist at the punch edge for point D.

How strain distribution develops in the shear affected zone, see figure 6.6 c), allows inferences about the loading conditions. Initially, the strain distribution in the shear affected zone is unstructured but arranges itself along a straight line in the second quadrant. Point C and point D show different behavior and the strain distribution follows the left branch of a scaled parabola. In order for the strains to be distributed and developed in this way, non-proportional loads are responsible in the shear zone, as already indicated by the changing horizontal material flow directions. The density distribution shows that the majority of the shear affected zone experiences only comparatively moderate deformation during shearing, but especially in the localized areas extreme strain states are present at the peak.

---

[2]Please note that the principal strain diagrams may not be interpreted similar to the well-known pendant from sheet metal forming, the forming limit diagram (FLD), since deformation boundary conditions are fundamentally different.
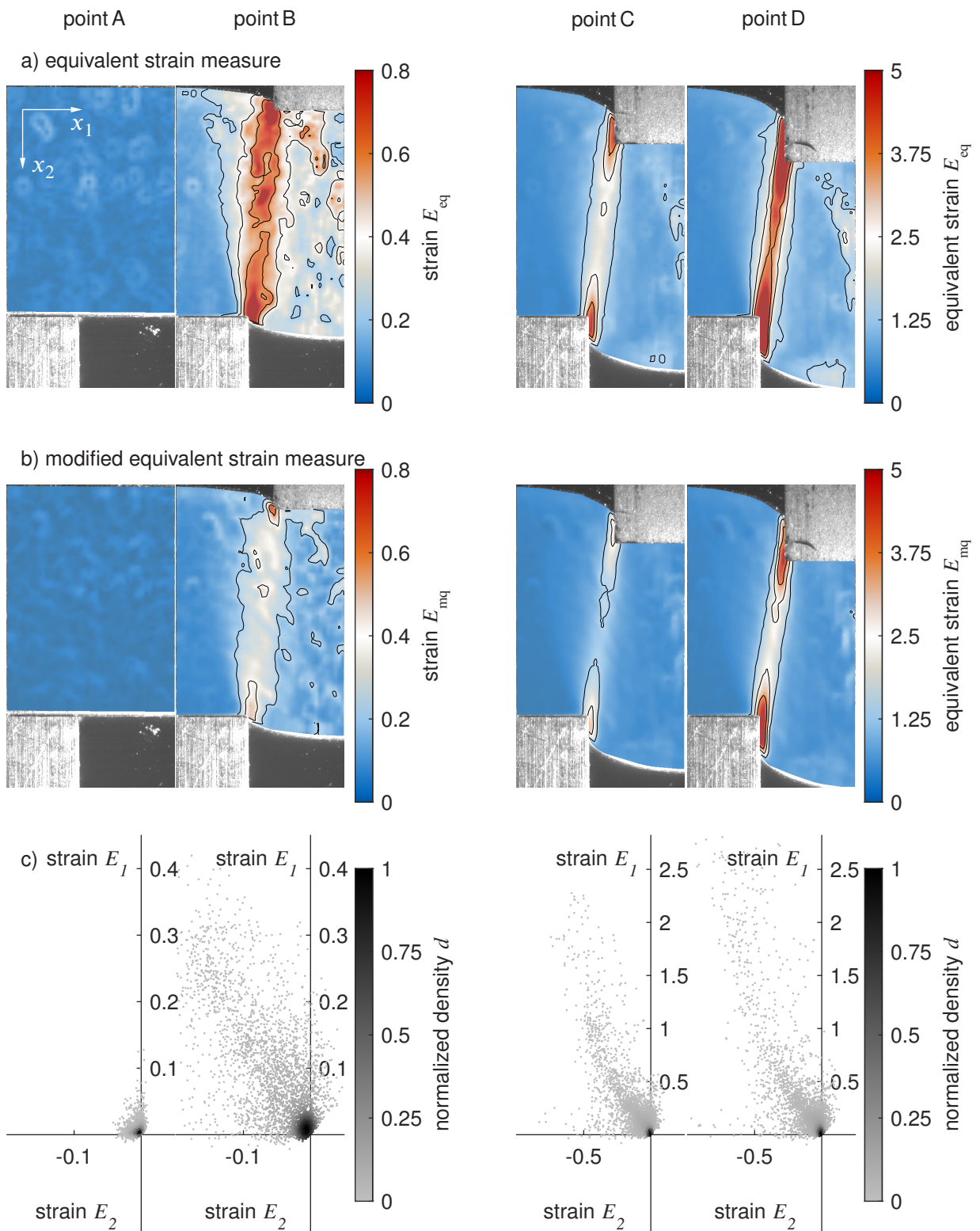
Figure 6.6: Equivalent strain measure fields of the reference experiment at the points A, B, C, and D. a) equivalent strain measure E_{eq} b) modified equivalent strain measure E_{mq} c) principal strain distribution in the ROI and its normalized density.

Strain Rate

The strain rates unify the local deformation behavior and the local dynamics. I use the Green strain rate tensor $\dot{\mathbf{E}}$, given in equation 2.13, to explore the local process dynamics. Figure 6.5 visualizes the three independent fields of the Green strain rate tensor components $\dot{E}_{11}$, $\dot{E}_{12} = \dot{E}_{21}$, and $\dot{E}_{22}$ for the reference experiment.

The horizontal strain rate components are represented by the field $\dot{E}_{11}$ in figure 6.5 a). During reversible deformation, until point A, the horizontal strain rates at the contact point of the punch edge increase locally with the transition to the irreversible deformation. Otherwise, a comparatively homogeneous strain rate field is obtained throughout the whole sheet metal. As the irreversible deformation progresses, the horizontal strain rate localizes in agreement to the specific areas of horizontal strains. As can be seen from the transition of the color scales from point B to point C, the dynamics of the shearing process increases abruptly. The incipient instability of motion manifests in the local dynamics by an extreme strain rate elevation at the end faces of the punch and the die. At point D, wedge-shaped strain rate peaks protrude into the deformation band starting from the blade edges. Maximum $\dot{E}_{11}$ strain rates of $13.32\,\mathrm{s}^{-1}$ occur in point D.

The shear fraction of the Green strain rates is expressed by the $\dot{E}_{12}$ field, which is drawn in figure 6.5 b). Analogous to the horizontal strain rates, initially, the reversible shear deformation is comparatively homogeneous. As the irreversible deformation progresses, sites of increased strain rates occur in point B. Contrary to their expression in the field $\dot{E}_{11}$, the peak values of these sites are not located directly at the cutting edges, but at a distance of $\sim 75\,\mu$m from the cutting edges. The origins of the islands of horizontal deformation fall on these positions, see figure 6.4 a). The shear strain rate is strongly localized at the faces of punch and die, reaching maximum values of $3.89\,\mathrm{s}^{-1}$ in point D.

The local dynamics in the $\dot{E}_{22}$ field is fundamentally different. The distribution of the vertical strain rates across the shear zone of influence is unsteady and characterized by changing signs. Only in point C a preferential direction forms and channels the vertical dynamics between the blade edges, which continues until point D. The absolute highest vertical strain rates occur at the punch edge and amount to $1.62\,\mathrm{s}^{-1}$.

In general, the strain rates precede the deformation. The local dynamics essentially determine how the material behaves, flows, and deforms as the shearing process progresses.
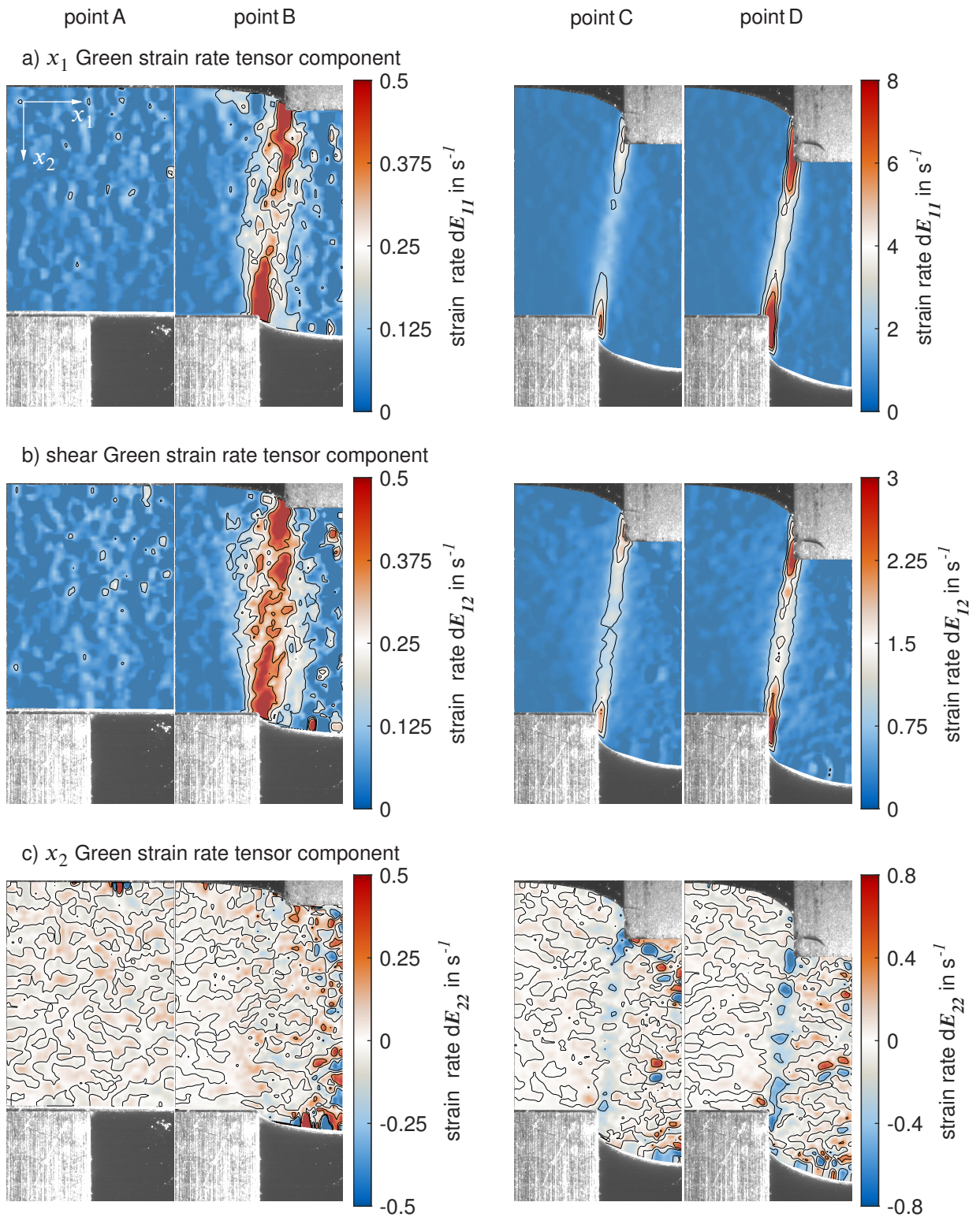
Figure 6.7: Strain rate tensor fields of the reference experiment at the points A, B, C, and D. a) x_1 Strain rate component $\dot{E}_{11} = dE_{11}$ b) shear Strain rate component $\dot{E}_{12} = dE_{12}$ c) x_2 Strain rate component $\dot{E}_{22} = dE_{22}$.

Crack Evolution

The crack initiation, crack propagation, and finally the crack consolidation finish the shearing process with the actual release of material cohesion. In terms of the continuum mechanics framework, the classical local deformation description loses its validity in the crack itself. But since I used the distinction between classical and non-classical strain in algorithm 5 to model, detect, and measure cracks, I visualize crack evolution using the components Green strain tensor E_{11}, $E_{12} = E_{21}$, and E_{22}, see figure 6.8 a), b), and c), respectively. Each component field contains the non-classical, e.g. hypothetical, strains to mimic the crack path evolution. I start the visualization with crack initiation, one time step after point D.[3] In continuation, four images at selected time intervals Δt_c are shown in figure 6.8.

Crack initiation takes place at the lateral surface of the die. That the material separates, initially, is evident in the horizontal component of the Green strain tensor E_{11}, where a macro crack is visible in the area of the strongest deformation localization. The shear components E_{12} and vertical components E_{22} already exhibit non-classical strain components at the die face. After $\Delta t_c = 0.0033\,\text{s}$, non-classical strain components also appear at the punch lateral surface.[4] But only after $\Delta t_c = 0.1020\,\text{s}$ the second macro crack in the horizontal strain component is clearly visible originating from the punch. The macro cracks are now also noticeable in the shear strain component and the vertical strain component. The time sequence in figure 6.8 shows the crack propagation up to the crack consolidation after $\Delta t_c = 0.1027\,\text{s}$. The crack consolidation is most obvious in the field of shear strains. The two macro cracks, which start from the blade edges, do not grow continuously and therefore do not have a constant propagation velocity. Especially after crack initiation, the cracks grow only slowly and shortly before material separation, crack propagation accelerates. Also, the behavior of how the macro cracks propagate through the sheet metal changes during crack evolution. Initially, the non-classical horizontal strains clearly trace the crack propagation. But at the latest after $\Delta t_c = 0.1024\,\text{s}$ the non-classical shear components dominate the reflection of crack evolution.

In addition to the macro cracks, the evaluation routine resolves micro cracks, which are most evident in the vertical Green strains E_{22}. Already after $\Delta t_c = 0.1020\,\text{s}$ local non-classical strains occur distributed along the deformation band. When these micro cracks unify, the macro crack propagates. This process shows up with a delay in the vertical strain, where macro crack propagation lags behind compared to the horizontal strain component and the shear strain component.

---

[3]At this time a non-smooth strain component occurs for the first time, so that it can be determined unambiguously. The integral in situ quantities allow a preselection and containment of the image raw data.

[4]I deliberately refrained from visualizing this point in time because the differences are not visually perceptible.

$\Delta t_{\rm c} = 0\,{\rm s}$ $\Delta t_{\rm c} = 0.1020\,{\rm s}$ $\Delta t_{\rm c} = 0.1022\,{\rm s}$ $\Delta t_{\rm c} = 0.1024\,{\rm s}$ $\Delta t_{\rm c} = 0.1027\,{\rm s}$

a) x_1 Green strain tensor component

b) shear Green strain tensor component

c) x_2 Green strain tensor component
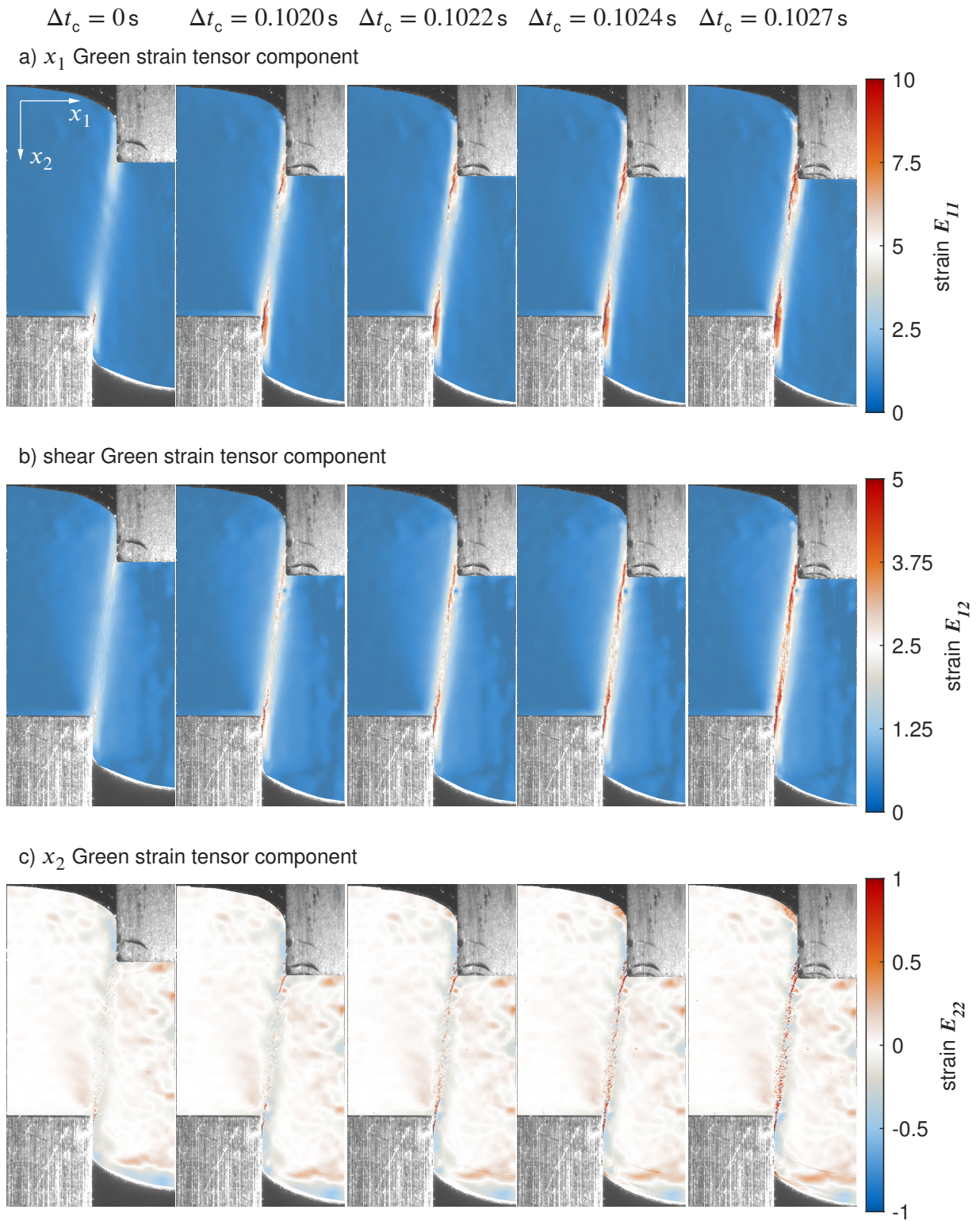
Figure 6.8: *Green strain tensor fields of the reference experiment during crack propagation. a) x_1 Green strain component E_{11} b) shear Green strain component E_{12} c) x_2 Green strain component E_{22}.*

6.2 Closed Cutting Line

The experimental investigations on closed cutting lines are defined in the experimental plan, see figure 4.7. For the sheet metal material S355MC, with a thickness of $s = 4\,\mathrm{mm}$, I have completely covered the process parameter space. I performed cutting clearance variation for the sheet metal material EN AW A5083, with a thickness of $s = 4\,\mathrm{mm}$, under reference settings.

In order to create the possibility to represent not only the integral in situ and ex situ quantities but also the local process quantities in the form of a single measure, I use the Hausdorff metric. This metric is used in the context of object matching as a measure of comparison, for example by Huttenlocher et al., 1993 and Dubuisson and Jain, 1994. The Hausdorff metric permits to measure the distance d between two non-empty point sets $\mathcal{X}_0$ and $\mathcal{X}_1$ in a metric space $\mathbb{M}$ (Hausdorff, 1914, p.290–304). I understand the three local in-situ flow field quantities u_1, u_2, and c as multidimensional point sets $\mathcal{X}$ of the metric space $\mathbb{M}$ spanned by the ROI and the field values. The distance of a point $\mathbf{m}_1 \in \mathcal{X}_1$ in the metric space to a point set $\mathcal{X}_0$ is calculated by

$$d_{\mathrm{H}}(\mathbf{m}_1, \mathcal{X}_0) = \inf_{\mathbf{m}_0 \in \mathcal{X}_0} \left(d_{\mathbb{M}}(\mathbf{m}_1, \mathbf{m}_0) \right) \ . \tag{6.1}$$

The distances between two sets of points follows as

$$d(\mathcal{X}_0, \mathcal{X}_1) = \max \left(d_{\mathrm{Ha}}(\mathcal{X}_0, \mathcal{X}_1), d_{\mathrm{Ha}}(\mathcal{X}_1, \mathcal{X}_0) \right) \ , \tag{6.2}$$

where

$$d_{\mathrm{Ha}}(\mathcal{X}_0, \mathcal{X}_1) = \sup_{\mathbf{m}_0 \in \mathcal{X}_0} \left(d_{\mathrm{H}}(\mathbf{m}_0, \mathcal{X}_1) \right) \ . \tag{6.3}$$

The computation of the Hausdorff distance d follows Moreno et al., 2013, where the $\mathcal{L}_2$-norm underlies the calculations. The use of the Hausdorff distance as a similarity measure, or rather dissimilarity measure, represents an extreme form of dimensionality reduction to a single value with respect to a predefined reference. As I explained in section 2.2.1, each full-field analysis may be reduced to a manageable number of characteristic modes, but in turn details are smeared out and each such comparative analysis leads to loss of information. However, since the investigations carried out are aimed precisely at resolving details under parameter variation, I am following a two-track approach in the presentation of the results of the parameter study. Next to the Hausdorff distance evolution, I show for each dimension of the parameter space additionally selected field quantities, such as those presented in figure 6.4 to figure 6.8 for the reference experiment. Based on that representative local evaluation data combined with the ex situ and in situ integral measures, I deduce the final results for the varied parameter at hand.

6.2.1 Cutting Clearance Variation

The conducted four additional cutting clearances are 2.5%, 6.0%, 12.5%, and 15%. The reference value is 10%. Figure 6.9 summarizes the resulting cut surface characteristics. Figure 6.10 shows the integral in situ measurements together with the Hausdorff distance computations at the evaluation points A, B, C, and D. The classical ex situ and in situ measurement parameters behave in the same way as described in section 2.4.1 when the cutting clearance is varied. A reduction of the cutting clearance reduces the edge draw-in as well as the burr height and in return increases the clean-shear share, see figure 6.9. The maximum cutting forces F increase, see figure 6.10 a). For larger cutting clearances, the classical measures react in the opposite direction. In the illustration of the Hausdorff distances, in figure 6.10 c), d), and e), all three tests are included in the form of an error bar. The outer ends represent the maximum and minimum values, respectively. The point which is included in the polyline represents the third attempt.[5] The horizontal displacements u_1, shown in figure 6.10 c), display the highest values consistently for 2.5% cutting clearance, followed by the other end of the parameter space at 15%. Overall, the differences in the horizontal movements appear comparatively stable over time, also with regard to crack propagation. The vertical displacements u_2, on the other hand, approach each other from point A to point D. Hence, the influence of the cutting clearance becomes smaller with increased punch penetration depth. This trend ends with crack propagation, which, analogous to the horizontal displacement, does not show any distinct trend. The local movement complexity, expressed by the Hausdorff distance of the normalized motion curl c draws a less clear picture. In the area prior to crack initiation, point A to point D, all cutting clearance variants show similar differences in motion complexity to the reference. In the case of crack propagation, the motion complexity for the 2.5% cutting clearance shows comparatively high values.

For the local analysis of the cutting clearance variation for closed cutting lines, I evaluate the sheet metal deformation behavior. For illustration purposes I use the representation of the Green strain tensor components of the configuration with 15% cutting clearance, since this configuration exhibits a changed deformation pattern in vertical direction that is not directly reflected through the characteristics of the integral measurement values. I have not changed the color scales of the individual representations compared to figure 6.5 for comparability reasons.

The Green strain tensor component E_{11} basic characteristic does not change, see figure 6.11 a). Due to the larger cutting clearance and, hence, resulting change in process kinematics, the axis of the deformation band includes a larger angle to the vertical x_2-axis. At point B the strain

---

[5]I would like to point out that the magnitude of the error bars justify the use of the Hausdorff distance as an evaluation measure.
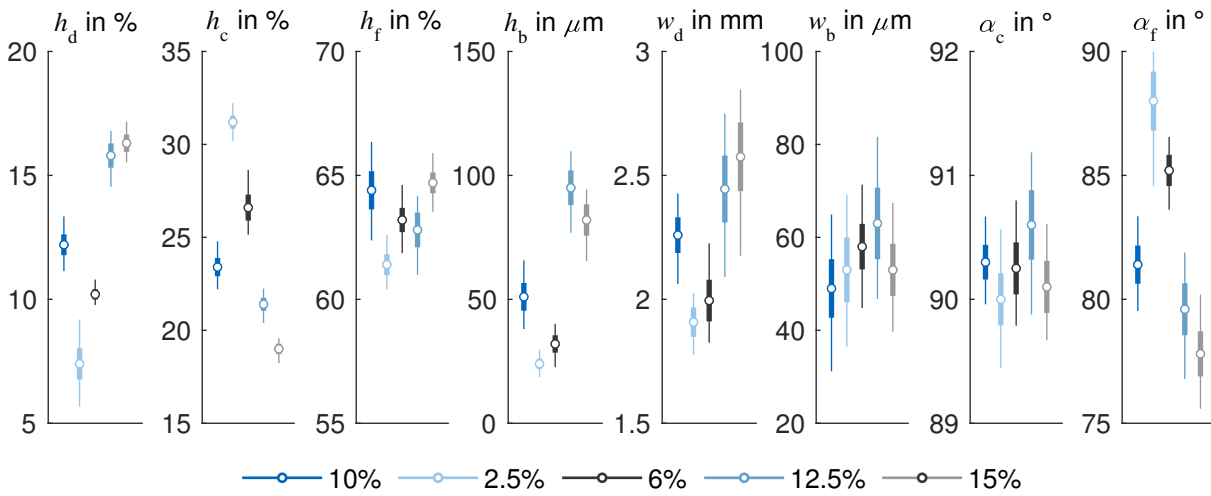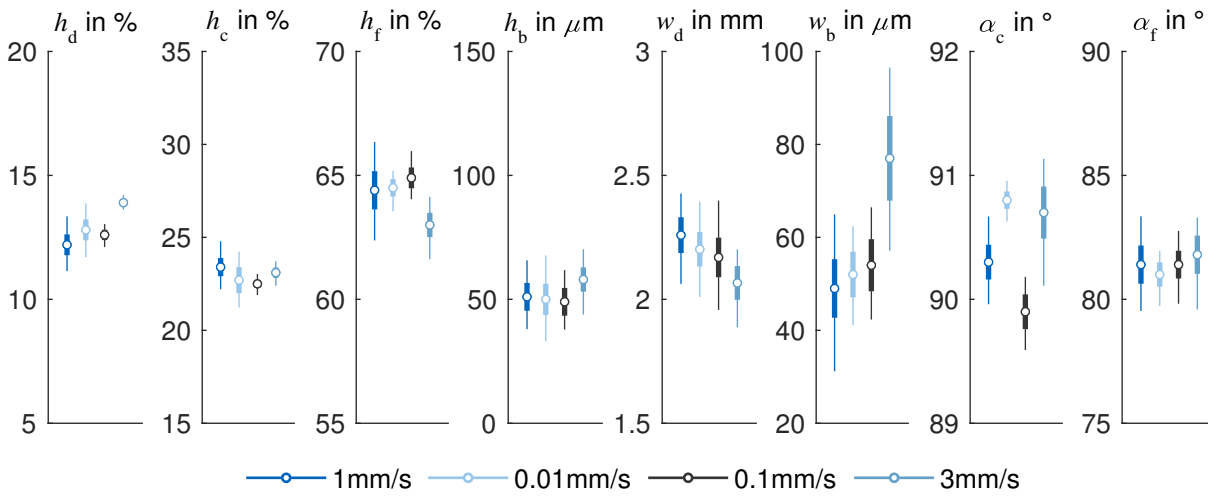
Figure 6.9: Cutting clearance c_c variation cut surface characteristics for closed cutting line experiments. (circle: mean, bold line: standard deviation, fine line: minimum and maximum based on 15 measurements)

distribution homogenizes for increasing cutting clearances and the affected zones in the edge draw-in area expand. Analogous to the observation based on the Hausdorff distance of the horizontal material flow, the horizontal deformation patterns in point C and point D converge, especially in the highly localized areas. The affected zone of moderate horizontal deformation grows before motion instability occurs. The green strain tensor component E_{12} also shows similar patterns compared to the reference experiment, see figure 6.11 b). In addition to the angular change, the deformation band widens in favor of less localization, which can be clearly seen from the shortened peaks of the contour lines. As a result, the maximum achieved equivalent strains also shrink before crack initiation, but the shear strain increases to a maximum of 2.00 with significantly decreasing maximum horizontal strains of 6.40. The most significant change in the local deformation behavior is shown in the horizontal component of the green strain tensor E_{22}, see figure 6.11 c). In the upper and lower surface-near fibers of the sheet metal, regions are formed in the edge draw-in area, which show an opposite sign. This deformation mode does not occur for the other cutting clearance variants. Between 12.5% and 15% cutting clearance, a point is reached which changes the process geometry in such a way that the edge regions in particular experience changed loading conditions. This constellation occurs early in the process, which becomes clear in point B. At point C and point D, the deformation pattern is broken by a negative strain island on the punch side on the free sheet surface in the draw-in area. On the clamped side of the sheet metal, the deformation state remains unchanged. At point C and point D the area of negative vertical strains stands out much more than in the reference experiment. Especially point D shows much higher absolute values along the axis of the deformation band, with values up to 1.09 compared to 0.65 in the reference experiment.
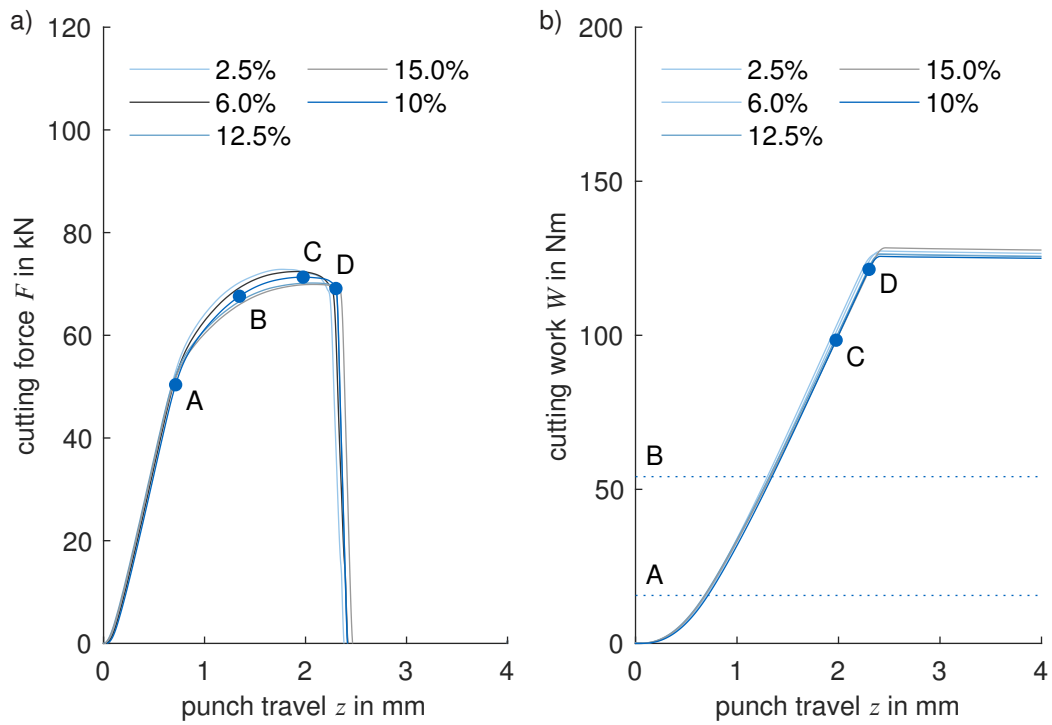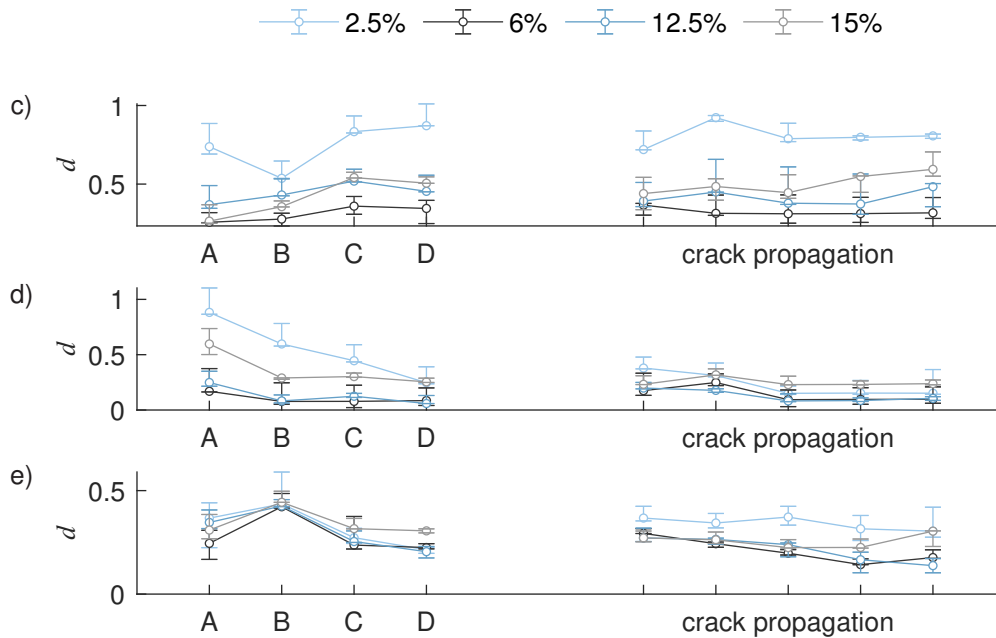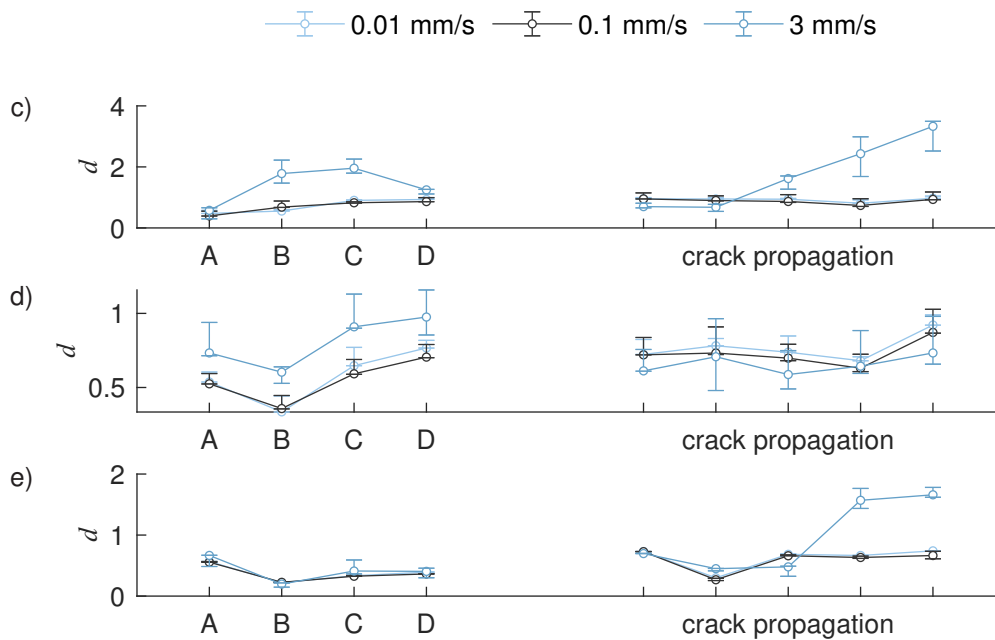
Figure 6.10: In situ data for cutting clearance variation experiments with closed cutting line: a) cutting force F vs. punch travel z curve. b) cutting work W vs. punch travel z curve. Hausdorff distance d of the motion fields from three tests (error bar) to the reference: c) u_1, d) u_2, e) normalized motion curl c.

point A   point B   point C   point D

a) x_1 Green strain tensor component

b) shear Green strain tensor component

c) x_2 Green strain tensor component
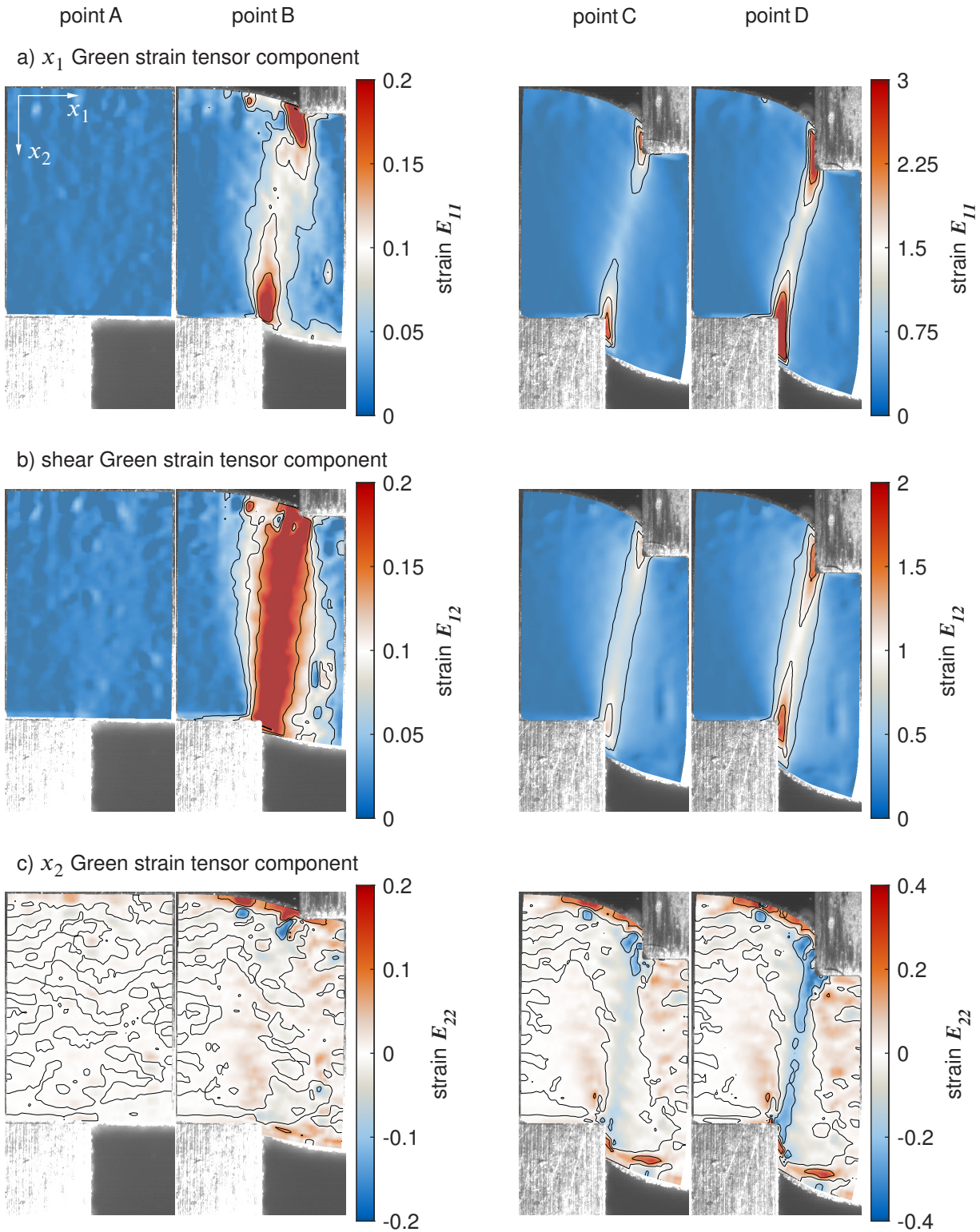
Figure 6.11: Green strain tensor fields of the closed cutting line experiment with 15% clearance at the time A, B, C, and D. a) x_1 Green strain component E_{11} b) shear Green strain component E_{12} c) x_2 Green strain component E_{22}.

6.2.2 Blade Edge Variation

The conducted eight additional blade edge pairings include all permutations from $>20\,\mu$m, $50\,\mu$m, and $70\,\mu$m blade edge roundings. The reference pair has a $r_\mathrm{d} = 50\,\mu$m radius at the die edge and a $r_\mathrm{p} = 50\,\mu$m radius at the punch edge, as listed in the first column of figure 6.12 that summarizes the resulting cut surface characteristics. Figure 6.13 shows the integral in situ measurements together with the Hausdorff distance computations at the evaluation points A, B, C, and D. The classical in situ and ex situ measures follow the tendencies, which I have described in section 2.4.1, when cutting edge geometry is varied. For identical cutting edge geometry at the die and the punch, smaller edge rounding results in less edge draw-in, less clean-shear share, and reduced burr height. A larger edge rounding has the opposite effect, as illustrated in figure 6.12. The permutations basically react according to the same principle at the respective cutting edge. But changed geometric conditions in the cutting clearance follow and yield different deformation behavior and in particular crack behavior. Within the covered parameter spectrum I could not detect any significant influence on the cutting force curves and cutting work curves, see figure 6.13. The Hausdorff distances d of the displacement quantities u_1 and u_2 to the reference, see figure 6.13 c) and d), behave analogously throughout the shearing process until crack initiation. The Hausdorff distances d of the movement complexity c already show more strongly deviating courses. In the area of the crack propagation, larger differences become apparent and the curves diverge in value and form for all flow fields.
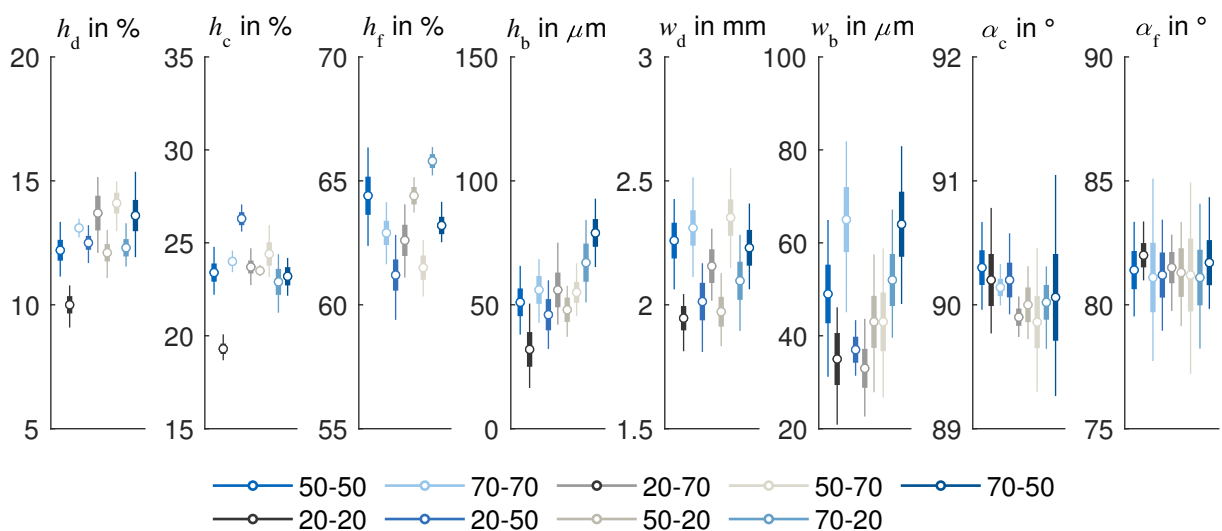
Figure 6.12: Blade edge variation r_d-r_p cut surface characteristics for closed cutting line experiments. (circle: mean, bold line: standard deviation, fine line: minimum and maximum based on 15 measurements)
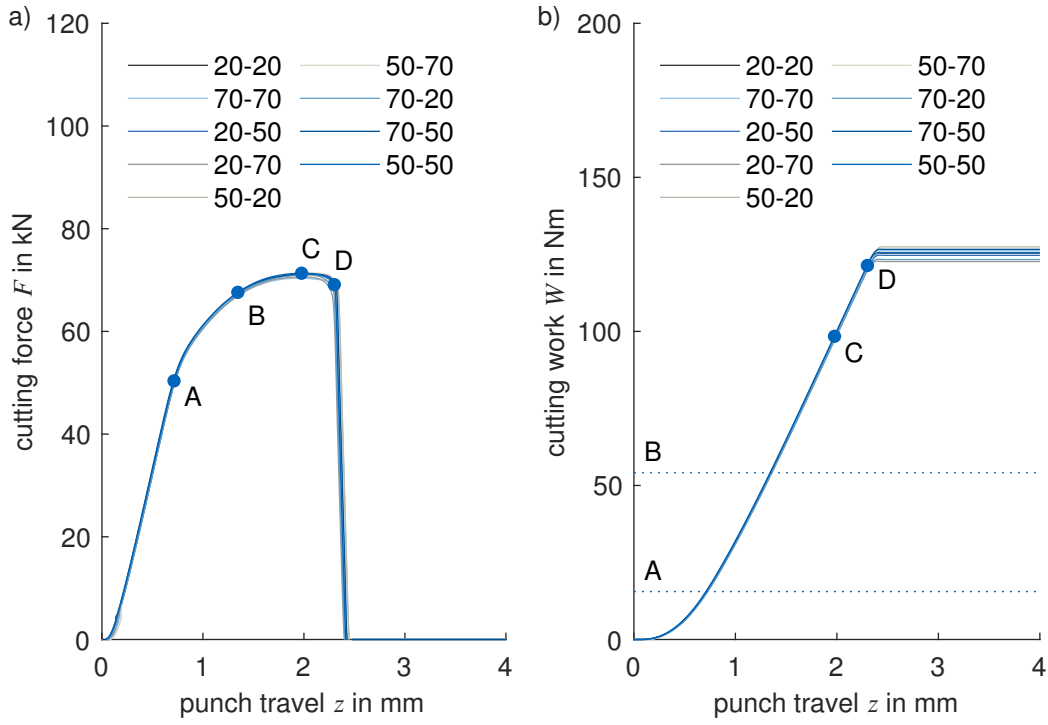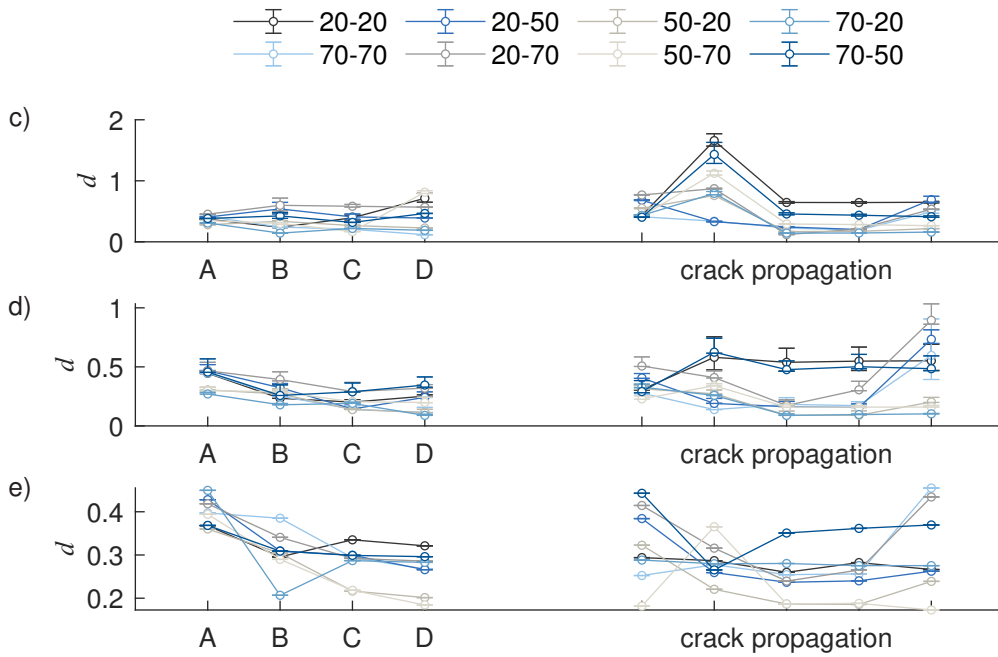
Figure 6.13: In situ data for blade edge variation experiments with closed cutting line: a) cutting force F vs. punch travel z curve. b) cutting work W vs. punch travel z curve. Hausdorff distance d of the motion fields from three test (error bar) to the reference: c) u_1, d) u_2, e) normalized motion curl c.

In the local analysis of the variation of the cutting edge geometry, I focus on crack propagation using the pairing r_d <20 μm the edge radius and r_p =70 μm punch edge radius. The result of the analysis shows figure 6.14, which uses the combined classical and non-classical Green strain tensor components for visualization. I have not changed the color scales of the individual displays compared to the crack analysis of reference experiment in figure 6.8 for better comparability.

The configuration under consideration forces the early onset of the crack at the die, which in the first image is already clearly visible in all three Green strain tensor components. With respect to the cutting force curve, this means a clear displacement of the point D in the direction of the maximum cutting force, point C, in the case of the considered cutting edge pairing. The crack initiation at the punch does not take place immediately afterwards, as in the reference experiment, but only after Δt_c=0.3106 s. During this period, I could hardly detect any further crack propagation at the die and the crack freezes. Only when the punch crack starts to grow and appears more clearly on the punch after Δt_c, a directed propagation takes place again on the die side crack. The consolidation of both macro cracks takes place in the center of the sheet in the same way as in the reference experiment. But the shape of the crack propagation differs. If the crack still takes an approximately linear course in the reference, it runs S-shaped in the deformation band in the experiment under consideration with asymmetrically prepared cutting edges. At no time does either macro crack leave the deformation band, but it seems as if the deformation band would even guide them. The S-shaped course is a mere consequence of the entrance angle of the crack, which includes an increased angle with the x_2-axis.

Similar to the crack propagation in the reference experiment, initially, the horizontal Green strain tensor component E_{11} clearly indicates the crack in figure 6.14 a). In contrast to the reference, higher classical horizontal strain components accompany the crack at the punch and at the die, which makes the crack appear more open overall, especially around the die. The Green strain tensor component E_{12} reveals crack propagation until final material separation after Δt_c=0.4270 s, see figure 6.14 b). Analogous to the horizontal strain component, the non-classical shear strain components are accompanied by classical strain components, and this is reinforced in contrast to the reference experiment. These additional strains occur mainly at the curved sections along the crack shape. The Green strain tensor component E_{22} resolves numerous micro cracks in the sheet metal material analogous to the reference experiment. The micro cracks are also found in the experiment under consideration with asymmetrical cutting edge preparation for the largest part in the deformation band. But micro cracks also appear outside this area mainly around the die edge, where they occur at a distance of ~80μm from the upper side of the sheet metal resting on the die and run in x_1-direction.

$\Delta t_{\mathrm{c}} = 0\,\mathrm{s}$ $\Delta t_{\mathrm{c}} = 0.4263\,\mathrm{s}$ $\Delta t_{\mathrm{c}} = 0.4265\,\mathrm{s}$ $\Delta t_{\mathrm{c}} = 0.4268\,\mathrm{s}$ $\Delta t_{\mathrm{c}} = 0.4270\,\mathrm{s}$

a) x_1 Green strain tensor component
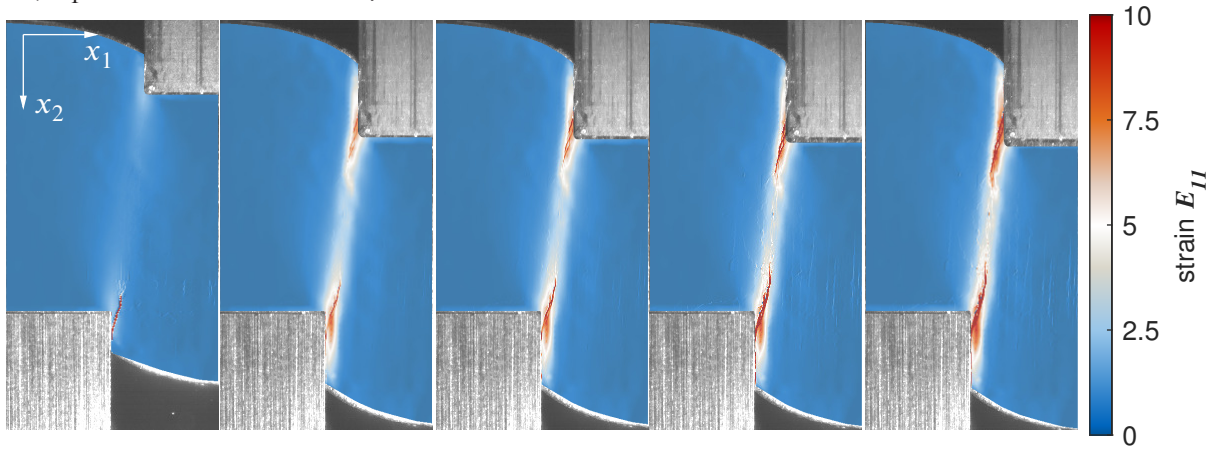
b) shear Green strain tensor component
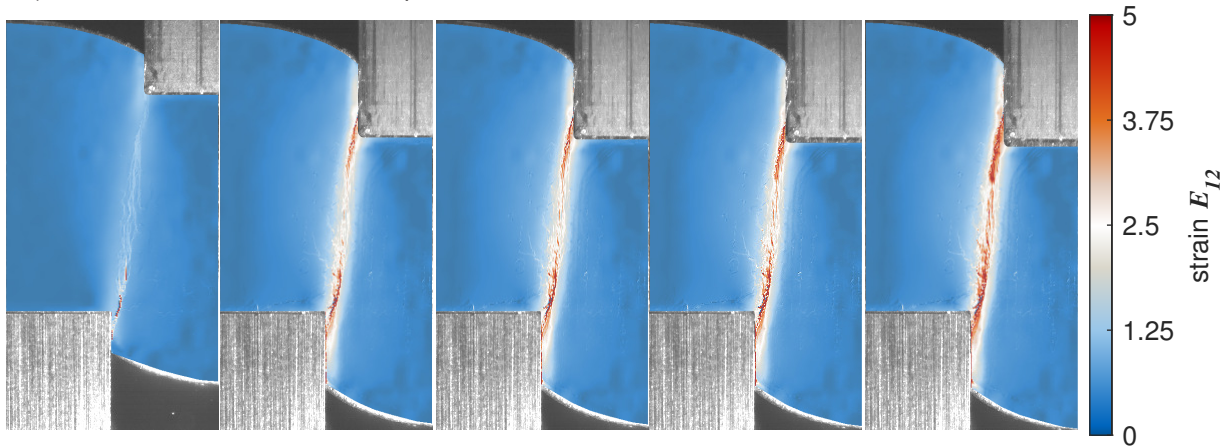
c) x_2 Green strain tensor component
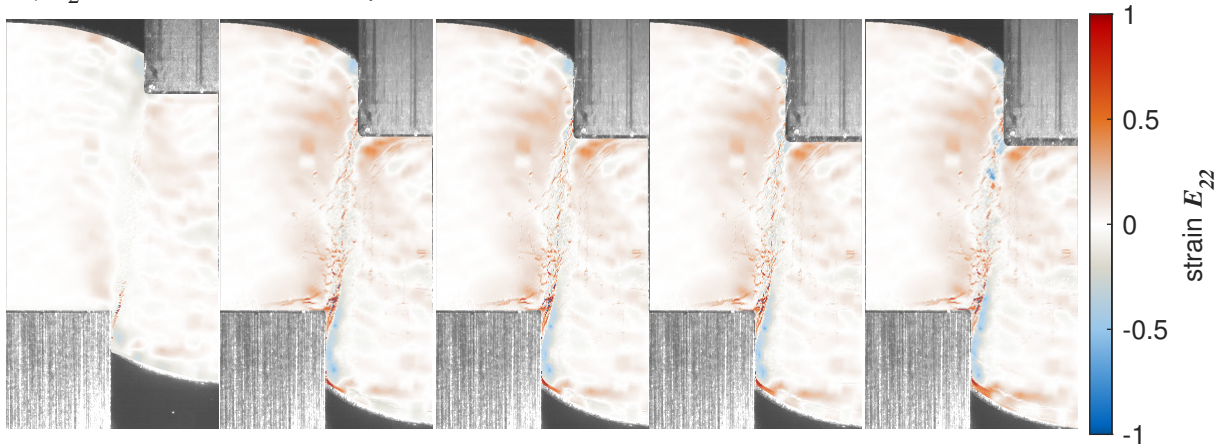
Figure 6.14: Green strain tensor fields of the close cutting line experiment with <20 μm die and 70 μm punch edge radius at the time A, B, C, and D. a) x_1 Green strain component E_{11} b) shear Green strain component E_{12} c) x_2 Green strain component E_{22}.

6.2.3 Cutting Velocity Variation

The conducted four additional cutting velocities v_c are 0.01 mm/s, 0.1 mm/s, and 3 mm/s. The reference value is 1 mm/s. Figure 6.16 shows the integral in situ measurements together with the Hausdorff distance computations at the evaluation points A, B, C, and D. The classical ex situ and in situ evaluation quantities confirm the observations listed in section 2.4.1 with respect to their cutting velocity dependence. Within the scope of measurement accuracy and process reproducibility, the cut surface characteristics presented in figure 6.15 do not show any significant differences. The cutting force curves and cutting work curves, on the other hand, have changed due to the rate-dependent material behavior, as shown in figure 6.16 a) and b). Lower cutting velocities result in lower maximum forces and less cutting work. At least for the low punch speed of 0.01 mm/s isothermal conditions may be assumed, since the heat generated by dissipation during irreversible deformation process can be conducted entirely, see section 2.1.2. Here, strain rate and temperature effects may be excluded. Figure 6.16 c), d), and e) show that the Hausdorff distance d of the material flow fields takes approximately identical courses for the two quasi-static shear cutting tests with 0.01 mm/s and 0.1 mm/s cutting speed.[6] The increased cutting velocity compared to the reference shows stronger deviations especially for the vertical and horizontal displacements, whereas the movement complexity stays at a constant level with the two quasi-static experiments. If the basic characteristics of the curve for the vertical displacements remain the same, the shape of the vertical displacement changes in point B and point C. Further, the scatter in the two quasi-static experiments presents much lower compared to the 3 mm/s experiment. Concerning the crack behavior, motion complexity additionally shows a discrepancy between slow and increased punch velocities, especially short before material separation.

Based on the experiment with 3 mm/s punch velocity I show the changes of the local process dynamics during shearing for the closed cutting line. The calculated fields of the Green strain rate tensor are shown in figure 6.17. Since the value changes are very extreme compared to the reference, I had to change the color scales of the individual displays compared to figure 6.7. The basic characteristics of the strain rate fields are preserved, especially the spatial extent of the dynamic deformation zone. The strain rate fields present more homogeneous, even in point A and point B for the horizontal and shear tensor components. In this sense, the increase in speed compared to the reference stabilizes the local dynamic deformation. The vertical local dynamic deformation pattern contains an identical scatter with regard to the present order of magnitude compared to the reference experiment. However, vertical deformation concentrates more on the

---

[6]I would like to point out at this point that this behavior of the Hausdorff distance curves is not an unequivocal proof that the similarity also applies to the fields themselves, but can only be taken as an indication.

Figure 6.15: Cutting velocity v_c variation cut surface characteristics for closed cutting line experiments. (circle: mean, bold line: standard deviation, fine line: minimum and maximum based on 15 measurements)

cutting clearance region, which yields also a lenticular deformation band, especially in point C. In general, the strain rates precede the strains, as in the reference experiment. Already with the transition to irreversible deformation in point A the shear zone of influence forms and is clearly visible. In the present test, the maximum force practically coincides with crack initiation, which is why point C and point D almost match. Therefore, around the point of motion instability, point C, already strain rates arise, which are at the level of the strain rates at crack initiation in point D. This holds for all Green strain rate components.

The Green strain rate tensor component $\dot{E}_{11}$, shown in figure 6.17 a) has maximum values of $36.11\,\mathrm{s}^{-1}$ at the punch lateral surface in point C and maximum values of $36.09\,\mathrm{s}^{-1}$ in point D. Also the hourglass shape of the deformation band does not change anymore between these two times. The shear strain rates also saturate with the onset of motion instability and the shape of the shear band persists. In point C $9.09\,\mathrm{s}^{-1}$ are reached, in point D $8.82\,\mathrm{s}^{-1}$ each at the lateral surface of the punch. The Green strain rate tensor component $\dot{E}_{22}$ obtains maximum absolute values of 2.1. Thus, the tripling of the cutting speed in relation to the maximum strain rates is approximately linear between the reference experiment and the conducted experiment.

The extreme changes in local dynamics do result in significant differences in the classical integral measurands. Even though the Hausdorff distance d with respect to the vertical displacements fields, which, after changed behavior, strive back to lower values, still in point D the Green strain tensor component fields presents different to the reference experiment. The local deformation behavior in the shear zone gives higher maximum strain values especially in the localized area around the blade edges, as shown in figure 6.18.
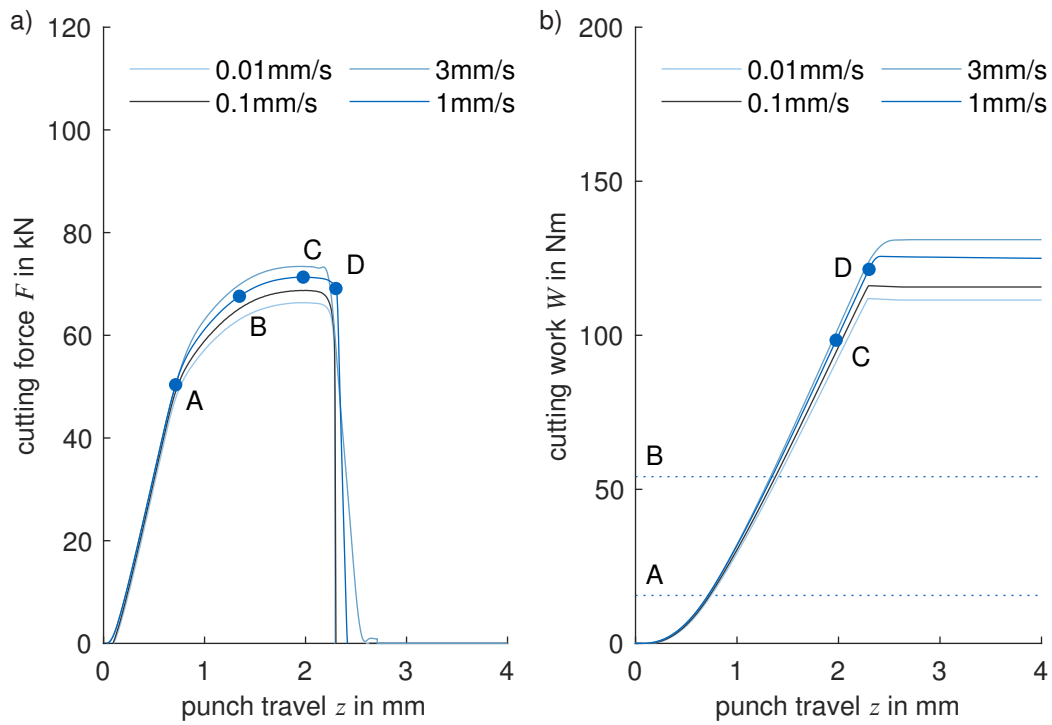
Figure 6.16: *In situ data for cutting velocity variation experiments with closed cutting line: a) cutting force F vs. punch travel z curve. b) cutting work W vs. punch travel z curve. Hausdorff distance d of the motion fields from three test (error bar) to the reference: c) u_1, d) u_2, e) normalized motion curl c.*
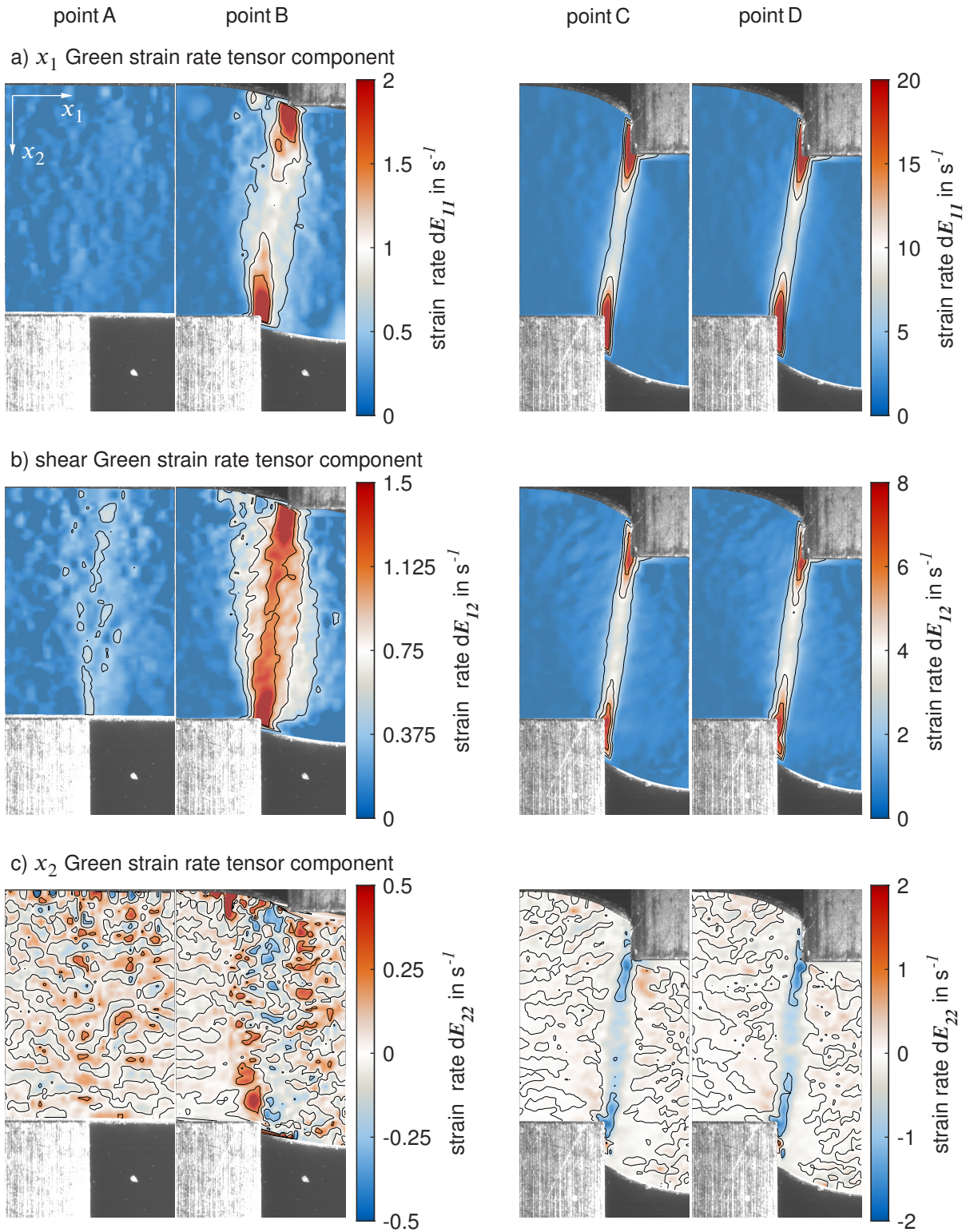
Figure 6.17: Strain rate tensor fields of the closed cutting line experiment with 3 mm/s at the time A, B, C, and D. a) x_1 Strain rate component $\dot{E}_{11} = dE_{11}$ b) shear Strain rate component $\dot{E}_{12} = dE_{12}$ c) x_2 Strain rate component $\dot{E}_{22} = dE_{22}$.
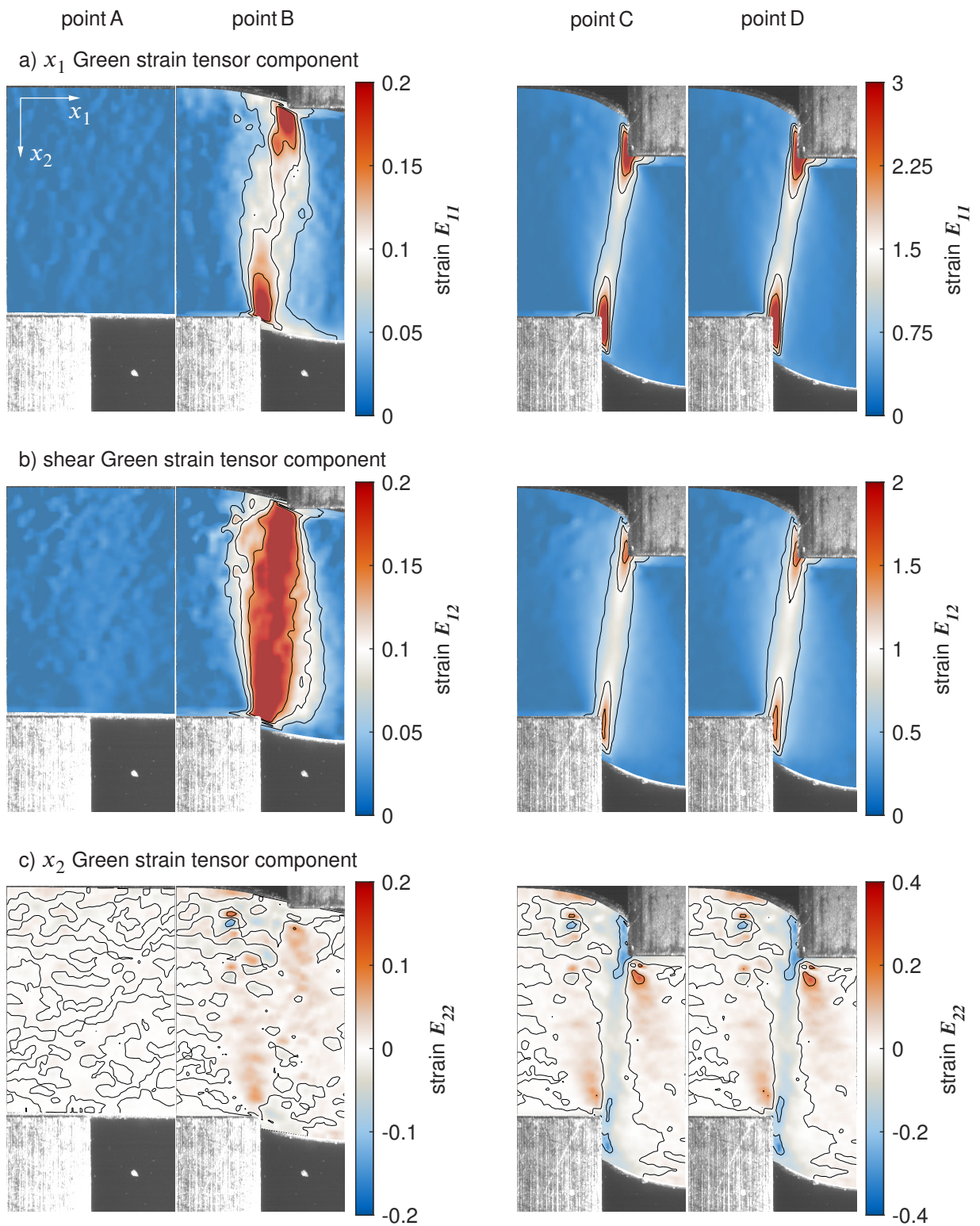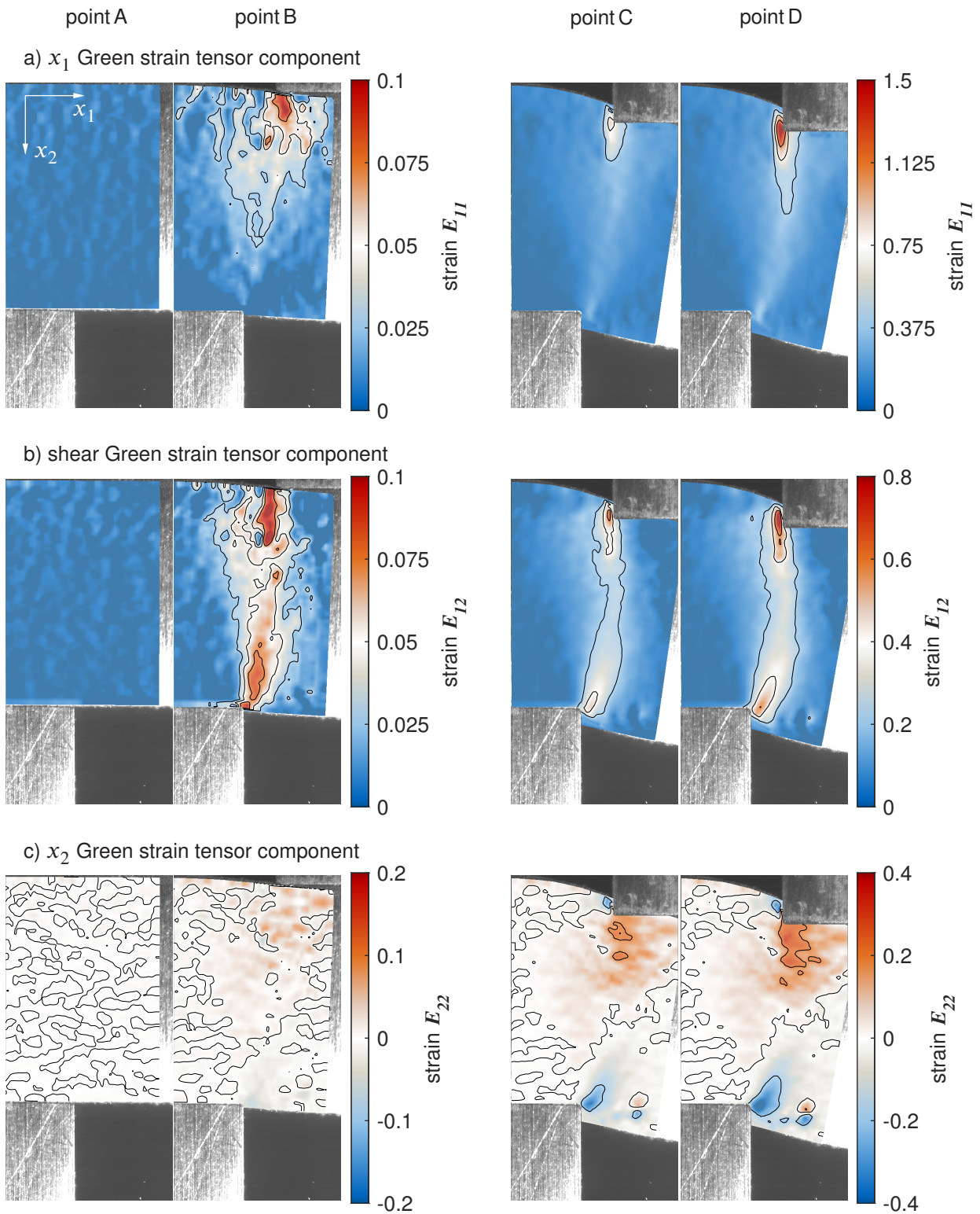
Figure 6.18: Green strain tensor fields of the closed cutting line experiment with 3 mm/s at the time A, B, C, and D. a) x_1 Green strain component E_{11} b) shear Green strain component E_{12} c) x_2 Green strain component E_{22}.

6.2.4 Aluminum

I conducted aluminum EN AW A5083 sheet metal with a thickness of $s = 4\,\text{mm}$ to vary the processed material. For the aluminum material, I focused on cutting clearance and analyzed 2.5%, 6.0%, 10%, 12.5%, and 15%. Figure 6.19 summarizes the resulting cut surface characteristics using the different cutting clearances. Figure 6.20 shows the integral in situ measurements together with the Hausdorff distance computations at the evaluation points A, B, C, and D. The reference value for the Hausdorff computations is the aluminum experiment with 10% cutting clearance. As for the S355MC sheet metal, the classical ex situ and in situ measurement parameters behave as expected from section 2.4.1 for cutting clearance variation. Smaller cutting clearances lead to reduced edge draw-in and burr height. The clean-shear share increases, see figure 6.19. As figure 6.20 a) indicates, the maximum cutting forces F increase. Larger cutting clearances obtain contrary behavior for the classical measures . The Hausdorff distances d of the horizontal displacements u_1, shown in figure 6.20 c), display the highest values consistently for the two small cutting clearances with 2.5% and 6% before crack initiation. Afterwards ongoing crack propagation shows larger Hausdorff distances for the two larger cutting clearances. The vertical displacements u_2 draw a similar picture between point A to point D. During crack propagation the Hausdorff distances also diverge for the vertical displacements u_2. The Hausdorff distance of the normalized motion curl c yields no trend for motion complexity development, but shows an almost constant evolution prior to crack initiation for all cutting clearance variants. Motion complexity splits more during crack propagation, where the cutting clearances 2.5% and 15%, show the highest deviations. Compared to the reference material, aluminum EN AW A5083 has a smaller deformation range, which promotes the similarity of the Hausdorff distance values prior to crack propagation and a more diverse behavior when the cracks propagate through the sheet metal.

For the presentation of the local deformation differences, when cutting clearance is varied for aluminum, I show the results for the experiment with 10% cutting clearance, see figure 6.21, and 2.5% cutting clearance, see figure 6.22. The results of the experiment with 10% cutting clearance further allow a direct comparison of the materials with respect to the reference configuration of the process parameters. The deformation behavior is shown using the fields of the Green strain tensor components using an adapted color scale compared to the reference figure 6.5. For the green strain tensor component E_{11}, both experiments have basically the same deformation pattern, as figure 6.21 a) and figure 6.22 a) show. Analogous to the steel material S355MC, material deformation localizes in point B near the two cutting edges. Not only from the experiment for 10% cutting clearance, but also recognizable for 2.5% cutting clearance, the shape of the deformation zone of the horizontal strains changes for the material EN AW A5083.
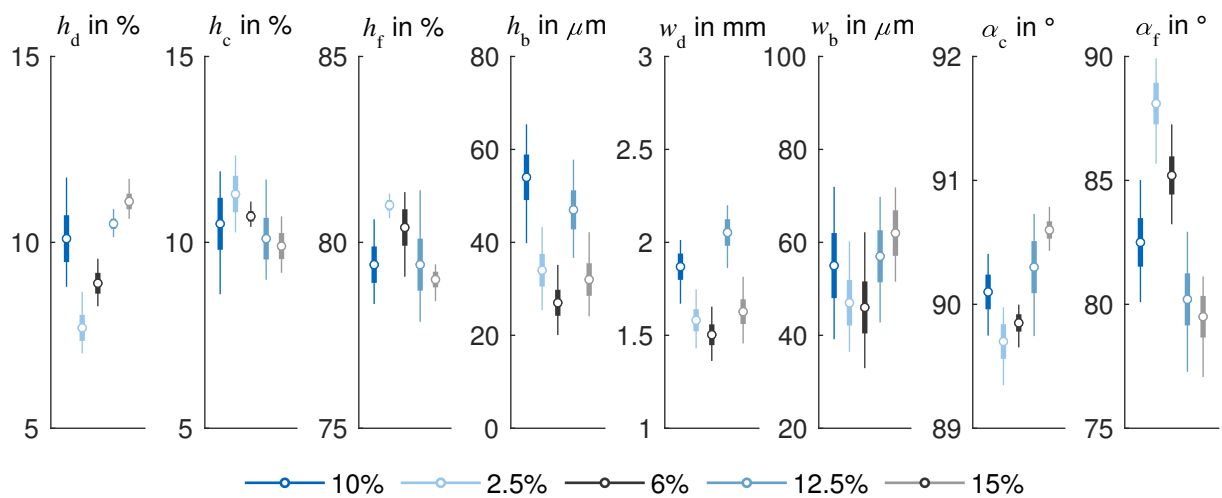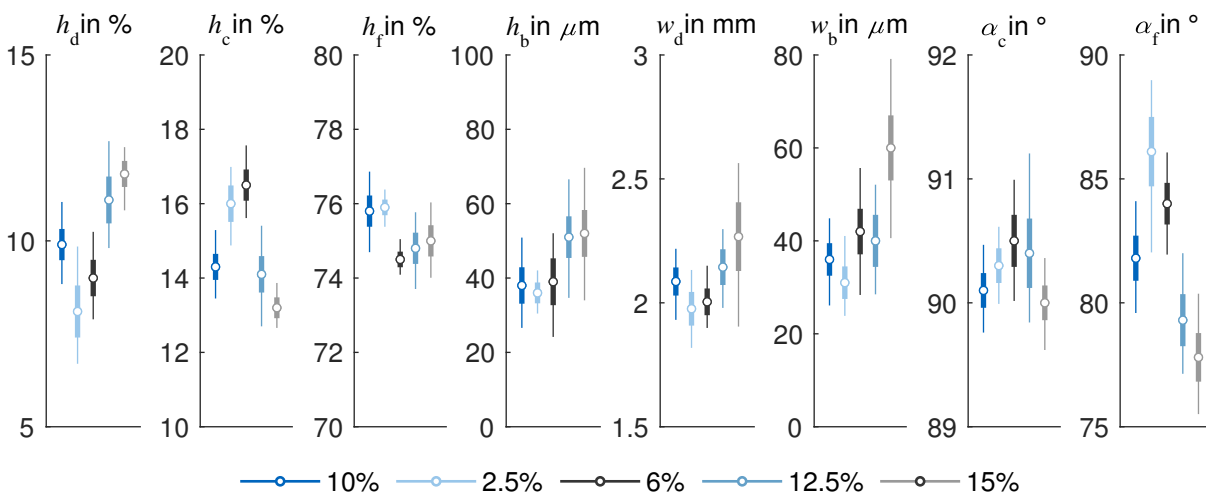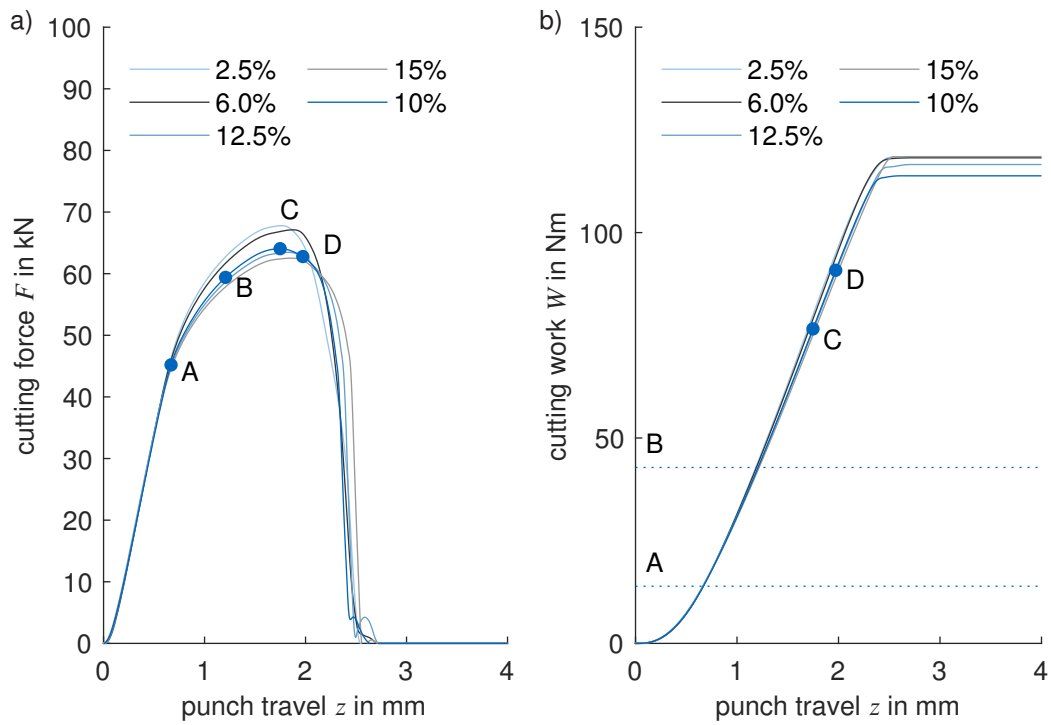
Figure 6.19: Cutting clearance c_c variation cut surface characteristics for closed cutting line aluminum experiments. (circle: mean, bold line: standard deviation, fine line: minimum and maximum based on 15 measurements)

The lenticular deformation band becomes curved and additionally follows an S-shaped axis. The entrance angles of the strain localization zones are practically parallel to the x_2 axis for both 10% cutting clearance and 2.5% cutting clearance. The aluminum sheet metal shows increasing strain localization at point C and point D. The deformation band becomes narrower for smaller die clearances and the maximum horizontal strains increase for the aluminum material from 1.78 at 10% die clearance to 3.19 at 2.5% die clearance at the punch edge. The shear strains in figure 6.21 b) and figure 6.22 b), also show strain localization along an S-shaped axis between the cutting edges. In contrast to the S355MC steel material, the deformation band is also more upright for the shear components and runs approximately vertically upwards in the center of the cutting clearance as soon as the curved sections are left. The deformation band becomes narrower for smaller cutting clearances and localization grows stronger. For 10% cutting clearance the maximum shear strain values are 1.00, for 2.5% cutting clearance 1.36, in each case at the punch lateral surface. The strains in the vertical direction in figure 6.21 c) and figure 6.22 c), in contrast to steel material, distribute more evenly and appear significantly more homogeneous. For 10% cutting clearance, a corridor of negative vertical strains forms in the cutting clearance, analogous to the steel material observations, see reference figure 6.5. This formation process takes place posterior compared to the steel material, e.g. the consolidation of the two negative vertical strain branches in the cutting clearance occur only shortly before crack initiation in point D, see figure 6.21 c). For the experiment with 2.5% cutting clearance, the negative strain components in the cutting clearance are not combined at all, see figure 6.22 c). At point D, minimum and maximum strain values of -0.20 and 0.32 for 10% blade clearance and -0.49 and 0.25 for 2.5% blade clearance are achieved.
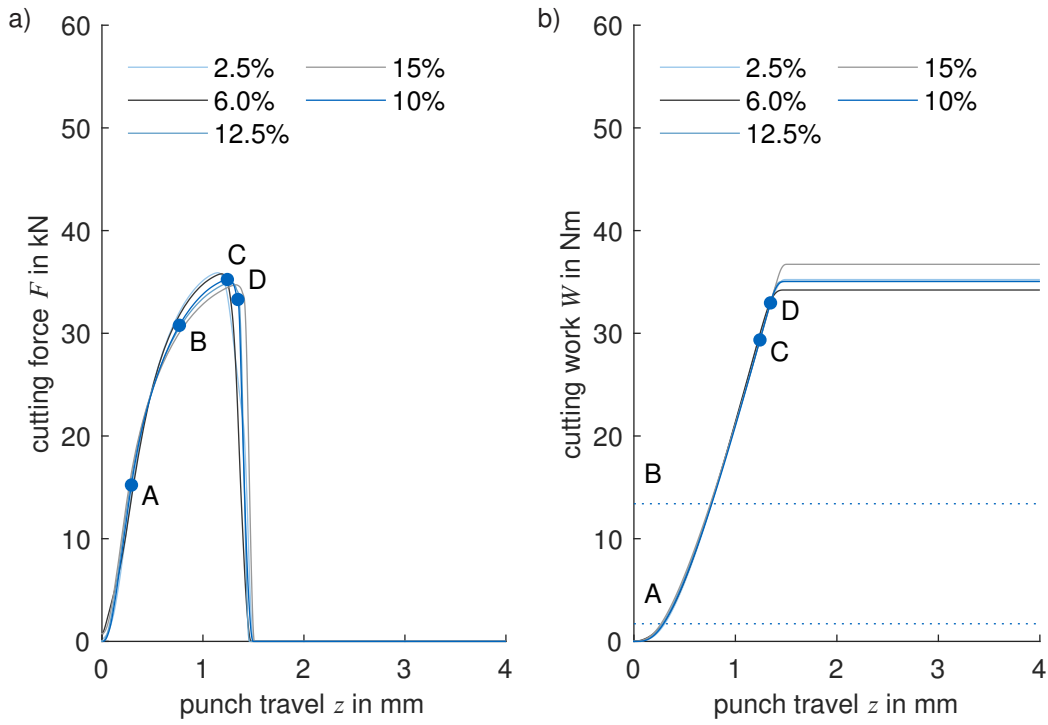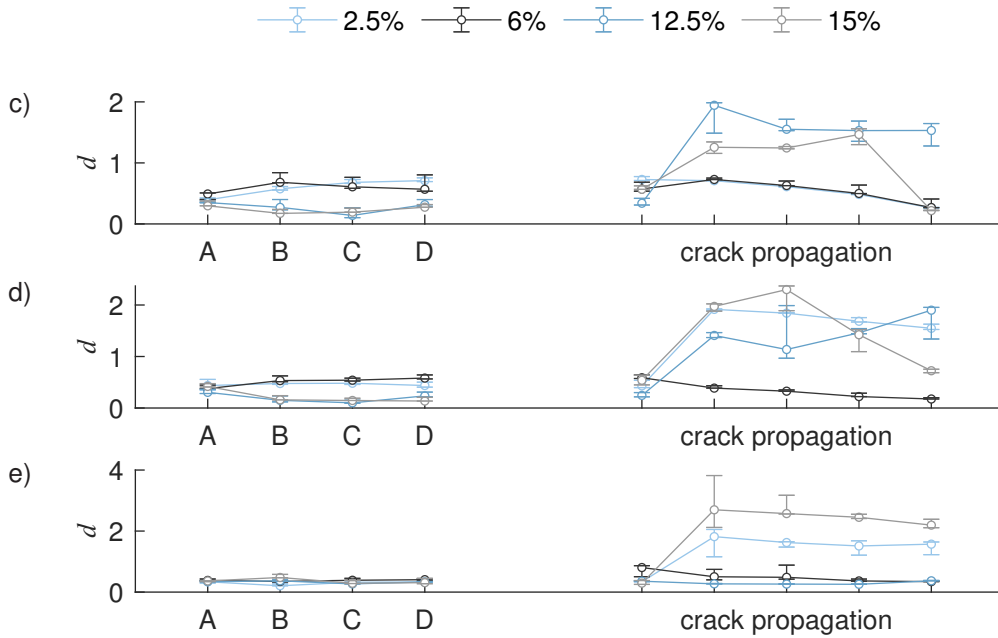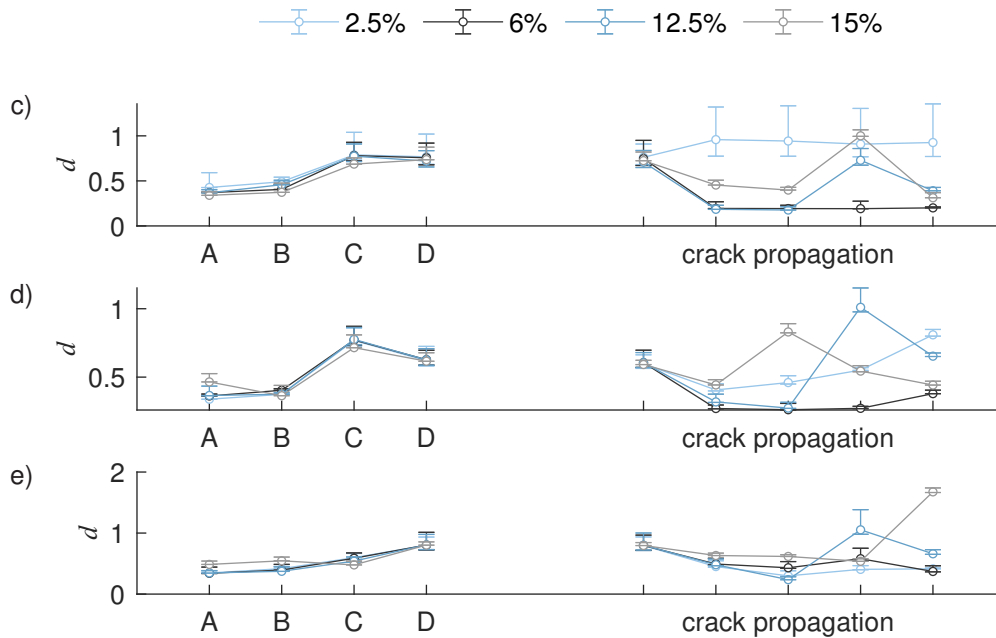
Figure 6.20: *In situ data for cutting clearance variation aluminum experiments with closed cutting line: a) cutting force F vs. punch travel z curve. b) cutting work W vs. punch travel z curve. Hausdorff distance d of the motion fields from three tests (error bar) to the aluminum reference: c) u_1, d) u_2, e) normalized motion curl c.*
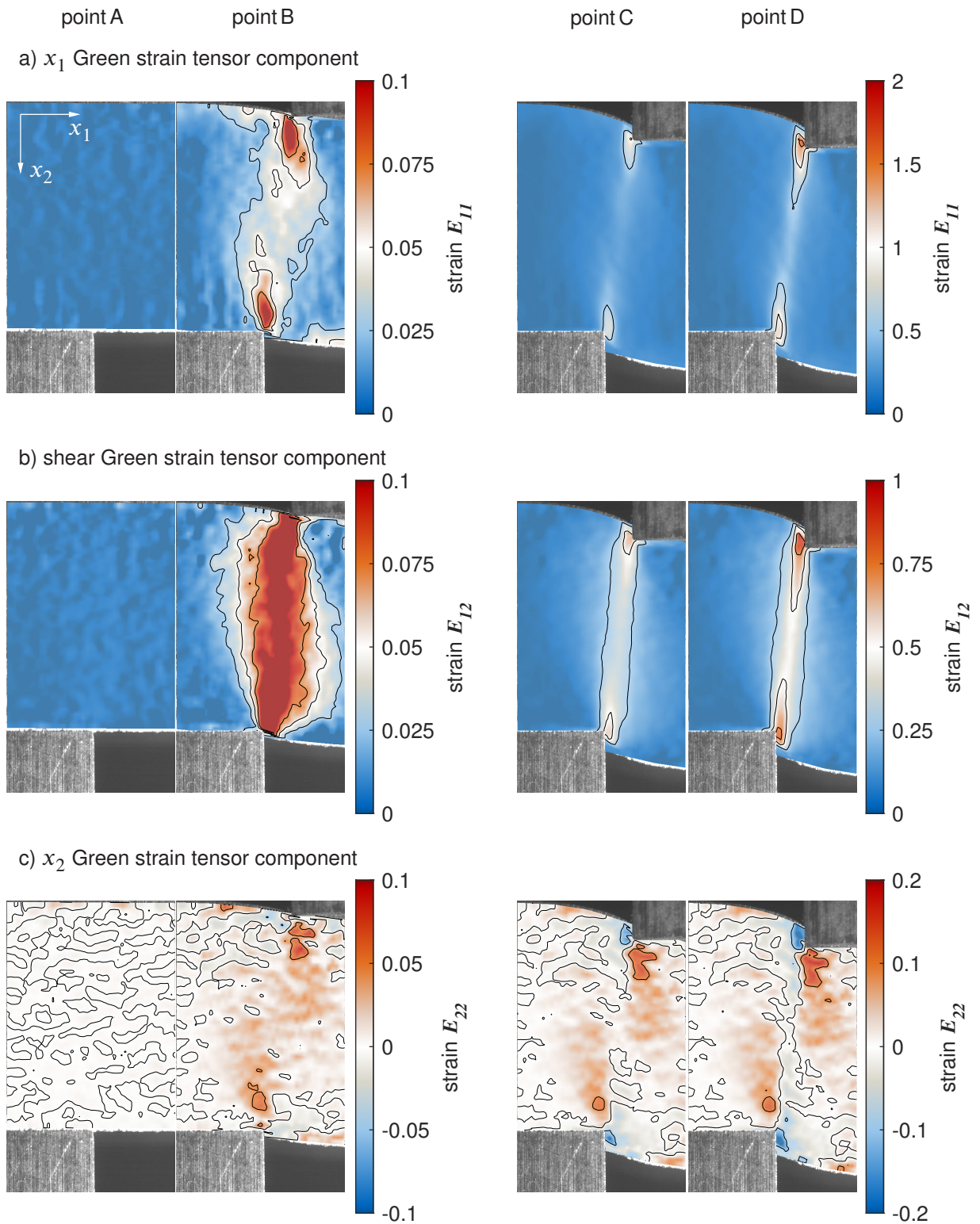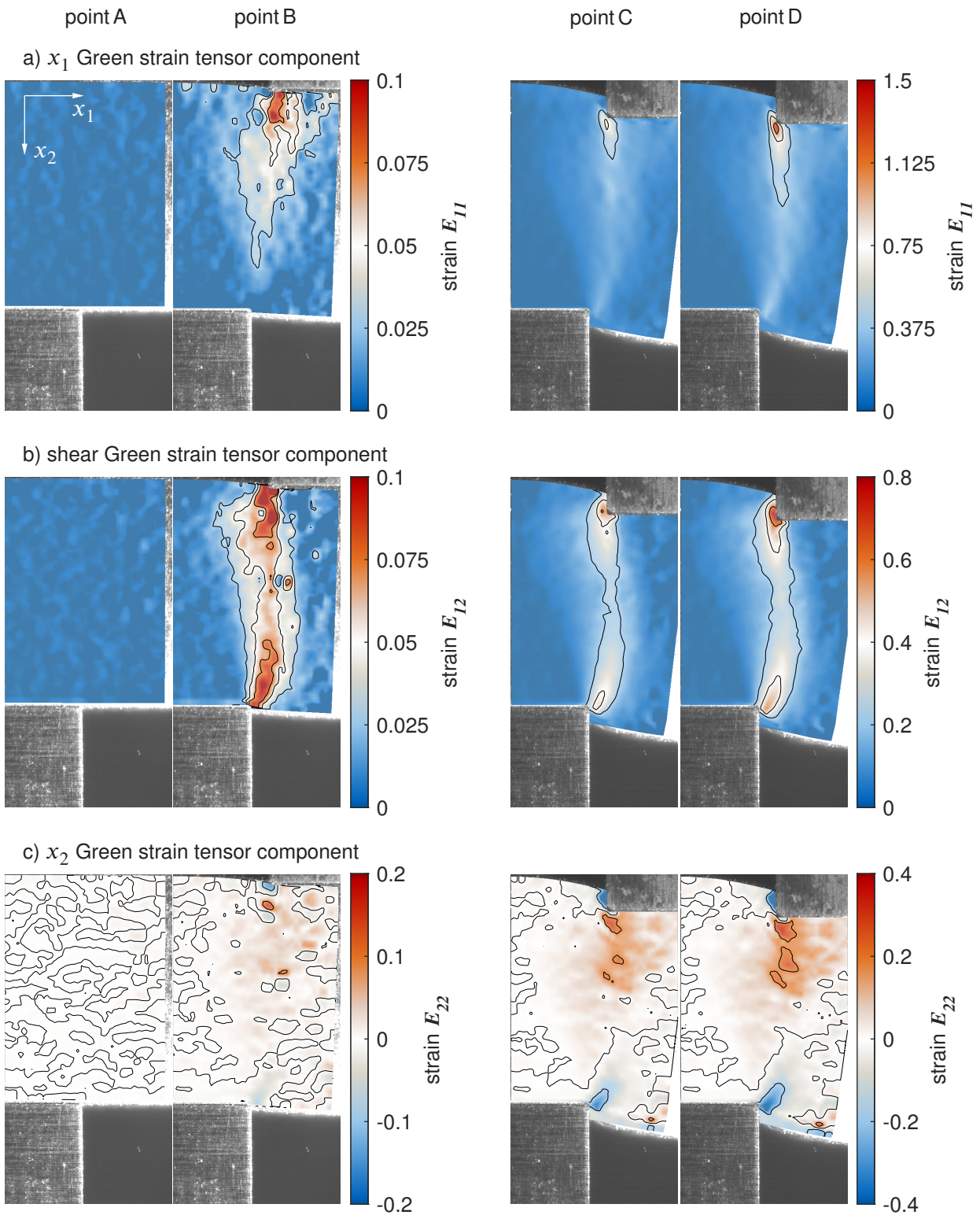
Figure 6.21: *Green strain tensor fields of the aluminum experiment with 10% cutting clearance and closed cutting line at the time A, B, C, and D. a) x_1 Green strain component E_{11} b) shear Green strain component E_{12} c) x_2 Green strain component E_{22}.*
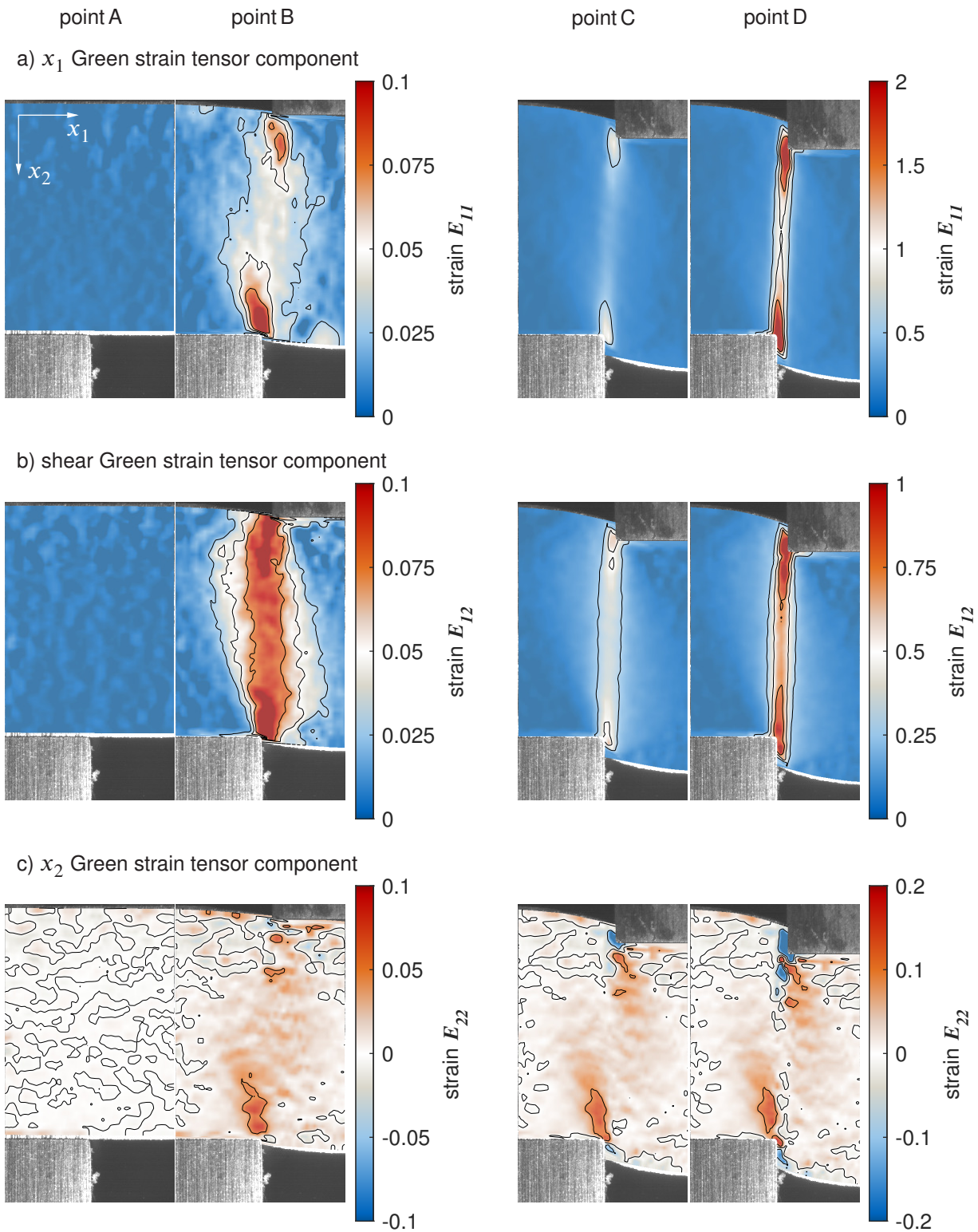
Figure 6.22: Green strain tensor fields of the aluminum experiment with 2.5% cutting clearance and closed cutting line at the time A, B, C, and D. a) x_1 Green strain component E_{11} b) shear Green strain component E_{12} c) x_2 Green strain component E_{22}.

6.3 Open Cutting Line

The experimental investigations on open cutting lines are structured in the experimental plan, see figure 4.7. For the sheet metal material S355MC with a thickness of $s = 4\,\text{mm}$, I have investigated different die clearances and cutting edge pairings from the process parameter space. Additionally, I performed tests using the reference settings for the sheet metal material EN AW A5083 with a thickness of $s = 4\,\text{mm}$. The reference process parameters, 10% cutting clearance, symmetric $50\,\mu\text{m}$ cutting edge roundings, and 1 mm/s, determine the new reference experiment for the open cutting line analysis. I again conducted S355MC as the reference sheet material. The reference values are used for the computations of the Hausdorff distances d.

When performing shear cutting with an open cutting line, motion behavior in particular on the punch side changes its characteristic compared to closed cutting lines because of the free boundary condition there. I examine the local flow, deformation, and dynamic behavior for using the experiment with 12.5% cutting clearance. The theoretical point symmetry of the closed cutting line, which of course may be disturbed by the blank holder, in case of open cutting lines, is substituted by asymmetric motion patterns in the shear zone, as shown by the flow fields in figure 6.23.

The horizontal motion pattern changes most evident by the modified boundary conditions. Significantly higher absolute values occur in the horizontal displacement fields u_1 throughout the entire shearing process, as shown in figure 6.23 a). In the open cutting line experiment, the horizontal deformation pattern did not change its characteristic over time as was the case for closed cutting lines, see figure 6.4. The vertical deformation pattern is closer related to its counterpart from closed cutting line experiments, as the comparison of figure 6.23 b) and figure 6.4 b) shows. After initial homogeneous deformation, the sheet metal remains above the die and almost does not move further in x_2 direction, whereas the material below the punch follows the shear cutting process kinematics. Due to the changed boundary conditions, the transition area of the imaginary sigmoids, which connect these two areas, changes. The saddle points of the imaginary sigmoids no longer lie on a straight line but on a double-curved line connecting the lateral surfaces of the punch and the die. The motion complexity also clearly reflects the change in the boundary condition. Already in point B the material flow indicators show its asymmetry between motion over the die and motion under the punch. Increased motion complexity is found in particular at point C along the imaginary double-curved line of the sigmoid saddle points. With the beginning of the crack at point D, the movement complexity clearly indicates its point of origin at the front side of the punch.
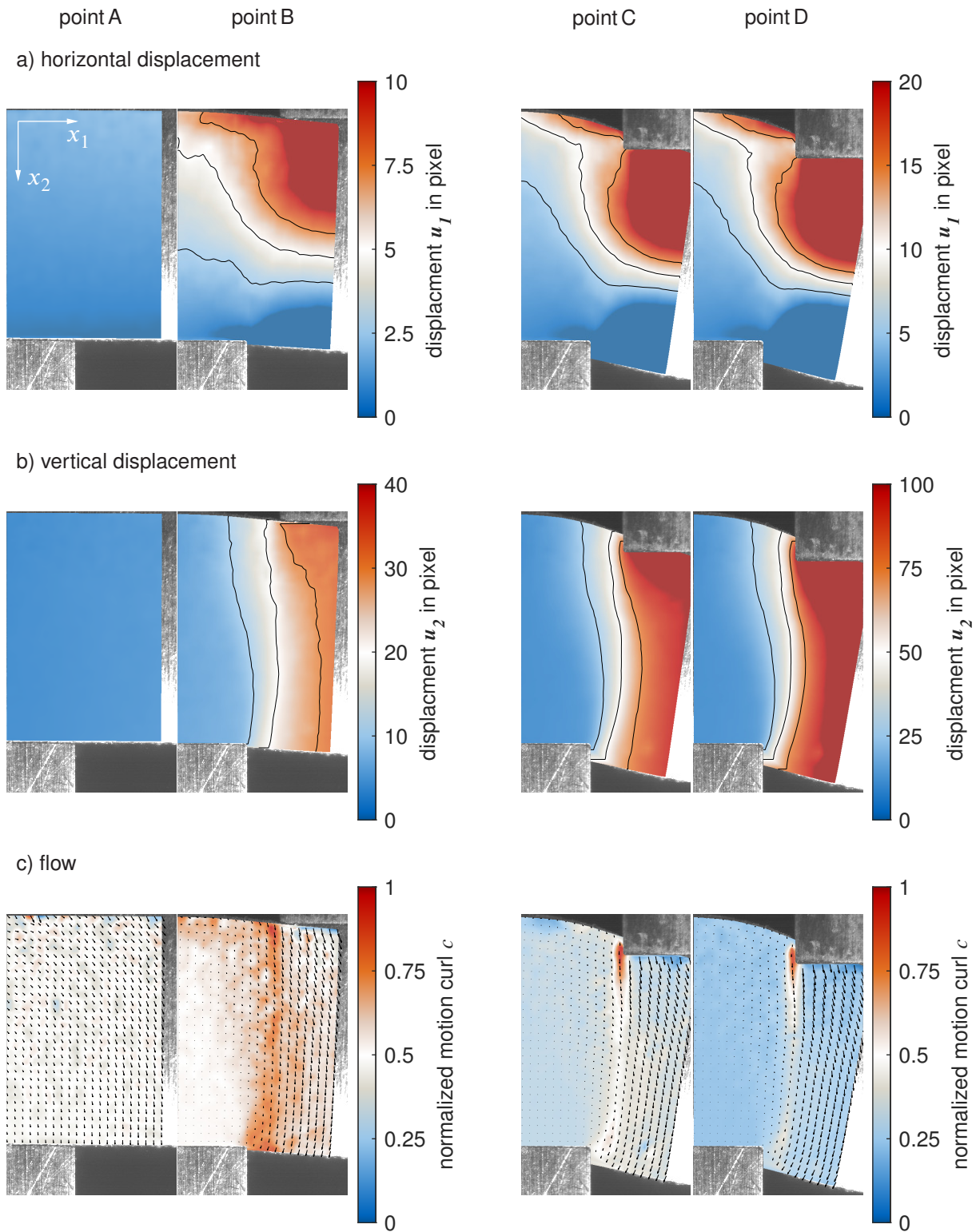
Figure 6.23: Motion fields of the open cutting line experiment with 12.5% clearance at the time A, B, C, and D. a) horizontal displacement u₁ b) vertical displacement u₂ c) normalized motion curl c and flow field indicators.

To display the local material deformation for open cutting lines, I utilize the Green strain tensor $\mathbf{E}$. Figure 6.24 shows the fields of the Green strain tensor components for the open cutting line experiment with 12.5% cutting clearance. The field E_{11}, shown in figure 6.5 a), draws a fundamentally different deformation pattern than for closed cutting lines. The reversible deformations until point A still behave relatively homogeneous and small, such as with the closed cutting line experiments. Afterwards, a triangular-shaped deformation zone at the sheet metal upper surface shows up at point B. The tip of the triangle points towards the die edge. On the right hand side of the triangle baseline center, which coincides with the center of the cutting clearance, a small localization area forms around the punch edge. When the punch further penetrates into the material, the triangle twists in the direction of the punch, see point C and point D. The localization of the horizontal deformation increases at the punch edge and reaches maximum values of 1.77 in point D. The maximum strains are thus well below those of closed cutting line configurations. The field of the shear strain, the E_{12} component, develops more similarities to the close cutting line deformation pattern, see figure 6.5 b). After point A, the shear deformation still concentrates on a band around the cutting clearance, however, the localization intensity is higher at the punch edge compared to the die edge. Shear strains mainly originate from the punch and die lateral surfaces. This behavior continues for point C and point D. The maximum value of the Green shear strain component E_{12} is 1.01. Analog to the closed cutting line, the absolute values of the Green shear components are therefore below those of the horizontal strain component. The dominant deformation pattern changes over time and at the latest with the onset of motion instability at point C, where the horizontal strains begin to dominate and to increase disproportionately. The vertical strain field E_{22} also exhibits a different deformation behavior, see figure 6.5 c). The free bending of the sheet metal causes a dichotomy between a negative and a positive vertical strain region. A neural section divides the two strain areas that clearly appears in point C and point D. Analogous to the closed cut, the vertical strain pattern homogenizes as the deformation progresses. At the surface of the punch, the sheet metal stretches in vertical direction, where at the die surface it shrinks accordingly. Point D reveals maximum and minimum vertical strain levels of 0.33 and -0.51, respectively. To show the local deformation dynamics for open cutting lines, I use the components of the Green Strain rate tensor, see figure 6.25. Globally, the strain rates distribute inhomogeneous compared to the strains, especially when hardening effects dominate in point A and point B. Nevertheless, strain rates still precede the strains, govern their appearance, and hence, reflect the geometry of their deformation patterns. The maximum rate is measured at the punch edge for horizontal strains and is $7.26\,\mathrm{s}^{-1}$. Maximum shear rates of $3.04\,\mathrm{s}^{-1}$ occur in point D and the absolute highest values in vertical direction are $1.79\,\mathrm{s}^{-1}$. The maximum local strain rates for open cutting lines lie under those of closed cutting lines but show the same order of magnitude.

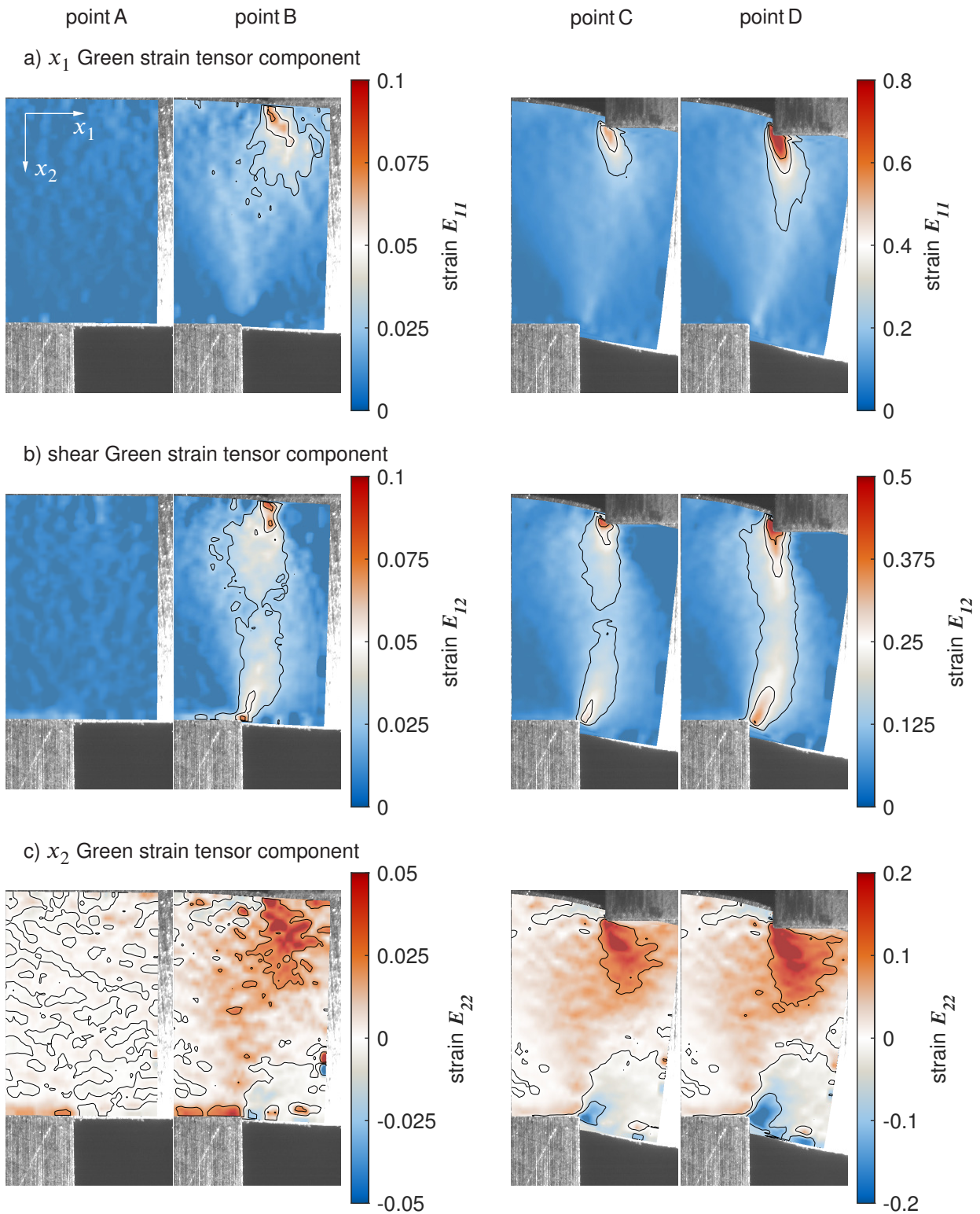*Figure 6.24: Green strain tensor fields of the open cutting line experiment with 12.5% clearance at the time A, B, C, and D. a) x_1 Green strain component E_{11} b) shear Green strain component E_{12} c) x_2 Green strain component E_{22}.*
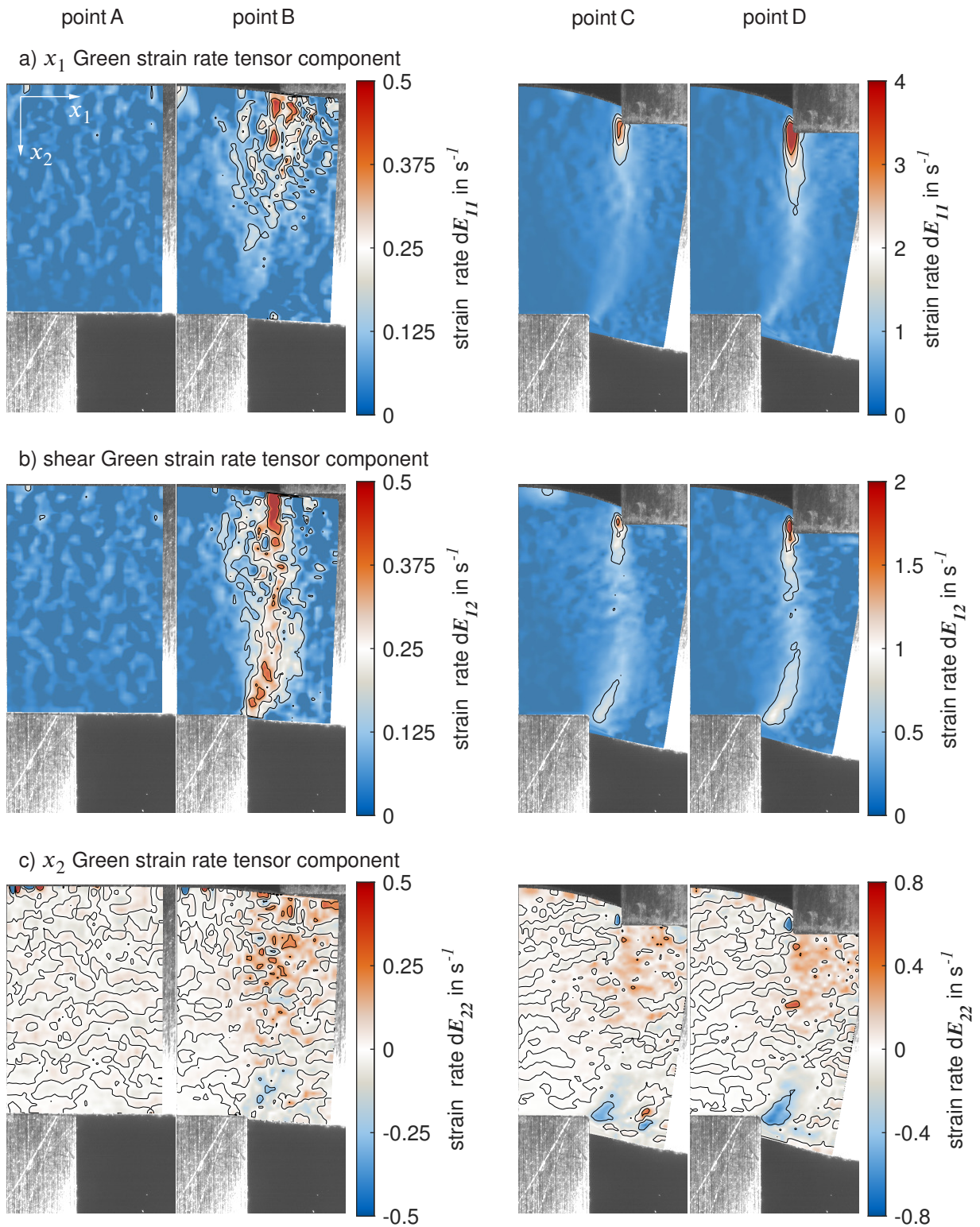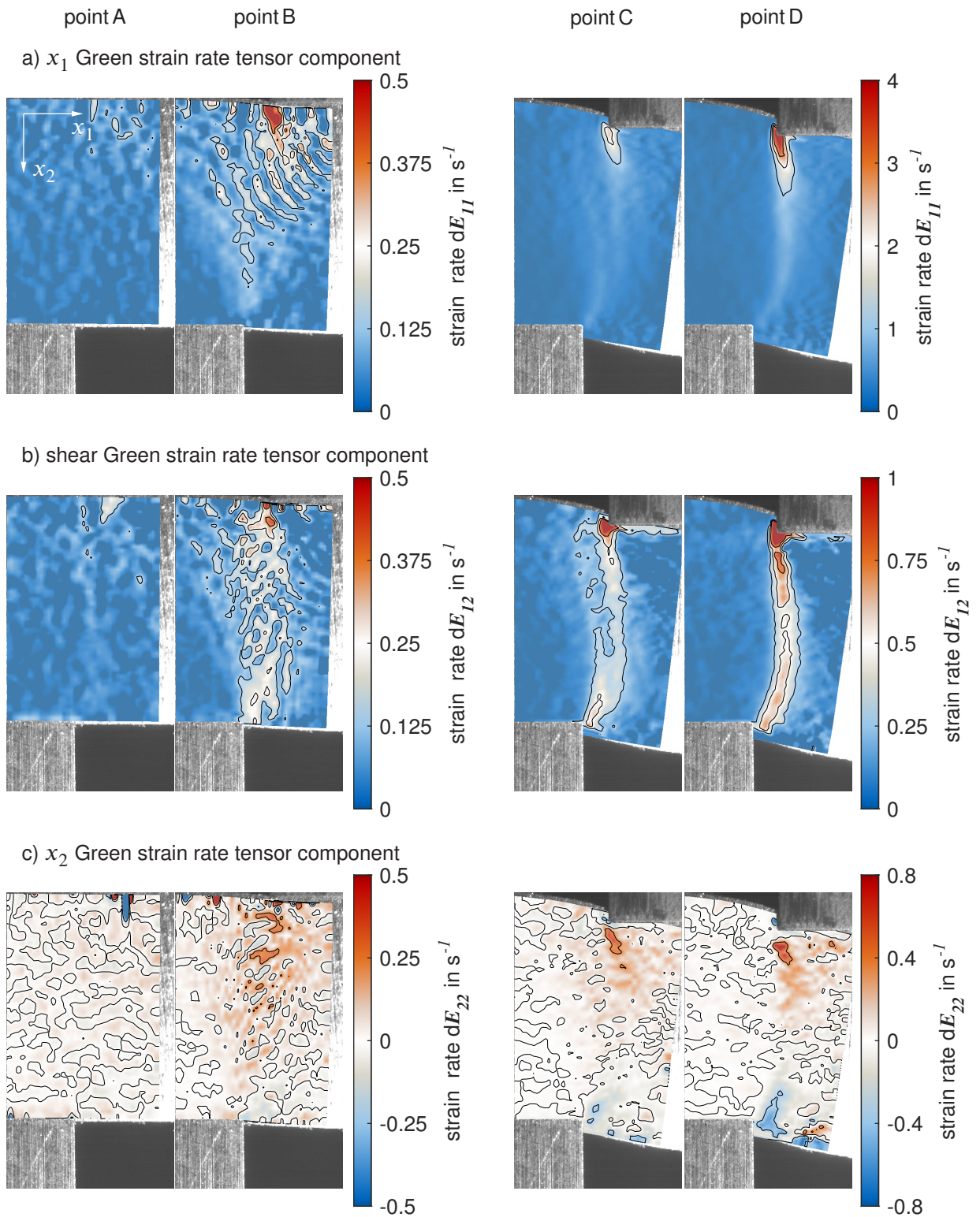
Figure 6.25: *Strain rate tensor fields of the open cutting line experiment with 12.5% clearance at the time A, B, C, and D. a) x_1 Strain rate component $\dot{E}_{11} = dE_{11}$ b) shear Strain rate component $\dot{E}_{12} = dE_{12}$ c) x_2 Strain rate component $\dot{E}_{22} = dE_{22}$.*

6.3.1 Cutting Clearance Variation

The conducted cutting clearances are 2.5%, 6.0%, 10%, 12.5%, and 15%, with the comparative value of 10%. Figure 6.27 gives the integral in situ measurements and the Hausdorff distance computations. The classical ex situ and in situ measurement parameters appear inconspicuous with regard to the descriptions in section 2.4.1. A smaller cutting clearance reduces the edge draw-in, reduced burr height and in return increases the clean-shear share, see figure 6.26. Larger cutting clearances cause the opposite. The maximum cutting forces F increases with smaller cutting clearance, see figure 6.10 a). Overall, the Hausdorff distances d present stable for varying cutting clearances prior to crack initiation, from where motion behavior diverge. Figure 6.28 gives the Green strain tensor component fields for an open cutting line experiment using 6% cutting clearance. The changes in local deformation behavior are less fundamental but rather continuous adaptation. In the E_{11} component, the triangular deformation zone narrows, as can be seen for example in the point B figure 6.28 a) compared to figure 6.24 a). The deformation localizes in a smaller area and the maximum horizontal strains reach 1.4. The shape of the band of shear strains changes smoothly with the cutting clearance. Decreasing cutting clearance narrows the deformation band and reduces its bulge in the direction of the punch, as shown in the comparison of figure 6.28 b) and figure 6.28 b). The shear strains reach their maximum of 0.79 in point D. The vertical strains increase for smaller cutting clearances without changing their appearance, see figure 6.24 c). Also, the extreme values increase so that the vertical strain field in point D contains maximum and minimum vertical strain levels of 0.70 and -0.35, respectively.

Figure 6.26: *Cutting clearance c_c variation cut surface characteristics for open cutting line experiments. (circle: mean, bold line: standard deviation, fine line: minimum and maximum based on 15 measurements)*

Figure 6.27: In situ data for cutting clearance variation experiments with open cutting line: a) cutting force F vs. punch travel z curve. b) cutting work W vs. punch travel z curve. Hausdorff distance d of the motion fields from three test (error bar) to the reference: c) u_1, d) u_2, e) normalized motion curl c.

Figure 6.28: *Green strain tensor fields of the open cutting line experiment with 6% clearance at the time A, B, C, and D. a) x_1 Green strain component E_{11} b) shear Green strain component E_{12} c) x_2 Green strain component E_{22}.*

6.3.2 Cutting Edge Variation

I analyzed two different blade edge pairings with die radii of $r_d = 50\,\mu m$ and $r_d < 20\,\mu m$ both combined with a punch edge radius of $r_p = 70\,\mu m$ for open cutting lines. Figure 6.29 summarizes the resulting cut surface characteristics, where the values for $r_d = r_p = 50\,\mu m$ serve for comparison. Figure 6.30 shows the integral in situ measurements together with the Hausdorff distance computations. The classical in situ and ex situ measures comply with the descriptions in section 2.4.1 in terms of blade geometry. Larger punch rounding gives higher edge draw-in for both asymmetric configurations compared to the symmetric configuration, see figure 6.29. The reduced die edge radius yields smaller burr height and width. But changed geometric conditions in the cutting clearance promote differences in material flow and deformation behavior. The Hausdorff distances d of the displacement quantities u_1, u_2, and motion complexity c to the symmetric comparative value behave similar throughout the shearing process until crack initiation, see figure 6.30 c) d), and e). Motion complexity even indicates that both configurations approach prior to point D. I focus on the Green strain tensor component fields for the blade edge variation in open cutting line experiments. Figure 6.31 shows the results for $r_d < 20\,\mu m$ and $r_p = 70\,\mu m$. The asymmetric cutting edge rounding mainly influences the maximum shear strain values occurring at the blade edges. For the symmetric $r_d = r_p = 50\,\mu m$, at point D, maximum shear strain values of 0.92 occur at the punch and 0.42 at the die. Using the asymmetric pairing, maximum shear strain values balance and amount to 0.81 occur at the punch and 0.67 at the die, however, crack initiation still takes places at the punch edge.
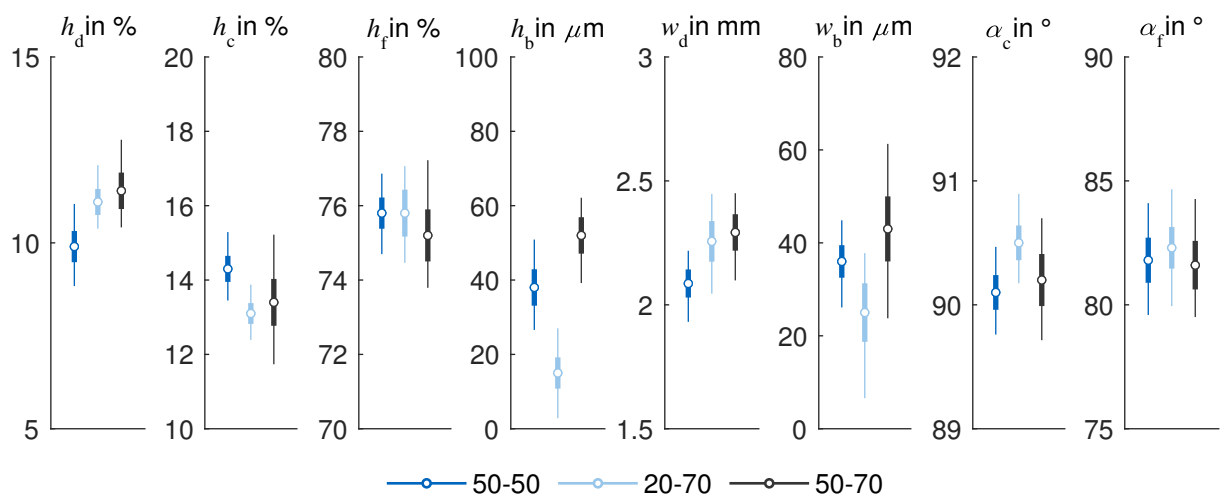
Figure 6.29: Blade edge variation r_d-r_p cut surface characteristics for open cutting line experiments. (circle: mean, bold line: standard deviation, fine line: minimum and maximum based on 15 measurements)
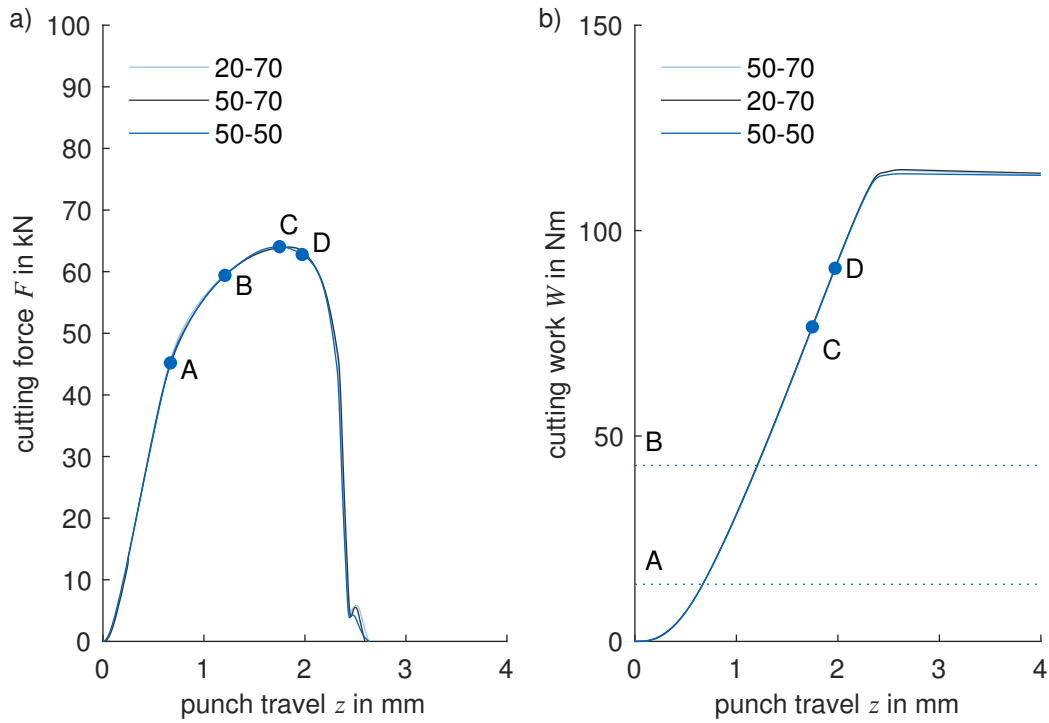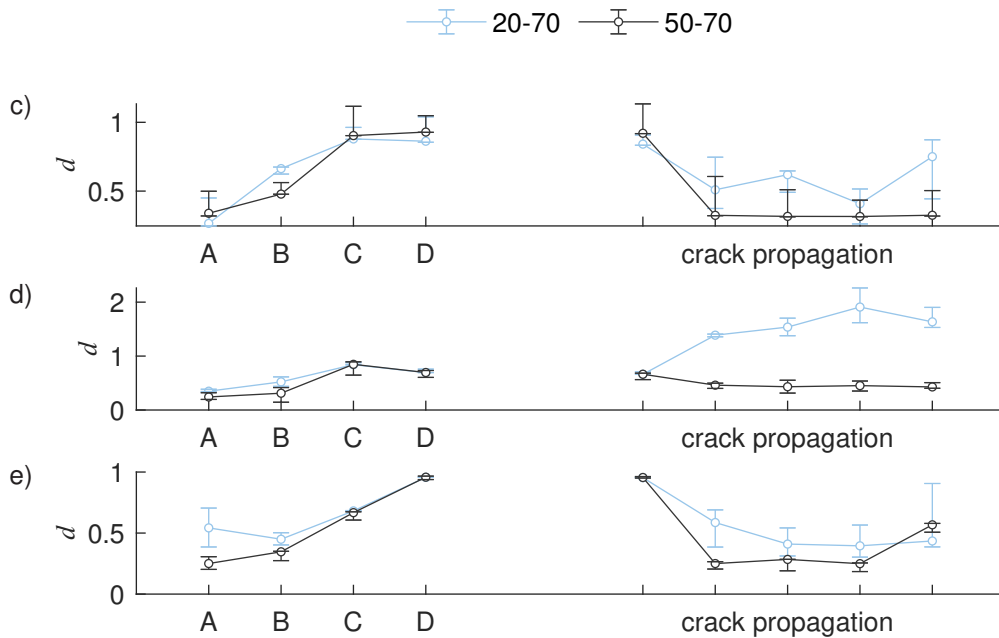
Figure 6.30: Integral in situ data for cutting edge variation experiments with open cutting line. a) cutting force F vs. punch travel z curve. b) cutting work W vs. punch travel z curve. Hausdorff distance d of the motion fields from three test (error bar) to the reference: c) u_1 d) u_2 e) normalized motion curl.
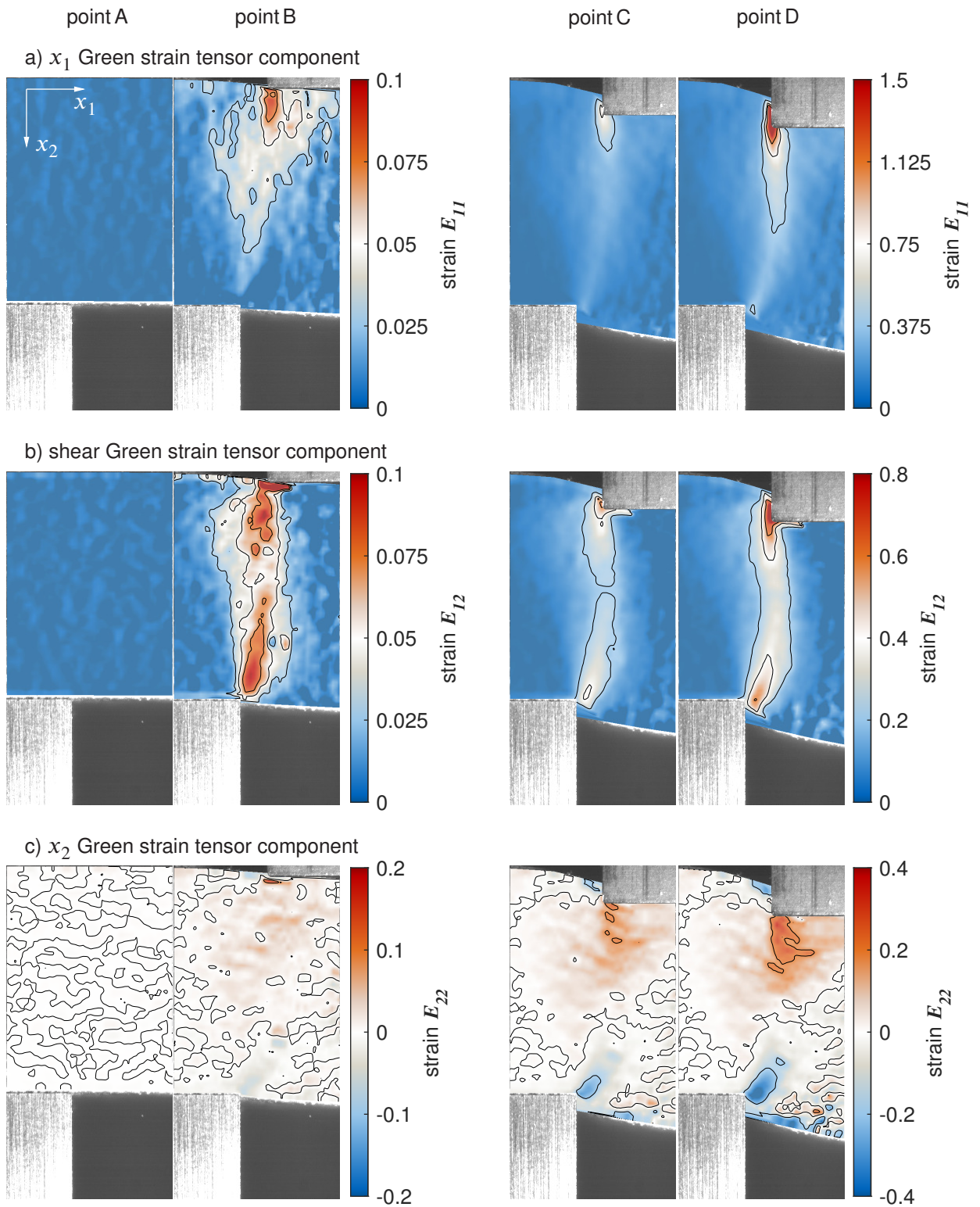
Figure 6.31: Green strain tensor fields of the open cutting line experiment with <20 μm die and 70 μm punch edge radius at the time A, B, C, and D. a) x_1 Green strain component E_{11} b) shear Green strain component E_{12} c) x_2 Green strain component E_{22}.

6.3.3 Aluminum

For the open cutting line experiments, I additionally conducted aluminum EN AW A5083. The results comprise the experiment for reference process parameters, where figure 6.32 summarizes the cut surface characteristics. Figure 6.33 shows the integral in situ measurements and the conducted evaluation points A, B, C, and D. I employ the Green strain tensor components for local deformation analysis, see figure 6.21 and further show the strain rate evaluation, see figure 6.35. The global deformation pattern conserve between the mild steel S355MC and the aluminum EN AW A5083 sheet metal. Deformation localization starts in the phase where hardening effects dominate shear cutting. The vertical components of the Green strain tensor E_{11} localizes especially at the punch edge, where at point D maximum values of 0.98 are reached, see figure 6.21 a). The shear strains in figure 6.34 b) also span a deformation band that bulges under the punch due to the free boundary there. Strong shear strain localization occurs at both cutting edges, but amplifies faster at the punch edge. In contrast to the S355MC steel material, the maximum strain values stay more balanced between die and punch. Prior to crack initiation maximum strain values of 0.73 occur at the punch edge and 0.39 at the die edge. The strains in the vertical direction in figure 6.34 c) shows the same basic patterns as for S355MC steel. Two vertical strain regions emerge, a negative vertical strain region at the edge draw-in area of the punch and a positive area that originates from the punch front face. This positive area is disturbed by a small negative region at the punch surface, where the clean-shear forms. Within these two regions the strains localize from the blade edges. There, the extreme values of the vertical strain field in point D are almost equal and amount to 0.35 and -0.36, respectively. The strain rate distributions show local dynamic deformation patterns that do not occur in for
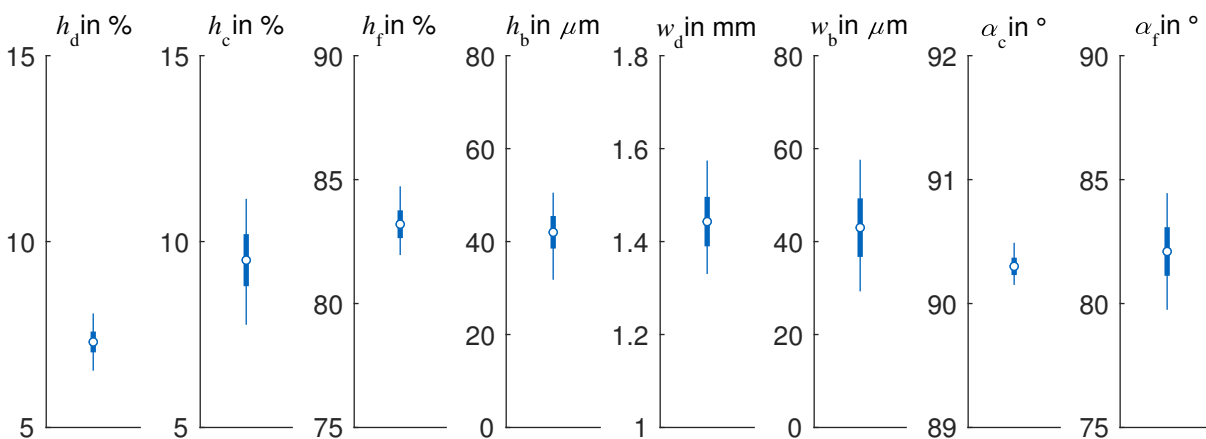
Figure 6.32: Aluminum cut surface characteristics for open cutting line experiments in reference process parameter configuration. (circle: mean, bold line: standard deviation, fine line: minimum and maximum based on 15 measurements)
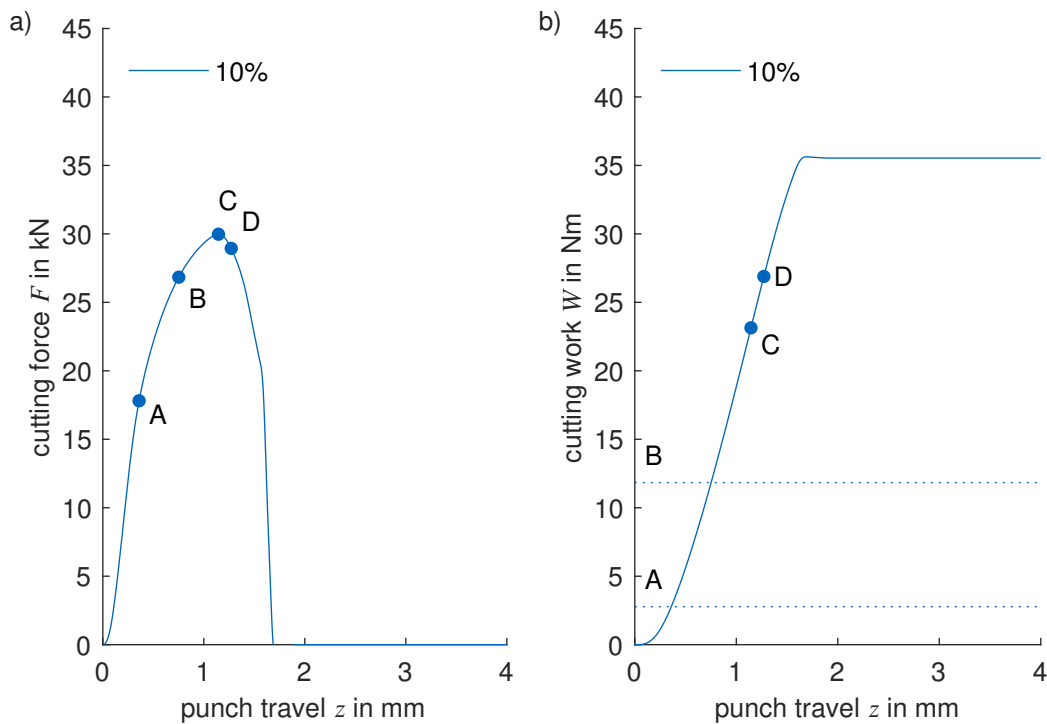
Figure 6.33: Integral in situ data for aluminum experiments with open cutting line. a) cutting force F vs. punch travel z curve. b) cutting work W vs. punch travel z curve. A, B, C, and D indicate the evaluation points for the full-field in situ data.

the S355MC steel counterpart. All three components of the Green strain rate tensor reflect the dynamic effect, however, the horizontal component draws the clearest picture, see figure 6.35. At point B, the $\dot{E}_{11}$ component, in addition to the onset of localization at the punch edge, shows a regular quarter-circular wave pattern that extends from the bottom of the punch into the shear cutting affected zone. The wavelength of the pattern is $\sim 85\,\mu$m and the pattern stops by the die edge boarder of the cutting clearance. Although strain rates act as precursors of strains, they do not give obvious indication of this pattern but present smooth and well-behaved. The wave pattern either disappears in by further shearing, or is disproportionately superimposed by strain localization. Thus, point C and point D finally show comparable strain rate distribution appearances as the steel material S355MC. The maximum values of the horizontal strain rates at the punch edge are $5.37\,\mathrm{s}^{-1}$, the shear strain rates $2.03\,\mathrm{s}^{-1}$ and the vertical strain rates $1.04\,\mathrm{s}^{-1}$. The maximum values are below those of the test with the steel material S355MC, but in the same order of magnitude. Compared to the closed cutting line aluminum tests, the open cutting line show significantly lower maximum values, but in the same order of magnitude. For the closed cutting line the maximum rate values at point D, are $9.90\,\mathrm{s}^{-1}$ for the horizontal strain rate, $4.07\,\mathrm{s}^{-1}$ for the shear strain rates, and $1.80\,\mathrm{s}^{-1}$ for the absolute vertical strain rate.

Figure 6.34: Green strain tensor fields of the aluminum open cutting line experiment with 10% clearance at the time A, B, C, and D. a) x_1 Green strain component E_{11} b) shear Green strain component E_{12} c) x_2 Green strain component E_{22}.

Figure 6.35: *Strain rate tensor fields of the aluminum open cutting line experiment with 10% clearance at the time A, B, C, and D. a) x_1 Strain rate component $\dot{E}_{11} = dE_{11}$ b) shear Strain rate component $\dot{E}_{12} = dE_{12}$ c) x_2 Strain rate component $\dot{E}_{22} = dE_{22}$.*

7 Discussion

With the discussion in this chapter, I synthesize the experimental outcome of chapter 6 *Results* to the research objectives formulated in chapter 3 *Aims and Scope*. In section 7.1, I reflect the concept to induce the natural process boundary condition, also with reference to chapter 4 *Approach and Experiments*. Section 7.2 discusses the accuracy and precision of the experimental results facing the background of the spatio-temporal methods developed in chapter 5 *Methods*. Considering both the experimental design and the evaluation routines, I dare to generalize from the experimental findings regarding the process dynamics, localization phenomena, and the shear affected zone in section 7.3.

7.1 Experimental Setup and Boundary Condition

The examination of the experimental setup and the natural process boundary condition, a plane strain boundary condition in the case of shear cutting, equally stands for the discussion of the first research question posed in section 3.2.

How to design a temporally and spatially resolved observation of the entire shear cutting process, which maintains the natural process conditions?

In the work of Hartmann et al., 2021, my coworkers and I already studied the plane strain boundary condition experimentally and numerically using three-dimensional finite element analysis for the S355MC sheet metal. The experiments has been carried out on an academic pretest rig, which served to challenge and validate the glass stop concept of Takahashi and Aoki, 1996b and Takahashi and Aoki, 1996a. Our experimental results validated and verified the concept with respect to tactile ex situ measurement values. We used the three-dimensional finite element model to test the in situ behavior of the glass stop and even proved the stress state in the observation plane to be reasonable and on the same level as along the rest of the cutting line. Within the scope of this thesis, I extend the validation presented in Hartmann et al., 2021 by two further investigations, one ex situ and one in situ. First, I utilize three-dimensional cut surface models from laser confocal microscope measurements to overcome the inadequacies of tactile measuring devices directly at the sheet edge. The high-resolution three-dimensional surface models allow a precise comparison of cut surfaces characteristics for experiments performed

with glass stop and without glass stop. Second, I illustrate how strains in the shear affected zone evolve for tests with and without a glass stop mounted.

For the analysis I used the reference experiment, see section 6.1 and the open cutting line pendant, see section 6.3, each performed with and without glass stop. The resulting cut surfaces show completely different characteristics at the sheet metal edge. For a cut without glass stop, the clean-shear share reduces towards the sheet metal edge in favor of the fracture share, as shown in figure 7.2 b) for closed cutting lines and figure 7.2 d) for open cutting lines. If, on the other hand, the free surface is constrained by a stop, bulging in the x_3-direction is limited and a constant ratio of the clean-shear share to fracture share forms along the entire cutting line, as illustrated in figure 7.2 a) and c).[1] To quantify the visual results, I extracted the cut surface characteristics from three-dimensional geometry data. Three-dimensional surface models enable to sense exactly along the edge between cut surface and sheet side face, what tactile measuring devices prevent (Hartmann et al., 2021). In this way, the measurements provide increased accuracy for the ex situ investigation of the process boundary condition. Figure 7.1 shows the extracted cut surface characteristics from the three-dimensional cut surface models. I also Incorporated the values measured inside the sheet metal to give a pivotal point. As the visual impression already suggests, the experiments with glass stop are on the same level as the experiments without glass stop. The values for the tests without glass stop are both characterized by a reduced edge draw-in, reduced clean-shear share and high fracture share.

Next to the laser confocal microscopic images of the cut surfaces, figure 7.2 c) and f) show the evolution of the principal strain distribution diagram in the shear affected zone for closed and open cutting line, each with and without glass stop. Both principal strain distributions are shown for the evaluation points A, B, C, and D. Without the glass stop, deformation has an additional degree of freedom perpendicular to the observation plane in x_3-direction. Hence, the third principal strain of the Green strain tensor may be no longer seen as approximately zero. This additional motion yields a reduction in the two first principle components shown in each of the presented diagrams, see figure 7.2 c) and f). The free sheet surface also leads to reduced hydrostatic pressure in the shear zone, which promotes premature fracture initiation in the observation plane area.

Since the final geometry of the cut surface is governed by the motion flow of the material particles to the respective positions, the ex situ analysis also allows conclusions to be drawn about the cutting process. Although the procedure seems to have close resemblance to the

---

[1]I further ensured by measuring the width of the samples before and after the experiments that the forces acting due to the plane strain boundary condition do not cause bending of the 4 mm thick sheet specimen around the x_1-axis.

calibration of numerical simulations based on cut surface parameters, I would like to point out distinct differences. The performed experimental analyses of the shear cutting process solve at any time the problem of shear cutting, see equation 2.59, forward directed. The inverse calibration does not do this, so no bidirectional unambiguity can be inferred. Therefore, these two methods are fundamentally different and the experimental analyses of the natural process boundary conditions allow even stronger statements. Based on the reproducibility of the experiments using the developed experimental setup I conclude that the movement of the material particles into their final position, e.g. also their arrangement along the cut surface, is governed by deterministic behavior. Therefore, the shear cutting experiment can be understood as a deterministic forward model, both in space and time, which ideally represents the nature of the process. If the forward model generates identical cut surfaces, the statement about the equivalence of the kinematic state variables that cause these cut surfaces is unique and even valid for the course of the process. With regard to the prevailing stress state in the shear affected zone, the constitutive behavior of the material intervenes in the forward model. I consider as a thought experiment the case that the stress state changes in the observation plane despite the same kinematic state variables. This means that the material flows in the same way despite changed stress conditions. The same case is conceivable for changed hydrostatic stresses while deviatoric stresses stay constant. This reduces the question of material behavior to the dependence on the hydrostat. Since the tested materials depend on the hydrostatic stresses, especially with regard to crack initiation, I conclude from this consideration that the experimental data of the forward model also confirm the consistency of the underlying stress state.
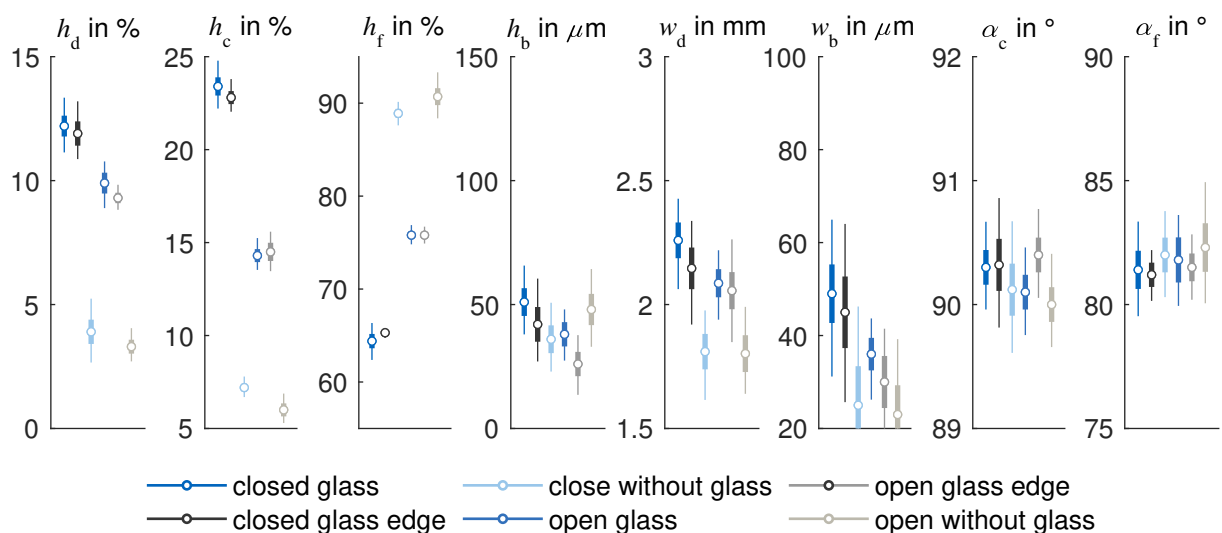
Figure 7.1: Boundary condition validation experiments cut surface characteristics for close and open cutting lines with and without a glass stop. (circle: mean, bold line: standard deviation, fine line: minimum and maximum)
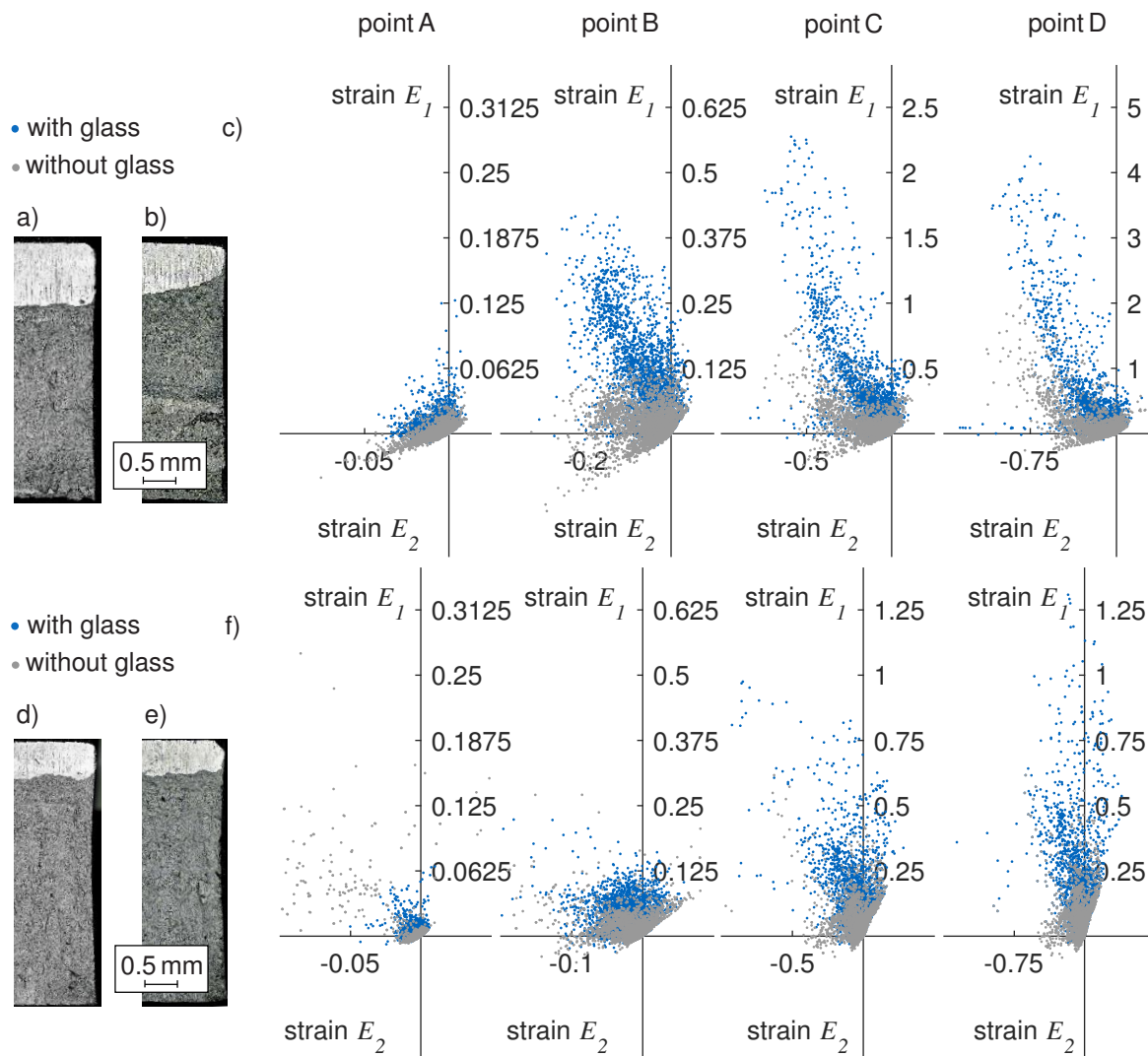
Figure 7.2: Microscopic images of the shear cut surface for close cutting line with glass stop a) and without glass stop b), and open cutting line with glass stop d) and without glass stop e). Principal strain distribution. c) closed cutting line and f) open cutting line at the evaluation points A, B, C, and D.

7.2 Accuracy and Precision Analysis

Determining the accuracy and precision of an optical deformation analysis poses different challenges. The absolute evaluation can be done in the true sense of the word only by using artificially generated data, as I have done to determine the algorithm parameters in section 5.4. The absolute accuracy regarding artificial test data offset with real noise is thus guaranteed within the developed approach itself. However, the accuracy and precision in use cannot be determined with this either. In my opinion, the question about the accuracy has to be formulated differently and more specific anyway. Measurement methods and test benches should not be

judged exclusively by absolute values but by their purpose, the available raw data, and the underlying models given by the descriptive framework. This view is also reflected in the second research question, I asked in section 3.2.

How to curate and evaluate data to capture the extreme phenomena of shear cutting?

Measurement routines must first make it possible to process the underlying database and extract the information content. The acquisition of the shearing process generates extreme amounts of data, which are required especially at the end of the process in order to be able to detect dynamic and local phenomena in high resolution.

For the curation of the raw data, I designed a dimension reduction algorithm (algorithm 2), which determines an adjustment of the raw data extraction in interaction with the motion estimation (algorithm 1). I show the effectiveness of this procedure by the PARAFAC analysis of the field of the equivalent strain E_{eq}, as illustrated in figure 7.3. The PARAFAC analysis of the three dimensional equivalent strain E_{eq} array has been performed with identical parameters as the initial analysis of the raw image data in figure 6.1. I also normalized the results for visualization purposes. Within the region of interest in x_1-direction the modes clearly indicate the cutting clearance. In the x_2-direction a more inhomogeneous distribution of the modes arise. To discuss the dimensional reduction, I focus on the PARAFAC analysis along the time axis, i.e. the number of images. The extracted information shows a curve divided into two parts. In the first part, which contains the process up to point D, the extracted information describes an exponential curve. With the crack initiation, the deformation part of the shear cutting process is replaced by crack evolution. The second part of the curve again shows an exponential increase, which however describes much stronger growth. The PARAFAC analysis thus reveals on the one hand that information could be obtained from the raw data using the developed measurement routines. On the other hand, the cooperative dimension reduction algorithm curates the raw data in such a way that this information follows the extreme phenomena of the shear cutting process characteristics expressed in the sequential curves with exponential growth.

Next to reasonable data processing is quality of results. In addition to the comparison of measurement results with artificially generated ground truth data (section 5.4), independent reference measurements using another measurement system or evaluation routine established. Referential statements based on comparisons between the two results deduce. I use the complementary properties of the developed motion estimation algorithms to evaluate the conducted deformation analysis. By performing time integration of the Green strain rate tensor fields $\dot{\mathbf{E}}$, determined by algorithm 4, I calculate an independent set of deformation results to the Green strain tensor values $\mathbf{E}$ computed using the algorithm 2, algorithms 1, and algorithm 3. Both computations
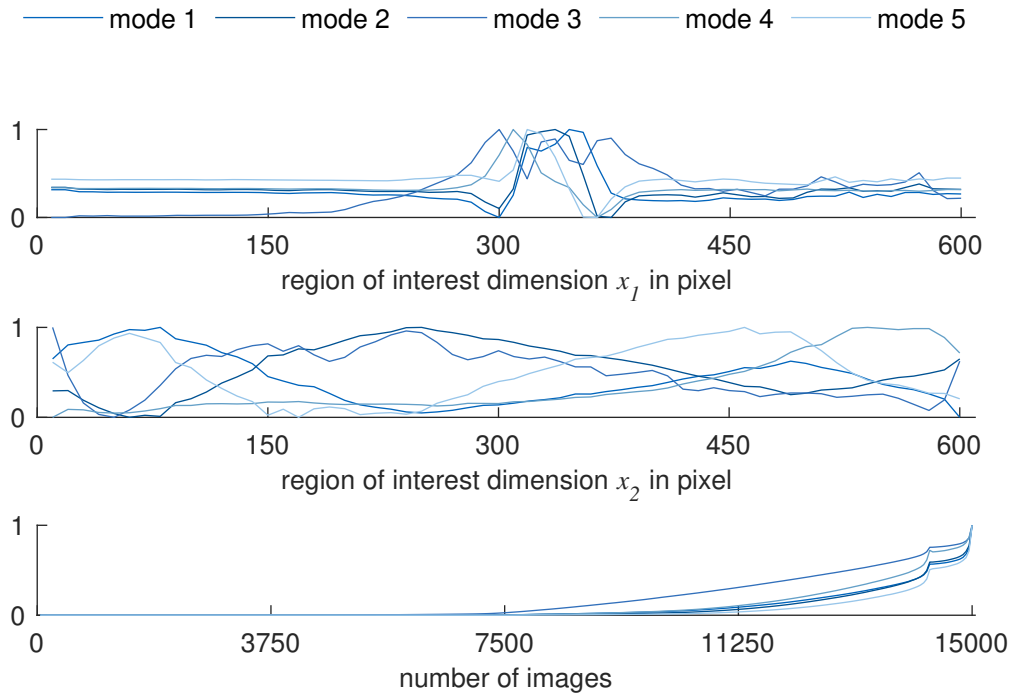
Figure 7.3: PARAFAC analysis of the three-dimensional equivalent strain E_{eq} data array for the first five modes along the horizontal dimension x_1 of the region of interest, the vertical dimension x_2 of the region of interest, and the raw number of images representing the time axis.

use the same raw data. Figure 7.4 a) and b) compare the calculation results by equivalent strain E_{eq}, for an aluminum experiment performed with closed cutting line and 12% cutting clearance. Figure 7.4 a) shows the standard calculation path, whereas figure 7.4 b) draws the results based on time integration of the Green strain rate tensor $\dot{\mathbf{E}}$. The independently obtained results show very strong agreement, which is also quantitatively reflected in the calculation of the Hausdorff distance d. With normalized deviation values of the Hausdorff distances d between the calculated equivalent strain fields E_{eq} of 3%, 2%, 1%, and 3% at the evaluation points A, B, C, and D, the comparative values remain within the scatter range[2] of the individual experiments that amount to 5%, 4%, 3%, and 3%. The results of the block-matching evaluation tend to be locally more volatile, which is due to the characteristic of independent motion estimation of each pixel region and the only spatially performed regularization. The results of the time integrated strain rates have a comparatively smooth behavior. The regularization in both spatial and temporal direction yields enhanced stabilization of the calculations. Nevertheless, especially the maximum values remain nearly constant with values of 3.08 in figure 7.4 a) and 2.93 in figure 7.4 b) at point D.

---

[2]Please note that the given scatter values in addition are a measure for the precision of the shear cutting experiment with respect to local resolution.

The spatio-temporal regularization does not act as a excessive smoother, but the developed models describe the deformation adequately. The correspondence of the two evaluation paths proves the coherence and compatibility of both approaches within the established descriptive framework. The hybrid use of block-matching algorithms, such as algorithm 1, and variable algorithms 4, is consistent and closed in itself. To further analyze and evaluate the properties of the spatio-temporal computation, figure 7.4 c) shows the deformation curvature[3] κ, which is a quantity based on a second-order spatial derivative (Volk, 1999, p. 22–26; Steinmann, 2015, p. 18–29). Volk, 1999, p. 31–34 deduces the curvature tensor $\boldsymbol{\kappa}$ based solely as a function of the strain gradient $\nabla \boldsymbol{\varepsilon}$

$$\boldsymbol{\kappa} = \frac{1}{2} \mathbf{E}_\mathrm{R} \left(\nabla \boldsymbol{\varepsilon} + \nabla \boldsymbol{\varepsilon}^{\mathrm{T}_{13}} - \nabla \boldsymbol{\varepsilon}^{\mathrm{T}_{23}} \right) \ , \tag{7.1}$$

where $\mathbf{E}_\mathrm{R}$ is the second degree Ricci permutation tensor. Volk, 1999, p. 31–34 further shows the curvature tensors connection to internal lengths, such as grain size. The extreme values of the curvature κ seam the deformation band and yield its geometric boundary between the blade edges. The robust performance of the deformation curvature evaluation additionally validates and verifies the spatio-temporal optical flow method and gives a first idea of their potential.

To evaluate the fracture analysis that is based on algorithm 5, I use the ex situ measurement of the shear cut surface. Since the crack propagates along the fracture share of the cut surface, it represents an independent measure to reference against. Figure 7.5 confronts four different cut surface contour (line in blue color) with the equivalent strain E_eq calculated from the non-classical parts of the Green strain tensor $\mathbf{E}$ (black structures). Two closed cutting line variants and two open cutting line variants are illustrated. Figure 7.5 a) gives the results for the reference experiment, figure 7.5 b) for closed cutting using $20\,\mu\mathrm{m}$ die edge radius and $70\,\mu\mathrm{m}$ punch edge radius. Two closed cutting line variants and two open cutting line variants are illustrated. Figure 7.5 c) and d) shows open cutting line results using reference process parameters and $20\,\mu\mathrm{m}$ die edge radius and $70\,\mu\mathrm{m}$ punch edge radius, respectively. The equivalent strain measure E_eq of the non-classical parts of the Green strain tensor $\mathbf{E}$ may be also seen as a binary indicator, where a crack occurs in the shear affected zone, hence, I plotted it in uniform color. The crack indicator almost perfectly follows each of the fracture shares along each of the four cut surface contours that provide different shape characteristics. The fracture share traces the united macro cracks in the material. In addition to the macro-cracks, however, further micro-cracks are displayed in the material, which do not cause the material separation, but arrange themselves around the macro-crack. The fracture surface in figure 7.5 a) is approximately linear, which also reflects the structure of the crack indicator. In contrast, the fracture surface for the asymmetrical cutting edge rounding is double curved, see figure 7.5 b). This characteristic can also be traced

---

[3]For plane strain, the curvature tensor only has a single independent element.
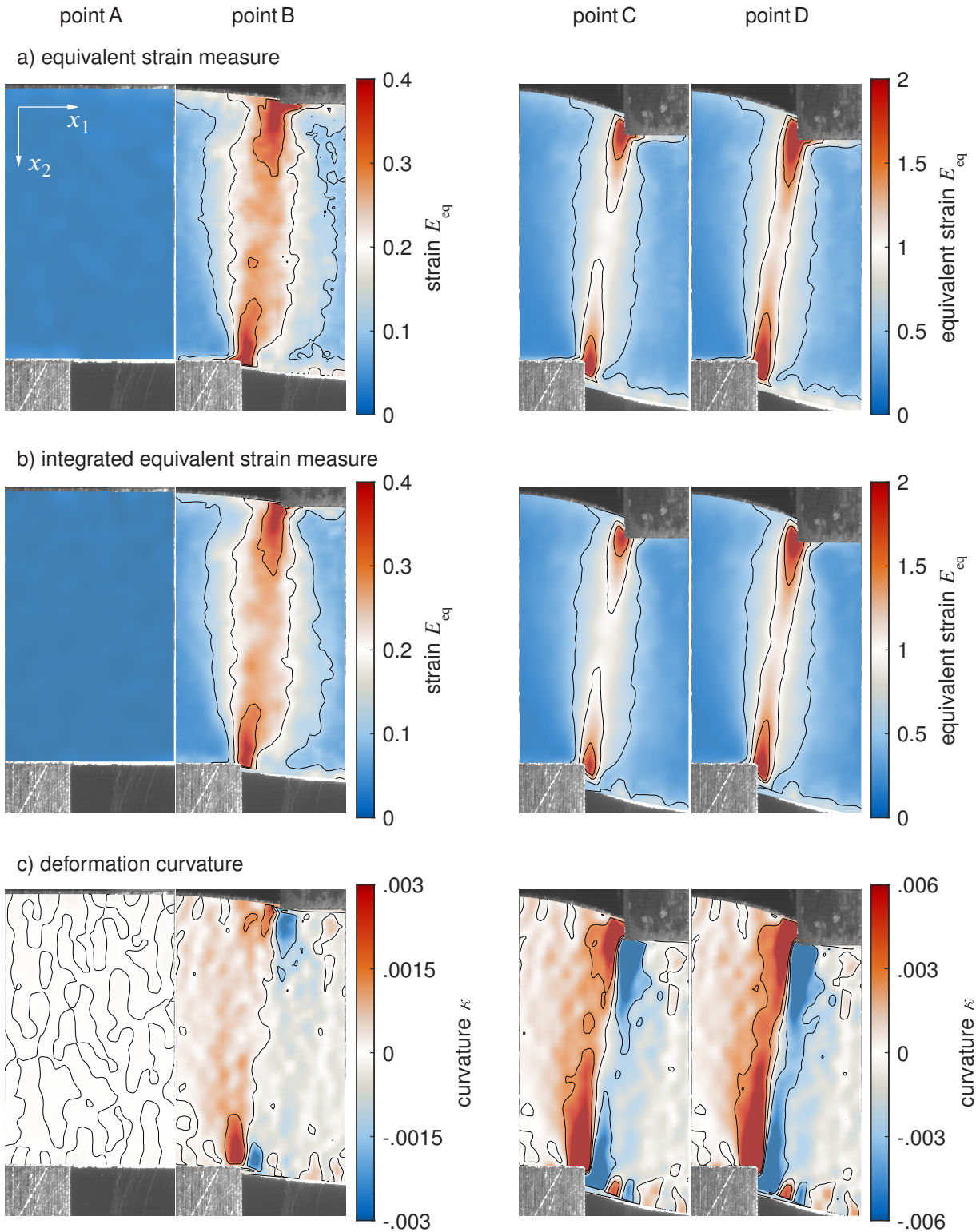
Figure 7.4: Results for aluminum closed cutting line experiment with 12.5% cutting clearance at the points A, B, C, and D. a) equivalent strain E_{eq} based on $\mathbf{E}$ results, b) integrated equivalent strain E_{eq} based on $\dot{\mathbf{E}}$ results, c) deformation curvature κ.
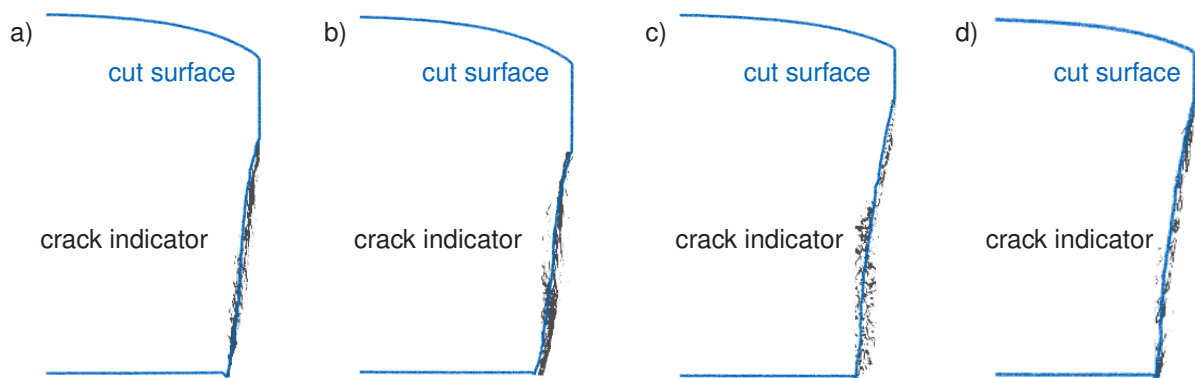
Figure 7.5: Crack paths in relation to the measured cut surfaces for the reference experiment a) the closed cutting line experiment using 20 μm die edge radius and 70 μm punch edge radius b), the open cutting line with reference process parameter setting c), and the open cutting line using 20 μm die edge radius and 70 μm punch edge radius.

using the crack indicator. For the open cutting line, the reference process parameters create a single curved fracture surface, as shown in figure 7.5 c). In this experiment, a wide band of micro-cracks accompany the macro-crack according to the crack indicator. The single curved shape of the fracture surface can nevertheless be found in the structure of the crack indicator. The asymmetrical arrangement for the open cutting line in figure 7.5 d) yields a lighter curvature of the fracture surface, whose characteristics are also reproduced by the structure of the crack indicator. The independent comparison between ex situ measurement and non-classical strain measures ensures both the static statements about the localization of the crack in the shear affected zone and, in an integral form, its dynamic progress. Since I embedded the calculations of the crack evolution in the overall framework of the motion evaluation, an incremental update of the crack progress is achieved. Only the addition of the calculated non-classical increments allows to trace the crack from initiation to final part separation. Therefore, the results in figure 7.5 confirms also the dynamic features of the crack analysis in a time integrated form.

7.3 Dynamics, Localization, and Shear Affected Zone

The presented analyses deliver self-contained results within the descriptive framework. As pointed out in section 7.1 and section 7.2, the assumptions and analyses made in the scope of this thesis pass a cross-validation between all conducted in situ and ex situ measurements. On this basis, I build the discussion of the shear cutting process, in particular, how its dynamic and local behavior changes under certain process modifications. This falls back to answering the third research question formulated in section 3.2.

How do modifications in the shear cutting process affect its dynamics and the development of the shear affected zone?

Reduced cutting clearance promote high strain values and narrow the shear affected zone for both sheet materials, S355MC and EN AW 5083, however tendencies turn out weaker for aluminum, which I mainly attribute to earlier crack initiation. The change of the boundary condition from closed to open cutting lines does not influence the global trend that a reduction in cutting clearance yields higher maximum strain values and narrows the shear affected zone. Quantitative differences between the two materials are obvious, due to the different constitutive behavior. Experiments for S355MC steel material reach higher strain levels in general, however, for open cutting lines, the differences become lower since process conditions are more moderate. Due to the larger material deformation and accompanying material flow when shearing S355MC, the shear affected zone grows larger compared to EN AW 5083. In comparison to open cutting line experiments, closed cutting line experiments reach higher strain levels prior to crack initiation especially for the steel S355MC sheet metal mainly due to higher hydrostatic pressure in the cutting clearance driven through the kinematic boundary condition. Sharp cutting edges promotes early crack initiation due to higher local stress peaks. On the other hand, the high local stresses also yield increased local deformation resulting in higher maximum strain values and smaller shear affected zone. Asymmetric blade edge pairings mainly show their influence in crack initiation and crack propagation, but also control the shape of the deformation band during shearing. The blade edge radius dictates the exit angle of the deformation band, which is responsible for the whole shape of the shear band and a precursor for crack propagation. Higher cutting velocities lead to increased maximum strain values and slightly smaller shear affected zone, which I attribute to the strain rate hardening effect of the steel S355MC sheet metal.

The dynamics of cutting is significantly influenced by all process variables and large differences emerge regarding the dynamic history of each variant in the experimental parameter space.[4] However, this differences are less evident in the classical measurements or even in the final strain distributions. Whether and to what extent the dynamic history influence the properties of the shear affected zone, i.e. whether the dependency $\mathbf{\Phi}(\dot{\mathbf{E}})$ exists, may be determined using the proposed experimental and measurement technology. I identify as a basic tendency that growing strain values during shear cutting are accompanied by increasing strain rates in the shear affected zone, which corresponds to the expected localizing behavior in the deformation band and especially at the cutting edges. Shearing with open cutting line, only achieves significantly lower strain rates, thus behaves much more moderately in the strain space as well as in the strain rate domain. Despite the lower absolute strain values, for the closed cutting

---

[4]In appendix F.4, I introduce two supplemental representations to visualize the results in a more comparable way.

line, EN AW 5083, achieves high strain rates, which are even significantly higher than the strain rates of the reference experiment using S355MC. The process dynamics are therefore not expressed or contained implicitly in the strain values but are determined by the interaction with the material behavior. The dynamic of the shear cutting process is characterized by the balance of hardening and softening effects in the shear affected zone. Strain hardening, strain rate hardening, temperature softening, and damage, I would like to mention as important phenomena in this context. Their constellation for the aluminum promotes faster deformation, which I attribute to abrupt domination of the softening effect after the point of motion instability, see also the force punch travel curve in figure 6.20. The reduction of the cutting clearance also leads to reduced dynamics. Larger cutting clearance obtain wider deformation bands with smaller maximum rate values. Cutting edge variation yields higher dynamics values using sharp blade radii that promote strain localization. Cutting velocity has the largest influence on the shearing process dynamics of the process, where higher punch velocities yield increased strain rate.

Analyzing the dynamics of crack propagation, I found an analogous characteristic for both cutting line settings. For closed cutting lines the crack starts at the die within the investigated parameter domain. The asymmetry of the cutting edge rounding control the subsequent crack initiation at the punch edge. After crack initiation, the crack does not propagate uniformly through the material, but remains in place after a certain penetration depth, both on the punch and the die. This static status holds for a certain period of time, where only scattered and undirected micro-cracks form. The duration of this state is also controlled by the cutting edge pairing. Just before the material separation, the crack propagation accelerates abruptly and finally leads to the consolidation of the macro-cracks. The stress peaks induced by sharper cutting edges seem to fade out within the material after crack initiation. Consequently different cutting edge preparations have an effect on crack initiation but do not influence the how fast the crack propagates through the sheet metal. I argue that with the fading of the stress peaks, a new stable state is established in the material, which prevents further crack propagation. Scattered and undirected growth of the micro-cracks further weakens the sheet metal material and promotes the present softening. Within the investigated parameter space, all other process parameters show significant influence on the crack propagation dynamics for closed cutting lines. In case of open cut lines, crack initiation takes place at the punch. The point of crack initiation is controlled by the rounding of the cutting edge on the punch in analogy to the closed cutting line. Against the closed cut, the crack propagation takes place at an almost constant velocity. The modified boundary condition prevents the formation of a new equilibrium state that prevents further crack growth. A second macro crack also develops on the die just before the material is finally separated.

8 Conclusion and Potentials

This thesis goes the complete way from the measurement concept, the raw data generation, the evaluation routines up to the results of the experimental investigations and their interpretation. Within these closed, consistent, and transparent framework, I conclude with the last question posed in section 3.2.

What consequences may be drawn for the modeling, design, and control of shear cutting from its dynamic behavior?

8.1 Modeling and Inverse Analysis

When modeling shear cutting, similar challenges arise as in the experimental observation, which I have briefly explained in section 3.1. With the vivid and detailed chapter 6 *Results*, this work provides a starting point and reference for process model conception. I disclosed all evaluation algorithms used, so that a specific classification of the presented results in the respective context is possible. Especially for the choice of constitutive laws, see section 2.1.3, the bandwidths of the kinematic state variables are decisive to select suitable material characterization experiments and robust extrapolation methods.

Inverse analyses use databases to determine model parameters. The implemented overall methodology is well suited for this purpose. The initial boundary value problem, see section 2.1.4, of shearing does not change much during the course of the process and is hence well-suited for inverse analysis. High-resolution temporal and spatial measurements of the shear cutting process exist, which drastically improves the condition of the inverse problem. Since the shear cutting experiment may be measured and evaluated from the beginning until final material separation, the database has a large information content and basically allows the inverse analysis of various constitutive models, or even tribological conditions, for example.

To prove and illustrate the possibilities of inverse analysis, I implemented a forward model of the shear cutting process. The static-implicit forward model calculates the cutting work as a function of the elastic constants, Young's modulus Y and Poisson's ratio ν, and thus solves the initial boundary value problem in an integral, hence weak form. The implemented model allows an inverse analysis using the sequence of Green strain tensor $\mathbf{E}$ fields in the shear affected
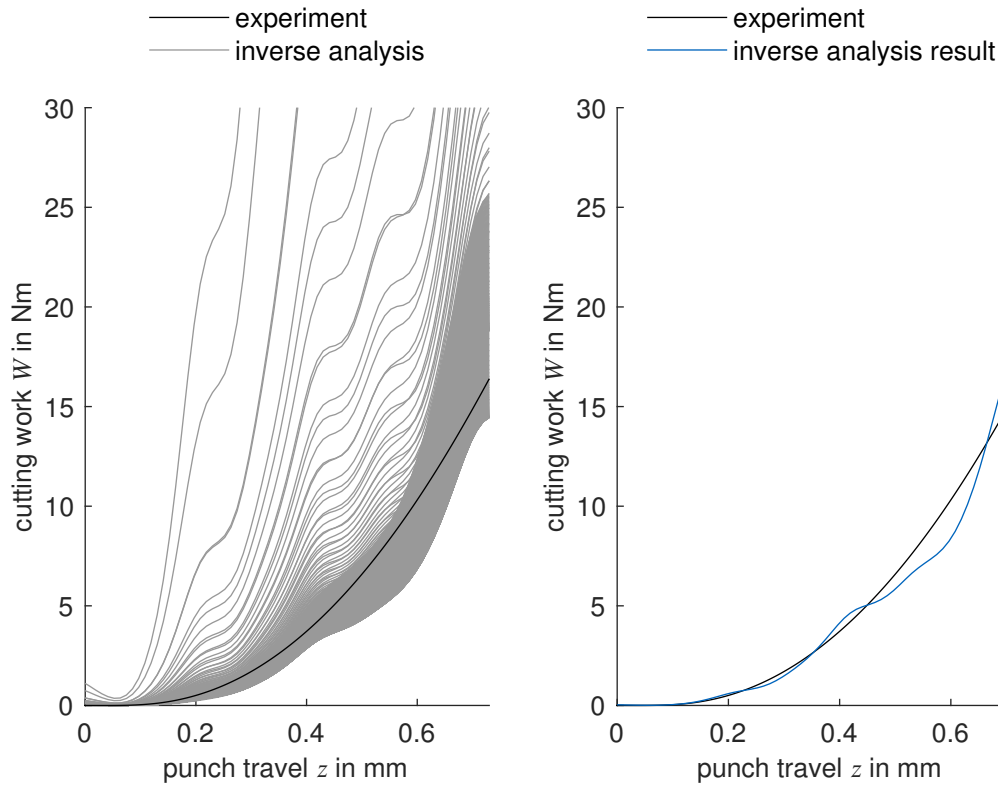
Figure 8.1: Cutting work W vs. punch travel z curves for inverse elastic constants identification.

zone. Since the model works purely elastically and statically, I ended the evaluation at the point A, where irreversible deformation enters the process. The modeling requirements for this inverse analysis are admittedly low, but the demands on data accuracy are high for inverse elastic analysis. Especially full-field, optical measured strains often fail in the elastic domain (Grédiac, 2004; Padmanabhan et al., 2006). Figure 8.1 shows the inverse analysis for the reference shear cutting experiment. Figure 8.1 a) gives a selection of calculated trials for the variation of the two elastic constants. The objective function of the inverse analysis minimizes the model error in the sense of the $\mathcal{L}_2$-norm. I used a straightforward optimization framework without regularization to solve for this parameter identification problem, see section 2.2.2. The value thus obtained for Young's modulus Y is 208.7 GPa, and the value for the Poisson's ratio v is 0.325. To assess the inverse analysis results I directly determined the two elastic constants of the sheet material using the enhanced methods provided by Vitzthum et al., 2019 for Young's modulus and Lechner et al., 2020 for Poisson's ratio, which I had the pleasure of being involved in. The direct measurement values of $Y = 210.4$ GPa and $v = 0.341$ agree by 0.7% and 4.7%, respectively, with the inverse analysis results. The strong coincidence illustrates on the one hand the power of experimentally determined databases and the possibilities that arise from the developed framework. On the

other hand, it further confirms the quality of the full-field measurement data, which even allow computations in the elastic strain domain.

The experimental setup and the developed algorithms also provide tools for comprehensive validation of numerical models for shear cutting. The temporal and spatial resolution is competitive with current state of the art resolutions achieved in the simulation of shearing processes. Especially with regard to numerical derivatives adjusted resolutions are essential for validation purposes. As a consistent variant for validation, I propose to use algorithm 7 as a preprocessor for numerical data. Algorithm 7 enables the generation of artificial image data directly from calculated displacement fields of simulation results. The artificial image data can then be evaluated analogously to the experimental data running through the entire measurement chain virtually. Since now both data sets possess the same evaluation history, consistent model validation is possible. Especially using the same methods to compute the partial derivatives of the continuum mechanics state variables is of importance. This methodology removes many imponderables from the validation chain.

8.2 Process Design and Control

Predictive models utilize databases to learn from or for pure validation purposes. Based on valid predictive models, process design and control is feasible. Process design pursues the robust and targeted setting of objective variables without further intervention during the duration of the process. Since the presented approach and methods allow validating and calibrating models additionally based on local dynamics new opportunities arise. Process design may be no longer tailored towards the cut surface characteristics φ alone, but also allow to derive target values for the shear affected zone $\mathbf{\Phi}$. As I have already outlined in section 2.4.3, the material motion in the shear affected zone definitely determines the properties of the shear affected zone, when no other external stimuli act on the material. Hence, the shear affected zone is uniquely determined and describable through the history of the kinematic state variables. The proposed experimental setup and evaluation routine traces the history of those variables and hence allow a systematic quantification of the field quality parameters $\mathbf{\Phi}(\mathbf{u}, \mathbf{E}, \dot{\mathbf{E}})$ of the shear affected zone. The coupling of quality parameters to kinematic state variables can be achieved within a comprehensive model, for example, such as in a coupled finite element simulation (Haiping et al., 2009; Schreiber and van Rienen, 2006), or subsequently by means of further investigations (Feistle et al., 2015; Weiss et al., 2017). Using the coupling, I reformulate the process model of shear cutting, see equation (2.59), in such a way that the target values can be optimized by varying the process

parameter input values $(\boldsymbol{\gamma}, \boldsymbol{\Gamma})$.

$$\mathbb{R}^c \to \mathbb{R}^p\,,\quad (\boldsymbol{\gamma}, \boldsymbol{\Gamma}) \mapsto (\boldsymbol{\varphi}(\mathbf{u}, \mathbf{E}, \dot{\mathbf{E}}), \boldsymbol{\Phi}(\mathbf{u}, \mathbf{E}, \dot{\mathbf{E}})) = \mathfrak{S}(\boldsymbol{\gamma}, \boldsymbol{\Gamma})\,. \tag{8.1}$$

In the case of process control, model-based adjustments take place within the process environment, for which various approaches exist (D. Pan et al., 2008; Sadoyan et al., 2006). Process measurements are one source to build up a database for process control models. Within the framework of process control, I show principles on how the presented experimental results can be transferred to practical use. In order to make the spatio-temporal measurements usable, especially with regard to process control, they must be coupled to classical measurements, such as the punch travel z or the cutting force F. These are robust, proven, and are already integrated as standard in industrial shear cutting tools. For the coupling, I employ the cutting work W as an integral process measure, as shown in chapter 6 *Results* for the respective experiments. The cutting work W contains both the cutting force F and the punch path z information. I generate characteristic tuples on the basis of the cutting energy W and kinematic state fields, which represent the corresponding state of the shear affected zone, described by $\boldsymbol{\Phi}(\mathbf{u}, \mathbf{E}, \dot{\mathbf{E}})$. By way of illustration, I characterize the condition of the shear affected zone by $\boldsymbol{\Phi}(\mathbf{u}, \mathbf{E}, \dot{\mathbf{E}}) = E_{\mathrm{eq}}$ without loss of generality. The database entries do not include the whole field, but basic elements. Therefore, I extract the temporally descriptive modes of E_{eq} using the dynamic mode decomposition (DMD) proposed by Schmid, 2010. The DMD uses the SVD in equation (2.33) as basis to build a low rank representation of the data. It obtains the eigenfaces of the equivalent strain field E_{eq} from its temporal evolution. The eigenfaces are the basic building blocks to calculate future predictions based on the currently available values of the cutting work W. Apart from the database and the current measured values, no additional information is given, i.e. no ordering or temporal components that could provide conclusions about the course of the shear cutting process. Figure 8.2 compares the results of the predictive calculations with the experimental results for the reference experiment. For the case under consideration, I used the measured values of the cutting work W between the evaluation points A and B as an input. The prediction reaches from the current evaluation point B by Δt_{p} into the future up to the point $\Delta t_{\mathrm{p}} = 0.6333$, which corresponds to the point C. The calculated fields show that in principle it is possible to predict the state of the shear affected zone from integral measurements, even using this basic straightforward approach. This outcome indicates besides the predictability[1] that basically the process is controllable from a measurement point of view.[2] With increasing distance from the current working point, the significance of the results decreases only slightly until Δt_{p}. In point C,

---

[1]This data-driven model also works offline with complete cutting work curves when process monitoring is concerned.

[2]Of course, the actuator side must also be taken into account for process control and represents an own challenge.

$\Delta t_{\mathrm{p}} = 0.1267\,\mathrm{s}$ $\Delta t_{\mathrm{p}} = 0.2533\,\mathrm{s}$ $\Delta t_{\mathrm{p}} = 0.3799\,\mathrm{s}$ $\Delta t_{\mathrm{p}} = 0.5066\,\mathrm{s}$ $\Delta t_{\mathrm{p}} = 0.6333\,\mathrm{s}$

a) experimental equivalent strain distribution
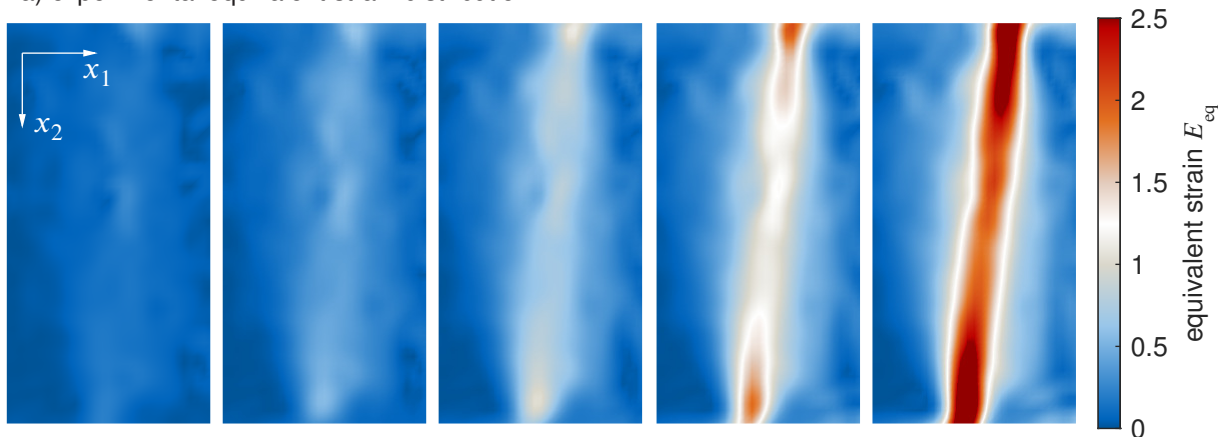
b) data-based model prediction
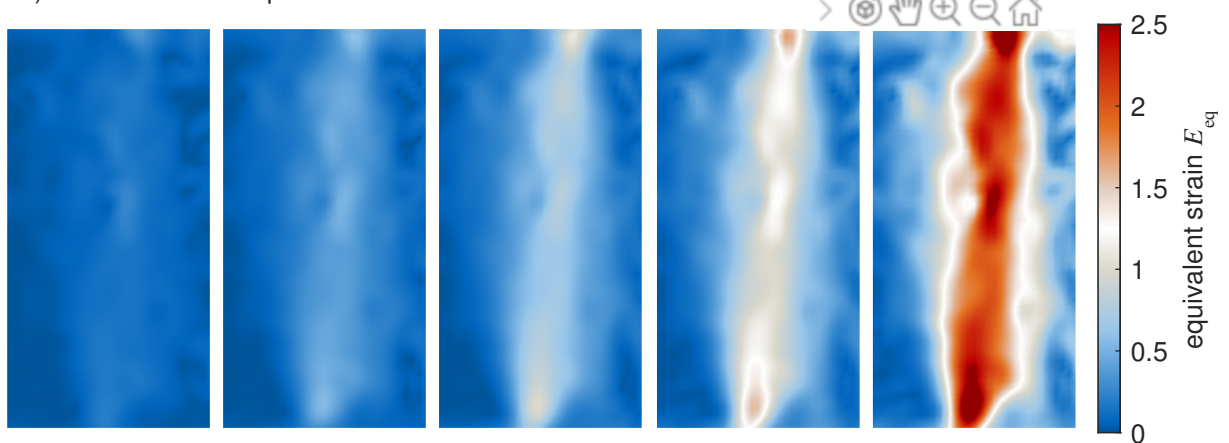
c) enhanced data-based model prediction
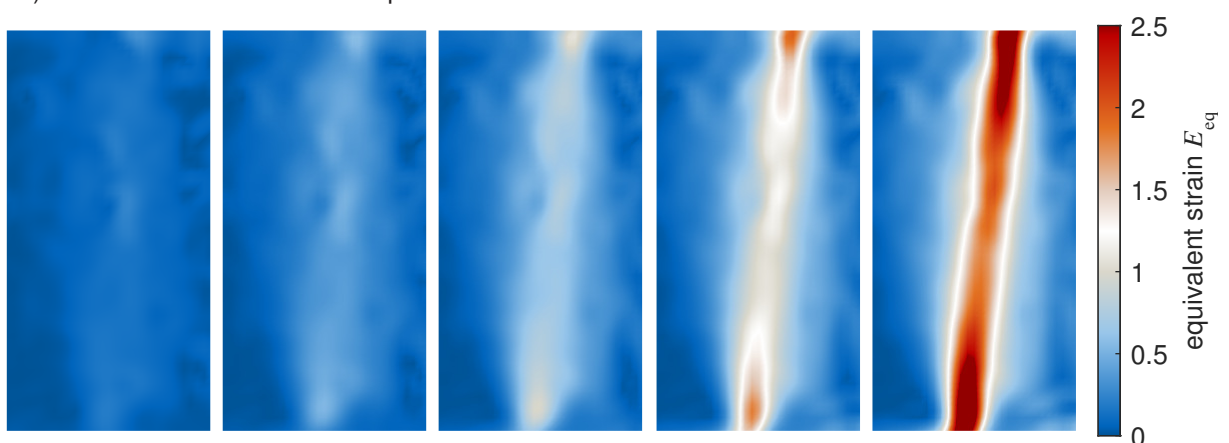
Figure 8.2: Equivalent strain E_{eq} distribution for the reference shear cutting process ahead of point B to point C. a) real experimental data. b) prediction based on data between point A and B, and c) prediction based on data between point A and B+$\Delta t_p = 0.5\,s$

however, the process behavior changes fundamentally with the onset of motion instability, so that the prediction based on the data available in point B fails, see figure 8.2 b).

However, when enlarging the database, the prediction quality may be increased again and the data-based model prediction of the development of the shear affected zone is in agreement with the experimental data, see figure 8.2 c). Data-based calculations depend on the quality of the database provided. Dependencies on the process variables (γ, Γ) can be achieved by extending the test spectrum, or by parameterization. Whether and in which format the data base of primary element combinations may be described in the variables (γ, Γ) remains open at this point. However, my coworkers and I have already successfully implemented such generalization for an ill-conditioned manufacturing process. An experimental primary element database suffice to compute complex tool paths for an incremental sheet metal free-forming process by using data-driven techniques (Hartmann et al., 2019; Hartmann and Volk, 2019c).

8.3 Enhanced Measurement Approaches

Variational methods in image processing, in particular spatio-temporal optical flow methods, open up completely new possibilities in full-field measurement. Especially in continuum mechanics derivatives play a key role in modeling, since differential calculus gives it its basic logic and language. Consistent and promising theories based on higher-order derivatives exist in large numbers, as for example the review of Hirschberger and Steinmann, 2009 describes. But practical implementation, validation, and determination of associated model parameters requires robust measurement technology to evaluate respective experiments.

In my opinion, spatio-temporal optical flow methods can fill this gap and provide robust measurement results of higher-order derivatives. Again I show two calculations of the local deformation curvature κ in figure 8.3 to support my statement. Figure 8.3 a) and b) illustrates the effect of different cutting clearances on the deformation curvature distribution, where the results are well-behaved and even indicate the reach of the shear affected zone as well as the deformation band geometry. Same applies to steel experiments, which I exemplify using an experiment with 6% cutting clearance, see figure 8.3 c). The deformation curvature κ represents a quantity that falls into the so called gradient continuum, for which no additional spatial degrees of freedom needs to be introduced in classical modeling frameworks (Kirchner and Steinmann, 2005). However, the higher-order boundary conditions causing problems in numerical implementations maybe could be addressed jointly through spatio-temporal regularization approaches.
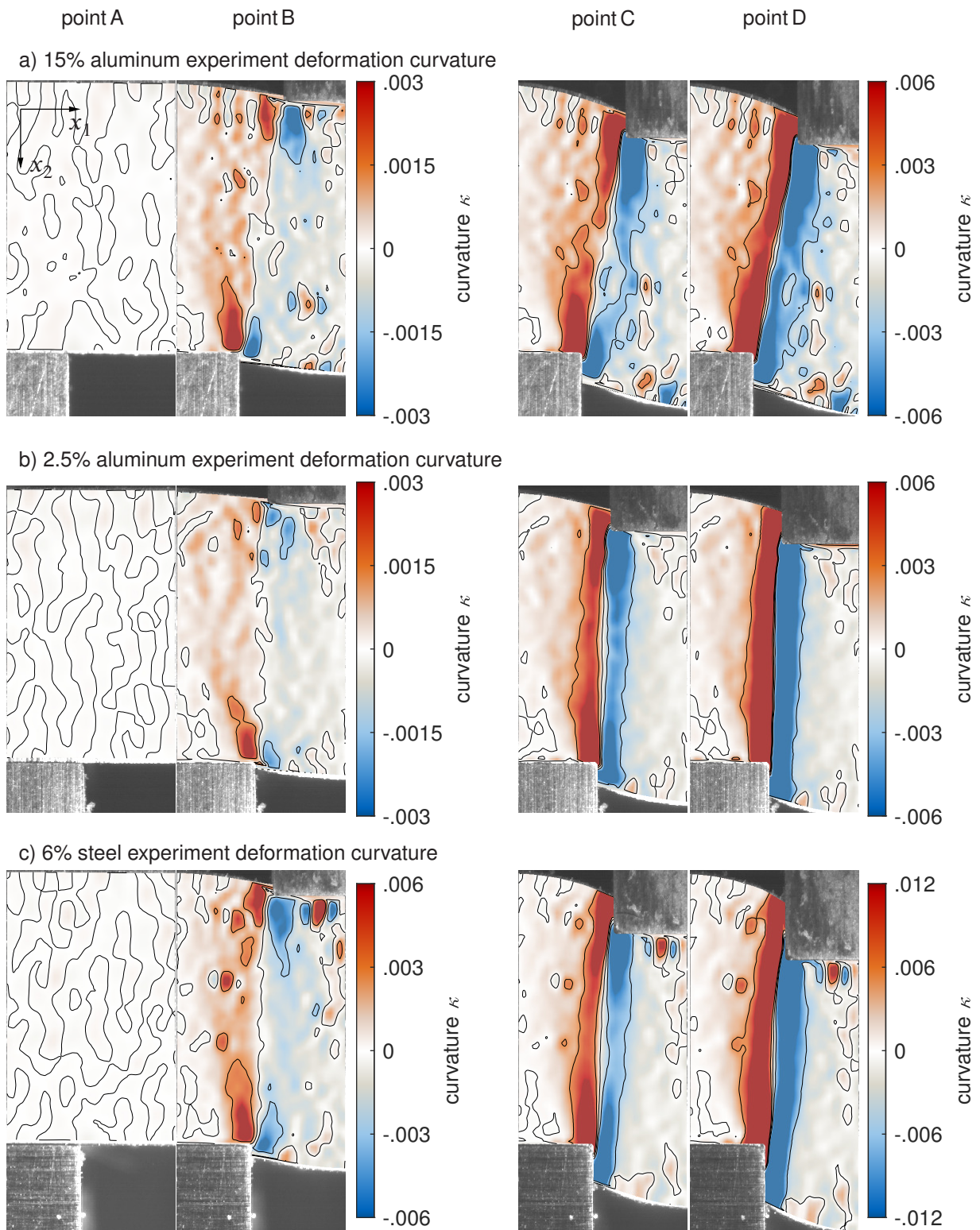
Figure 8.3: Deformation curvature κ distribution for closed cutting line experiments. a) aluminum EN AW 5083 using 15% cutting clearance, b) aluminum EN AW 5083 using 2.5% cutting clearance, and c) steel S355MC using 6% cutting clearance.

8.4 Outlook

With the spatio-temporal framework for process analysis, I provide for the first time a test arrangement and holistic evaluation routine to record the kinematic state variables in shear cutting. Besides the dynamics and localization phenomena of the deformation, the hybrid evaluation routine developed also resolves the initiation, propagation, and consolidation of cracks. Hence, the complex behavior of the shear cutting process could be revealed from the beginning until complete material separation. The created methodologies and research results serve as a departure for further investigations and a starting point for new fields of research.

I see a broad field of application in experimental mechanics for the developed spatio-temporal, hybrid evaluation routine that measures highly dynamic processes that induce large deformations and where also fracture evolution is critical. In particular, material parameter identification experiments that covers a large spectrum of strains and strain rates are predestined fields of application. Furthermore, the proposed methods also do not require any interfering artificial speckle patterns, what may additionally widen the scope. In the work of Lechner et al., 2020, we already used parts of algorithm 1 in a different experimental context to detect crack initiation and to validate fracture strain values of brittle material.

The hybrid use of block-matching and variational methods emphasizes the strengths of each method. Variational approaches provide the possibility to bring in additional information using the modeling capacities of the regularization. I see chances to incorporate prior knowledge for example about the test object or the process directly into the measurement. The basic concept behind that is what I aimed also to show within this thesis: measurement needs to be understood as a part of modeling in the descriptive framework at hand. In my opinion, the incorporation of prior knowledge can be done in many ways and the potential of this approach is currently not exhausted and even barely touched. As an example, I would like to mention the trend of sensor data fusion. The regularization term gives the possibility to couple different sensor systems in order to improve the signal quality of the overall system. The continuum mechanics framework couples motion and temperature through first and second law of thermodynamics, see equation (2.22) and inequality (2.24). I suspect that the introduction of temperature-coupled regularization terms may enhance experimental practice, especially for systems that allow high-resolution temperature measurements but are difficult to observe in terms of motion analysis. These coupling terms could be integrated straightforward into the existing evaluation framework.

I have already prepared temperature measurements in the developed shear cutting tool. The

installed ceramic plates insulate the blank holder, the punch, and the die from the rest of the shear cutting tool, so that the highly dynamic temperature measurement by Demmel, 2014 may be carried out. The thermomechanical measurement data generate further fields of application for inverse analysis of materials in general. In my opinion, the experimental setup should be regarded as a novel test rig that can be used beneficial in materials testing even apart from the shearing process. Combined with inverse analysis dynamic, high strain, and fracture testing under defined loading and boundary conditions is possible. When combining the developed evaluation routine with temperature measurement and inverse analysis, in my opinion, it even may be possible to decouple strain, strain rate, temperature, and damage phenomena. This would also contribute to the still open discussion on the behavior of the Taylor-Quinney coefficient.

In terms of production engineering, I see the whole research approach, developed test arrangement, and measurement methods as a role model for the experimental, data-driven analysis of manufacturing processes. Especially processes that may also assume a plane strain boundary condition are obvious to adapt the conducted approach, such as bending operations or broaching.

8.5 Closing Statement

On the meta-level, I have designed and implemented a holistic framework that allows in situ analysis of a complex process. This was only possible through open-mindedness towards new ideas and interdisciplinary methods. The omnipresent data-driven approaches point in the same direction and need such closed and consistent measurement data as a basic foundation. The possibilities to observe and quantify higher-order derivatives and complex phenomena will also determine the modeling, the design, and the control of complex processes. I hope that my work will provide other researchers and engineers a helpful blueprint for approaching and implementing such experimental analysis.

A List of Figures

B List of Tables

C List of Algorithms

D Bibliography

ABRAHAM, R. and J. MARSDEN (2008). *Foundations of Mechanics*. Providence: American Mathematical Society.

AKAIKE, H. (1974). "A new look at the statistical model identification". In: *IEEE Transactions on Automatic Control* 19 (6), pp. 716–723.

ALTENBACH, H. (2015). *Kontinuumsmechanik*. Berlin, Heidelberg: Springer.

AMIOT, F., M. BORNERT, P. DOUMALIN, J.-C. DUPRÉ, M. FAZZINI, J.-J. ORTEU, C. POILÂNE, L. ROBERT, R. ROTINAT, E. TOUSSAINT, B. WATTRISSE, and J. WIENIN (2013). "Assessment of Digital Image Correlation Measurement Accuracy in the Ultimate Error Regime: Main Results of a Collaborative Benchmark". In: *Strain* 49 (6), pp. 483–496.

ANANDAN, P. (1989). "A computational framework and an algorithm for the measurement of visual motion". In: *International Journal of Computer Vision* 2 (3), pp. 283–310.

ANDERSSEN, R. and P. BLOOMFIELD (1974). "Numerical differentiation procedures for non-exact data". In: *Numerische Mathematik* 22 (3), pp. 157–182.

AOKI, I. and T. TAKAHASHI (2003). "Material flow analysis on shearing process by applying Fourier phase correlation method—analysis of piercing and fine-blanking". In: *Journal of Materials Processing Technology* 134 (1), pp. 45–52.

APPEL, K. and W. HAKEN (1977). "Every planar map is four colorable. Part I: Discharging". In: *Illinois Journal of Mathematics* 21 (3), pp. 429–490.

APPEL, K., W. HAKEN, and J. KOCH (1977). "Every planar map is four colorable. Part II: Reducibility". In: *Illinois Journal of Mathematics* 21 (3), pp. 491–567.

ARLOT, S. and A. CELISSE (2010). "A survey of cross-validation procedures for model selection". In: *Statistics Surveys* 4, pp. 40–79.

ARRIAGA, M. and H. WAISMAN (2017). "Combined stability analysis of phase-field dynamic fracture and shear band localization". In: *International Journal of Plasticity* 96, pp. 81–119.

ASARO, R. and J. RICE (1977). "Strain localization in ductile single crystals". In: *Journal of the Mechanics and Physics of Solids* 25 (5), pp. 309–338.

ATKINS, A. (1980). "On cropping and related processes". In: *International Journal of Mechanical Sciences* 22 (4), pp. 215–231.

AUBERT, G. and P. KORNPROBST (1999). "A Mathematical Study of the Relaxed Optical Flow Problem in the Space BV(Ω)". In: *SIAM Journal on Mathematical Analysis* 30 (6), pp. 1282–1308.

AUERBACH, T., M. BECKERS, G. BUCHHOLZ, U. EPPELT, Y.-S. GLOY, P. FRITZ, T. AL KHAWLI, S. KRATZ, J. LOSE, T. MOLITOR, A. RESSMANN, U. THOMBANSEN, D. VESELOVAC, K. WILLMS, T. GRIES, W. MICHAELI, C. HOPMANN, U. REISGEN, R. SCHMITT, and F. KLOCKE (2011). "Meta-modeling for Manufacturing Processes". In: *Intelligent Robotics and Applications*. Ed. by S. JESCHKE, H. LIU, and D. SCHILBERG. Vol. 7102. Lecture Notes in Computer Science. Berlin, Heidelberg: Springer, pp. 199–209.

AVRIL, S., M. BONNET, A.-S. BRETELLE, M. GRÉDIAC, F. HILD, P. IENNY, F. LA-TOURTE, D. LEMOSSE, S. PAGANO, E. PAGNACCO, and F. PIERRON (2008). "Overview of Identification Methods of Mechanical Parameters Based on Full-field Measurements". In: *Experimental Mechanics* 48 (4), pp. 381–402.

BACH, E. (1924). *Die Spannungen unter einem kreisrunden Stempel, PhD thesis*. Karlsruhe.

BAI, T., H. YAN, X. JIA, S. JIANG, G. WANG, and X. MOU (2017). "Z-Index Parameterization for Volumetric CT Image Reconstruction via 3-D Dictionary Learning". In: *IEEE Transactions on Medical Imaging* 36 (12), pp. 2466–2478.

BAKER, S. and I. MATTHEWS (2001). "Equivalence and efficiency of image alignment algorithms". In: *Conference on Computer Vision and Pattern Recognition*. IEEE, pp. 1090–1097.

– (2004). "Lucas-Kanade 20 Years On: A Unifying Framework". In: *International Journal of Computer Vision* 56 (3), pp. 221–255.

BALLE, F., T. BECK, D. EIFLER, J. FITSCHEN, S. SCHUFF, and G. STEIDL (2019). "Strain analysis by a total generalized variation regularized optical flow model". In: *Inverse Problems in Science and Engineering* 27 (4), pp. 540–564.

BALLE, F., D. EIFLER, J. FITSCHEN, S. SCHUFF, and G. STEIDL (2015). "Computation and Visualization of Local Deformation for Multiphase Metallic Materials by Infimal Convolution of TV-Type Functionals". In: *Scale Space and Variational Methods in Computer Vision*. Ed. by J.-F. AUJOL, M. NIKOLOVA, and N. PAPADAKIS. Cham: Springer, pp. 385–396.

BARENBLATT, G. (1962). "The Mathematical Theory of Equilibrium Cracks in Brittle Fracture". In: *Advances in Applied Mechanics*. Vol. 7. Elsevier, pp. 55–129.

BARRON, J., D. FLEET, and S. BEAUCHEMIN (1994). "Performance of optical flow techniques". In: *International Journal of Computer Vision* 12 (1), pp. 43–77.

BAUER, H., F. BRANDL, C. LOCK, and G. REINHART (2018). "Integration of Industrie 4.0 in Lean Manufacturing Learning Factories". In: *Procedia Manufacturing* 23, pp. 147–152.

BAZANT, Z. (1998). "Easy-to-Compute Tensors With Symmetric Inverse Approximating Hencky Finite Strain and Its Rate". In: *Journal of Engineering Materials and Technology* 120 (2), pp. 131–136.

BELL, G., T. HEY, and A. SZALAY (2009). "Computer science. Beyond the data deluge". In: *Science* 323 (5919), pp. 1297–1298.

BEN ISMAIL, A., M. RACHIK, P.-E. MAZERAN, M. FAFARD, and E. HUG (2009). "Material characterization of blanked parts in the vicinity of the cut edge using nanoindentation technique and inverse analysis". In: *International Journal of Mechanical Sciences* 51 (11-12), pp. 899–906.

BIGUN, J., G. GRANLUND, and J. WIKLUND (1991). "Multidimensional orientation estimation with applications to texture analysis and optical flow". In: *IEEE Transactions on Pattern Analysis and Machine Intelligence* 13 (8), pp. 775–790.

BIOT, M. (1958). "Linear Thermodynamics and the Mechanics of Solids". In: *United States National Congress of Applied Mechanics*. Vol. 6, pp. 1–18.

BLABER, J., B. ADAIR, and A. ANTONIOU (2015). "Ncorr: Open-Source 2D Digital Image Correlation Matlab Software". In: *Experimental Mechanics* 55 (6), pp. 1105–1122.

BLACK, M. and P. ANANDAN (1991). "Robust dynamic motion estimation over time". In: *Conference on Computer Vision and Pattern Recognition*. IEEE, pp. 296–302.

– (1996). "The Robust Estimation of Multiple Motions: Parametric and Piecewise-Smooth Flow Fields". In: *Computer Vision and Image Understanding* 63 (1), pp. 75–104.

BÖCK, N. and G. HOLZAPFEL (2004). "A new two-point deformation tensor and its relation to the classical kinematical framework and the stress concept". In: *International Journal of Solids and Structures* 41 (26), pp. 7459–7469.

BOHDAL, L., L. KUKIELKA, K. KUKIELKA, A. KUŁAKOWSKA, L. MALAG, and R. PATYK (2014). "Three Dimensional Finite Element Simulation of Sheet Metal Blanking Process". In: *Applied Mechanics and Materials* 474, pp. 430–435.

BOLKA, S., J. SLAVIČ, and M. BOLTEŽAR (2015). "Identification of Out-of-Plane Material Characteristics through Sheet-Metal Blanking". In: *Strojniški vestnik – Journal of Mechanical Engineering* 61 (4), pp. 217–226.

BOTEV, Z., J. GROTOWSKI, and D. KROESE (2010). "Kernel density estimation via diffusion". In: *Annals of Statistics* 38 (5), pp. 2916–2957.

BREDIES, K., K. KUNISCH, and T. POCK (2010). "Total Generalized Variation". In: *SIAM Journal on Imaging Sciences* 3 (3), pp. 492–526.

BRO, R. (1997). "PARAFAC. Tutorial and applications". In: *Chemometrics and Intelligent Laboratory Systems* 38 (2), pp. 149–171.

BRO, R. and H. KIERS (2003). "A new efficient method for determining the number of components in PARAFAC models". In: *Journal of Chemometrics* 17 (5), pp. 274–286.

BROKKEN, D., W. BREKELMANS, and F. BAAIJENS (2000). "Discrete ductile fracture modelling for the metal blanking process". In: *Computational Mechanics* 26 (1), pp. 104–114.

BROX, T., A. BRUHN, N. PAPENBERG, and J. WEICKERT (2004). "High Accuracy Optical Flow Estimation Based on a Theory for Warping". In: *European Conference on Computer Vision*. Ed. by T. KANADE, J. KITTLER, J. M. KLEINBERG, F. MATTERN, J. MITCHELL, O. NIERSTRASZ, C. PANDU RANGAN, B. STEFFEN, M. SUDAN, D. TERZOPOULOS, D. TYGAR, M. VARDI, G. WEIKUM, T. PAJDLA, and J. MATAS. Vol. 3024. Lecture Notes in Computer Science. Berlin, Heidelberg: Springer, pp. 25–36.

BROX, T. and J. MALIK (2011). "Large displacement optical flow: descriptor matching in variational motion estimation". In: *IEEE Transactions on Pattern Analysis and Machine Intelligence* 33 (3), pp. 500–513.

BRUHN, A. and J. WEICKERT (2005). "Towards ultimate motion estimation: combining highest accuracy with real-time performance". In: *International Conference on Computer Vision*. Vol. 1. IEEE, pp. 749–755.

BRUHN, A., J. WEICKERT, T. KOHLBERGER, and C. SCHNÖRR (2006). "A Multigrid Platform for Real-Time Motion Computation with Discontinuity-Preserving Variational Methods". In: *International Journal of Computer Vision* 70 (3), pp. 257–277.

BRUNTON, S. and J. KUTZ (2019). *Data-Driven Science and Engineering*. Vol. 237. Cambridge University Press.

BUCHMANN, K. (1962). *Beitrag zur Verschleißbeurteilung beim Schneiden von Stahlfeinblechen*. Köln, Opladen: Westdeutscher Verlag.

– (1963). "Über den Einfluß einiger Schneidbedingungen auf den Werkzeugverschleiß beim Schneiden von Stahlfeinblechen im geschlossenen Schnitt". In: *Werkstattstechnik* 53 (11), pp. 561–565.

BÜHLER, H. and F. POLLMAR (1971). "Die Gratbildung beim Schneiden von Feinblech". In: *Bänder Bleche Rohre* 12 (3), pp. 105–111.

BURNHAM, K. and D. ANDERSON (2010). *Model selection and multimodel inference: A practical information-theoretic approach*. 2nd ed. New York: Springer.

BURT, P. and E. ADELSON (1983). "The Laplacian Pyramid as a Compact Image Code". In: *IEEE Transactions on Communications* 31 (4), pp. 532–540.

BUTCHER, C. and A. ABEDINI (2017). "Shear confusion: Identification of the appropriate equivalent strain in simple shear using the logarithmic strain measure". In: *International Journal of Mechanical Sciences* 134, pp. 273–283.

CHAMBOLLE, A. and T. POCK (2011). "A First-Order Primal-Dual Algorithm for Convex Problems with Applications to Imaging". In: *Journal of Mathematical Imaging and Vision* 40 (1), pp. 120–145.

CHARBONNIER, P., L. BLANC-FERAUD, G. AUBERT, and M. BARLAUD (1994). "Two deterministic half-quadratic regularization algorithms for computed imaging". In: *International Conference on Image Processing*. IEEE, pp. 168–172.

CHARTRAND, R. (2011). "Numerical Differentiation of Noisy, Nonsmooth Data". In: *ISRN Applied Mathematics* 2011 (1-4), pp. 1–11.

– (2017). "Numerical differentiation of noisy, nonsmooth, multidimensional data". In: *Global Conference on Signal and Information Processing*. IEEE, pp. 244–248.

CHARTRAND, R. and V. STANEVA (2008). "Total variation regularisation of images corrupted by non-Gaussian noise using a quasi-Newton method". In: *IET Image Processing* 2 (6), pp. 295–303.

CHEN, Z. and S. HAYKIN (2002). "On different facets of regularization theory". In: *Neural Computation* 14 (12), pp. 2791–2846.

CHEN, Z., L. CHAN, T. LEE, and C. TANG (2003). "An investigation on the formation and propagation of shear band in fine-blanking process". In: *Journal of Materials Processing Technology* 138 (1-3), pp. 610–614.

CHEN, Z., C. TANG, T. LEE, and L. CHAN (1999). "A study of strain localization in the fine-blanking process using the large deformation finite element method". In: *Journal of Materials Processing Technology* 86 (1-3), pp. 163–167.

CHU, C. and A. NEEDLEMAN (1980). "Void Nucleation Effects in Biaxially Stretched Sheets". In: *Journal of Engineering Materials and Technology* 102 (3), pp. 249–256.

CHU, T., W. RANSON, and M. SUTTON (1985). "Applications of digital-image-correlation techniques to experimental mechanics". In: *Experimental Mechanics* 25 (3), pp. 232–244.

CIRP (2019). *Dictionary of Production Engineering I / Wörterbuch der Fertigungstechnik I / Dizionario di Ingegneria della Produzione I*. Berlin, Heidelberg: Springer.

CLAUSIUS, R. (1865). "Ueber verschiedene für die Anwendung bequeme Formen der Hauptgleichungen der mechanischen Wärmetheorie". In: *Annalen der Physik und Chemie* 201 (7), pp. 353–400.

CLEVELAND, W. (1979). "Robust Locally Weighted Regression and Smoothing Scatterplots". In: *Journal of the American Statistical Association* 74 (368), pp. 829–836.

– (2001). "Data Science: an Action Plan for Expanding the Technical Areas of the Field of Statistics". In: *International Statistical Review* 69 (1), pp. 21–26.

CLOCKSIN, W., J. QUINTA DA FONSECA, P. WITHERS, and P. TORR (2002). "Image Processing Issues in Digital Strain Mapping". In: *Applications of Digital Image Processing XXV*. Ed. by A. G. TESCHER. SPIE Proceedings. SPIE, pp. 384–395.

COCKROFT, M. and D. LATHAM (1968). "Ductility and the workability of metals". In: *Journal of the Institute of Metals* 96, pp. 33–39.

CORPETTI, T., E. MEMIN, and P. PEREZ (2002). "Dense estimation of fluid flows". In: *IEEE Transactions on Pattern Analysis and Machine Intelligence* 24 (3), pp. 365–380.

CRUMP, T., G. FERTÉ, A. JIVKOV, P. MUMMERY, and V.-X. TRAN (2017). "Dynamic fracture analysis by explicit solid dynamics and implicit crack propagation". In: *International Journal of Solids and Structures* 110-111, pp. 113–126.

CULLUM, J. (1971). "Numerical Differentiation and Regularization". In: *IET Image Processing* 8 (2), pp. 254–265.

CURNIER, A. and L. RAKOTOMANANA (1991). "Generalized Strain and Stress Measures : Critical Survey and New Results". In: *Engineering Transactions* 39 (3-4), pp. 461–538.

CURNIER, A. and P. ZYSSET (2006). "A family of metric strains and conjugate stresses, prolonging usual material laws from small to large transformations". In: *International Journal of Solids and Structures* 43 (10), pp. 3057–3086.

DEMMEL, P. (2014). *In-situ Temperaturmessung beim Scherschneiden, PhD thesis*. Vol. 65. München: Hieronymus.

DEMMEL, P., H. HOFFMANN, R. GOLLE, C. INTRA, and W. VOLK (2015). "Interaction of heat generation and material behaviour in sheet metal blanking". In: *CIRP Annals* 64 (1), pp. 249–252.

DOEGE, E. and B.-A. BEHRENS (2010). *Handbuch Umformtechnik*. Berlin, Heidelberg: Springer.

DOEGE, E., K.-H. SCHMIDT, and C.-P. NEUMANN (1977). "Ein Beitrag zur Beurteilung der Schneidbarkeit von Elektroblech – Schwingungsfreier Schneidvorgang". In: *Blech Rohre Profile* (10), pp. 382–387.

DOYLE, T. and J. ERICKSEN (1956). "Nonlinear Elasticity". In: *Advances in Applied Mechanics*. Vol. 4. Advances in Applied Mechanics. Elsevier, pp. 53–115.

DUBUISSON, M.-P. and A. JAIN (1994). "A modified Hausdorff distance for object matching". In: *International Conference on Pattern Recognition*. Vol. 12. IEEE, pp. 566–568.

DZIAK, J., D. COFFMAN, S. LANZA, R. LI, and L. JERMIIN (2020). "Sensitivity and specificity of information criteria". In: *Briefings in Bioinformatics* 21 (2), pp. 553–565.

ECKART, C. and G. YOUNG (1936). "The approximation of one matrix by another of lower rank". In: *Psychometrika* 1 (3), pp. 211–218.

EGNER, H. (2012). "On the full coupling between thermo-plasticity and thermo-damage in thermodynamic modeling of dissipative materials". In: *International Journal of Solids and Structures* 49 (2), pp. 279–288.

FARNEBÄCK, G. (2001). "Very high accuracy velocity estimation using orientation tensors, parametric motion, and simultaneous segmentation of the motion field". In: *International Conference on Computer Vision*. IEEE, pp. 171–177.

– (2003). "Two-Frame Motion Estimation Based on Polynomial Expansion". In: *Image Analysis*. Ed. by G. GOOS, J. HARTMANIS, J. VAN LEEUWEN, J. BIGUN, and T. GUSTAVSSON. Vol. 2749. Lecture Notes in Computer Science. Berlin, Heidelberg: Springer, pp. 363–370.

FARREN, W. and I. TAYLOR (1925). "The heat developed during plastic extension of metals". In: *Proceedings of the Royal Society of London. Series A* 107 (743), pp. 422–451.

FEISTLE, M., M. KRINNINGER, I. PÄTZOLD, and W. VOLK (2015). "Edge-Fracture-Tensile-Test". In: *60 Excellent Inventions in Metal Forming*. Ed. by A. TEKKAYA, W. HOMBERG, and A. BROSIUS. Berlin, Heidelberg: Springer, pp. 193–198.

FERNANDEZ, N. (2018). "Two-stream convolutional networks for end-to-end learning of self driving cars". In: *arxiv* 2 (1811.05785), pp. 1–5.

FISHER, R. (1922). "On the mathematical foundations of theoretical statistics". In: *Philosophical Transactions of the Royal Society of London. Series A* 222 (594-604), pp. 309–368.

FLETCHER, R. (1976). "Conjugate gradient methods for indefinite systems". In: *Numerical Analysis*. Ed. by G. WATSON. Vol. 506. Lecture Notes in Mathematics. Berlin, Heidelberg: Springer, pp. 73–89.

FLÜGGE, S. (1960). *Principles of Classical Mechanics and Field Theory / Prinzipien der Klassischen Mechanik und Feldtheorie*. Vol. 2 / 3 / 1. Berlin, Heidelberg: Springer.

FLÜGGE, S., C. TRUESDELL, and W. NOLL (1965). *The Non-Linear Field Theories of Mechanics / Die Nicht-Linearen Feldtheorien der Mechanik*. Vol. 2 / 3 / 3. Berlin, Heidelberg: Springer.

FORSSTRÖM, A., S. BOSSUYT, G. SCOTTI, and H. HÄNNINEN (2020). "Quantifying the Effectiveness of Patterning, Test Conditions, and DIC Parameters for Characterization of Plastic Strain Localization". In: *Experimental Mechanics* 60 (1), pp. 3–12.

FRASER, C. (1992). "lsoperimetric Problems in the Variational Calculus of Euler and Lagrange". In: *Historia Mathematica* 19, pp. 4–23.

FREUDENTHAL, A. (1950). *The Inelastic Behavior of Engineering Materials and Structures*. New York: John Wiley & Sons, Ltd.

FROHN-SCHAUF, C., S. HENN, and K. WITSCH (2004). "Nonlinear multigrid methods for total variation image denoising". In: *Computing and Visualization in Science* 7 (3-4), pp. 199–206.

GABAY, D. and B. MERCIER (1976). "A dual algorithm for the solution of nonlinear variational problems via finite element approximation". In: *Computers & Mathematics with Applications* 2 (1), pp. 17–40.

GALTON, F. (1886). "Towards Mediocrity in Hereditary Stature". In: *Journal of the Anthropological Institute of Great Britain and Ireland* 15, pp. 246–263.

GARCIA, D. (2010). "Robust smoothing of gridded data in one and higher dimensions with missing values". In: *Computational Statistics and Data Analysis* 54 (4), pp. 1167–1178.

GAVISH, M. and D. DONOHO (2014). "The Optimal Hard Threshold for Singular Values". In: *IEEE Transactions on Information Theory* 60 (8), pp. 5040–5053.

GERMAIN, P., Q. NGUYEN, and P. SUQUET (1983). "Continuum Thermodynamics". In: *Journal of Applied Mechanics* 50 (4b), pp. 1010–1020.

GHADBEIGI, H., A. AL-RUBAYE, F. ROBINSON, D. HAWEZY, S. BIROSCA, and K. ATALLAH (2020). "Blanking induced damage in thin 3.2% silicon steel sheets". In: *Production Engineering* 14 (1), pp. 53–64.

GIACHETTI, A. (2000). "Matching techniques to compute image motion". In: *Image and Vision Computing* 18 (3), pp. 247–260.

GIBBS, J. (1884). "On the fundamental formula of statistical mechanics, with applications to astronomy and thermodynamics". In: *Proceedings of the American Association for the Advancement of Science* 33, pp. 57–58.

GIBSON, J. (1950). *The perception of the visual world*. Cambridge: The Riverside Press.

GIROSI, F., M. JONES, and T. POGGIO (1995). "Regularization Theory and Neural Networks Architectures". In: *Neural Computation* 7 (2), pp. 219–269.

GOIJAERTS, A. (1999). *Prediction of ductile fracture in metal blanking, PhD thesis*. Eindhoven.

GOIJAERTS, A., L. GOVAERT, and F. BAAIJENS (2000). "Prediction of Ductile Fracture in Metal Blanking". In: *Journal of Manufacturing Science and Engineering* 122 (3), pp. 476–483.

GONZÁLEZ, D., F. CHINESTA, and E. CUETO (2019). "Thermodynamically consistent data-driven computational mechanics". In: *Continuum Mechanics and Thermodynamics* 31 (1), pp. 239–253.

GOTOH, M. and M. YAMASHITA (2001). "A study of high-rate shearing of commercially pure aluminum sheet". In: *Journal of Materials Processing Technology* 110 (3), pp. 253–264.

GRAY, J. (2007). *eScience: A Transformed Scientific Method*. Mountain View, United States.

GRÉDIAC, M. (2004). "The use of full-field measurement methods in composite material characterization: interest and limitations". In: *Composites Part A: Applied Science and Manufacturing* 35 (7-8), pp. 751–761.

GREEN, M. (2002). "Statistics of images, the TV algorithm of Rudin-Osher-Fatemi for image denoising and an improved denoising algorithm: (Tech. Rep.)" In: *UCLA Computational and Applied Mathematics* 55, pp. 1–40.

GREVE, R. (2003). *Kontinuumsmechanik*. Berlin, Heidelberg: Springer.

GU, C. and G. WAHBA (1991). "Minimizing GCV/GML Scores with Multiple Smoothing Parameters via the Newton Method". In: *SIAM Journal on Scientific and Statistical Computing* 12 (2), pp. 383–398.

GUCKENHEIMER, J. and P. HOLMES (1983). *Nonlinear Oscillations, Dynamical Systems, and Bifurcations of Vector Fields*. Vol. 42. New York: Springer.

GURSON, A. (1977). "Continuum Theory of Ductile Rupture by Void Nucleation and Growth: Part I—Yield Criteria and Flow Rules for Porous Ductile Media". In: *Journal of Engineering Materials and Technology* 99 (1), pp. 2–15.

GURTIN, M. and W. WILLIAMS (1966). "On the Clausius-Duhem inequality". In: *ZAMP Zeitschrift für angewandte Mathematik und Physik* 17 (5), pp. 626–633.

GUSTAFSSON, E., L. KARLSSON, and M. OLDENBURG (2016). "Experimental study of forces and energies during shearing of steel sheet with angled tools". In: *International Journal of Mechanical and Materials Engineering* 11 (10), pp. 1–12.

HADAMARD, J. (1903). *Lecons sur la propagation des ondes et les equations de l'hydrodynamique*. Paris: College de France.

HAIPING, Y., L. CHUNFENG, and D. JIANGHUA (2009). "Sequential coupling simulation for electromagnetic–mechanical tube compression by finite element analysis". In: *Journal of Materials Processing Technology* 209 (2), pp. 707–713.

HALPHEN, B. and Q. NGUYEN (1975). "Sur les Matériaux Standard Généralisés". In: *Journal de Mécanique* 14 (1), pp. 39–63.

HAMADA, S., K. ZHANG, J. ZHANG, M. KOYAMA, T. YOKOI, and H. NOGUCHI (2018). "Effect of shear-affected zone on fatigue crack propagation mode". In: *International Journal of Fatigue* 116, pp. 36–47.

HAMBLI, R. (2001). "Finite element model fracture prediction during sheet-metal blanking processes". In: *Engineering Fracture Mechanics* 68 (3), pp. 365–378.

HAMBLI, R. and A. POTIRON (2000). "Finite element modeling of sheet-metal blanking operations with experimental verification". In: *Journal of Materials Processing Technology* 102 (1-3), pp. 257–265.

HAMBLI, R. and M. RESZKA (2002). "Fracture criteria identification using an inverse technique method and blanking experiment". In: *International Journal of Mechanical Sciences* 44 (7), pp. 1349–1361.

HAMEL, G. (1908). "Über die Grundlagen der Mechanik". In: *Mathematische Annalen* 66 (3), pp. 350–397.

HANKE, M. and O. SCHERZER (2001). "Inverse Problems Light: Numerical Differentiation". In: *American Mathematical Monthly* 108 (6), pp. 512–521.

HARSHMAN, R. (1970). "Foundations of the PARAFAC procedure: Model and conditions for an 'explanatory' multi-mode factor analysis". In: *UCLA Working Papers in Phonetics* 16 (1), pp. 1–84.

HARTMANN, C., M. EDER, D. OPRITESCU, D. MAIER, M. SANTAELLA, and W. VOLK (2018). "Geometrical compensation of deterministic deviations for part finishing in bulk forming". In: *Journal of Materials Processing Technology* 261, pp. 140–148.

HARTMANN, C., M. EDER, D. OPRITESCU, and W. VOLK (2017). "Process-integrated Compensation of Geometrical Deviations for Bulk Forming". In: *Procedia Engineering* 207, pp. 466–471.

HARTMANN, C., D. OPRITESCU, and W. VOLK (2019). "An artificial neural network approach for tool path generation in incremental sheet metal free-forming". In: *Journal of Intelligent Manufacturing* 30 (2), pp. 757–770.

HARTMANN, C. and W. VOLK (2019a). "Digital image correlation and optical flow analysis based on the material texture with application on high-speed deformation measurement in shear cutting". In: *International Conference on Digital Image and Signal Processing*. Ed. by F. HIDOUSSI. Corgascience, pp. 1–8.

– (2019b). "Variational methods in comparison to digital image correlation for full field deformation analysis under variable conditions". In: *Forming Technology Forum*. Ed. by W. VOLK. Technical University of Munich, pp. 1–7.

– (2019c). "Knowledge-based incremental sheet metal free-forming using probabilistic density functions and voronoi partitioning". In: *Procedia Manufacturing* 29, pp. 4–11.

HARTMANN, C., J. WANG, D. OPRISTESCU, and W. VOLK (2018). "Implementation and evaluation of optical flow methods for two-dimensional deformation measurement in comparison to digital image correlation". In: *Optics and Lasers in Engineering* 107, pp. 127–141.

HARTMANN, C., H. WEISS, P. LECHNER, W. VOLK, S. NEUMAYER, J. FITSCHEN, and G. STEIDL (2021). "Measurement of strain, strain rate and crack evolution in shear cutting". In: *Journal of Materials Processing Technology* 228, pp. 1–11.

HATANAKA, N., K. YAMAGUCHI, and N. TAKAKURA (2003). "Finite element simulation of the shearing mechanism in the blanking of sheet metal". In: *Journal of Materials Processing Technology* 139 (1-3), pp. 64–70.

HATANAKA, N., K. YAMAGUCHI, N. TAKAKURA, and T. IIZUKA (2003). "Simulation of sheared edge formation process in blanking of sheet metals". In: *Journal of Materials Processing Technology* 140 (1-3), pp. 628–634.

HAUSDORFF, F. (1914). *Grundzüge der Mengenlehre*. Leipzig: von Veit & Comp.

HAUSSECKER, H. and D. FLEET (2001). "Computing optical flow with physical models of brightness variation". In: *IEEE Transactions on Pattern Analysis and Machine Intelligence* 23 (6), pp. 661–673.

HELMHOLTZ, H. (1887). "Zählen und Messen, erkenntnisstheoretisch betrachtet." In: *Philosophische Aufsätze*, pp. 17–52.

HESTENES, M. (1969). "Multiplier and gradient methods". In: *Journal of Optimization Theory and Applications* 4 (5), pp. 303–320.

HEWER, A., J. WEICKERT, H. SEIBERT, T. SCHEFFER, and S. DIEBELS (2013). "Lagrangian Strain Tensor Computation with Higher Order Variational Models". In: *British Machine Vision Conference*. Ed. by T. BURGHARDT, D. DAMEN, W. MAYOL-CUEVAS, and M. MIRMEHDI. British Machine Vision Association, pp. 129.1–129.11.

HEY, T., ed. (2009). *The fourth paradigm: Data-intensive scientific discovery*. Washington: Microsoft Research.

HILDITCH, T. and P. HODGSON (2005). "Development of the sheared edge in the trimming of steel and light metal sheet". In: *Journal of Materials Processing Technology* 169 (2), pp. 184–191.

HILL, R. (1968a). "On constitutive inequalities for simple materials—I". In: *Journal of the Mechanics and Physics of Solids* 16 (4), pp. 229–242.

– (1968b). "On constitutive inequalities for simple materials—II". In: *Journal of the Mechanics and Physics of Solids* 16 (5), pp. 315–322.

– (1979). "Aspects of Invariance in Solid Mechanics". In: *Advances in Applied Mechanics*. Vol. 18. Advances in Applied Mechanics. Elsevier, pp. 1–75.

HIRSCH, M., P. DEMMEL, R. GOLLE, and H. HOFFMANN (2011). "Light Metal in High-Speed Stamping Tools". In: *Key Engineering Materials* 473, pp. 259–266.

HIRSCHBERGER, C. and P. STEINMANN (2009). "Classification of Concepts in Thermodynamically Consistent Generalized Plasticity". In: *Journal of Engineering Mechanics* 135 (3), pp. 156–170.

HITCHCOCK, F. (1927). "The Expression of a Tensor or a Polyadic as a Sum of Products". In: *Journal of Mathematics and Physics* 6 (1-4), pp. 164–189.

HOFFMANN, H., G. SPUR, and R. NEUGEBAUER (2012). *Handbuch Umformen*. 2nd ed. Edition Handbuch der Fertigungstechnik. München: Carl Hanser Fachbuchverlag.

HOLLAND, P. and R. WELSCH (1977). "Robust regression using iteratively reweighted least-squares". In: *Communications in Statistics - Theory and Methods* 6 (9), pp. 813–827.

HOLLER, M. and K. KUNISCH (2014). "On Infimal Convolution of TV-Type Functionals and Applications to Video and Image Reconstruction". In: *SIAM Journal on Imaging Sciences* 7 (4), pp. 2258–2300.

HOOGEN, M. (1999). *Einfluß der Werkzeuggeometrie auf das Scherschneiden und Reißen von Aluminiumfeinblechen, PhD thesis*. Vol. 6. München: Hieronymus.

HÖRMANN, F. (2008). *Einfluss der Prozessparameter auf einstufige Scherschneidverfahrenzum Ausschneiden mit endkonturnaher Form, PhD thesis*. Vol. 46. München: Hieronymus.

HORN, B. and B. SCHUNCK (1981). "Determining optical flow". In: *Artificial Intelligence* 17 (1-3), pp. 185–203.

HSU, T. (1966). "A study of large deformations by matrix algebra". In: *Journal of Strain Analysis* 1 (4), pp. 313–321.

HU, D.-C., M.-H. CHEN, J.-D. OUYANG, and L.-M. YIN (2015). "Finite element analysis of the thermal effect in high-speed blanking of thick sheet metal". In: *The International Journal of Advanced Manufacturing Technology* 80 (9-12), pp. 1481–1487.

HUNT, J. (1987). "Vorticity and Vortex Dynamics in Complex Turbulent Flows". In: *Transactions of the Canadian Society for Mechanical Engineering* 11 (1), pp. 21–35.

HUTTENLOCHER, D., G. KLANDERMAN, and W. RUCKLIDGE (1993). "Comparing images using the Hausdorff distance". In: *IEEE Transactions on Pattern Analysis and Machine Intelligence* 15 (9), pp. 850–863.

HUTTER, K. (1993). *Continuum Mechanics in Environmental Sciences and Geophysics*. Vienna: Springer.

IBAÑEZ, R., E. ABISSET-CHAVANNE, J. AGUADO, D. GONZALEZ, E. CUETO, and F. CHINESTA (2018). "A Manifold Learning Approach to Data-Driven Computational Elasticity and Inelasticity". In: *Archives of Computational Methods in Engineering* 25 (1), pp. 47–57.

IBÁÑEZ, R., E. ABISSET-CHAVANNE, D. GONZÁLEZ, J.-L. DUVAL, E. CUETO, and F. CHINESTA (2019). "Hybrid constitutive modeling: data-driven learning of corrections to plasticity models". In: *International Journal of Material Forming* 12 (4), pp. 717–725.

INTEGRATED DESIGN TOOLS INC. (2016). *mOst flexible highspeed video system*. Pasadena.

– (2019). *Motion Studio User Manual*. Pasadena.

ITOH, M., F. YOSHIDA, M. INOUE, and M. OHMORI (1987). "Combined Effects of Hydrostatic Pressure and Punching Speed on Blanking Behaviors of 2S-Aluminum". In: *Advanced Technology of Plasticity* 1, pp. 307–312.

JANA, S. and N. S. ONG (1989). "Effect of punch clearance in the high-speed blanking of thick metals using an accelerator designed for a mechanical press". In: *Journal of Mechanical Working Technology* 19 (1), pp. 55–72.

JIMMA, T. (1963). "The Theoretical Research on the Blanking of a Sheet Material". In: *Bulletin of JSME* 6 (23), pp. 568–576.

JOHNSON, G. and W. COOK (1983). "A constitutive model and data for materials subjected to large strains, high strain rates, and high temperatures". In: *Proceedings 7th International Symposium on Ballistics* 4, pp. 541–547.

– (1985). "Fracture characteristics of three metals subjected to various strains, strain rates, temperatures and pressures". In: *Engineering Fracture Mechanics* 21 (1), pp. 31–48.

JOHNSON, R. and D. WICHERN (2014). "Multivariate Analysis". In: *Wiley StatsRef: Statistics Reference Online*. Ed. by N. BALAKRISHNAN, T. COLTON, B. EVERITT, W. PIEGORSCH, F. RUGGERI, and J. L. TEUGELS. Vol. 23. Chichester: John Wiley & Sons, Ltd, pp. 1–20.

JOHNSON, R. and D. WICHERN (2007). *Applied multivariate statistical analysis*. 6th ed. Upper Saddle River: Pearson/Prentice Hall.

JOHNSON, W. and R. SLATER (1967). "A survey of the slow and fast blanking of metals at ambient and high temperatures". In: *International Conference on Manufacturing Technology*, pp. 825–851.

JOLLIFFE, I. (2002). *Principal Component Analysis*. New York: Springer-Verlag.

JOSHI, S., Y. LAM, and X.-L. LIU (2000). "Mass conservation in numerical simulation of resin flow". In: *Composites Part A: Applied Science and Manufacturing* 31 (10), pp. 1061–1068.

KACHANOV, L. (1958). "Rupture time under creep conditions (in Russian)". In: *Izvestia Akademii Nauk SSSR* 8, pp. 26–31.

KAHEMAN, K., E. KAISER, B. STROM, J. KUTZ, and S. BRUNTON (2019). "Learning Discrepancy Models From Experimental Data". In: *arxiv* 1 (1909.08574), pp. 1–8.

KAMBLE, S., N. THAKUR, and P. BAJAJ (2016). "A Review on Block Matching Motion Estimation and Automata Theory based Approaches for Fractal Coding". In: *International Journal of Interactive Multimedia and Artificial Intelligence* 4 (2), p. 91.

KASUGA, Y., S. TSUTSUMI, and T. MORI (1977). "On the Shearing Process of Ductile Sheet Metals". In: *Bulletin of JSME* 20 (148), pp. 1336–1343.

KEELER, S. (1961). *Plastic Instability and Fracture in Sheets Stretched over Rigid Punches, PhD thesis*. Cambridge.

KELLER, F. (1951). "Messungen zum Einfluß des Schneidspaltes auf Kraftbedarf und Schnittarbeit beim Lochen von Stahlblech". In: *Werkstatt und Betrieb* 84 (2), pp. 67–73.

KENNEDY, F. (1982). "Single Pass Rub Phenomena—Analysis and Experiment". In: *Journal of Lubrication Technology* 104 (4), pp. 582–588.

KEYENCE CORPORATION (2018). *Laserscanningmikroskop für die Oberflächenanalyse VK-X250K/X150K/X120K Serie*. Osaka.

KIENZLE, O. and W. KIENZLE (1958). "Werkzeugverschleiß beim Schneiden von Stahlfeinblechen". In: *Stahl und Eisen (Zeitschrift für das deutsche Hüttenwesen)* 78 (12), pp. 820–829.

KIENZLE, O. and M. MEYER (1963). *Verfahren zur Erzielung glatter Schnittflächen beim vollkantigen Schneiden von Blech: Forschungsberichte des Landes Nordrhein-Westfalen: 1162*. Köln, Opladen: Westdeutscher Verlag.

KIRCHDOERFER, T. and M. ORTIZ (2016). "Data-driven computational mechanics". In: *Computer Methods in Applied Mechanics and Engineering* 304, pp. 81–101.

– (2017). "Data Driven Computing with noisy material data sets". In: *Computer Methods in Applied Mechanics and Engineering* 326, pp. 622–641.

KIRCHNER, N. and P. STEINMANN (2005). "A unifying treatise on variational principles for gradient and micromorphic continua". In: *Philosophical Magazine* 85 (33-35), pp. 3875–3895.

KITAMURA, K., T. MAKINO, M. NAWA, and S. MIYATA (2016). "Tribological effects of punch with micro-dimples in blanking under high hydrostatic pressure". In: *CIRP Annals* 65 (1), pp. 249–252.

KLINGENBERG, W. and U. SINGH (2003). "Finite element simulation of the punching/blanking process using in-process characterisation of mild steel". In: *Journal of Materials Processing Technology* 134 (3), pp. 296–302.

KLOCKE, F., K. SWEENEY, and H.-W. RAEDT (2001). "Improved tool design for fine blanking through the application of numerical modeling techniques". In: *Journal of Materials Processing Technology* 115 (1), pp. 70–75.

KNOWLES, I. and R. WALLACE (1995). "A variational method for numerical differentiation". In: *Numerische Mathematik* 70 (1), pp. 91–110.

KNUTSSON, H. (1989). "Representing Local Structure Using Tensors". In: *Technical Report, Linköping University, Computer Vision Laboratory*, pp. 1–8.

KOCH, J., M. KUROSAKA, C. KNOWLEN, and J. KUTZ (2020). "Mode-locked rotating detonation waves: Experiments and a model equation". In: *Physical review. E* 101 (1), pp. 1–11.

KOMORI, K. (2013). "Simulation of crack arrest in blanking using the node separation method". In: *International Journal of Mechanical Sciences* 68, pp. 150–159.

KOPP, T., J. STAHL, P. DEMMEL, P. TRÖBER, R. GOLLE, H. HOFFMANN, and W. VOLK (2016). "Experimental investigation of the lateral forces during shear cutting with an open cutting line". In: *Journal of Materials Processing Technology* 238, pp. 49–54.

KRABBE, E. (1953). "Stanztechnik: Erster Teil". In: *Werkstattbücher*. Ed. by H. HAAKE. Berlin, Göttingen, Heidelberg: Springer.

KRINNINGER, M., D. OPRITESCU, R. GOLLE, and W. VOLK (2017). "On the opportunities of problem- and process-adapted shear cutting simulations for effective process design". In: *Procedia Engineering* 207, pp. 1570–1575.

KRISHNAN, S. and C. SEELAMANTULA (2013). "On the Selection of Optimum Savitzky-Golay Filters". In: *IEEE Transactions on Signal Processing* 61 (2), pp. 380–391.

KUHN, H., P. LEE, and T. ERTURK (1973). "A Fracture Criterion for Cold Forming". In: *Journal of Engineering Materials and Technology* 95 (4), pp. 213–218.

KULLBACK, S. and R. LEIBLER (1951). "On Information and Sufficiency". In: *The Annals of Mathematical Statistics* 22 (1), pp. 79–86.

LAGRANGE, J. (1797). *Théorie des fonctions analytiques contenant les principes du calcul différentiel, dégagés de toute considération d'infiniment petits ou d'évanouissans, de limies ou de fluxions, et réduits à l'analyse algébrique des quantités finies*. Paris.

LAGRANGE, J., A. BOISSONNADE, and V. VAGLIENTE (1811). *Analytical Mechanics: Translated in 1997 from the Mecanique analytique, novelle edition of 1811*. Dordrecht: Springer.

LANDAU, P., S. OSOVSKI, A. VENKERT, V. GÄRTNEROVÁ, and D. RITTEL (2016). "The genesis of adiabatic shear bands". In: *Scientific Reports* 6 (37226), pp. 1–6.

LANDMAN, U., W. LUEDTKE, and E. RINGER (1992). "Molecular Dynamics Simulations of Adhesive Contact Formation and Friction". In: *Fundamentals of Friction: Macroscopic and Microscopic Processes*. Ed. by I. SINGER and H. POLLOCK. Vol. 58. Dordrecht: Springer, pp. 463–510.

LANGE, K. (1990). *Umformtechnik*. Berlin, Heidelberg: Springer.

LANGLEY, P. and J. ZYTKOW (1989). "Data-driven approaches to empirical discovery". In: *Artificial Intelligence* 40 (1-3), pp. 283–312.

LARSON, S. (1931). "The shrinkage of the coefficient of multiple correlation". In: *Journal of Educational Psychology* 22 (1), pp. 45–55.

LATORRE, M. and F. MONTÁNS (2016). "Stress and strain mapping tensors and general work-conjugacy in large strain continuum mechanics". In: *Applied Mathematical Modelling* 40 (5-6), pp. 3938–3950.

LE GOURRIÉREC, C., S. ROUX, and F. HILD (2020). "Measuring acceleration fields via regularized digital image correlation". In: *Advanced Modeling and Simulation in Engineering Sciences* 7 (30), pp. 1–18.

LECHNER, P., G. FUCHS, C. HARTMANN, F. STEINLEHNER, F. ETTEMEYER, and W. VOLK (2020). "Acoustical and Optical Determination of Mechanical Properties of Inorganically-Bound Foundry Core Materials". In: *Materials* 13 (11), pp. 1–11.

LEMAITRE, J. (1985). "A Continuous Damage Mechanics Model for Ductile Fracture". In: *Journal of Engineering Materials and Technology* 107 (1), pp. 83–89.

LEMAITRE, J., J.-L. CHABOCHE, and B. SHRIVASTAVA (1998). *Mechanics of solid materials*. 1st ed. Cambridge: Cambridge University Press.

LEMIALE, V., J. CHAMBERT, and P. PICART (2009). "Description of numerical techniques with the aim of predicting the sheet metal blanking process by FEM simulation". In: *Journal of Materials Processing Technology* 209 (5), pp. 2723–2734.

LEUNG, Y., L. CHAN, C. TANG, and T. LEE (2004a). "Re-etched grids for large-strain measurement in fine-blanking". In: *Journal of Strain Analysis for Engineering Design* 39 (5), pp. 423–436.

– (2004b). "An effective process of strain measurement for severe and localized plastic deformation". In: *International Journal of Machine Tools and Manufacture* 44 (7-8), pp. 669–676.

LEVY, B. and C. VAN TYNE (2012). "Review of the Shearing Process for Sheet Steels and Its Effect on Sheared-Edge Stretching". In: *Journal of Materials Engineering and Performance* 21 (7), pp. 1205–1213.

LEYGUE, A., M. CORET, J. RÉTHORÉ, L. STAINIER, and E. VERRON (2017). "Data Driven Constitutive identification". In: *HAL archives-ouvertes* 2 (01452494), pp. 1–13.

LI, M. (2000). "Micromechanisms of deformation and fracture in shearing aluminum alloy sheet". In: *International Journal of Mechanical Sciences* 42 (5), pp. 907–923.

LIOUVILLE, J. (1838). "Note sur la Théorie de la Variation des constantes arbitraires." In: *Journal de Mathématiques Pures et Appliquées* 1 (3), pp. 342–349.

LIU, T. and L. SHEN (2008). "Fluid flow and optical flow". In: *Journal of Fluid Mechanics* 614, pp. 253–291.

LOPEZ, E., D. GONZALEZ, J. V. AGUADO, E. ABISSET-CHAVANNE, E. CUETO, C. BINETRUY, and F. CHINESTA (2018). "A Manifold Learning Approach for Integrated Computational Materials Engineering". In: *Archives of Computational Methods in Engineering* 25 (1), pp. 59–68.

LU, H. and P. CARY (2000). "Deformation measurements by digital image correlation: Implementation of a second-order displacement gradient". In: *Experimental Mechanics* 40 (4), pp. 393–400.

LUCAS, B. (1984). *Generalized Image Matching by the Method of Differences, PhD thesis*. Pittsburgh.

LUCAS, B. and T. KANADE (1981). "An Iterative Image Registration Technique with an Application to Stereo Vision". In: *International Joint Conference on Artificial Intelligence*. Vol. 2, pp. 674–679.

MACVEAN, D. (1968). "Die Elementararbeit in einem Kontinuum und die Zuordnung von Spannungs- und Verzerrungstensoren". In: *ZAMP Zeitschrift für angewandte Mathematik und Physik* 19 (2), pp. 157–185.

MAHR GMBH (2005). *Betriebsanleitung MarSurf XR 20*. Esslingen am Neckar: Mahr GmbH.

MANDELBROT, B. (1967). "How long is the coast of britain? Statistical self-similarity and fractional dimension". In: *Science* 156 (3775), pp. 636–638.

MANOPULO, N. (2011). *An ALE based FE Formulation for the 3D Simulation of the Fineblanking Process, PhD thesis*.

MAROUANI, H., A. BEN ISMAIL, E. HUG, and M. RACHIK (2009). "Numerical investigations on sheet metal blanking with high speed deformation". In: *Materials and Design* 30 (9), pp. 3566–3571.

MAROUANI, H., M. RACHIK, and E. HUG (2012). "Experimental investigations and FEM simulations of parameters influencing the Fe-(wt.3%)Si shearing process". In: *Mechanics and Industry* 13 (4), pp. 271–278.

MAZZOCCHI, F. (2015). "Could Big Data be the end of theory in science? A few remarks on the epistemology of data-driven science". In: *EMBO Reports* 16 (10), pp. 1250–1255.

MEYER, M. (1962). "Verfahren zum Erzielen glatter Schnittflächen beim Blechschneiden". In: *Mitteilung der Forschungsgesellschaft Blechverarbeitung* (19), pp. 282–293.

MITICHE, A. and A.-R. MANSOURI (2004). "On convergence of the Horn and Schunck optical-flow estimation method". In: *IEEE Transactions on Image Processing* 13 (6), pp. 848–852.

MOGHADAM, M., M. VILLA, P. MOREAU, A. DUBOIS, L. DUBAR, C. V. NIELSEN, and N. BAY (2020). "Analysis of lubricant performance in punching and blanking". In: *Tribology International* 141, p. 105949.

MONTÁNS, F., F. CHINESTA, R. GÓMEZ-BOMBARELLI, and J. KUTZ (2019). "Data-driven modeling and learning in science and engineering". In: *Comptes Rendus Mécanique* 347 (11), pp. 845–855.

MOORE, E. (1920). "On the reciprocal of the general algebraic matrix: The fourteenth western meeting of the American Mathematical Society". In: *Bulletin of the American Mathematical Society* 26 (9), pp. 394–395.

MOORE, G. (1965). "Cramming more components onto integrated circuits". In: *Electronics* 38 (8), pp. 114–117.

MOORE, J. and J. MOORE (1983). "Entropy Production Rates From Viscous Flow Calculations, Part I: A Turbulent Boundary Layer Flow". In: *Turbomachinery*. Vol. 1. American Society of Mechanical Engineers.

MORENO, R., S. KOPPAL, and E. DE MUINCK (2013). "Robust estimation of distance between sets of points". In: *Pattern Recognition Letters* 34 (16), pp. 2192–2198.

MORI, K.-I., Y. ABE, and Y. SUZUI (2010). "Improvement of stretch flangeability of ultra high strength steel sheet by smoothing of sheared edge". In: *Journal of Materials Processing Technology* 210 (4), pp. 653–659.

MORTON, K. and D. MAYERS (2005). *Numerical solution of partial differential equations: An introduction*. 2nd ed. New York: Cambridge University Press.

MÜLLER, I. (1971). "The coldness, a universal function in thermoelastic bodies". In: *Archive for Rational Mechanics and Analysis* 41 (5), pp. 319–332.

MURRAY, D. and B. BUXTON (1987). "Scene segmentation from visual motion using global optimization". In: *IEEE Transactions on Pattern Analysis and Machine Intelligence* 9 (2), pp. 220–228.

NAGEL, H. (1990). "Extending the 'Oriented smoothness constraint' into the temporal domain and the estimation of derivatives of optical flow". In: *European Conference on Computer Vision*. Ed. by G. GOOS, J. HARTMANIS, D. BARSTOW, W. BRAUER, P. BRINCH HANSEN, D. GRIES, D. LUCKHAM, C. MOLER, A. PNUELI, G. SEEGMÜLLER, J. STOER, N. WIRTH, and O. FAUGERAS. Vol. 427. Lecture Notes in Computer Science. Berlin, Heidelberg: Springer, pp. 139–148.

NATTERER, F. (1983). "On the Order of Regularization Methods". In: *Improperly Posed Problems and Their Numerical Treatment*. Ed. by G. HÄMMERLIN and K.-H. HOFFMANN. Vol. 8. Basel: Birkhäuser Basel, pp. 189–203.

NEEDLEMAN, A. and V. TVERGAARD (1984). "An analysis of ductile rupture in notched bars". In: *Journal of the Mechanics and Physics of Solids* 32 (6), pp. 461–490.

NEFF, P., B. EIDEL, and R. MARTIN (2016). "Geometry of Logarithmic Strain Measures in Solid Mechanics". In: *Archive for Rational Mechanics and Analysis* 222 (2), pp. 507–572.

NGUYEN, L. and M.-A. KEIP (2018). "A data-driven approach to nonlinear elasticity". In: *Computers & Structures* 194, pp. 97–115.

NOTHHAFT, K. (2014). *Scherschneiden höchstfester Blechwerkstoffe im offenen Schnitt, PhD thesis*. Vol. 64. München: Hieronymus.

ONG, N. and L. CHAN (1989). "Blanking of thick-gauge metals using a variable-speed pneumatic accelerator designed for a mechanical press". In: *Journal of Mechanical Working Technology* 18 (1), pp. 17–31.

PADMANABHAN, S., J. P. HUBNER, A. V. KUMAR, and P. G. IFJU (2006). "Load and Boundary Condition Calibration Using Full-field Strain Measurement". In: *Experimental Mechanics* 46 (5), pp. 569–578.

PAN, B. (2009). "Reliability-guided digital image correlation for image deformation measurement". In: *Applied optics* 48 (8), pp. 1535–1542.

– (2018). "Digital image correlation for surface deformation measurement: historical developments, recent advances and future goals". In: *Measurement Science and Technology* 29, pp. 1–32.

PAN, B., K. LI, and W. TONG (2013). "Fast, Robust and Accurate Digital Image Correlation Calculation Without Redundant Computations". In: *Experimental Mechanics* 53 (7), pp. 1277–1289.

PAN, B., K. QIAN, H. XIE, and A. ASUNDI (2009). "Two-dimensional digital image correlation for in-plane displacement and strain measurement: a review". In: *Optical Engineering* 20 (6), pp. 1–17.

PAN, B., Z. WANG, and Z. LU (2010). "Genuine full-field deformation measurement of an object with complex shape using reliability-guided digital image correlation". In: *Optics express* 18 (2), pp. 1011–1023.

PAN, D., P. YU, M. CHO, A. RAMALINGAM, K. KIM, A. RAJARAM, and S. SHI (2008). "Design for manufacturing meets advanced process control: A survey". In: *Journal of Process Control* 18 (10), pp. 975–984.

PAPENBERG, N., A. BRUHN, T. BROX, S. DIDAS, and J. WEICKERT (2006). "Highly Accurate Optic Flow Computation with Theoretically Justified Warping". In: *International Journal of Computer Vision* 67 (2), pp. 141–158.

PATHAK, N., C. BUTCHER, and M. J. WORSWICK (2019). "Experimental Techniques for Finite Shear Strain Measurement within Two Advanced High Strength Steels". In: *Experimental Mechanics* 59 (2), pp. 125–148.

PEARSON, K. (1901). "LIII. On lines and planes of closest fit to systems of points in space". In: *London, Edinburgh, and Dublin Philosophical Magazine and Journal of Science* 2 (11), pp. 559–572.

PENROSE, R. (1955). "A generalized inverse for matrices". In: *Mathematical Proceedings of the Cambridge Philosophical Society* 51 (3), pp. 406–413.

PETERS, W. and W. RANSON (1982). "Digital Imaging Techniques In Experimental Stress Analysis". In: *Optical Engineering* 21 (3), pp. 1–5.

PHILLIPS, D. (1962). "A Technique for the Numerical Solution of Certain Integral Equations of the First Kind". In: *Journal of the ACM* 9 (1), pp. 84–97.

POCK, T., A. CHAMBOLLE, D. CREMERS, and H. BISCHOF (2009). "A convex relaxation approach for computing minimal partitions". In: *Conference on Computer Vision and Pattern Recognition*. IEEE, pp. 810–817.

POPAT, P., A. GHOSH, and N. KISHORE (1989). "Finite-element analysis of the blanking process". In: *Journal of Mechanical Working Technology* 18 (3), pp. 269–282.

PRESS, W. (2007). *Numerical recipes: The art of scientific computing*. 3rd ed. Cambridge: Cambridge University Press.

RACHIK, M., J. ROELANDT, and A. MAILLARD (2002). "Some phenomenological and computational aspects of sheet metal blanking simulation". In: *Journal of Materials Processing Technology* 128 (1-3), pp. 256–265.

RAFSANJANI, A., S. ABBASION, A. FARSHIDIANFAR, and N. IRANI (2009). "Investigation of the viscous and thermal effects on ductile fracture in sheet metal blanking process". In: *The International Journal of Advanced Manufacturing Technology* 45 (5-6), pp. 459–469.

RAMULU, M. and A. S. KOBAYASHI (1985). "Mechanics of crack curving and branching: a dynamic fracture analysis". In: *International Journal of Fracture* 27 (3-4), pp. 187–201.

RANC, N. and A. CHRYSOCHOOS (2013). "Calorimetric consequences of thermal softening in Johnson–Cook's model". In: *Mechanics of Materials* 65, pp. 44–55.

RENISHAW PLC. (2018). "SP25M". In: *Technical Paper*, pp. 1–11.

RICE, J. (1971). "Inelastic constitutive relations for solids: An internal-variable theory and its application to metal plasticity". In: *Journal of the Mechanics and Physics of Solids* 19 (6), pp. 433–455.

RIGNEY, D. and J. HIRTH (1979). "Plastic deformation and sliding friction of metals". In: *Wear* 53 (2), pp. 345–370.

ROESSIG, K. and J. MASON (1999). "Adiabatic shear localization in the dynamic punch test, part I: experimental investigation". In: *International Journal of Plasticity* 15 (3), pp. 241–262.

ROMANOWSKI, W. (1959). *Handbuch der Stanzereitechnik*. Berlin: VEB Verlag Technik.

– (1979). *Handbuch der Kaltumformung (in Russian: spravochnikpo holodnoj shtampovke)*. 6th ed. Leningrad: Leningradskoe otdelenie.

ROSAKIS, P., A. J. ROSAKIS, G. RAVICHANDRAN, and J. HODOWANY (2000). "A thermodynamic internal variable model for the partition of plastic work into heat and stored energy in metals". In: *Journal of the Mechanics and Physics of Solids* 48 (3), pp. 581–607.

ROSATI, L. (1999). "Derivatives and Rates of the Stretchand Rotation Tensors". In: *Journal of Elasticity* 56 (3), pp. 213–230.

RUDIN, L. I., S. OSHER, and E. FATEMI (1992). "Nonlinear total variation based noise removal algorithms". In: *Physica D: Nonlinear Phenomena* 60 (1-4), pp. 259–268.

RUHNAU, P., A. STAHL, and C. SCHNÖRR (2007). "Variational estimation of experimental fluid flows with physics-based spatio-temporal regularization". In: *Measurement Science and Technology* 18 (3), pp. 755–763.

SADOYAN, H., A. ZAKARIAN, and P. MOHANTY (2006). "Data mining algorithm for manufacturing process control". In: *The International Journal of Advanced Manufacturing Technology* 28 (3-4), pp. 342–350.

SALGADO, A. and J. SÁNCHEZ (2007). "Temporal Constraints in Large Optical Flow Estimation". In: *Computer Aided Systems Theory*. Ed. by R. MORENO DÍAZ and A. PICHLER F.and Quesada Arencibia. Vol. 4739. Lecture Notes in Computer Science. Berlin, Heidelberg: Springer, pp. 709–716.

SANTOSA, F. and W. W. SYMES (1986). "Linear Inversion of Band-Limited Reflection Seismograms". In: *SIAM Journal on Scientific and Statistical Computing* 7 (4), pp. 1307–1330.

SASADA, M. and J. TAMURA (2016). "Investigation of the Relationship between Material Flow and Rollover in Double-Sided Shearing Using Image Processing". In: *Key Engineering Materials* 716, pp. 451–457.

SASADA, M. and T. TOGASHI (2014). "Measurement of Rollover in Double-sided Shearing Using Image Processing and Influence of Clearance". In: *Procedia Engineering* 81, pp. 1139–1144.

SAVITZKY, A. and M. J. E. GOLAY (1964). "Smoothing and Differentiation of Data by Simplified Least Squares Procedures". In: *Analytical Chemistry* 36 (8), pp. 1627–1639.

SCHENK, H., E. PRÖLSS, and K. G. GÜNTHER (1978). "Blanking of sheet metal relationship between process conditions and fracture of cut edge." In: *CIRP Annals* 27, pp. 159–163.

SCHMID, P. (2010). "Dynamic mode decomposition of numerical and experimental data". In: *Journal of Fluid Mechanics* 656, pp. 5–28.

SCHMIDT, E. (1907). "Zur Theorie der linearen und nichtlinearen Integralgleichungen". In: *Mathematische Annalen* 63 (4), pp. 433–476.

SCHNÖRR, C. (1991). "Determining optical flow for irregular domains by minimizing quadratic functionals of a certain class". In: *International Journal of Computer Vision* 6 (1), pp. 25–38.

SCHREIBER, U. and U. VAN RIENEN (2006). "Coupled Calculation of Electromagnetic Fields and Mechanical Deformation". In: *Scientific Computing in Electrical Engineering*. Ed. by H.-G. BOCK, F. de HOOG, A. FRIEDMAN, A. GUPTA, H. NEUNZERT, W. R. PULLEYBLANK, T. RUSTEN, F. SANTOSA, A.-K. TORNBERG, A. M. ANILE, G. ALÌ, and G. MASCALI. Vol. 9. Mathematics in Industry. Berlin, Heidelberg: Springer Berlin Heidelberg, pp. 63–68.

SCHREIER, H. and M. SUTTON (2002). "Systematic errors in digital image correlation due to undermatched subset shape functions". In: *Experimental Mechanics* 42 (3), pp. 303–310.

SCHWARZ, G. (1978). "Estimating the Dimension of a Model". In: *Annals of Statistics* 6 (2), pp. 461–464.

SEITZ, A., W. WALL, and A. POPP (2018). "A computational approach for thermo-elasto-plastic frictional contact based on a monolithic formulation using non-smooth nonlinear complementarity functions". In: *Advanced Modeling and Simulation in Engineering Sciences* 5 (5), pp. 1–37.

SETH, B. (1961). *Generalized strain measure with applications to physical problems*. Vol. 248. MRC Technical Summary Report.

SHANNON, C. (1948). "A Mathematical Theory of Communication". In: *Bell System Technical Journal* 27 (3), pp. 379–423.

SHARPE, W. (2008). *Springer handbook of experimental solid mechanics*. Springer handbooks. New York: Springer.

SHRIVASTAVA, S., C. GHOSH, and J. J. JONAS (2012). "A comparison of the von Mises and Hencky equivalent strains for use in simple shear experiments". In: *Philosophical Magazine* 92 (7), pp. 779–786.

SILVA, B. M. d., D. M. HIGDON, S. L. BRUNTON, and J. N. KUTZ (2019). "Discovery of Physics from Data: Universal Laws and Discrepancies". In: *arxiv* 3 (1906.07906), pp. 1–37.

SOBEL, I. and G. FELDMAN (1968). *A 3x3 Isotropic Gradient Operator for Image Processing*. Stanford, United States.

SONKAMBLE, V., P. DHONDAPURE, K. NARASIMHAN, and A. TEWARI (2019). "Experimental investigation of shear band and shear strain field evolution during blanking of AA6082 sheet". In: *Journal of Strain Analysis for Engineering Design* 54 (2), pp. 149–158.

SONTAMINO, A. and S. THIPPRAKMAS (2019). "Development of a shaving die design for reducing rollover". In: *International Journal of Advanced Manufacturing Technology* 103 (5-8), pp. 1831–1845.

SPIEGELHALTER, D., N. BEST, B. CARLIN, and A. VAN DER LINDE (2002). "Bayesian measures of model complexity and fit". In: *Journal of the Royal Statistical Society. Series B* 64 (4), pp. 583–639.

SRA, S., S. NOWOZIN, and S. WRIGHT (2012). *Optimization for machine learning*. Neural information processing series. Cambridge: MIT Press.

STAINIER, L. (2013). "A Variational Approach to Modeling Coupled Thermo-Mechanical Nonlinear Dissipative Behaviors". In: vol. 46. Advances in Applied Mechanics. Elsevier, pp. 69–126.

STAINIER, L. and M. ORTIZ (2010). "Study and validation of a variational theory of thermo-mechanical coupling in finite visco-plasticity". In: *International Journal of Solids and Structures* 47 (5), pp. 705–715.

STEGEMAN, Y., A. GOIJAERTS, D. BROKKEN, W. BREKELMANS, L. GOVAERT, and F. BAAIJENS (1999). "An experimental and numerical study of a planar blanking process". In: *Journal of Materials Processing Technology* 87 (1-3), pp. 266–276.

STEINBRUCKER, F., T. POCK, and D. CREMERS (2009). "Large displacement optical flow computation without warping". In: *International Conference on Computer Vision*. IEEE, pp. 1609–1614.

STEINMANN, P. (2015). *Geometrical Foundations of Continuum Mechanics*. Vol. 2. Berlin: Springer.

STEPHANOPOULOS, G., H. ALPER, and J. MOXLEY (2004). "Exploiting biological complexity for strain improvement through systems biology". In: *Nature Biotechnology* 22 (10), pp. 1261–1267.

STOICA, P. and Y. SELEN (2004). "Model-order selection". In: *IEEE Signal Processing Magazine* 21 (4), pp. 36–47.

SU, S. (2012). *Energy-Based Variational Modeling of Adiabatic Shear Band Structure, PhD thesis*. Nantes.

SU, X. and W. CHEN (2004). "Reliability-guided phase unwrapping algorithm: a review". In: *Optics and Lasers in Engineering* 42 (3), pp. 245–261.

SUBRAMONIAN, S., T. ALTAN, C. CAMPBELL, and B. CIOCIRLAN (2013). "Determination of forces in high speed blanking using FEM and experiments". In: *Journal of Materials Processing Technology* 213 (12), pp. 2184–2190.

SUN, D., S. ROTH, and M. BLACK (2010). "Secrets of optical flow estimation and their principles". In: *Conference on Computer Vision and Pattern Recognition*. IEEE, pp. 2432–2439.

SUSSMAN, T. and K.-J. BATHE (2009). "A model of incompressible isotropic hyperelastic material behavior using spline interpolations of tension-compression test data". In: *Communications in Numerical Methods in Engineering* 25 (1), pp. 53–63.

SZALAY, A. and J. GRAY (2006). "2020 computing: science in an exponential world". In: *Nature* 440 (7083), pp. 413–414.

SZELISKI, R. (2011). *Computer Vision*. London: Springer.

TADDY, M. (2019). *Business data science: Combining machine learning and economics to optimize, automate, and accelerate business decisions*. New York: McGraw-Hill Education.

TAKAHASHI, T. and I. AOKI (1996a). "Analysis of Shearing by Visioplasticity Method Using Image Processing: Proposal and Verification of Displacement Measurement Method Usable for Large Deformations". In: *Transactions of the Japan Society of Mechanical Engineers (C)* (62), pp. 3196–3201.

– (1996b). "Development of analyzing system applicable for large plastic deformation". In: *International Conference on the Technology of Plasticity*. Columbus, pp. 583–590.

TAUPIN, E., J. BREITLING, W.-T. WU, and T. ALTAN (1996). "Material fracture and burr formation in blanking results of FEM simulations and comparison with experiments". In: *Journal of Materials Processing Technology* 59 (1-2), pp. 68–78.

TAYLOR, G. (1931). "The plastic distortion of metals". In: *Philosophical Transactions of the Royal Society of London. Series A* 230 (681-693), pp. 323–362.

TAYLOR, G. and M. QUINNEY (1934). "The latent energy remaining in a metal after cold working". In: *Proceedings of the Royal Society of London. Series A* 143 (849), pp. 307–326.

TIBSHIRANI, R. (1996). "Regression Shrinkage and Selection Via the Lasso". In: *Journal of the Royal Statistical Society. Series B* 58 (1), pp. 267–288.

TIKHONOV, A. (1963). "On the solution of ill-posed problems and the method of regularization". In: *Doklady Akademii Nauk SSSR* 151 (3), pp. 501–504.

TIMMERBEIL, F. (1956). "Der Einfluß der Schneidkantenabnutzung auf den Schneidvorgang am Blech". In: *Werkstattstechnik und Maschinenbau* 46 (2), pp. 58–66.

– (1957a). "Untersuchung des Schneidvorganges bei Blech, insbesondere beim geschlossenen Schnitt. Erster Teil: Der Schneidvorgang bei scharfen Werkzeugkanten - die Schneidkräfte". In: *Werkstattstechnik und Maschinenbau* 47 (5), pp. 231–239.

– (1957b). "Untersuchung des Schneidvorganges bei Blech, insbesondere beim geschlossenen Schnitt. Zweiter Teil: Die Schnittflächengüte von Schnittteilen". In: *Werkstattstechnik und Maschinenbau* 47 (7), pp. 350–356.

TONG, W. (2005). "An Evaluation of Digital Image Correlation Criteria for Strain Mapping Applications". In: *Strain* 41 (4), pp. 167–175.

TRAPHÖNER, H., T. CLAUSMEYER, and A. TEKKAYA (2018). "Material characterization for plane and curved sheets using the in-plane torsion test – An overview". In: *Journal of Materials Processing Technology* 257, pp. 278–287.

TREFETHEN, L. and D. BAU (1997). *Numerical linear algebra*. Philadelphia: Society for Industrial and Applied Math.

TRUESDELL, C., R. ARIS, L. COLLATZ, G. FICHERA, P. GERMAIN, J. KELLER, M. SCHIFFER, A. SEEGER, and M. BUNGE (1967). *Foundations of Physics*. Vol. 10. Berlin, Heidelberg: Springer.

TRUESDELL, C. (1952). "A program of physical research in classical mechanics". In: *ZAMP Zeitschrift für angewandte Mathematik und Physik* 3 (2), pp. 79–95.

TUKEY, J. (1962). "The Future of Data Analysis". In: *Annals of Mathematical Statistics* 33 (1), pp. 1–67.

TVERGAARD, V. (1981). "Influence of voids on shear band instabilities under plane strain conditions". In: *International Journal of Fracture* 17 (4), pp. 389–407.

– (1982). "On localization in ductile materials containing spherical voids". In: *International Journal of Fracture* 18, pp. 237–252.

UETZ, H. and J. FÖHL (1978). "Wear as an energy transformation process". In: *Wear* 49 (2), pp. 253–264.

VEENSTRA, P. and J. RAMAEKERS (1978). "A Criterion for Critical Tool Wear in Blanking". In: *CIRP Annals* 27 (1), pp. 157–158.

VITZTHUM, S., C. HARTMANN, M. EDER, and W. VOLK (2019). "Temperature-based determination of the onset of yielding using a new clip-on device for tensile tests". In: *Procedia Manufacturing* 29, pp. 490–497.

VOLK, W. (1999). *Untersuchung des Lokalisierungsverhaltens mikropolarer poröser Medien mit Hilfe der Cosserat-Theorie, PhD thesis*.

VOLK, W., P. GROCHE, A. BROSIUS, A. GHIOTTI, B. KINSEY, M. LIEWALD, L. MADEJ, J. MIN, and J. YANAGIMOTO (2019). "Models and modelling for process limits in metal forming". In: *CIRP Annals* 68 (2), pp. 775–798.

VOLK, W., G. HEINLE, and H. GRASS (2011). "Accurate determination of plastic yield curves and an approximation point for the plastic yield locus with the bulge test". In: *International Conference on the Technology of Plasticity*. Aachen, pp. 799–804.

VOLK, W. and J. STAHL (2014). "Shear Cutting". In: *CIRP Encyclopedia of Production Engineering*. Ed. by T. I. A. f. PRODU, L. LAPERRIÈRE, and G. REINHART. Berlin, Heidelberg: Springer, pp. 1–9.

VOLK, W. and J. SUH (2014). "Prediction of formability for non-linear deformation history using generalized forming limit concept (GFLC)". In: *NUMISHEET Conference*. Vol. 1567, pp. 556–561.

VOLZ, S., A. BRUHN, L. VALGAERTS, and H. ZIMMER (2011). "Modeling temporal coherence for optical flow". In: *International Conference on Computer Vision*. IEEE, pp. 1116–1123.

WANG, C., J. CHEN, C. XIA, F. REN, and J. CHEN (2014). "A New Method to Calculate Threshold Values of Ductile Fracture Criteria for Advanced High-Strength Sheet Blanking". In: *Journal of Materials Engineering and Performance* 23 (4), pp. 1296–1306.

WANG, K., L. GREVE, and T. WIERZBICKI (2015). "FE simulation of edge fracture considering pre-damage from blanking process". In: *International Journal of Solids and Structures* 71, pp. 206–218.

WANG, K. and T. WIERZBICKI (2015). "Experimental and numerical study on the plane-strain blanking process on an AHSS sheet". In: *International Journal of Fracture* 194 (1), pp. 19–36.

WATSON, G. (1964). "Smooth Regression Analysis". In: *Indian Journal of Statistics. Series A* 26 (4), pp. 359–372.

WEICKERT, J. and C. SCHNÖRR (2001). "A Theoretical Framework for Convex Regularizers in PDE-Based Computation of Image Motion". In: *International Journal of Computer Vision* 45 (3), pp. 245–264.

WEISS, H., N. LEUNING, K. HAMEYER, H. HOFFMANN, and W. VOLK (2019). "Manufacturing efficient electrical motors with a predictive maintenance approach". In: *CIRP Annals* 68 (1), pp. 253–256.

WEISS, H., N. LEUNING, S. STEENTJES, K. HAMEYER, T. ANDORFER, S. JENNER, and W. VOLK (2017). "Influence of shear cutting parameters on the electromagnetic properties of non-oriented electrical steel sheets". In: *Journal of Magnetism and Magnetic Materials* 421, pp. 250–259.

WEN, Y., Z. CHEN, and Y. ZANG (2013). "Failure Analysis of a Sheet Metal Blanking Process Based on Damage Coupling Model". In: *Journal of Materials Engineering and Performance* 22 (11), pp. 3288–3295.

WENZEL METROMEC AG (2013). *Metrosoft Quartis*. Chur: Wenzel Metromec AG.

WENZEL PRÄZISION GMBH (2012). *Betriebsanleitung 3D-Koordinatenmessgerät LH 87*. Wiesthal: Wenzel Präzision GmbH.

WHITTAKER, E. (1922). "On a New Method of Graduation". In: *Proceedings of the Edinburgh Mathematical Society* 41, pp. 63–75.

WIERZBICKI, T., Y. BAO, Y.-W. LEE, and Y. BAI (2005). "Calibration and evaluation of seven fracture models". In: *International Journal of Mechanical Sciences* 47 (4-5), pp. 719–743.

WU, X., H. BAHMANPOUR, and K. SCHMID (2012). "Characterization of mechanically sheared edges of dual phase steels". In: *Journal of Materials Processing Technology* 212 (6), pp. 1209–1224.

YANG, J. and K. BHATTACHARYA (2019). "Augmented Lagrangian Digital Image Correlation". In: *Experimental Mechanics* 59 (2), pp. 187–205.

YAO, B. and H. YANG (2016). "Physics-driven Spatiotemporal Regularization for High-dimensional Predictive Modeling: A Novel Approach to Solve the Inverse ECG Problem". In: *Scientific Reports* 6, p. 39012.

YIN, Q., B. ZILLMANN, S. SUTTNER, G. GERSTEIN, M. BIASUTTI, A. TEKKAYA, M.-X. WAGNER, M. MERKLEIN, M. SCHAPER, T. HALLE, and A. BROSIUS (2014). "An experimental and numerical investigation of different shear test configurations for sheet metal characterization". In: *International Journal of Solids and Structures* 51 (5), pp. 1066–1074.

YOUNG, D. (1950). *Iterative Methods for Solving Partial Difference Equations of Elliptic Type, PhD thesis*. Cambridge.

YU, S. and J. ZHAO (2012). "Investigation on blanking of thick sheet metal using the ductile fracture initiation and propagation criterion". In: *Journal of Shanghai Jiaotong University* 17 (5), pp. 531–536.

ZEHNDER, A. T. (1991). "A model for the heating due to plastic work". In: *Mechanics Research Communications* 18 (1), pp. 23–28.

ZHENG, P., T. LEE, and L. CHAN (2005). "Application of a large-strain analysis technique to the combined fine-blanking and extrusion process". In: *Journal of Strain Analysis for Engineering Design* 40 (3), pp. 263–273.

ZHU, Y., Q. YAN, and J. LU (2020). "Deformation characteristics and grain size effect of thin silicon steel sheet during shearing". In: *Machining Science and Technology* 1987 (6), pp. 1–25.

ZIEGLER, H. (1958). "An attempt to generalize Onsager's principle, and its significance for rheological problems". In: *ZAMP Zeitschrift für angewandte Mathematik und Physik* 9 (5-6), pp. 748–763.

– (1974). "Eine neue Begründung des Orthogonalittsprinzips". In: *Ingenieur-Archiv* 43 (6), pp. 381–394.

– (1977). "Grundprobleme der Thermomechanik". In: *ZAMP Zeitschrift für angewandte Mathematik und Physik* 28 (5), pp. 965–977.

ZIMMER, V., K. LEKADIR, C. HOOGENDOORN, A. FRANGI, and G. PIELLA (2015). "A framework for optimal kernel-based manifold embedding of medical image data". In: *Computerized medical imaging and graphics* 41, pp. 93–107.

ZOU, H. and T. HASTIE (2005). "Regularization and variable selection via the elastic net". In: *Journal of the Royal Statistical Society. Series B* 67 (2), pp. 301–320.

ZWICK GMBH & CO. KG (1998). *Betriebsanleitung Material Prüfmaschine*. Ulm: Zwick GmbH & Co. KG.

– (2009). *Sheet Metal Testing Machine*. Ulm: Zwick GmbH & Co. KG.

E Standards

DIN 7500-1 (2016). *Metallische Werkstoffe – Kalibrierung und Überprüfung von statischen einachsigen Prüfmaschinen – Teil 1: Zug- und Druckprüfmaschinen – Kalibrierung und Überprüfung der Kraftmesseinrichtung.*

DIN EN 10149-2 (1995). *Warmgewalzte Flacherzeugnisse aus Stählen mit hoher Streckgrenze zum Kaltumformen – Teil 2: Lieferbedingungen für thermomechanisch gewalzte Stähle.*

DIN EN 485-2 (2016). *Aluminium und Aluminiumlegierungen - Bänder, Bleche und Platten - Teil 2: Mechanische Eigenschaften.*

DIN EN 573-3 (2019). *Aluminium und Aluminiumlegierungen - Chemische Zusammensetzung und Form von Halbzeug – Teil 3: Chemische Zusammensetzung und Erzeugnisformen.*

DIN EN ISO 4957 (2018). *Werkzeugstähle.*

DIN6930-2 (2011). *Stanzteile aus Stahl - Teil 2 - Allgemeintoleranzen.*

DIN8580 (2003). *Fertigungsverfahren - Begriffe, Einteilung.*

DIN8588 (2013). *Fertigungsverfahren Zerteilen - Einordnung, Unterteilung, Begriffe.*

DIN9869-1 (1967). *Begriffe für Werkzeuge zur Fertigung dünner, vorwiegend flächenbestimmter Werkstücke.*

DIN9869-2 (1969). *Begriffe für Werkzeuge der Stanztechnik - Schneidwerkzeuge.*

DIN9870-2 (1972). *Begriffe der Stanztechnik - Fertigungsverfahren und Werkzeuge zum Zerteilen.*

VDI2906-2 (1994). *Schnittflächenqualität beim Schneiden, Beschneiden und Lochen von Werkstücken aus Metall - Scherschneiden.*

VDI3368 (1982). *Schneidspalt- Schneidstempel- und Schneidplattenmaße für Schneidwerkzeuge der Stanztechnik.*

F Appendix

F.1 Testing Equipment

F.1.1 Testing Machine

The testing machine used is a universal tension-compression testing machine of type 1484/DUPS-M from Zwick GmbH & Co.KG, Ulm, Germany (Zwick GmbH & Co. KG, 1998). Two guide columns connect the upper and lower head of the machine and guide the cross-head. Two servo-driven spindles installed parallel to the guide columns move the traverse. The guide columns together with the upper and lower head close an O-frame The testing machine has two test chambers by the central arrangement of the crosshead. Force measurements are possible in the upper test chamber up to 20 kN and in the lower test chamber up to 200 kN. The force measurements are categorized in class 1 according to DIN 7500-1, 2016. In the context of this work only the lower test space is used. The testing machine was controlled by the software Test Expert II V3.0 by Zwick GmbH & Co.KG, Ulm, Germany (Zwick GmbH & Co. KG, 2009).

F.1.2 High-Speed Camera

The high-speed camera used is of the type Os3-S2 from Integrated Design Tools Inc., Pasadena, United States (Integrated Design Tools Inc., 2016). The camera has a non-volatile internal SSD memory with 16 GB. The camera is acceleration resistant up to 200 G and resists vibrations up to 40 G. The built-in CMOS sensor has light sensitivities up to 30000 ASA, and a maximum color depth of 12-bit. At a resolution of 1280 pixel by 1024 pixel, a recording frequency of 5 kHz is possible. Reduced resolution allow to work with even higher frame rates, for example 7 kHz using a resolution of 720 pixel by 1280 pixel with 8-bit color depth. The camera was operated using IDT Motion Studio 2.15 from Integrated Design Tools Inc., Pasadena, United States (Integrated Design Tools Inc., 2019).

F.1.3 Coordinate Measuring Machine

The coordinate measuring machine used is of type LH 87 of the company Wenzel Group GmbH & Co KG, Wiesthal, Germany (Wenzel Präzision GmbH, 2012). By mechanical contact between workpiece and probe the coordinates of the touch point can be calculated in the machine coordinate system. It is therefore a tactile measuring method. The moving axes are guided on stone, are motor-driven, and are controlled by a computer. The built-in Renishaw SP25M sensor allows measurement accuracy of up to $0.05\,\mu$m (Renishaw plc., 2018). For evaluation and control the software Metrosoft Quartis R9, Wenzel Metromec AG, Chur, Switzerland, is available (Wenzel Metromec AG, 2013).

F.1.4 Contour Measuring Device

The contour measuring device is of type MarSurf XCR 20 by the company Mahr GmbH, Göttingen, Germany. The measuring system works according to the principle of tactile stepping (Mahr GmbH, 2005). A tactile unit with stylus tip is moved by the PCV 200 feed unit over the measured object for contour capturing. The measurement system achieves an accuracy of up to $0.5\,\mu$m. The control of the tests is performed by the MarWin XC 20 software (Mahr GmbH, 2005).

F.1.5 Laser Confocal Microscope

The laser confocal microscope is of type VK-X150K from Keyence Corporation, Osaka, Japan (Keyence Corporation, 2018). The microscope uses a red semiconductor laser with a wavelength of 658 nm. With this laser, height differences of $0.005\,\mu$m can be recorded with a repeatability of $0.04\,\mu$m. The lateral measurement resolution is $0.01\,\mu$m showing a repeatability of $0.1\,\mu$m. The measurements are controlled and stitched using the software VK-H1XVD2 from Keyence Corporation, Osaka, Japan (Keyence Corporation, 2018).

F.2 Materials

F.2.1 Steel S355MC

The micro-alloyed fine-grained structural steel S355MC bears the material number 1.0976. The steel sheet is hot-rolled, low-carbon and has a high yield strength and good cold formability.

element	C	Mn	Si	P	S	Al	Nb	V	Ti
mass-%	>0.12	>1.50	>0.50	>0.25	>0.020	>0.015	>0.09	>0.20	>0.15

Table F.1: Alloy composition of the steel sheet metal S355MC (DIN EN 10149-2, 1995).

YP	UTS	MUE
< 355 MPa	430 − 550 MPa	19%

Table F.2: Basic mechanical properties of the steel sheet metal S355MC (DIN EN 10149-2, 1995); YP: yield point, UTS: Ultimate tensile strength, MUE: Maximum uniform elongation.

F.2.2 Aluminum EN AW 5083

The material EN AW 5083, AlMg4.5Mn0.7, categorizes into the group of aluminum-magnesium alloys and bears the material number 3.3547. The aluminum sheet has a significant natural hardness.

element	Si	Fe	Cu	Mn	Mg	Zn	Cr	Ti
mass-%	0.1	0.4	0.1	0.4-1	4-4.9	0.25	0.05-0.25	0.15

Table F.3: Alloy composition of the aluminum sheet metal EN AW 5083 (DIN EN 573-3, 2019).

YP	UTS	MUE
124 MPa	270 MPa	15%

Table F.4: Basic mechanical properties of the aluminum sheet metal EN AW 5083 (DIN EN 485-2, 2016); YP: yield point, UTS: Ultimate tensile strength, MUE: Maximum uniform elongation.

F.3 Algorithms

F.3.1 Displacement Estimation Algorithm

Algorithm 1 DIC algorithm for displacement field estimation.

---

algorithm parameters convergence threshold ϵ_c, subset size $|S|$, grid step for subset selection δ

INPUT image I_0, image I_1, n subsets S_i, seed point index i_s

BUILD queue with n elements

i_s = first element in the queue

BUILD storage for C_{ZSSD} with n elements

INITIALIZE counter $= 0$

%% loop over all subsets

while counter $\leq n$ **do**

    i = first element in the queue

    %% compute integer pixel result

    $\mathbf{u}_i = \underset{\mathbf{u}}{\operatorname{argmax}} \left(C_{\mathrm{ZSSD}} \left(I_0, I_1(\mathbf{u}), S_i \right) \right) \forall \mathbf{x}_0 \in S_i$

    %% compute sub-pixel result

    INITIALIZE $\mathfrak{W}^{(0)}(\boldsymbol{\xi}, \boldsymbol{\varphi})$ based on integer pixel calculation $\mathbf{u}_i$

    COMPUTE $J_0 = \frac{1}{|S|} \sum_{S_i} I_0(\mathbf{x_0} + \boldsymbol{\xi})$

    COMPUTE $L_0 = \sqrt{\sum_{S_i} \left(I_0(\mathbf{x_0} + \boldsymbol{\xi}) - J_0(\mathbf{x_0} + \boldsymbol{\xi}) \right)^2}$

    COMPUTE Hessian matrix $\mathbf{H} = \sum_{S_i} \left(\left(\nabla I_0 \frac{\partial \mathfrak{W}}{\partial \boldsymbol{\varphi}} \right)^T \times \left(\nabla I_0 \frac{\partial \mathfrak{W}}{\partial \boldsymbol{\varphi}} \right) \right)$

    while $||\Delta \boldsymbol{\varphi}||_2 > \epsilon_c$ **do**

$$\Delta \boldsymbol{\varphi}^{(j+1)} = \mathbf{H} \times \sum_{S_i} \left(\left(\nabla I_0 \frac{\partial \mathfrak{W}}{\partial \boldsymbol{\varphi}} \right)^T \times \left(\frac{I_0(\mathbf{x_0} + \boldsymbol{\xi}) - J_0}{L_0} - \frac{I_1^{(j)}(\mathbf{x}_0 + \mathfrak{W}^{(j)}(\boldsymbol{\xi}; \boldsymbol{\varphi})) - J_1^{(j)}}{L_1^{(j)}} \right) \right)$$

$$\mathfrak{W}^{(j+1)}(\boldsymbol{\xi}, \boldsymbol{\varphi}) = \mathfrak{W}^{(j)}(\mathfrak{W}(\boldsymbol{\xi}, \Delta \boldsymbol{\varphi}^{(j+1)})^{-1}, \boldsymbol{\varphi})$$

$$I_1^{(j+1)}(\mathbf{x}_0 + \mathfrak{W}^{(j+1)}(\boldsymbol{\xi}; \Delta \boldsymbol{\varphi})) = I_1^{(j)}(\mathbf{x}_0 + \boldsymbol{\xi}) + \nabla I_1^{(j)} \frac{\partial \mathfrak{W}}{\partial \boldsymbol{\varphi}} \Delta \boldsymbol{\varphi}^{(j+1)}$$

    end while

    %% store sub-pixel displacement calculation for subset S_i

    $\mathbf{u}_i = \mathfrak{W}(0; \boldsymbol{\varphi})$

    UPDATE C_{ZSSD} storage

    REMOVE i from queue

    SORT queue according to C_{ZSSD} values in storage

    counter $=$ counter $+ 1$

end while

OUTPUT displacement field $\mathbf{u}$

F.3.2 Dimensionality Reduction Algorithm

Algorithm 2 Image handling routine for dimensionality reduction.

---

algorithm parameters threshold $\epsilon_{\mathbf{u}}$, threshold $\epsilon_{\nabla\mathbf{u}}$, refinement λ_{re}, coarsening λ_{co}

INPUT image stack $I = \{I^{(0)}, I^{(1)}, I^{(2)}, \ldots, I^{(n)}\}$, initial image interval v_0

INITIALIZE $v = v_0$, $i = 1 + v_0$

%% updated Lagrangian evaluation scheme with moving reference

while $i + v \leq n + 1$ **do**

    $u^{(i-1)} = $ result of algorithm 1 for $I_0 = I^{(i-1)}$ and $I_1 = I^{(i-1+v)}$

    if $\max(||\mathbf{u}_S^{(i-1)}||_2) \leq \epsilon_{\mathbf{u}} \wedge \max(||\nabla\mathbf{u}_S^{(i-1)}||_2) \leq \epsilon_{\nabla\mathbf{u}}$ **then**

        STORE $\mathbf{u}^{(i-1)}$

        $i = i - 1 + v$

        $v = $ CEIL $\lambda_{\mathrm{co}} v$

    else if $v > 2$ **then**

        $i = i - 1 + v$

        $v = $ CEIL $\dfrac{v}{\lambda_{\mathrm{re}}}$

    else

        $i = i + 1$, $v = 1$

    end if

end while

OUTPUT stack of displacement fields $\mathbf{u} = \{\mathbf{u}^{(v_0)}, \mathbf{u}^{(v_0+v_1)}, \mathbf{u}^{(v_0+v_1+v_2)}, \ldots, \mathbf{u}^{(n)}\}$

F.3.3 Strain Estimation Algorithm

Algorithm 3 Total variation deformation gradient $\mathbf{F}$ estimation.

---

algorithm parameters weighting factors: λ_1, λ_2, number of iterations n_{it}, update parameter λ_3

INPUT displacement field $\mathbf{u} = (\mathbf{u}_1, \mathbf{u}_2)$

BUILD differentiation operator $(\mathbf{Dq})_k = \begin{cases} \mathbf{q}_{k+1} - \mathbf{q}_k & : k < N_{1,2} - 1 \\ \mathbf{q}_0 - \mathbf{q}_{N_{1,2}-1} & : k = N_{1,2} - 1 \end{cases}$

%% Loop for horizontal and vertical displacement components

for $i = 1, 2$ **do**

    INITIALIZE $\mathbf{w}^{(0)}$

    INITIALIZE $\mathbf{\Lambda}^{(0)}$

    %% Loop of alternating directions and multiplier update

    for $j = 1, \ldots, n_{\text{it}}$ **do**

$$\widehat{\mathbf{w}}^{(j)} = \mathfrak{F}\left(\mathbf{w}^{(j)}\right), \widehat{\mathbf{\Lambda}}^{(j)} = \mathfrak{F}^{-1}\left(\mathbf{\Lambda}^{(j)}\right)$$

    %% update in k-direction

$$\widehat{\mathbf{F}}_{i1}^{(j+1)}(k,l) = \frac{\frac{1}{\lambda_2}\xi_k\left(\widehat{\mathbf{w}}_{11}^{(j)}(k,l) - \widehat{\mathbf{\Lambda}}_{11}^{(j)}(k,l)\right) + \frac{1}{\lambda_2}\xi_l\left(\widehat{\mathbf{w}}_{12}^{(j)}(k,l) - \widehat{\mathbf{\Lambda}}_{12}^{(j)}(k,l)\right) + \lambda_1\xi_k\widehat{\mathbf{u}}_i(k,l)}{\frac{1}{\lambda_2}||\xi_k||_1^2 + \frac{1}{\lambda_2}||\xi_l||_1^2 + \lambda_2\frac{1}{||\xi_k||_1^2}}$$

    %% update in l-direction

    with $\xi_k = e^{\frac{-2\pi i k}{N_1}} - 1$

    for $k > 0$, and $\widehat{\mathbf{F}}_{i1}^{(j+1)}(0,l) = 0$

$$\widehat{\mathbf{F}}_{i2}^{(j+1)}(k,l) = \frac{\frac{1}{\lambda_2}\xi_k\left(\widehat{\mathbf{w}}_{21}^{(j)}(k,l) - \widehat{\mathbf{\Lambda}}_{21}^{(j)}(k,l)\right) + \frac{1}{\lambda_2}\xi_l\left(\widehat{\mathbf{w}}_{22}^{(j)}(k,l) - \widehat{\mathbf{\Lambda}}_{22}^{(j)}(k,l)\right) + \lambda_1\xi_l\widehat{\mathbf{u}}_i(k,l)}{\frac{1}{\lambda_2}||\xi_k||_1^2 + \frac{1}{\lambda_2}||\xi_l||_1^2 + \lambda_2\frac{1}{||\xi_l||_1^2}}$$

    with $\xi_l = e^{\frac{-2\pi i k}{N_2}} - 1$

    for $l > 0$, and $\widehat{\mathbf{F}}_{i2}^{(j+1)}(k,0) = 0$

$$\mathbf{F}_i^{(j+1)} = \mathfrak{F}^{-1}\left(\widehat{\mathbf{F}}_i^{(j+1)}\right), \mathbf{w}^{(j)} = \mathfrak{F}^{-1}\left(\widehat{\mathbf{w}}_i^{(j)}\right), \mathbf{\Lambda}^{(j)} = \mathfrak{F}^{-1}\left(\widehat{\mathbf{\Lambda}}_i^{(j)}\right)$$

$$\mathbf{w}^{(j+1)} = \frac{\mathbf{DF}_i^{(j+1)} + \mathbf{\Lambda}^{(j)}}{||\mathbf{DF}_i^{(j+1)} + \mathbf{\Lambda}^{(j)}||_1}\max\left\{\mathbf{DF}_i^{(j+1)} + \mathbf{\Lambda}^{(j)} - \lambda_2, 0\right\}$$

$$\mathbf{\Lambda}^{(j+1)} = \lambda_3\left(\mathbf{\Lambda}^{(j)} + \mathbf{DF}_i^{(j+1)} - \mathbf{w}^{(j+1)}\right)$$

    end for

end for

OUTPUT deformation gradient field $\mathbf{F}$

F.3.4 Strain Rate Estimation Algorithm

Algorithm 4 Robust rate of the deformation gradient $\dot{\mathbf{F}}$ estimation.

---

algorithm parameters weighting factors: λ_s, λ_t, λ_{ba}, λ_{ti}, λ_{s1}, λ_{s2}, λ_{s3}, penalty parameters: ε_d, ε_t
relaxation parameter r_{SOR}, number of iterations n_{out}, n_{in}, thresholds $\epsilon_{\mathbf{d}}$, $\epsilon_{\mathbf{A}}$, $\epsilon_{\mathbf{B}}$,
pyramid levels n_{lev}, resize factor ρ_{re}, Gaussian kernel K_σ

INPUT images $I^{(i-2)}, \dots, I^{(i+2)}$, time step Δt

INITIALIZE $\mathbf{u}_0^{(i-2)}, \dots, \mathbf{u}_0^{(i+1)} = 0$, $\mathbf{A}_0^{(i)}, \dots, \mathbf{A}_0^{(i+1)} = 0$, $\mathbf{B}_0^{(i)}, \dots, \mathbf{B}_0^{(i+1)} = 0$
for $k = n_{lev} : -1 : 0$ **do**
    INITIALIZE $\mathbf{d} = 0$
    RESIZE $I^{(i-2)}, \dots, I^{(i+2)}, \mathbf{u}_{k-1}^{(i-2)}, \dots, \mathbf{u}_{k-1}^{(i+1)}, \mathbf{A}_{k-1}^{(i)}, \dots, \mathbf{A}_{k-1}^{(i+1)}, \mathbf{B}_{k-1}^{(i)}, \dots, \mathbf{B}_{k-1}^{(i+1)}$ with ρ_{re}^k
    for $l = 1 : n_{out}$ **do**
        COMPUTE $\mathbf{V}^{(i-2)}, \dots, \mathbf{V}^{(i-1)}$ from $\{I^{(i-2)}, \dots, I^{(i+2)}\}$ and $\mathbf{d}$
        COMPUTE $\mathbf{W}^{(i-2)}, \dots, \mathbf{W}^{(i-1)}$ from $\{I^{(i-2)}, \dots, I^{(i+2)}\}$ and $\mathbf{d}$
        $\mathbf{d}_l = \text{SOR}\left(\mathbf{d}_{l-1}, \mathbf{u}_{k-1}^{(i-2)}, \dots, \mathbf{u}_{k-1}^{(i+1)}, \mathbf{V}_{k-1}^{(i-2)}, \dots, \mathbf{V}_{k-1}^{(i-1)}, \mathbf{W}_{k-1}^{(i-2)}, \dots, \mathbf{W}_{k-1}^{(i-1)}, \mathbf{A}_{k-1}^{(i)}, \dots, \mathbf{A}_{k-1}^{(i+1)}, \dots\right.$
            $\left. \lambda_s, \lambda_t, \lambda_{ti}, \lambda_{ba}, \lambda_{s1}, \varepsilon_d, \varepsilon_t, r_{SOR}, \epsilon_{\mathbf{d}}, n_{in}\right)$
        if $||\mathbf{d}_l||_2 \leq \epsilon_{\mathbf{d}}$ **then**
            BREAK
        end if
    end for
    UPDATE $\mathbf{u}_k^{(i-2)}, \dots, \mathbf{u}_k^{(i+1)}$ with $\mathbf{d}$
    for $m = (i-2), \dots, (i+1)$ **do**
        $\mathbf{A}_k^m = \text{SOR}\left(\mathbf{A}_{k-1}^m, \mathbf{B}_{k-1}^m, \lambda_{s2}, r_{SOR}, \epsilon_{\mathbf{A}}, n_{in}\right)$
    end for
    for $m = (i-2), \dots, (i+1)$ **do**
        for $n = 1 : n_{out}$ **do**
            $\mathbf{B}_{k,n}^m = \mathbf{B}_{k,n-1}^m$
            $\mathbf{B}_{k,n}^m = \text{SOR}\left(\mathbf{A}_k^m, \mathbf{B}_{k,n-1}^m, \lambda_{s3}, r_{SOR}, \epsilon_{\mathbf{B}}, n_{in}\right)$
            if $||\mathbf{B}_{k,n}^m||_2 \leq \epsilon_{\mathbf{B}}$ **then**
                BREAK
            end if
        end for
    end for
end for
$\dot{\mathbf{F}}^{(i)} = \frac{1}{2\Delta t}\left(\mathbf{A}^{(i-1)} + \mathbf{A}^{(i+1)}\right)$

OUTPUT rate of the deformation gradient $\dot{\mathbf{F}}^{(i)}$

F.3.5 Fracture Analysis Algorithm

Algorithm 5 Total generalized variation motion estimation.

---

algorithm parameters weighting factors: λ_{f1}, λ_{f2}, number of iterations n_{it}, pyramid levels n_{lev}, resize factor ρ_{re}, Gaussian kernel K_σ, primal dual algorithm settings: τ_1, τ_2, θ

INPUT images $I^{(i)} = I_0$, $I^{(i+1)} = I_1$

INITIALIZE $\mathbf{u}_{k+1} = 0$

INITIALIZE $\mathbf{a}_{k+1} = 0$

for $k = n_{lev} : -1 : 0$ **do**

    RESIZE I_0, I_1 with ρ_{re}^k and Gaussian kernel K_σ

    $\mathbf{u}_{k,0} = \dfrac{\rho_{re}^k}{\rho_{re}^k + 1} \text{resize}\left(\mathbf{u}_{k+1}, \rho_{re}^k N_1 \times \rho_{re}^k N_2\right)$

    $\mathbf{a}_{k,0} = \text{resize}\left(\mathbf{u}_{k+1}, \rho_{re}^k N_1 \times \rho_{re}^k N_2\right)$

    INITIALIZE $\mathbf{b}_{k,0} = 0$, $\mathbf{e}_{k,0} = 0$, $\text{d}\mathbf{b}_{k,0} = \mathbf{0}$, $\text{d}\mathbf{e}_{k,0} = 0$

    for $r = 1 : n_{it}$ **do**

        $\mathbf{u}_{k,r+1} = \underset{\mathbf{u}}{\text{argmin}}\left\{ \left|\left| \dfrac{\partial I_1(\mathbf{du})}{\partial x_1}\mathbf{u}_1 + \dfrac{\partial I_1(\mathbf{du})}{\partial x_2}\mathbf{u}_2 + I_1(\mathbf{u}) - I_0 \right|\right|_1 + \dfrac{1}{2\tau_1}\left|\left| \mathbf{u} - \left(\mathbf{u}_{k,r} - \tau_1\tau_2\nabla^T \text{d}\mathbf{b}_{k,r}\right) \right|\right|_2^2 \right\}$

        $\mathbf{a}_{k,r+1} = \mathbf{a}_{k,r} - \tau_1\tau_2\left(\nabla_\varepsilon^T \text{d}\mathbf{e}_{k,r} - \text{d}\mathbf{b}_{k,r}\right)$

        $\mathbf{s}_{k,r+1} = \underset{\mathbf{s}}{\text{argmin}}\left\{ \lambda_{f1}||\mathbf{s}||_{2,1} + \dfrac{\tau_2}{2}\left|\left| \mathbf{s} - \left(\mathbf{b}_{k,r} + \nabla\mathbf{u}_{k,r+1} - \mathbf{a}_{k,r+1}\right) \right|\right|_2^2 \right\}$

        $\mathbf{t}_{k,r+1} = \underset{\mathbf{t}}{\text{argmin}}\left\{ \lambda_{f2}||\mathbf{t}||_{2,1} + \dfrac{\tau_2}{2}\left|\left| \mathbf{t} - \left(\mathbf{e}_{k,r} + \nabla_\varepsilon a_{k,r+1}\right) \right|\right|_2^2 \right\}$

        $\mathbf{b}_{k,r+1} = \mathbf{b}_{k,r} + \nabla\mathbf{u}_{k,r+1} - \mathbf{a}_{k,r+1} - \mathbf{s}_{k,r+1}$

        $\mathbf{e}_{k,r+1} = \mathbf{e}_{k,r} + \nabla_\varepsilon\mathbf{a}_{k,r+1} - \mathbf{t}_{k,r+1}$

        $\text{d}\mathbf{b}_{k,r+1} = 2\mathbf{b}_{k,r+1} - \mathbf{b}_{k,r}$

        $\text{d}\mathbf{e}_{k,r+1} = 2\mathbf{e}_{k,r+1} - \mathbf{e}_{k,r}$

    end for

    $\mathbf{u}_k = \text{medfilt}(\mathbf{u}_k)$

    $\mathbf{a}_k = \text{medfilt}(\mathbf{a}_k)$

end for

OUTPUT displacement $\mathbf{u}$, Lagrange strain tensor components $\mathbf{a}$, discontinuous part $\mathbf{s}$

F.3.6 Geometry Analysis Algorithm

Algorithm 6 Sampling-based geometry analysis of the cut surface.

---

algorithm parameters polynomial degree vector $\mathbf{d}_{\mathrm{p}}$

INPUT contour coordinates $\mathbf{x} = (x_1, x_2)_n$, where $n = 1 \dots L$

INITIALIZE $\boldsymbol{\iota} = (d_1 + 1, d_1 + d_2 + 2, d_1 + d_2 + d_3 + 3, d_1 + d_2 + d_3 + d_4 + 4, L)$

for $i = 1, \dots, 5$ **do**

    $\mathbf{x} = (x_1)|_{\iota_{i-1}}, \dots, (x_1)|_{\iota_i}, \mathbf{y} = (x_2)|_{\iota_{i-1}}, \dots, (x_2)|_{\iota_i}$

    COMPUTE Vandermonde matrix $\mathbf{V}$ with degree d_i and polynomial coefficients $\mathbf{p}$

    SOLVE $\mathbf{Vp} = \mathbf{y}$

    $\mathbf{y}_{\mathrm{p}} = \mathbf{Vp}(\mathbf{x})$

    $R_i = ||\mathbf{y}_{\mathrm{p}} - \mathbf{y}||_2$

end for

$R_{\mathrm{m}} = \sum_{i=1}^{5} R_i$

for $l = 1, 2, 3, \dots, L - \sum_{i=2}^{5}(d_i + 1)$ **do**

    for $m = l, l + 1, l + 2, \dots, L - \sum_{i=3}^{5}(d_i + 1)$ **do**

        for $n = m, m + 1, m + 2, \dots, L - \sum_{i=4}^{5}(d_i + 1)$ **do**

            for $o = n, n + 1, n + 2, \dots, L - d_5 + 1$ **do**

                for $i = 1, \dots, 5$ **do**

                    $\mathbf{x} = (x_1)|_{\iota_{i-1}}, \dots, (x_1)|_{\iota_i}, \mathbf{y} = (x_2)|_{\iota_{i-1}}, \dots, (x_2)|_{\iota_i}$

                    COMPUTE $\mathbf{V}$ with d_i and $\mathbf{p}$

                    SOLVE $\mathbf{Vp} = \mathbf{y}$

                    $\mathbf{y}_{\mathrm{p}} = \mathbf{Vp}(\mathbf{x})$

                    $R_i = ||\mathbf{y}_{\mathrm{p}} - \mathbf{y}||_2$

                end for

                $R_{\mathrm{t}} = \sum_{i=1}^{5} R_i$

                if $R_{\mathrm{t}} < R_{\mathrm{m}}$ **then**

                    $R_{\mathrm{m}} = R_{\mathrm{t}}$

                    $\boldsymbol{\iota}_{\mathrm{m}} = (l, m, n, o, L)$

                end if

            end for

        end for

    end for

end for

COMPUTE $\boldsymbol{\varphi}$ from $(x_1, x_2)_i$ with $\boldsymbol{\iota}_{\mathrm{m}}$

OUTPUT model parameters $\boldsymbol{\varphi}$

F.3.7 Algorithm Parameter Selection Routine

Algorithm 7 Assessment of motion estimation algorithm parameter selection.

---

algorithm parameters number of synthetic output images N, time step Δt, model parameter vector $\mathbf{p}_i$ and number of model parameters p_i for $i = 1, \ldots, 5$

INPUT images $\{I_0, \ldots, I_{0+n}\}$, ground truth motion $^{\text{GT}}\mathbf{u} = (\mathbf{u}_1, \mathbf{u}_2)$, discontinuities $^{\text{GT}}\mathbf{d} = (\mathbf{d}_1, \mathbf{d}_2)$

BUILD differentiation operator $(\mathbf{Dq})_k = \begin{cases} \mathbf{q}_{k+1} - \mathbf{q}_k & : k < N_{1,2} - 1 \\ \mathbf{q}_0 - \mathbf{q}_{N_{1,2}-1} & : k = N_{1,2} - 1 \end{cases}$

COMPUTE σ from images $\{I_0, \ldots, I_{0+n}\}$

for $j = 1, \ldots, N$ **do**

$\quad ^{\text{GT}}\mathbf{u}^{(j)} = \dfrac{j-1}{N-1}(\mathbf{u} + \mathbf{d}), \; ^{\text{GT}}\mathbf{F}^{(j)} = \dfrac{j-1}{N-1}\mathbf{Du}, \; ^{\text{GT}}\dot{\mathbf{F}}^{(j)} = \dfrac{j-1}{N-1}\dfrac{1}{\Delta t}\mathbf{Du}$

$\quad$ **for** $k = 1, \ldots, N_1$ **do**

$\quad\quad$ **for** $l = 1, \ldots, N_2$ **do**

$\quad\quad\quad I^{(j)}\left(\mathbf{x}_1(k,l) + {}^{\text{GT}}\mathbf{u}_1(k,l), \mathbf{x}_2(k,l) + {}^{\text{GT}}\mathbf{u}_2(k,l)\right) = I_0\left(\mathbf{x}_1(k,l), \mathbf{x}_2(k,l)\right)$

$\quad\quad$ **end for**

$\quad$ **end for**

$\quad$ SAMPLE $\sigma^{(j)}$ from σ

$\quad I^{(j)} = I^{(j)} + \sigma^{(j)}$

end for

COMPUTE $\{\mathbf{u}^{(3)}, \ldots, \mathbf{u}^{(N-2)}\}$ from $\{I^{(1)}, \ldots, I^{(N)}\}$ using algorithm 1 with $\mathbf{p}_1$, algorithm 2 with $\mathbf{p}_2$

COMPUTE $\{\mathbf{F}^{(3)}, \ldots, \mathbf{F}^{(N-2)}\}$ from $\{\mathbf{u}^{(3)}, \ldots, \mathbf{u}^{(N-2)}\}$ using algorithm 3 with $\mathbf{p}_3$

COMPUTE $\{\dot{\mathbf{F}}^{(3)}, \ldots, \dot{\mathbf{F}}^{(N-2)}\}$ from $\{I^{(1)}, \ldots, I^{(N)}\}$ using algorithm 4 with $\mathbf{p}_4$

COMPUTE $\{^{\text{C}}\mathbf{u}^{(3)}, \ldots, {}^{\text{C}}\mathbf{u}^{(N-2)}\}$ from $\{I^{(1)}, \ldots, I^{(N)}\}$ using algorithm 5 with $\mathbf{p}_5$

for $j = 3, \ldots, N-2$ **do**

$\quad D_{\text{BIC},\mathbf{u}}^{(j)} = 2N_1 N_2 \ln\left(\dfrac{1}{2N_1 N_2} \sum_{a=1}^2 \sum_{l=1}^{N_1} \sum_{k=1}^{N_2} \left(u_a^{(j)}(k,l) - {}^{\text{GT}}u_a^{(j)}(k,l)\right)^2\right) + (p_1 + p_2)\ln(2N_1 N_2)$

$\quad D_{\text{BIC},\mathbf{F}}^{(j)} = 4N_1 N_2 \ln\left(\dfrac{1}{4N_1 N_2} \sum_{a=1}^2 \sum_{b=1}^2 \sum_{l=1}^{N_1} \sum_{k=1}^{N_2} \left(F_{ab}^{(j)}(k,l) - {}^{\text{GT}}F_{ab}^{(j)}(k,l)\right)^2\right) + p_3 \ln(2N_1 N_2)$

$\quad D_{\text{BIC},\dot{\mathbf{F}}}^{(j)} = 4N_1 N_2 \ln\left(\dfrac{1}{4N_1 N_2} \sum_{a=1}^2 \sum_{b=1}^2 \sum_{l=1}^{N_1} \sum_{k=1}^{N_2} \left(\dot{F}_{ab}^{(j)}(k,l) - {}^{\text{GT}}\dot{F}_{ab}^{(j)}(k,l)\right)^2\right) + 2p_4$

$\quad D_{\text{BIC},^{\text{C}}\mathbf{u}}^{(j)} = 2N_1 N_2 \ln\left(\dfrac{1}{2N_1 N_2} \sum_{a=1}^2 \sum_{l=1}^{N_1} \sum_{k=1}^{N_2} \left(^{\text{C}}u_a^{(j)}(k,l) - {}^{\text{GT}}u_a^{(j)}(k,l)\right)^2\right) + 2p_5$

end for

OUTPUT $\{D_{\text{BIC},\mathbf{u}}^{(3)}, \ldots, D_{\text{BIC},\mathbf{u}}^{(N-2)}\}, \{D_{\text{BIC},\mathbf{F}}^{(3)}, \ldots, D_{\text{BIC},\mathbf{F}}^{(N-2)}\}, \{D_{\text{BIC},\dot{\mathbf{F}}}^{(3)}, \ldots, D_{\text{BIC},\dot{\mathbf{F}}}^{(N-2)}\}, \{D_{\text{BIC},^{\text{C}}\mathbf{u}}^{(3)}, \ldots, D_{\text{BIC},^{\text{C}}\mathbf{u}}^{(N-2)}\}$

F.4 Supplemental Results and Discussion

F.4.1 Strain Path Families

To cope with the multilayered and multidimensional result figures, I introduce two supplemental types of representation that originate from chapter 6 *Results* to deduce the effects of the conducted shear cutting process modifications and to make it transparent for the chapter 7 *Discussion*. Figure F.1 summarizes the fundamental characteristics for the modification of the sheet metal material, the cutting line condition, and the process parameters cutting clearance, blade edge radii, and cutting velocity. I plotted at least three representative experiments from the parameter study to visualize the tendencies that are caused by the respective variation. Each line in the diagrams represents a material particle's strain path. Each dot indicates a measurement point.

Figure F.1 a) shows the principal strain diagram for the variation of the cutting clearance using the steel sheet metal S355MC. A reduction of the cutting clearance, represented through the three values 2.5%, 10%, and 15%, yields lower maximum values for the first principal strain E_1 components but gives higher values in the second principal strain E_2. The shape of the strain paths family compresses against the E_2 axis, which resembles the reach of the shear affected zone into the sheet metal. Reduced cutting clearance promote high strain values and narrow the affected zone.

I want to hint another way of thinking about the principal strain diagram, which is the Mohr's strain circle that gives a redundant representation for each material particle. In terms of Mohr's strain circle, the reduction of the cutting clearance reduces its diameter and shifts the center of the circle to lower values. The principal strain diagram for the variation of the cutting clearance using the aluminum sheet metal EN AW A5083 is given in figure F.1 b), also for values of 2.5%, 10%, and 15%. The obtained results support the findings from the S355MC sheet metal, however, the tendencies are weaker. In terms of Mohr's strain circle, the diameter reduction turns out lower but the shift of the circle center to lower values presents stronger.

Figure F.1 c) shows the principal strain diagram for the variation of the cutting clearance for open cutting lines using the steel sheet metal S355MC. The change of the boundary condition also does not influence the global trend that a reduction in cutting clearance yields higher maximum first principal strain values and narrows the shear affected zone. The diameter of Mohr's circle shrinks but lower compared to the closed cutting line and the circle center shifts more towards lower values. As a summary of sheet metal material and cutting line dependence, figure F.1 d)

shows the principal strain diagram for the aluminum EN AW A5083 and steel S355MC, each using open and closed cutting line under reference process parameter settings.

In comparison to open cutting lines, closed cutting lines reach higher strain states until crack initiation especially for the steel S355MC sheet metal. The change in boundary condition drastically reduces the diameter of Mohr's circle and moves the center of the circle far towards lower strains. Differences between the two materials are also obvious, due to the different constitutive behavior. Maximum first principal strain values E_1 reach higher levels for the S355MC steel material. For closed cutting lines, when switching from S355MC steel to aluminum EN AW 5083 the diameter of Mohr's circle shrinks and the center travels towards the coordinate origin. However, for open cutting lines, the differences are lower and the center shift turns out to be much lower.

The principal strain diagram in figure F.1 e) illustrates the effect of symmetric cutting edge variation using the steel sheet metal S355MC and the blade edge pairs of <20 μm, 50 μm, and 70 μm. The sharp cutting edge pair promotes early crack initiation, but on the other hand also yields increased local deformation, which is indicated in the diagram by the sporadic strain paths that escape the rest of the strain path family for $r_p=r_d$ <20 μm. Differences between 50 μm, and 70 μm are comparably, but the maximum strain levels using 50 μm reaches higher levels. In terms of Mohr's strain circle, sharper the blade edges partially increases the diameter extremely, which is accompanied by a strong shift of the circle center to higher values. Especially in the low first principal strain regions E_1 increased blade edge rounding enforces a strong reduction in diameter from increasing E_2 values, which works against the shift of the circle center towards lower values from the reduction of the first principal strains E_1. In the mid range of the first principal strain value E_1, cutting edge radii do not influence the strain distribution in shear affected zone significantly.

Figure F.1 f) draws the principal strain diagram for the variation of the cutting velocity using the steel sheet metal S355MC. I conducted the quasi-static experiment, the reference experiment, and the experiment using a cutting velocity of 3 mm/s. Higher cutting velocity leads to higher first principal strain values E_1, where the quasi-static experiment show comparably low strain values also in the second principal strain E_2. Increasing punch velocities widen the diameter of Mohr's circle and displace the circle center in the direction of the coordinate origin.
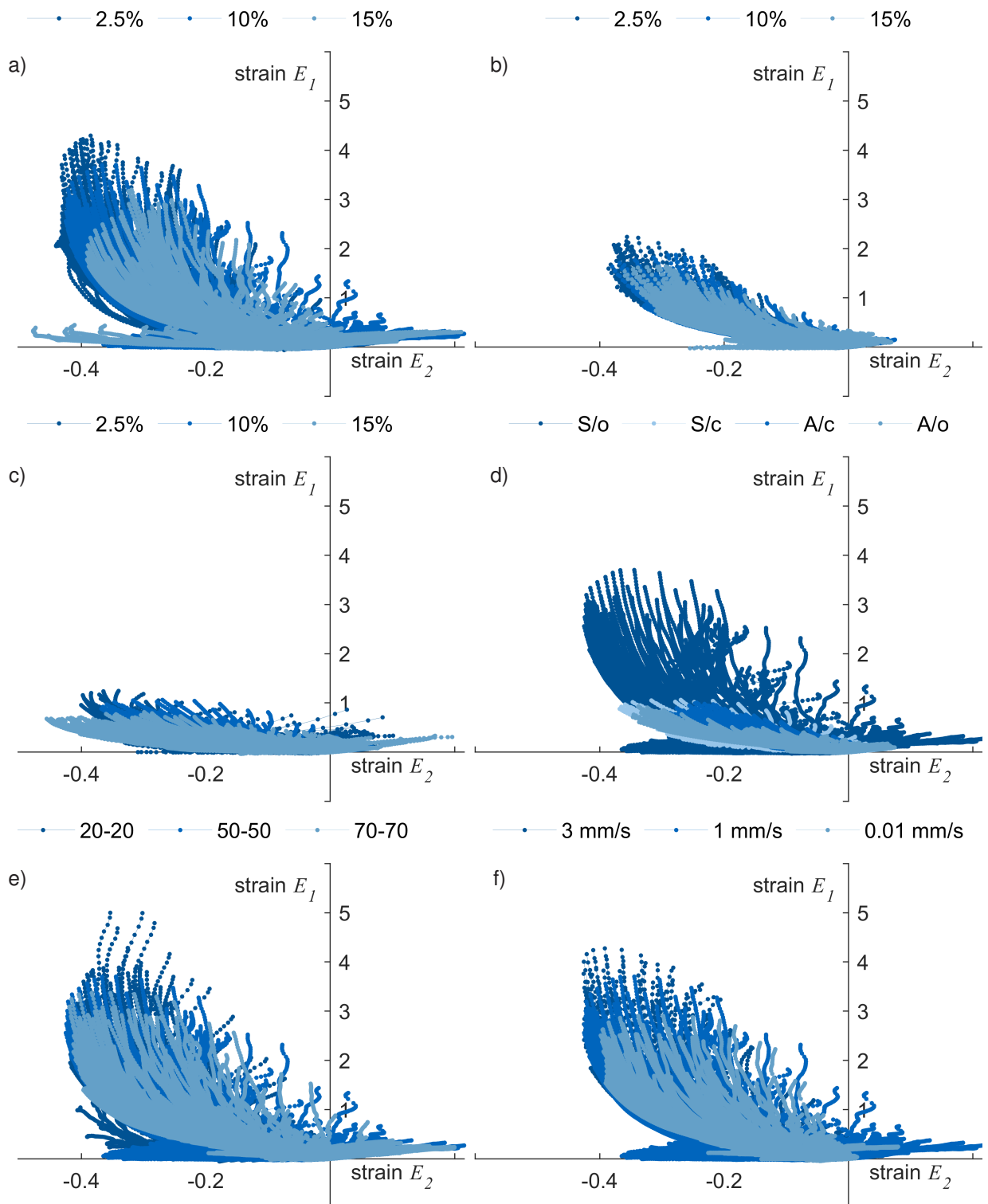
Figure F.1: Strain paths families until point D. a) S355MC closed cut varying cutting clearance, b) EN AW 5083 closed cut varying cutting clearance, c) S355MC open cut varying cutting clearance, d) open vs. closed cut reference settings, e) S355MC closed cut varying blade edge radii r_p-r_d, f) S355MC closed cut varying cutting velocity.

F.4.2 Dynamic Strain Path Families

To incorporate the dynamics in the analysis, I expanded figure F.2 by a rate indicator, which represents the equivalent rate calculated from the Green strain rate tensor $\dot{\mathbf{E}}$. Figure F.2 e), the central diagram, shows the reference experiment. The row consisting of figure F.2 d), e), and f) represents the dynamic process characteristics for cutting clearance from 2.5%, over 10%, to 15%. The column b), e), and h) of figure F.2 shows the dynamics for changing cutting velocities for 0.01 mm/s, 1 mm/s, and 3 mm/s. Along the diagonal consisting of Figure a), e), and i) I draw the influence of the blade edge rounding on the process dynamics from <20 μm, over 50 μm, to 70 μm. Figure F.2 c) describes the open cutting line experiment using reference settings and figure F.2 g) the closed cutting line experiment with aluminum EN AW 5083 sheet metal. Already at first glance, dynamic behavior differs significantly in the tested parameter space. I identify as a basic tendency that higher strain values within a single experiment are accompanied by higher strain rates. Referring back to Mohr's strain circle, strain rates indicate, how fast the diameter and the circle center change in between a time increment. This corresponds to the expected localizing behavior in the deformation band and especially at the cutting edges. The experiment with the open cutting line, only achieves significantly lower strain rates, see figure F.2 c), thus behaves much more moderately in the strain space as well as in the strain rate space. For the closed cutting line, the aluminum EN AW 5083, see figure F.2 g), achieves high strain rates despite the lower absolute principal strain values, which are even significantly higher than the strain rates of the reference experiment. The process dynamics are therefore not expressed or contained implicitly in the absolute principal strain values but are determined by the interaction with the material behavior. The dynamic behavior of the shear cutting process is characterized by the balance of hardening and softening effects in the shear affected zone. Strain hardening, strain rate hardening, temperature softening and damage, I would like to mention as important phenomena in this context. Their constellation for the aluminum promotes fast deformation, which I attribute to abrupt domination of the softening effect after the point of motion instability, see also the force punch travel curve in figure 6.20. The reduction of the cutting clearance also leads to reduced dynamics, see figure F.2 d), e), and f). Larger cutting clearance obtain wider deformation bands with smaller maximum values. Cutting edge variation yields high values for radii of <20 μm. Regarding maximum values the experiments using 50 μm, and 70 μm blade edge radii show similar results, but 70 μm shows earlier acceleration in the process. Cutting velocity has the largest influence on the dynamics of the process, see figure F.2 b), e), and h). The quasi-static cutting experiment does not show any anomalies in its behavior and shows no dynamics. The experiment performed with 3 mm/s shows the highest strain rate values that already arise in early process stages.
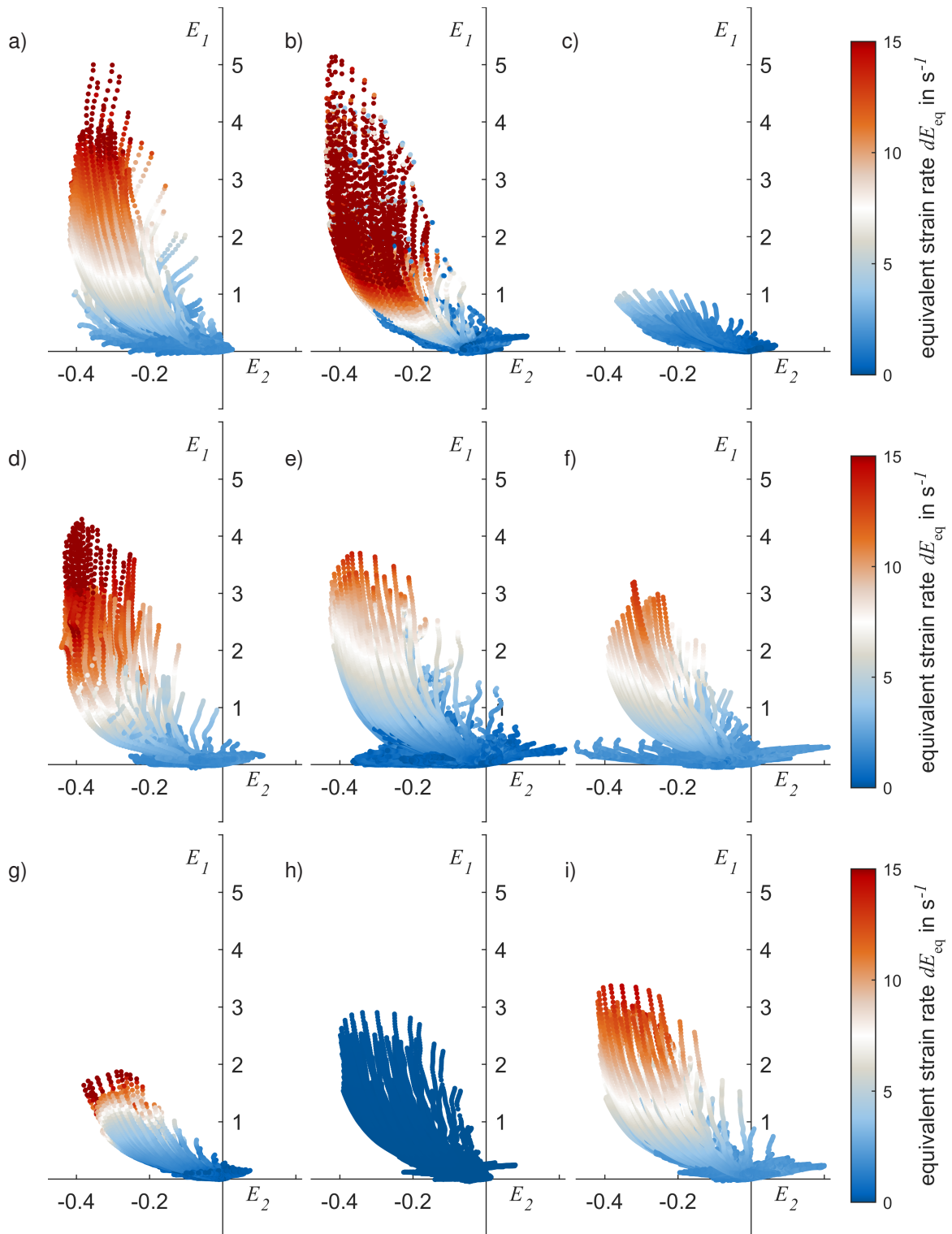
Figure F.2: Dynamic strain paths families until point D. a) S355MC radii <20 μm, b) S355MC velocity 3 mm/s, c) S355MC reference open cut settings, d) S355MC cutting clearance 2.5%, e) reference, f) S355MC cutting clearance 15%, g) EN AW 5083 reference settings, h) S355MC velocity 0.01 mm/s, i) S355MC radii of 70 μm.

Dissertationen des Lehrstuhls für Umformtechnik und Gießereiwesen, Prof. Dr.-Ing. Wolfram Volk

10   *Christoph Kaiser*
Effiziente Produkt- und Prozessabsicherung für
gefalzte Karosseriebauteile durch ein metamodellbasiertes
Assistenzsystem; 2018; ISBN: 978-3-95884-018-8

11   *Daniel Marian Opritescu*
Risikominimale Überbrückung von Kapazitätsengpässen
im Presswerksverbund der Automobilindustrie; 2018;
ISBN: 978-3-95884-020-1

12   *Maria Anna Hiller*
Fügen durch Clinchen mit rotierender Werkzeugbewegung;
2019; ISBN: 978-3-95884-024-9

13   *Hannes Alois Weiss*
Fertigung effizienter Elektromotoren; 2019;
ISBN: 978-3-95884-037-9

14   *Wan-Gi Cha*
Formability Consideration in Bead Optimization to stiffen Deep
Drawn Parts; 2019; ISBN: 978-3-95884-036-2

15   *Sven Peter Jansen*
Methodik zur Auslegung konturnaher Temperiersysteme
in Druckgusswerkzeugen; 2019; ISBN: 978-3-95884-035-5

16   *Georg Baumgartner*
Das mikromechanische Verhalten von binären
Aluminium-Silizium-Legierungen unter Last;
2019; ISBN: 978-3-95884-032-4

17   *Simon Vogt*
Entwicklung eines Verfahrens zur Herstellung von
verpressten Spulen für effizientere E-Traktionsantriebe; 2019;
Urn: urn:nbn:de:bvb:91-diss-20191001-1483133-1-0

18   *Patrick Thomas Helmut Woisetschläger*
Beitrag zur Optimierung der Schichtanbindung bei
thermisch gespritzten Zylinderlaufflächen im Verbrennungsmotor;
2020; ISBN: 978-3-95884-042-3

19   *Michael Walter Krinninger*
Ansätze zur Reduzierung der prozessbedingten Flitterbildung
beim Scherschneiden von Aluminiumblechen im offenen Schnitt;
2020; ISBN: 978-3-95884-045-4

20   *Tim Benkert*
Blechradkörper für Leichtbauzahnräder – Eine Machbarkeitsstudie zur
Herstellung von tiefgezogenen und feingeschnittenen Innenteilen
mehrteiliger Zahnräder; 2020; ISBN: 978-3-95884-046-1

21   *Benjamin Himmel*
Material Jetting of Aluminium – Analysis of a Novel Additive
Manufacturing Process; 2020; ISBN: 978-3-95884-049-2

22   *Florian Martin Hofbauer*
Großserientaugliche Umsetzung von dünnwandigem Stahlguss
für den Automobilbau; 2020; ISBN: 978-3-95884-050-8

23   *Annika Weinschenk*
Simulative und experimentelle Untersuchungen zur Detektion und
Prävention von Einfallstellen in Außenhautbauteilen; 2020;
ISBN: 978-3-95884-052-2

24   *Florian Heilmeier*
Ermittlung schwindungsbedingter Gussteilspannungen mit Hilfe
eingegossener, faseroptischer Dehnungssensoren; 2020;
ISBN: 978-3-95884-053-9

25   *Ferdinand Neumayer*
Ermittlung und Auswirkung der Durchbruchkraft beim Scherschneiden;
2020; Urn: urn:nbn:de:bvb:91-diss-20200729-1530885-1-5

26   *Manuel Pintore*
Gießtechnische Herstellung und technologische Charakterisierung
von Kupfer-Aluminium-Schichtverbunden; 2021;
ISBN: 978-3-95884-059-1

27   *Tim Mittler*
Verbundstranggießen von Kupferwerkstoffen; 2021;
ISBN: 978-3-95884-058-4

28   *Christoph Hartmann*
Spatio-Temporal Optical Flow Methods for Process Analysis
– Robust Strain, Strain Rate, and Crack Propagation Measurement
 in Shear Cutting; 2021; ISBN: 978-3-95884-066-9